

The role of thioredoxin and T-type Ca²⁺ channels in vascular smooth muscle cell proliferation

Emily Louise Johnson

Submitted in accordance with the requirements for the degree of Doctor
of Philosophy

The University of Leeds, Faculty of Medicine and Health, Leeds Institute of
Cardiovascular and Metabolic Medicine, Division of Cardiovascular and
Diabetes Research

April 2016

Intellectual Property and Publication Statements

The candidate confirms that the work submitted is her own, except where work which has formed part of jointly authored publications has been included. The contribution of the candidate and the other authors to this work has been explicitly indicated below. The candidate confirms that appropriate credit has been given within the thesis where reference has been made to the work of others. Work from the following jointly authored publication has been included within Chapter 3

- Duckles, H., Boycott, H.E., Al-Owais, M.M., Elies, J., Johnson, E., Dallas, M.L., Porter, K.E., Giuntini, F., Boyle, J.P., Scragg, J.L., & Peers, C. (2015). Heme oxygenase-1 regulates cell proliferation via carbon monoxide-mediated inhibition of T-type Ca^{2+} channels. *Pflugers Arch.* **467**, (2) 415-427.

I contributed to the patch-clamp electrophysiology of A7r5 cells examining the effects of CO, nifedipine and NNC55-0396 on native Ca^{2+} currents (with Dr Jacobo Elies) and also to the proliferation assays examining the effects of NNC55-0396 on A7r5 cells. All other experiments were conducted by Dr Hayley Duckles with following exceptions. Dr Hannah Boycott conducted some of the proliferation assays using recombinant Cav3.2-expressing and wt HEK293 cells and also gathered preliminary data. Dr Karen Porter designed the proliferation assay protocol and contributed to the saphenous vein smooth muscle cell isolation. Dr Francesca Giuntini synthesised the CORM-3. Professor Chris Peers, Dr Jason Scragg and Dr John Boyle contributed to paper authorship, project design and management. Dr Moza Al-Owais and Dr Mark Dallas contributed to preliminary data and provided technical expertise.

This copy has been supplied on the understanding that it is copyright material and that no quotation from the thesis may be published without proper acknowledgement

© 2016 The University of Leeds, Emily Louise Johnson

The right of Emily Louise Johnson to be identified as Author of this work has been asserted by her in accordance with the Copyright, Designs and Patents Act 1988.

Acknowledgements

Firstly, I would like to thank my supervisors Prof Chris Peers and Dr Jason Scragg for their excellent supervision, advice, support and guidance. Without your help this work would not have been possible. Also, many thanks to Dr John Boyle, Dr Jacobo Elies, Dr Hayley Duckles, Dr Nishani Hetterachi and Dr Moza Al-Owais, for teaching me new techniques patiently, offering practical and emotional support and for making the time to discuss ideas and problems. Thanks to David Myers and Philip Warbuton for your practical support. To the Peers' group as a whole including Faye Garrod and Jack Garnham, thanks to all of you for helping to create such a nice working environment and for making my PhD enjoyable.

To my wonderful family, friends and Andrew, thank you for your encouragement, love and support, for putting up with my single-mindedness and absences and for helping me see the bigger picture when I needed it.

Last but not least, thanks to the British Heart Foundation for funding this project.

Abstract

Elevated vascular smooth muscle cell (VSMC) proliferation is a feature of various cardiovascular conditions including restenosis, abdominal aortic aneurysm (AAA) and atherosclerosis. Voltage-gated T-type Ca^{2+} channels are implicated in VSMC proliferation as their expression is markedly up-regulated in proliferative phases of the VSMC cell-cycle (Kuga et al., 1996). The Thioredoxin (Trx) system is also associated with proliferative disorders of the heart and vasculature, e.g. Trx concentrations are elevated in AAA (Martinez-Pinna *et al.*, 2010) and atherosclerosis (Okuda *et al.*, 2001). Trx has recently been shown to regulate T-type Ca^{2+} channels (Boycott et al., 2013). This PhD has investigated the hypothesis that VSMC proliferation is modulated by interactions between Trx and T-type Ca^{2+} channels.

Proliferation assays revealed that the T-type Ca^{2+} channel inhibitor NNC55-0396 (NNC, 1-3 μM) decreased A7r5, HEK293/ $\text{Ca}_v3.1$ and HEK293/ $\text{Ca}_v3.2$, but not wt HEK293, cell proliferation. In contrast the L-type Ca^{2+} channel inhibitor nifedipine (2 μM) was without effect. The Trx inhibitors PX-12 (1 μM) and auranofin (AuF, 300nM) preferentially inhibited the proliferation of $\text{Ca}_v3.2$ -expressing cells, i.e. A7r5 and HEK293/ $\text{Ca}_v3.2$ cells. Basal Ca^{2+} influx in A7r5 cells was also significantly reduced by NNC (3 μM) and AuF (3 μM). Whole-cell patch-clamp recordings in recombinant cells revealed that PX-12 (1-300 μM) inhibited $\text{Ca}_v3.1$ and $\text{Ca}_v3.2$ currents with similar sensitivities. In contrast, Trx (4 $\mu\text{g}\cdot\text{ml}^{-1}$) enhanced $\text{Ca}_v3.2$, but not $\text{Ca}_v3.1$, peak current amplitude. Similarly, AuF (3 μM) selectively reduced the current-density of HEK293/ $\text{Ca}_v3.2$ cells. Data suggest that $\text{Ca}_v3.2$ channels are positively and selectively regulated by Trx, yet PX-12 could inhibit T-type Ca^{2+} channels independently of Trx. The sensitivity of $\text{Ca}_v3.2$ channels to Trx was found to be dependent on an extracellular histidine residue at position 191 (H191), especially as mutation to a glutamine (Q) residue (H191Q) abolished Trx-sensitivity. In summary, these data indicate that interactions between Trx and $\text{Ca}_v3.2$ channels can regulate the proliferation of $\text{Ca}_v3.2$ -expressing cells.

Table of contents

<i>Heading</i>	<i>page</i>
Intellectual Property and Publication Statements	II
Acknowledgements	III
Abstract	IV
Table of contents	V
Figures	XI
Tables	XV
Abbreviations	XVI
Chapter 1 – Introduction	1-46
1.1. Vascular smooth muscle cells (VSMCs) and blood vessels	1
1.1. Vascular smooth muscle cells (VSMCs) and blood vessels	1
1.2. Phenotypic switching, VSMC proliferation and cardiovascular disorders	2
1.2.1. Restenosis	2
1.2.2. Atherosclerosis	4
1.2.3. Aortic aneurysm	6
1.2.4. Hypertension	6
1.2.5. Diabetes	8
1.3. Voltage-gated Ca ²⁺ (Ca _v) channels	9
1.3.1. Structure-function relationships of Ca _v channels	10
1.3.2. T-type Ca ²⁺ channels: three distinct isoforms	12
1.4. Isoform specific expression and physiological roles of Ca _v 3.x channels	17

1.4.1. Peripheral and central nervous system	17
1.4.2. Heart	19
1.4.3. Endocrine tissue	21
1.4.4. Blood vessels and VSMCs	22
1.5. The role of T-type Ca ²⁺ channels in proliferation	28
1.6. The thioredoxin (Trx) system	32
1.6.1. Structure- function relationships of the Trx system	32
1.6.2. The intracellular functions of Trx as a disulphide reductase molecule	36
1.6.3. Emerging roles for Trx as an extracellular signalling molecule	38
1.7. Clinical implications of Trx expression in proliferative disorders	41
1.7.1. Cardiovascular disorders	41
1.7.2. Cancers	44
1.8. Aims and hypothesis:	45
Chapter 2 – Methods and materials	47-70
2.1. Cell culture	47
2.1.1. A7r5 cells	47
2.1.2. wt HEK293 and recombinant HEK293/Ca _v 3.1 and HEK293/Ca _v 3.2 cells	48
2.2. Real-time polymerase chain reaction (qRT-PCR)	48
2.2.1. Cell culture and RNA extraction	49
2.2.2. cDNA generation and qRT-PCR protocol	50
2.2.3. Data analysis- comparative CT method for relative quantification	50
2.3. Immunohistochemistry	51

2.3.1. Image acquisition and analysis	52
2.4. MTT viability assays	52
2.5. Proliferation assays - direct cell counting	54
2.6. Proliferation assays - EdU incorporation assay	55
2.6.1. Cell culture and EdU incubation	56
2.6.2. Cell fixation, permeabilization and EdU detection	56
2.6.3. Image acquisition and analysis	57
2.7. Ca ²⁺ microfluorimetry	57
2.7.1. Cell culture	58
2.7.2. Depolarisation induced intracellular Ca ²⁺ oscillation protocol - A7r5 cells	59
2.7.3. Window current protocol	61
2.7.4. Data analysis	61
2.8. Electrophysiology	62
2.8.1. Cell culture	63
2.8.2. Electrophysiology rig set up	63
2.8.3. Whole-cell recording configuration	64
2.8.4. Single step (SS) voltage protocols	65
2.8.5. Current-voltage (IV) relationship protocol and data analysis	66
2.9. Thioredoxin assays	66
2.9.2. Cell sample preparation	67
2.9.3. Bicinchoninic acid (BCA) assay	68
2.9.4. Assay protocol and data analysis	68
2.10. Preparation of reduced thioredoxin (rTRX)	69

2.11. Statistical analysis	69
Chapter 3 - The role of T-type Ca²⁺ channels in cellular proliferation and [Ca²⁺]_i mobilisation	71-120
3.1. Introduction	71
3.2. Results	72
3.2.1. Characterisation of Ca _v channels in A7r5 cells	72
3.2.2. The effects of subtype specific CCBs on A7r5 proliferation and Ca ²⁺ handling	86
3.2.3. Effects of Ca _v 3.1 and Ca _v 3.2 expression on HEK293 cell proliferation and Ca ²⁺ handling	98
3.2.4. Sub-cellular localisation of Ca _v 3.1 and Ca _v 3.2 within recombinant HEK293 cells	101
3.2.5. T-type Ca ²⁺ channels facilitate the window current in recombinant HEK293 cells.	107
3.3. Discussion	111
3.3.1. A7r5 cells express functional T- and L-type Ca ²⁺ channels	111
3.3.2. Potential expression of HVA T-type Ca ²⁺ channel splice variants	113
3.3.3. T-type Ca ²⁺ channels regulate A7r5 proliferation.	114
3.3.4. T- and L-type Ca ²⁺ channels regulate basal and oscillatory Ca ²⁺ levels within A7r5 cells	115
3.3.5. Recombinant expression of Ca _v 3.1 and Ca _v 3.2 increases cellular proliferation and window current.	119
3.3.6. Summary and conclusions	120
Chapter 4 - The role of thioredoxin (Trx) in cellular proliferation and [Ca²⁺]_i handling	121-163
4.1. Introduction	121
4.2. Results	123

4.2.1. Trx measurement within A7r5 and recombinant HEK293 cells	123
4.2.2. The effects of Trx inhibitors on A7r5 cell viability and proliferation	128
4.2.3. The effects of AuF on A7r5 Ca ²⁺ handling	133
4.2.4. Effects of Trx inhibitors on HEK293 cell viability and proliferation	138
4.3. Discussion	148
4.3.1. Comparison of methods for the quantification of endogenous Trx levels	148
4.3.2. High concentrations of Trx inhibitors induce cell death	152
4.3.3. Low concentrations of Trx inhibitors selectively reduce cellular proliferation in Ca _v -expressing cells.	155
4.3.4. The potential for Trx as a T-type Ca ²⁺ channel modulator	162
4.3.5. Summary and conclusions	163
Chapter 5 -The effects of thioredoxin (Trx) and inhibitors on voltage-gated Ca²⁺ (Ca_v) channels	164-204
5.1. Introduction	164
5.2. Results	165
5.2.1. The effects of Trx inhibitors on native and recombinant T-type Ca ²⁺ currents	165
5.2.2. Mechanism of Trx-mediated Ca _v 3.2 regulation	180
5.3. Discussion	191
5.3.1. Trx regulates Ca _v 3.2 channels via an extracellular histidine residue at position 191 (His191)	191
5.3.2. PX-12 may inhibit Ca _v 3.x channels via interaction with conserved cysteine residues	196
5.3.3. Potential interaction of Trx with Ca _v 3.2 channel trace metal binding	199

5.3.4. Summary and conclusions	204
Chapter 6 - The implications of Trx-mediated Ca_v3.2 channel regulation on cellular proliferation	205-213
6.1. Principle findings	205
6.1.1. HEK293 cells	205
6.1.2. A7r5 cells	206
6.2. Clinical significance	207
6.2.1. Hypoxia-induced vascular remodelling	207
6.2.2. MI-induced cardiac remodelling	209
6.2.3. Cancer	211
6.3. Summary and conclusion	212
References	214-236

Chapter 1 - Introduction

This PhD project has explored the regulation of T-type Ca^{2+} channels by thioredoxin (Trx) and the potential significance of this modulation on vascular smooth muscle cell (VSMC) proliferation. The following introduction initially outlines a range of cardiovascular disorders associated with pathological VSMC proliferation. Central observations detail how increased levels of T-type Ca^{2+} channels and Trx have coincidentally been reported in numerous proliferative disorders. The established structure-function relationships, expression profiles and physiological roles of T-type Ca^{2+} channels and Trx are subsequently discussed in detail.

1.1. Vascular smooth muscle cells (VSMCs) and blood vessels

Within the human body, the walls of arteries and veins are composed of three layers. The outer tunica adventitia is made up of connective tissue, the central tunica media is comprised of VSMCs and structural proteins i.e. collagen and elastin, and the internal tunica intima is formed by endothelial cells. Compared to veins, the medial layer of arteries is considerably thicker, as summarised by Figure 1.1. This underpins the greater tensile strength and elasticity of arterial vessels. Capillaries are contrastingly made up of a single intimal layer supported by pericytes (Zhang & Wang, 2015). VSMCs typically align circumferentially within the medial layer of blood vessels and are also present within the walls of organs and bronchi. Typically $100\mu\text{m} \times 5\mu\text{m}$ in size, differentiated VSMCs are spindle shaped in appearance. The contraction and relaxation of VSMCs underlies their primary function in the regulation of blood vessel diameter and correspondingly local blood flow (Matsumoto & Nagayama, 2012).

VSMC function is heavily reliant on Ca^{2+} signalling which is influenced by numerous factors including Ca^{2+} influx via plasma membrane channels and also Ca^{2+} release from internal stores. Regarding contraction, depolarisation of the VSMC plasma membrane can activate voltage-gated L-type Ca^{2+} channels which facilitate Ca^{2+} influx and large increases in intracellular Ca^{2+} levels ($[\text{Ca}^{2+}]_i$). Subsequent activation of Ca^{2+} /calmodulin-dependent myosin light chain kinase (MLCK) initiates VSMC contraction. Increases in $[\text{Ca}^{2+}]_i$ also activates ryanodine receptors (RyR) on the surface of the sarcoplasmic

reticulum (SR), leading to Ca^{2+} -induced Ca^{2+} release (CICR) and subplasmalemmal Ca^{2+} sparks. Activation of Ca^{2+} -activated K^+ channels can then repolarise the VSMC and enable blood vessel relaxation. Contraction of VSMCs occurs slowly and often tonically, which directly contrasts with the rapid contractile activities of cardiac myocytes, as reviewed (House *et al.*, 2008).

Excessive VSMC proliferation is a common pathological feature observed in a variety of cardiovascular disorders. VSMCs exhibit considerable phenotypic plasticity and readily dedifferentiate from their contractile phenotype in response to functional demand. There are several non-contractile phenotypes including proliferative, migratory and inflammatory VSMCs. This process of dedifferentiation is referred to as the “phenotypic switch” and is a key feature of normal blood vessel development and repair. Whilst adult VSMCs typically exhibit a stable contractile phenotype, in pathological conditions such as restenosis, hypertension and atherosclerosis, phenotypic switching is common. This often results in excessive VSMC proliferation and a narrowing of lumen diameter (Matchkov *et al.*, 2012), as shown in Figure 1.1(B). The following section discusses the significance of pathological VSMC proliferation within the development of specific cardiovascular disorders.

1.2. Phenotypic switching, VSMC proliferation and cardiovascular disorders

1.2.1. Restenosis

Restenosis is a common consequence of surgical vascular intervention, such as coronary artery bypass grafting. Arbitrarily defined as $\geq 50\%$ narrowing of luminal vessel diameter, restenosis is characterised by increased VSMC proliferation and migration, growth factor release, platelet aggregation and inflammatory cell invasion. Vascular injury produces platelet deposition which release mitogenic factors and cytokines, such as platelet-derived growth factor (PDGF). This stimulates the phenotypic switch and subsequent VSMC proliferation and migration. Two weeks post-injury, VSMCs can multiply 3-5 times resulting in neointima formation and luminal narrowing (Marx *et al.*, 2011).

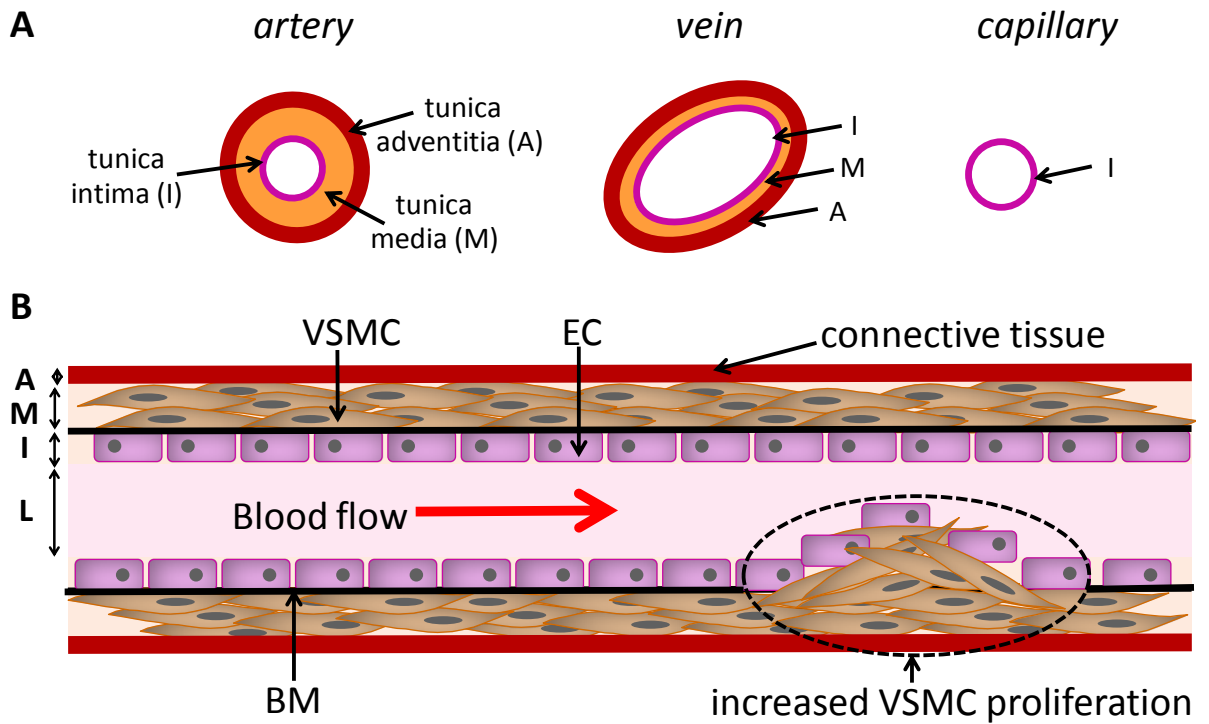


Figure 1.1. Schematic diagrams showing blood vessel structure

The walls of arteries and veins are made up of three layers: tunica adventitia (A), tunica media (M) and tunica intima (I). **A**, representative cross-sectional views of showing the thickness of layers within an artery, vein and capillary **B**, representation of the internal structure of an artery showing endothelial cells (ECs) within the intima on top of the basement membrane (BM), vascular smooth muscle cells (VSMCs) within the media and connective tissue comprising the adventitia. Dashed oval area highlights increased VSMC proliferation and subsequent narrowing of the lumen (L). Diagrams adapted from Clemmons (2007) and Lafleur *et al*, (2003).

Quiescent or contractile VSMCs are maintained in the non-proliferative G_0 phase of the cell-cycle. Following vascular injury, growth factors stimulate VSMCs to enter the G_1 gap phase, where factors are produced for DNA replication within the subsequent synthetic (S) phase. Cells then progress to the G_2 gap-phase where protein synthesis occurs prior to mitosis (M phase). Restriction (R) phases, at the interfaces of G_1 -S and G_2 -M, enable the regulation of VSMC cell-cycle progression by various factors including cyclins and cyclin-dependent kinases (CDKs). Regarding VSMC migration, activation of cell-surface receptors initiates remodelling of the cytoskeleton, reduces matrix adhesiveness and activates motor proteins. As VSMC migration can only occur within the G_1 phase of the cell-cycle, it is intimately associated with proliferation (Marx *et al*, 2011).

Carotid artery ligation or wire injury is commonly used to induce neointima formation in animals, and provides an effective model of arterial stenosis. For example, wire injury of carotid arteries of mice led to increased VSMC proliferation and significant neointima formation 2 weeks post-surgery (Lindner *et al.*, 1993; Tzeng *et al.*, 2012). Immunohistochemical staining demonstrated that VSMCs were the primary cell type within the neointimal tissue. 5-Bromo-2'-deoxyuridine (BrdU) labelling further revealed that the neointimal VSMCs were proliferative (Tzeng *et al.*, 2012). Interestingly, genetic knockdown of matrix metalloprotein-8 (MMP-8) within mice subjected to carotid wire injury significantly reduced VSMC proliferation and neointima formation. *In vitro* proliferation assays confirmed that VSMCs lacking MMP-8 exhibited slower proliferative rates and considerably less migration compared to controls (Xiao *et al.*, 2014).

1.2.2. Atherosclerosis

Atherosclerosis, an increasingly common chronic disease of the arterial wall, is a leading cause of death in the developed world (Barquera *et al.*, 2015). Atherosclerotic remodelling of blood vessel walls is heavily reliant on the VSMC phenotypic switch. VSMCs can also transdifferentiate into macrophage- and chondrocyte-like cells which additionally contribute to atherosclerotic plaque formation. Whilst proliferative VSMCs of local origin are the major component in atherosclerotic plaques, circulating peripheral blood mononuclear cells can also transform into VSMCs (Martin *et al.*, 2009). Within the intima of arteries, oxidation of low-density lipoprotein (LDL) is thought to provide the initial atherogenic factor. Lectin-type oxidised LDL (ox-LDL) receptors type-1 (LOX-1) are the primary mediators of ox-LDL activity and are expressed by VSMCs and endothelial cells (ECs) (Pirillo *et al.*, 2013). Within VSMCs, LOX-1 activation promotes the dedifferentiation of VSMCs to proliferative and migratory phenotypes (Liu *et al.*, 2014). At higher concentrations, ox-LDL can also initiate VSMC apoptosis, which destabilises the plaque eventually leading to its rupture. Plaque rupture is a serious event which can lead to acute coronary events such as myocardial infarction (MI). Arterial branch points are highly susceptible to atherosclerotic plaque formation due to disturbed (i.e. non-laminar) blood flow, leading to shear stress and VSMC dedifferentiation. Whilst laminar blood flow down-

regulates mitogenic factors, disturbed flow stimulates the vascular endothelium to secrete pro-inflammatory cytokines and adhesion molecules, such as interleukin-8 (IL-8) and vascular cell adhesion molecule-1 (VCAM-1). Adhesion molecules attract monocytes which secrete interleukin-1 β (IL-1 β) and tumour necrosis factor- α (TNF- α). The VSMC phenotypic switch is subsequently activated. During the advancement of plaque formation localised plaque regions are subject to different patterns of shear stress. Specifically, high shear stress at the plaque cap can induce VSMC apoptosis and subsequent plaque rupture, whilst lower shear stress levels around plaque shoulders increases VSMC proliferation and correspondingly plaque size (Fan & Karino, 2010). It is also important to consider that changes in many other factors, including gene expression, basal lamina (BM) composition and VSMC calcification have also been found to influence atherosclerotic phenotypic switching of VSMCs, as reviewed (Chistiakov *et al.*, 2015).

Atherosclerosis is a multi-factorial disease involving accumulation of foam cells and formation of fatty streaks in addition to plaque formation. The disease is also associated with complications such as aneurysms, blood vessel calcification, thrombosis and stenosis. As such, the development of an effective animal model encompassing all of these features has proven challenging (Kapourchali *et al.*, 2014). Apolipoprotein E (apoE) is a glycoprotein which is involved in the clearance of lipoproteins from the circulation. Correspondingly, although appearing healthy, apoE knockout (KO) (apoE^{-/-} or apoE^{+/-}) mice have increased circulating cholesterol and triglyceride levels, develop spontaneous foam-cell rich deposits within proximal aorta and show evidence of fatty streaks. Progressive occlusion of coronary arteries was also observed in these mice (Zhang *et al.*, 1992). As such, apoE-deficient mice are routinely used to study the induction and prevention of atherosclerosis. For example, treatment of apoE^{-/-} mice with S-adenosyl-homocysteine significantly increased VSMC proliferation and migration, leading to larger atheromatous plaque formation. These effects were attenuated by the antioxidant enzyme superoxide dismutase and thus confirmed a role for oxidative stress in the development of atherosclerosis (Luo *et al.*, 2012).

1.2.3. Aortic aneurysm

Localised or diffuse dilation of the aorta to $\geq 50\%$ normal diameter is classified as an aortic aneurysm. Aneurysms can occur throughout the body although aortic aneurysms are particularly common within the thoracic abdomen, where they are termed thoracic abdominal aortic aneurysms (TAAA). Upon diagnosis, TAAAs are generally asymptomatic however resultant acute aortic dissection can lead to peripheral malperfusion, cardiac tamponade, paraplegia, stroke and aortic regurgitation (Goldfinger *et al.*, 2014). Correspondingly, TAAAs are associated with high mortality and morbidity rates, and are increasingly prevalent. The incidence and likelihood of TAAA rupture (i.e. aortic dissection) correlates with co-morbid atherosclerosis and hypertension. Generally, aneurysms involve all three layers of the blood vessel wall. TAAAs put considerable strain on the aorta and dissection occurs via intimal tearing. This leads to separation of the aortic wall and the false passage of blood. Increased activity of MMPs can induce matrix degradation and medial degeneration which correspondingly weakens and reduces the elasticity of the aorta, as reviewed (Zhang & Wang, 2015). The role of the VSMC phenotypic switch within aneurysm development was also recently explored in more detail. Rat TAAA was successfully induced by soaking sections of aorta with porcine pancreatic elastase (PPE). Significant thickening of the aortic wall around the site of PPE administration was found to correspond with VSMC phenotypic switching. This was evident by a decline in contractile VSMC markers such as α -smooth muscle cell actin (α -SMA) and smooth muscle myosin heavy chain (SM-MHC). An increase in proliferative markers such as MMP-2 was also observed. In addition, VSMCs isolated from TAAA rats proliferated at a significantly higher rate when compared to those isolated from control animals (Mao *et al.*, 2015). As these pathological characteristics correlated closely with observations made in human thoracic aortic dissection (Wang *et al.*, 2012), the PPE animal model of AAA was validated.

1.2.4. Hypertension

Isolated clinical hypertension is defined by persistently elevated blood pressure, with mean daytime ambulatory values $> 135/85$ mmHg (Cuspidi *et al.*, 2007). Secondary hypertension is directly linked to a cause, such as renal disease or pheochromocytoma.

In contrast, essential hypertension accounts for approximately 90-95% of all hypertension cases, and is an insidious disease without an identifiable primary cause. Hypertension can lead to cardiac overload, aneurysms and organ damage. In patients with established hypertension, cardiac output remains unaltered whilst changes in total peripheral resistance (TPR) account for increases in blood pressure. In addition to functional changes (e.g. vascular tone), structural changes in resistance vessels resulting in luminal narrowing and increased intima/lumen ratios can contribute to increased TPR (Mulvany, 2012). Pulmonary hypertension (PH) relates to a group of individual conditions with differential causes, which share common hemodynamic dysfunction. Specifically, persistently elevated mean pulmonary arterial pressure leads to right ventricular (RV) overload, hypertrophic remodelling, RV failure and ultimately death (Bogaard *et al.*, 2009). While PH is commonly secondary to an underlying condition, familial and idiopathic forms also exist. The majority of research into PH relates to pulmonary artery hypertension (PAH), which is characterised by sustained vasoconstriction and remodelling of pulmonary vessels. Remodelling is believed to occur in response to pulmonary artery EC (PAEC) death and dysfunction. This has been shown to trigger the proliferation and migration of pulmonary artery SMCs (PASMCs), fibroblasts and PAECs (Hassoun *et al.*, 2009). Increased VSMC proliferation leads to a thickening of the medial layer of vessel walls and is accompanied by the formation of plexiform lesions and intimal fibrosis. This leads to the progressive obliteration of small-resistance pulmonary arteries and arterioles, a pathological hallmark of PAH (Vaillancourt *et al.*, 2015).

Current therapies aim to redress the functional effects of PH, for example by reducing vasoconstriction. The potential of targeting structural remodelling by reducing PASMC proliferation however, although suggested (Paulin *et al.*, 2014), remains clinically unexplored. The validity of various animal models of PH is a widely debated topic. It is correspondingly suggested that reliable assessment of novel therapeutics should involve at least two different models. The most commonly used method to induce PH within mice and rats is by exposure to chronic hypoxia (CH) or injection of monocrotaline (MCT). Single-pathological-insult (SPI) models, such as the two mentioned above, can be combined to produce multiple-pathological-insult (MPI) models, which exhibit more severe PH phenotypes (Lawrie, 2014; Maarman *et al.*,

2013). Specifically, exposure of mice to hypoxic conditions (10% O₂ and 90% N₂) for 4 weeks increased VSMC proliferation leading to medial thickening of pulmonary arteries. This was accompanied by increased RV systolic pressure and an increased ratio weight of the right ventricle, compared to the left ventricle plus septum. This study revealed that cyclophilin A (CyPA), which is secreted by VSMCs under conditions of oxidative stress, promotes VSMC proliferation and plays a key role in the pathogenesis of PH (Sato *et al.*, 2014). An alternative study subjected mice to the hypoxia SPI model, and rats to MCT and Su5416 SPI models. Brain derived neurotrophic factor (BDNF) was found to promote PASMCM proliferation in PH, in all three SPI models (Kwapiszewska *et al.*, 2012).

1.2.5. Diabetes

One of the caveats when assessing the effects of hypertension on blood vessel lumen diameter in humans is that many hypertensive patients often also suffer from diabetes (Rizzoni *et al.*, 2003). This is significant as diabetes itself is associated with pressure-independent arterial remodelling. Type 2 diabetes mellitus (T2DM) is an increasingly common chronic metabolic and inflammatory disease which accelerates vascular aging. It also commonly leads to numerous other cardiovascular complications such as restenosis and atherosclerosis. A growing amount of evidence shows that the metabolic disturbances caused by dysregulated blood glucose alter the phenotype of VSMCs which contribute to the increased incidence of macrovascular complications. Endothelial damage is believed to be an early pathological event in pre-diabetic patients. In addition, EC abnormalities are also commonly observed in T2DM, as reviewed (Porter & Riches, 2013). When human VSMCs isolated from T2DM patients are cultured *ex vivo* and compared with VSMCs isolated from non-diabetic patients, significant alterations in VSMC morphology are observed. Specifically, T2DM VSMCs have a flattened rhomboid morphology in contrast to the elongated “hill and valley” spindle-shaped morphology, which typifies contractile VSMCs. In addition, T2DM VSMCs have significantly elevated proliferative rates and show considerably more migration and adhesion. Collectively, this indicates that T2DM stimulates the dedifferentiation of VSMCs (Faries *et al.*, 2001).

There are numerous animal models of T2DM ranging from a leptin receptor mutant mouse (*db/db*), equivalent Zucker diabetic fatty (ZDF) rat model and diet-induced metabolic syndrome porcine models. These animal models have been shown to recapitulate many of the pathological features of T2DM, although to varying extents (Porter & Riches, 2013). Animal models of specific T2DM pathologies such as nephropathy (Betz & Conway, 2016), retinopathy (Jiang *et al.*, 2015) and neuropathy (Gao & Zheng, 2014) are also commonly implemented. For example, an experimental study examined the aorta of ZDF and obese Zucker rats (an alternative metabolic T2DM model) and compared them against controls, i.e. lean Zucker rats. The anti-proliferative effects of nitric oxide (NO) on aortic VSMCs isolated from T2DM rats were significantly greater than in controls. The degree of neointima formation induced by carotid artery wire injury was also far greater in T2DM rats (Ahanchi *et al.*, 2008).

To summarise, the dedifferentiation of VSMCs to a proliferative phenotype is a common pathology in a wide range of cardiovascular disorders which are associated with high degrees of mortality and morbidity. By developing a more detailed understanding of the mechanisms involved in phenotypic switching and elevated VSMC proliferation, the identification of much needed novel therapeutics may be possible.

1.3. Voltage-gated Ca^{2+} (Ca_v) channels

Considerable differences in $[Ca^{2+}]_i$ dynamics between different VSMC phenotypes are well established. Specifically, dedifferentiated VSMCs exhibit Ca^{2+} handling responses more typical of non-excitable cells such as sustained elevations in basal $[Ca^{2+}]_i$ (House *et al.*, 2008). Of significant interest to the current investigation is that dramatic changes in voltage-gated Ca^{2+} (Ca_v) channel expression are observed in proliferating VSMCs. Principally, a sharp decline in L-type Ca_v channels which mediate VSMC contraction, and a corresponding increase in T-type Ca_v channels which are believed to be crucial for cell-cycle progression (Kuga *et al.*, 1996).

In addition to being expressed in the majority of excitable cells, Ca_v channels are also present within the VSMC membrane. Activated by membrane depolarisation, Ca_v

channels facilitate Ca^{2+} influx which can stimulate a wide variety of cellular processes. As such, Ca^{2+} can function as a second messenger to electrical signalling. Within mammalian cells there are 10 subtypes of Ca_v channels which serve distinct roles in signal transduction. Ca_v channels are broadly categorised into two groups, high-voltage activated (HVA) and low-voltage activated (LVA). Biochemical, molecular cloning and co-expression studies have shown that HVA Ca_v channels are heteromeric protein complexes, which require the co-assembly of pore forming α_1 subunits with auxiliary β , $\alpha_2\delta$ and γ subunits. In contrast, LVA channels are rendered fully functional by expression of a single α_1 subunit, although auxiliary subunits may alter LVA channel trafficking (Catterall, 2011).

1.3.1. Structure-function relationships of Ca_v channels

The α_1 subunit is the key determinant of the Ca_v subtype. HVA channels include: L-type ($\text{Ca}_v1.1-1.4$), P- or Q-type ($\text{Ca}_v2.1$), N-type ($\text{Ca}_v2.2$) and R-type ($\text{Ca}_v2.3$) Ca_v channels. LVA channels or T-type Ca^{2+} channels facilitate tiny transient currents. Three distinct T-type isoforms ($\text{Ca}_v3.1-3.3$) have been identified, which are encoded by separate α_1 subunits (α_{1G} , α_{1H} and α_{1I} respectively). Key differences between LVA and HVA channels is that T-type Ca^{2+} channels are activated at relatively lower voltages, and inactivate over a shorter time period at comparatively lower membrane potentials, as reviewed extensively (Catterall, 2011; Perez-Reyes, 1999; Perez-Reyes, 2006; Simms & Zamponi, 2014).

Mammalian α_1 subunits are comprised of approximately 2000 amino acids and share a common membrane topology predicted to be similar to that of voltage-gated Na^+ (Na_v) channels. As illustrated by Figure 1.2 (A), α_1 subunits are arranged into four domains (DI-DIV) which are each made up of 6 transmembrane segments (S1-S6). DI-DIV arrange in a clockwise manner within the lipid bilayer to form the 3D α_1 subunit structure (Figure 1.2 (B)). A key feature within each domain is the charged S4 segment which controls voltage-dependent activation. The S4 segment is believed to physically orientate within the centre of each domain. It is thought that S4 segments slide upwards upon depolarisation to open the Ca_v channel. Conversely, upon repolarisation downward movement of S4 segments may close Ca_v channels. A further notable

feature is the P-loop, which forms between S5-S6 of each domain. The pore loops project to the centre of the channel to form a selectivity filter, which provides the ion permeation pathway (Figure 1.2 (B)). Highly conserved, negatively charged amino acid residues within the P-loop impart a high degree of Ca^{2+} selectivity. Within HVA channels, this sequence is composed of four Glu residues (EEEE), whereas aspartic acid residues also contribute to the selectivity filter of T-type Ca^{2+} channels (EEDD). The four domains of the α_1 subunit are connected by large cytoplasmic linker regions. The N- and C-termini, linked to DI and DIV respectively, are both cytoplasmic. The greatest amount of sequence variation between Ca_v subtypes is observed within cytoplasmic regions. Specifically, within the large repeats joining DI-DII and DII-DIII and within the relatively smaller linker region between DIII-DIV, illustrated in Figure 1.2(A). Within HVA channels, these regions provide an important contact site for regulatory proteins and auxiliary subunits. In contrast with LVA channels, the expression of auxiliary subunits is crucial for membrane trafficking and the overall biophysical properties of HVA channels (Perez-Reyes, 1999).

Prolonged depolarisation of the plasma membrane can result in Ca^{2+} overload, therefore most Ca_v channels possess both Ca^{2+} - and voltage-dependent inactivation mechanisms. The extent of voltage-dependent inactivation (VDI) varies drastically between different Ca_v subtypes. For HVA channels, VDI involves structural rearrangement of S6 segments to expose a docking site within the DI-DII linker region. VDI of HVA channels is also profoundly influenced by β subunit expression. Compared to HVA channels, T-type Ca^{2+} channels show considerably more VDI, predicted to involve the DIII-DIV cytoplasmic linker region acting as an inactivation particle. It is important to emphasise that resolution of the crystal structure of Ca_v channels will ultimately be required to fully determine structure-function relationships (Simms & Zamponi, 2014).

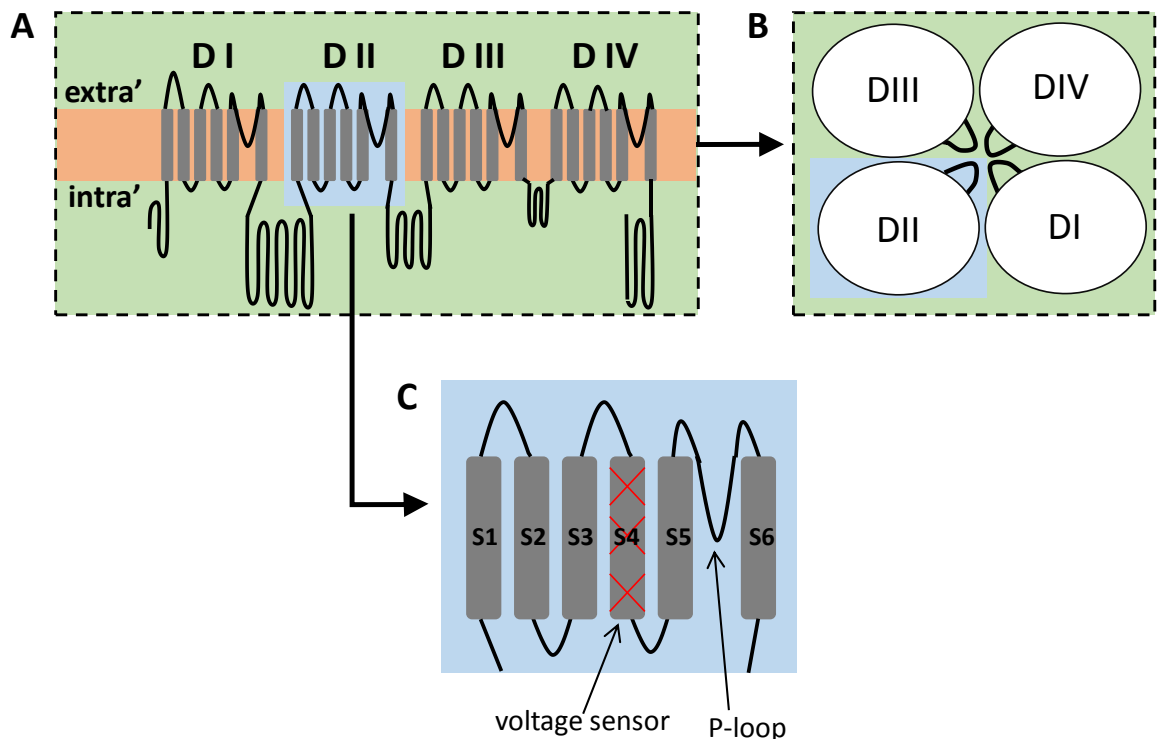


Figure 1.2. Schematic diagrams showing the structure of the Ca_v channel α_1 subunit
 All mammalian α_1 subunits share a similar membrane topology; i.e. four repeated domains (DI-DIV), each made up of 6 transmembrane segments (S1-S6). Views as though: (A, C) looking through a cross-section of a stretched lipid bilayer and (D, E) looking down on the channel from outside the cell. **A**, Snake-diagram showing the arrangement of the α_1 subunit within the lipid bilayer (orange box), DII is highlighted (blue box) and magnified in C. **B**, 3-dimensional (3D) representation of the predicted arrangement of DI-DIV, with pore loops angling towards the centre of the channel, DII is highlighted (blue box) and magnified in D. **C**, 2D structure of a single α_1 subunit domain (DII) magnified from (A), showing the S4 voltage-sensor (red hatched lines) and the pore loop between S5-S6, as labelled. Diagrams adapted from Perez-Reyes (1999).

1.3.2. T-type Ca^{2+} channels: three distinct isoforms

The expression of T-type Ca^{2+} ($\text{Ca}_v3.x$) channels has been identified in a number of species, ranging from humans to snails. By comparing the amino acid sequences of $\text{Ca}_v3.x$ channels isolated from human, cow, dog, rat and mice, several isoform specific differences are apparent. Between the five aforementioned species, $\text{Ca}_v3.1$ channels show the highest degree of sequence homology (90-95%), $\text{Ca}_v3.2$ channels show the lowest (70-80%) and $\text{Ca}_v3.3$ channels show an intermediate degree (85-90%). A high degree of evolutionary conservation indicates that $\text{Ca}_v3.1$ channels serve crucial physiological roles. Conversely, the lower degree of evolutionary conservation between $\text{Ca}_v3.2$ channels predicts that these channels have more diverse modulatory functions (Perez-Reyes, 2006).

In order to isolate T-type Ca^{2+} currents from native tissues, a major goal has been to identify specific pharmacological T-type Ca^{2+} channel blockers (CCBs). An early electrophysiological study conducted in rabbit sinoatrial (SA) node myocytes revealed that LVA currents were inhibited by Ni^{2+} ($40\mu\text{M}$), which was without effect on HVA currents (Hagiwara *et al.*, 1988). However, subsequent studies have noted considerable variation in the level of Ni^{2+} -sensitivity of LVA channels recorded from different tissues. Providing an extreme example, LVA currents recorded from rat clonal pituitary (GH3) cells showed Ni^{2+} -sensitivity comparable to HVA currents (IC_{50} of $777\mu\text{M}$) (Herrington & Lingle, 1992). Further investigation using recombinant expression systems revealed considerable differences in $\text{Ca}_v3.x$ isoform sensitivity. Specifically, when expressed in HEK293 cells, $\text{Ca}_v3.2$ channels were inhibited by significantly lower Ni^{2+} concentrations (IC_{50} of $13\mu\text{M}$) when compared to $\text{Ca}_v3.1$ and $\text{Ca}_v3.3$ channels (IC_{50} values of $250\mu\text{M}$ and $216\mu\text{M}$ respectively) (Lee *et al.*, 1999). As such, the differential Ni^{2+} -sensitivity of LVA currents recorded in native tissues is attributable to differential $\text{Ca}_v3.x$ channel isoform expression profiles.

A variety of preceding investigations generated chimeric $\text{Ca}_v3.x$ channels, whereby individual domains of the $\text{Ca}_v3.2$ channel were substituted with equivalent domains from an alternative $\text{Ca}_v3.x$ isoform. In combination with site-directed mutagenesis, these studies revealed a unique metal binding site within DII of the $\text{Ca}_v3.2$ channel, composed of an Asp-Gly-His (D189, G190, H191) motif within the extracellular S3-S4 loop. An additional Asp residue (D140) on the extracellular surface of S2 was also found to participate. This high affinity binding site was subsequently found to mediate the binding of endogenous trace metals such as zinc (Zn^{2+}). Interestingly, Zn^{2+} is thought to bind tonically to $\text{Ca}_v3.2$ channels in an isoform-specific manner (Kang *et al.*, 2006; Kang *et al.*, 2010; Nelson *et al.*, 2007b). Trace metal binding at this unique site is believed to stabilise $\text{Ca}_v3.2$ channels in their closed state, as reviewed (Perez-Reyes & Lee, 2014).

A further distinguishing feature of $\text{Ca}_v3.2$ channels is their unique sensitivity to redox modulators. This is highlighted by the observation that both native and recombinant $\text{Ca}_v3.2$ channels are selectively inhibited by ascorbate, whilst $\text{Ca}_v3.1$ and $\text{Ca}_v3.3$ channels are relatively insensitive (Nelson *et al.*, 2007a). Ascorbate is an endogenous

redox agent which can function as both an anti- and pro-oxidant. Regarding its functions as a pro-oxidant, ascorbate can reduce transition metals such as iron and copper to generate reactive oxygen species including hydroxyl radicals (OH^\cdot), via a process termed metal-catalysed oxidation (MCO) (Stadtman, 1991). Interestingly, the His¹⁹¹ residue which forms part of the Ca_v3.2 unique metal binding site has been shown to mediate the inhibitory effects of ascorbate on Ca_v3.2 activity. This indicates that ascorbate may inhibit Ca_v3.2 channels by interacting with metal contaminants bound to the metal binding site and/or by initiating MCO (Nelson *et al.*, 2007a).

Remarkably, ascorbate, Ni²⁺ and Zn²⁺ are the most isoform specific T-type Ca²⁺ channel inhibitors currently available. Ni²⁺ is still occasionally used to differentiate between LVA and HVA channels, although subtype specific pharmacological CCBs are more typically used for this purpose. Mibefradil is a widely used T-type CCB which was originally named Ro 40-5967 and previously licensed as an anti-hypertensive drug. Its potent inhibition of T-type Ca²⁺ channels (IC₅₀ =100nM) was first described in primary cultures of neonatal rat azygos VSMCs, although at higher concentrations (10μM) inhibition of L-type Ca²⁺ currents (66%) was also observed (Mishra & Hermsmeyer, 1994). Subsequent studies have shown that a metabolite of mibefradil accounts for its non-specific inhibition of HVA channels (Bezprozvanny & Tsien, 1995; Wu *et al.*, 2000). NNC55-0396 (NNC) is a structural analogue of mibefradil which is considerably more stable, and is not readily metabolised. As such, NNC was shown to inhibit T-type Ca²⁺ channels whilst having no effect on HVA channels expressed by pancreatic β (INS-1) cells when applied at 10-fold greater concentrations (Li *et al.*, 2005). Nifedipine belongs to a family of drugs called dihydropyridines (DHPs), which are highly selective L-type CCBs. The high selectivity arises as the pore forming α_{1C} subunit of L-type Ca²⁺ channels has a unique high affinity DHP binding site involving IIS6 and IVS6 transmembrane segments (Peterson *et al.*, 1996). In rat arterial smooth muscle cells, nifedipine (300nM) was shown to selectively inhibit L-type Ca²⁺ currents and thus enabled successful T-type Ca²⁺ current isolation (Abd El-Rahman *et al.*, 2013).

Before discussing the kinetic features of Ca_v3.x channels in detail, it is important to define the terminology used to describe ion channel gating in general. Depolarisation can stimulate ion channels in their resting state to open, which is referred to as

channel activation. A feature of $\text{Ca}_v3.x$ channels is that, similar to Na_v channels, they rapidly inactivate (close) during a depolarising stimulus. Removal of depolarisation and the return to lower (more hyperpolarized) membrane potential allows any channels that were still open to close – this process is called deactivation. Furthermore, hyperpolarisation enables recovery from inactivation, allowing channels to return to their resting state. Recombinant expression of $\text{Ca}_v3.x$ channels produces robust currents, with kinetics which are virtually identical to their equivalent, native counterparts. Figure 1.3, shows an example $\text{Ca}_v3.2$ current trace recorded from a HEK293 stably-expressing $\text{Ca}_v3.2$ channels. Importantly, $\text{Ca}_v3.x$ currents both activate and inactivate at low voltages, recover rapidly from inactivation and deactivate slowly leading to prominent tail currents (Perez-Reyes, 2003).

All three $\text{Ca}_v3.x$ channels begin to activate at approximately -70mV however as their current kinetics are highly voltage-dependent, variable current shapes are produced by small depolarisations. This is highlighted by the characteristic criss-cross pattern of traces evoked by current-voltage (I-V) protocols. As such, when comparing the kinetics of $\text{Ca}_v3.x$ isoforms it is useful to examine currents stimulated by relatively higher voltages (e.g. -10mV). Depolarisation to -10mV causes rapid activation of $\text{Ca}_v3.1$ and $\text{Ca}_v3.2$ channels ($\tau = 1\text{-}2\text{ms}$), alongside relatively slower inactivation ($\tau = 10\text{-}16\text{ms}$). Significantly, $\text{Ca}_v3.3$ channels activate and inactivate much more slowly when compared to $\text{Ca}_v3.1$ and $\text{Ca}_v3.2$ channels. Despite differences in inactivation rates, steady-state inactivation when measured by applying pre-pulses of varying potentials prior to the test pulse (e.g. -30mV), is similar for all $\text{Ca}_v3.x$ channels (Klockner *et al.*, 1999; Perez-Reyes 2003). Interestingly, the generalised half-maximal steady-state inactivation voltage of -72mV indicates that $\text{Ca}_v3.x$ channels can inactivate without passing through their open state. Regarding $\text{Ca}_v3.3$ channels, up to 30% of channels have been shown to inactivate without opening during a depolarising pulse (Frazier *et al.*, 2001). Recovery from inactivation of $\text{Ca}_v3.x$ channels is rapid, with $\text{Ca}_v3.1$ channels showing the fastest deinactivation and $\text{Ca}_v3.2$ channels showing the slowest (Klockner *et al.*, 1999). This feature is particularly important for the physiological roles of T-type Ca^{2+} channels in rapid oscillatory activity. Finally, when compared to HVA channels $\text{Ca}_v3.x$ channels deactivate (or close) more slowly (10-fold difference), which accounts for their prominent tail currents. Specifically, $\text{Ca}_v3.3$ channels display the quickest

deactivation ($\tau = 1\text{ms}$), with $\text{Ca}_v3.1$ channels exhibiting the slowest ($\tau = 3\text{ms}$) (Klockner *et al.*, 1999; Perez-Reyes, 2003).

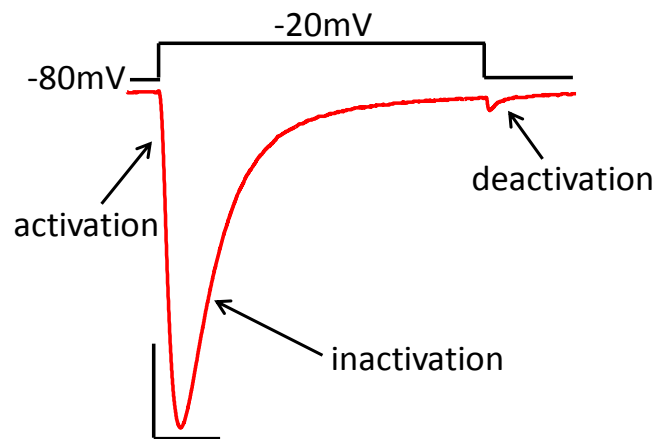


Figure 1.3. T-type Ca^{2+} channel gating parameters

Example $\text{Ca}_v3.2$ current trace recorded using whole-cell patch-clamp electrophysiology, evoked by 200ms step-depolarisations from -80 to -20mV. The depolarising pulse opens the channel (activation), the channel then closes in the continued presence of the depolarising pulse (inactivation). Removal of depolarisation allows the channel to return to its closed resting state (deactivation). Scale bar 200pA, 40ms.

As $\text{Ca}_v3.x$ channel activation and inactivation is observed at similar, relatively low voltages, T-type Ca^{2+} channels can open without fully inactivating. This can produce a “window current”, i.e. tonic Ca^{2+} influx at resting membrane potentials. Specifically, window current is defined as the overlap between voltage-dependent activation and steady-state inactivation curves, as illustrated in Figure 1.4. As electrophysiological protocols predict that T-type Ca^{2+} channels facilitate a window current at or around the resting membrane potential (V_m), $\text{Ca}_v3.x$ channels can be crucial mediators of intracellular Ca^{2+} concentration $[\text{Ca}^{2+}]_i$. All three $\text{Ca}_v3.x$ isoforms are predicted to mediate window current which is predicted to be facilitated by approximately 1% of channels (Perez-Reyes, 2003). As such, recombinant expression of $\text{Ca}_v3.1$ or $\text{Ca}_v3.2$ channels in HEK293 cells produced observable window currents which correspondingly resulted in a significant elevation in basal $[\text{Ca}^{2+}]_i$ (Chemin *et al.*, 2000).

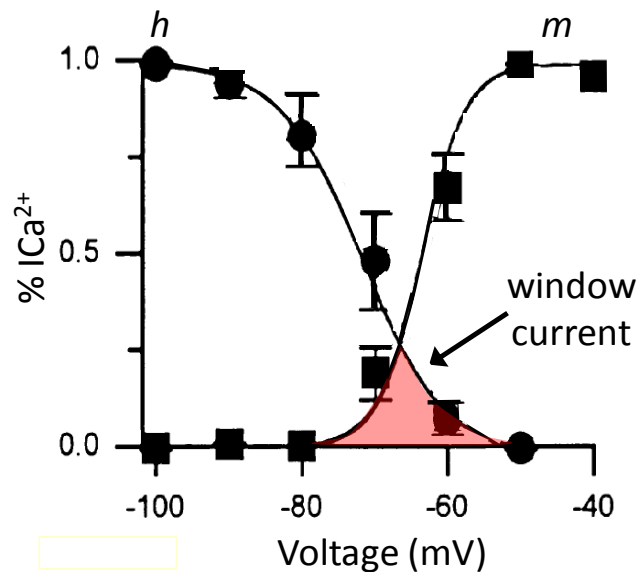


Figure 1.4. T-type Ca²⁺ channels can facilitate a window current

Schematic diagram showing the voltage-dependence of activation (*m*, squares) and steady-state inactivation (*h*, circles) of Ca_v3.2 channels, plotted as % of maximal current (I_{Ca²⁺}). Curves represent Boltzmann fits to activation and inactivation. Overlap between curves predicts the window current, as highlighted by the pink shaded region. Diagram reproduced with permission from data previously gathered by Prof Chris Peers (Fearon *et al.*, 2000).

1.4. Isoform specific expression and physiological roles of Ca_v3.x channels

T-type Ca²⁺ channel expression has been observed in many areas of the body including the heart, kidneys, smooth muscle, endocrine tissues and nervous systems. Interestingly, many of the physiological roles of Ca_v3.x channels within these areas concerns their ability to facilitate window currents, as reviewed (Perez-Reyes, 2003). This following section will outline some of the characterised expression profiles of Ca_v3.x channels and their associated functions within various areas. It should be noted that this summary is not an exhaustive list; a few examples have been selected to emphasise the range of physiological functions of T-type Ca²⁺ channels.

1.4.1. Peripheral and central nervous system

Due to their potential involvement in pathological brain disorders such as epilepsy, the expression and physiological roles of Ca_v3.x channels within the CNS has been studied extensively. Specifically, *in situ* hybridisation has revealed that Ca_v3.x channel mRNA expression shows unique and largely complementary patterns of distribution within the peripheral and central nervous systems (PNS and CNS respectively). Many regions

including the cerebral cortex, brainstem and thalamic relay neurons primarily expressed Ca_v3.1 channels. In contrast, dentate gyrus granule neurons and pituitary cells expressed Ca_v3.2 in isolation. In some areas such as the subthalamic nuclei and olfactory tubercles Ca_v3.1 co-localised with Ca_v3.2 channels. Similarly, Ca_v3.2 co-localised with Ca_v3.3 channels in thalamic reticular neurons. Expression of all three Ca_v3.x isoforms, at similar levels, was demonstrated in areas including the hippocampus, caudal hypothalamus and olfactory granule cells (Talley *et al.*, 1999).

Regarding the PNS, Ca_v3.2 was shown to be the most predominantly expressed isoform. Ca_v3.2 channels were identified within the dorsal root ganglia (DRG), nodose ganglia, pituitary and pineal glands. Contrastingly, co-expression of Ca_v3.3 and Ca_v3.2 channels was observed in the DRG, whilst the superior cervical ganglia expressed low levels of Ca_v3.1 mRNA in isolation (Talley *et al.*, 1999). Subsequent studies have also revealed differential patterns of Ca_v3.x channel distribution between dendritic, axonal and somatic neuronal compartments (McKay *et al.*, 2006). These studies collectively indicate that the physiological roles of Ca_v3.x channels within the CNS are highly complex.

Due to differential patterns of T-type Ca²⁺ channel isoform expression within different brain regions, neuronal subtypes and compartments, the repertoire of the effects of LVA Ca²⁺ channels on cellular excitability is vast. Within some neuronal populations activation of Ca_v3.x channels at low voltages can produce low-threshold Ca²⁺ spikes (LTCS), leading to the recruitment of Na_v channels and burst action potential (AP) firing (Powell *et al.*, 2014). Conclusive proof that T-type Ca²⁺ channels mediate LTCSs and correspondingly lead to burst AP firing, is provided by a study which used Ca_v3.1 KO (Ca_v3.1^{-/-}) mice. Thalamocortical relay (TCR) neurons play a key role in coordinating network activity and exhibit burst AP firing patterns. TCR neurons in Ca_v3.1^{-/-} mice were found to lack LTCSs and burst AP firing, although tonic AP firing patterns were preserved. Furthermore, Ca_v3.1^{-/-} mice were largely resistant to spike-and-wave discharges, which are characteristic of epileptic absence seizures, stimulated by GABA_B receptor agonists. It was resultantly shown that Ca_v3.1 channels within the thalamocortical pathways are mediators of epileptogenesis (Kim *et al.*, 2001). LTCSs facilitated by Ca_v3.x channels are believed to be central to their physiological roles in

controlling pacemaker activity. Due to the prominent voltage-dependency of $\text{Ca}_v3.x$ channel recovery from inactivation, LTCSs are generally activated by hyperpolarising, as opposed to depolarising stimulation. LTCSs induce depolarisation leading to Na_v and K_v channel activation and high frequency APs. HVA Ca_v channels, and subsequently Ca^{2+} -activated K^+ channels, activate leading to afterhyperpolarisation (AHP). The AHP allows $\text{Ca}_v3.x$ channels to deinactivate and the membrane potential returns back to resting levels (Perez-Reyes, 2003).

As reviewed by Powell *et al.*, (2014), T-type Ca^{2+} channels are further implicated in hypersynchronous oscillatory activity within thalamocortical neurons in generalised absence epilepsy (GAE); and also in the burst firing activity of hippocampal neurons associated with temporal lobe epilepsy (TLE). For example, genetic mutations in $\text{Ca}_v3.2$ channels have been detected in patients with genetic and childhood GAEs. These mutations typically lead to alterations in $\text{Ca}_v3.2$ surface expression and channel kinetics, and ultimately result in neuronal hyperexcitability (Chen *et al.*, 2003b; Heron *et al.*, 2007; Vitko *et al.*, 2005). Additionally, the Genetic Absence Epilepsy Rats from Strasbourg (GAERS) express a gain-of-function $\text{Ca}_v3.2$ channel splice variant, and correspondingly provide a valuable animal model of GAE. The GAERS splice variant arises from a single-point mutation of an arginine residue found within the intracellular DIII-DIV linker region of $\text{Ca}_v3.2$ channels (Powell *et al.*, 2009). In the GAERS model, $\text{Ca}_v3.2$ expression and LVA current amplitude within reticular thalamic nuclei is dramatically increased when compared to seizure free animals. Interestingly, as the increases in LVA current density were larger than the increases in $\text{Ca}_v3.2$ mRNA, evidence for elevated $\text{Ca}_v3.2$ membrane trafficking is provided (Tsakiridou *et al.*, 1995).

1.4.2. Heart

Whilst $\text{Ca}_v3.3$ channel expression is generally restricted to the nervous system, $\text{Ca}_v3.1$ and $\text{Ca}_v3.2$ channels are also prominently expressed within the cardiovascular system. Within the heart, the physiological role of T-type Ca^{2+} channels has been explored with a particular emphasis on pacemaker activity. Whilst $\text{Ca}_v3.x$ channels are generally lacking from adult ventricular myocytes, they are heavily expressed within pacemaker

and conduction cells, particularly in the sinoatrial (SA) node. In the human SA node, $Ca_v3.1$ is predominantly expressed (Chandler *et al.*, 2009). However, in the murine SA node, $Ca_v3.2$ channels have also been shown to be expressed alongside $Ca_v3.1$ channels (Bohn *et al.*, 2000). The SA node is the primary rhythmogenic centre of the heart and thus regulates myogenic contractility. Pacemaker activities of SA myocytes are dependent on the expression of a plethora of ion channels, including Ca_v and hyperpolarisation-activated cyclic-nucleotide-gated 4 (HCN4) channels. At maximal diastolic membrane potentials, T-type Ca^{2+} channels exhibit stable steady-state availability which can result in a window current. This contributes to pacemaker activity in a manner similar to that described within the CNS. $Ca_v3.x$ -mediated Ca^{2+} currents have also been detected within other components of the heart conduction system including the atrioventricular (AV) node and Purkinje fibres, as reviewed (Mesirca *et al.*, 2014). Whilst the complete physiological contribution of T-type Ca^{2+} channels to cardiac pacemaker activity remains to be fully elucidated within humans, KO mouse models have provided some valuable insights. For example, in $Ca_v3.1^{-/-}/Ca_v1.3^{-/-}$ double KO mice almost complete AV block was observed which resulted in dissociated atrial and ventricular rhythms. The myogenic nature of SA node myocyte activity was also considerably reduced within $Ca_v3.1^{-/-}/Ca_v1.3^{-/-}$ mice (Marger *et al.*, 2011).

Expression of $Ca_v3.1$ and $Ca_v3.2$ channels within cardiac myocytes, outside of the primary conduction system, is most apparent at birth and gradually declines with age. However, in some pathological conditions such as cardiac hypertrophy T-type Ca^{2+} channel re-expression is observed (Martinez *et al.*, 1999; Swynghedauw, 1999). Specifically, in rats, cardiac hypertrophy initiated by myocardial infarction increased $Ca_v3.1$ mRNA expression in viable left ventricular myocytes. Functional upregulation of $Ca_v3.2$ channels was also observed as an increased sensitivity of LVA currents to Ni^{2+} (Elvan, 2000). As hypertrophic ventricular modelling involves myocyte proliferation, this observation may bear significance to the role of T-type Ca^{2+} channels in the regulation of cell-cycle progression, as subsequently discussed (section 1.5).

A role of $Ca_v3.2$ channels within hypertrophic cardiac remodelling has also been ascertained from studies using KO mice. Although expressed developmentally, T-type

Ca²⁺ channel expression is typically absent within adult ventricular myocytes. Significantly, T-type Ca²⁺ channels are re-expressed following myocardial infarction which subsequently results in pathological hypertrophy (Huang *et al.*, 2000; Izumi *et al.*, 2003). Within wt and Ca_v3.1^{-/-} mice, cardiac hypertrophy could be induced by pressure overload, which was achieved by aortic banding or exposure to angiotensin II. In stark contrast, pressure- and angiotensin II-induced hypertrophy was suppressed in Ca_v3.2^{-/-} mice. Following aortic banding, the thickness of ventricular walls and also the cross sectional diameter of myocytes was significantly increased in wt mice but not in Ca_v3.2^{-/-} mice. As there were no apparent differences in blood pressure between wt and Ca_v3.2 mice, strong evidence that Ca_v3.2 channels contribute to pathological cardiac remodelling was therefore provided (Chiang *et al.*, 2009).

A final physiological role for atrial T-type Ca²⁺ channels is in the secretion of atrial natriuretic factor (ANF). ANF is a hormone which inhibits the release of renin, aldosterone and vasopressin. In addition to the diuretic and natriuretic effects on the kidney, ANF has vasodilatory effects (Inagami, 1989). Ca²⁺ currents recorded from atrial and ventricular myocytes freshly dissociated from 8-day old rats have been shown to be facilitated by both L-type (Ca_v1.2) and T-type (Ca_v3.1 and Ca_v3.2) Ca²⁺ channels. The predominant current species within atrial myocytes was LVA. Concurrently, ANF secretion evoked in 8-day old rats by small depolarisations was almost completely abolished by mibefradil (1µM). Evidence that ANF secretion by atrial myocytes is, at least partially, dependent on Ca_v3.x channels is thus provided. Consistent with previous reports, comparison of current density between young and adult rats revealed a progressive decline in functional T-type Ca²⁺ channels in atrial myocytes alongside a complete disappearance within ventricular myocytes (Leuranguer *et al.*, 2000).

1.4.3. Endocrine tissue

The role of T-type Ca²⁺ channels in hormone secretion is not restricted to atrial cells but is also applicable to adrenal, pituitary and pancreatic tissues. Within rat and bovine adrenal glands, Ca_v3.2 channels are the primary Ca_v3.x isoform. This was shown by both *in situ* hybridisation and the high Ni²⁺-sensitivity of LVA currents recorded from

both glomerulosa (Schrier *et al.*, 2001) and fasciculata (Mlinar *et al.*, 1993) cells. In adrenal glomerulosa cells, which also express HVA Ca_v channels, rises in extracellular K^+ concentrations can activate T-type Ca^{2+} channels leading to Ca^{2+} -dependent APs and the synthesis and release of aldosterone. Similarly, in adrenal fasciculata cells, depolarisation induced by adrenocorticotrophic hormone (ACTH) activates T-type Ca^{2+} channels leading to the synthesis and release of cortisol. It has correspondingly been suggested that $\text{Ca}_v3.2$ channels play important roles in stimulus-secretion activity, as reviewed (Perez-Reyes, 2003).

Pituitary cells are capable of generating LTCS and spontaneous APs which result in growth hormone secretion (Tomic *et al.*, 1999). The expression of all three $\text{Ca}_v3.x$ isoforms has been shown in pituitary tissue, with $\text{Ca}_v3.2$ channels being predominant (Talley *et al.*, 1999). The link between T-type Ca^{2+} channels, pacemaker activity and hormone secretion is similarly applicable to insulin secretion by pancreatic β -cells. Specifically, elevation of glucose levels increases ATP concentrations which results in the closure of ATP-gated K^+ channels. This can lead to the activation of T-type Ca^{2+} channels and high frequency Ca^{2+} -dependent spikes, as reviewed (Satin, 2000). Interestingly, the expression profiles of $\text{Ca}_v3.x$ channels in pancreatic β -cells shows considerable species variation. For example, whilst T-type Ca^{2+} channel currents are prominent within human pancreatic β -cells (Barnett *et al.*, 1995), T-type Ca^{2+} channel currents in the equivalent cells of mice are only detectable upon IL-1 β pre-treatment (Wang *et al.*, 1999).

1.4.4. Blood vessels and VSMCs

The expression of $\text{Ca}_v3.1$ and $\text{Ca}_v3.2$ channels has been demonstrated within a variety of blood vessels including the cerebral, mesenteric and renal microcirculations, as reviewed (Kuo *et al.*, 2011). As previously detailed, differentiated VSMCs primarily express L-type Ca_v channels which facilitate the Ca^{2+} influx required for VSMC contraction. In addition to prominent L-type HVA currents, LVA currents have also been detected within VSMCs isolated from veins, arteries and organs. Prior to the molecular cloning of $\text{Ca}_v3.x$ channels it was difficult to confirm conclusively that LVA currents were mediated by T-type Ca^{2+} channels. This was largely due to the fact that

LVA currents recorded from VSMCs are tiny, necessitating the use of very high concentrations of charge carriers. Importantly, this can shift current-voltage activation profiles to more positive potentials, which can be misleading when identifying LVA channels (Perez-Reyes, 2003). As a further complication, HVA P-type ($\text{Ca}_v2.1$) Ca^{2+} channel expression has also been identified in VSMCs isolated from rat aortic and renal preglomerular resistance vessels and in the rat thoracic aorta VSMC cell line (A7r5). P-type Ca^{2+} channels inactivate at similar voltages to LVA currents and are also inhibited by mibefradil. Electrophysiological studies have further indicated that functional P-type Ca^{2+} channels can contribute to depolarisation-induced contraction, particularly within renal afferent arterioles (Hansen *et al.*, 2000).

Subsequent studies have revealed that both $\text{Ca}_v3.1$ and $\text{Ca}_v3.2$ channels are expressed, in addition to $\text{Ca}_v1.2$ (L-type) channels, within renal blood vessels. In rats, regions of expression included pre- and post-glomerular resistance vessels and juxtamedullary efferent arterioles. Ca^{2+} imaging of rabbit afferent and rat juxtamedullary efferent arterioles revealed that exposure to high K^+ concentrations induced rises in $[\text{Ca}^{2+}]_i$. This response could be partially inhibited by the T-type CCB mibefradil (100nM) or the L-type selective CCB calciseptine (Hansen *et al.*, 2001). It was further demonstrated that K^+ -induced contraction of rabbit afferent arterioles could be completely abolished by mibefradil (1 μM), Ni^{2+} (1mM) and calciseptine (10pM). In contrast, no Ca_v channel expression was observed in cortical efferent arterioles. Furthermore, K^+ -induced rises in $[\text{Ca}^{2+}]_i$ within rabbit cortical efferent arterioles were considerably smaller than those observed in other vessels, and unaltered by CCBs. These data indicate that $\text{Ca}_v3.1$, $\text{Ca}_v3.2$ and $\text{Ca}_v1.2$ channel expression is functionally important for the contraction of certain renal blood vessels (Hansen *et al.*, 2001).

The contribution of T- and L-type Ca^{2+} channels to vasomotor function has also been compared between segments of the large thoracic aortic and small mesenteric vessels. Within rat aorta, $\text{Ca}_v3.1$, $\text{Ca}_v3.2$ and $\text{Ca}_v1.2$ channels were abundantly expressed in equal amounts. Within rat mesenteric resistance vessels however, the expression of $\text{Ca}_v3.1$ and $\text{Ca}_v3.2$ channels was considerably greater than that of $\text{Ca}_v1.2$ channels (Ball *et al.*, 2009). Vasomotor function was subsequently assessed using wire myograph recordings. Contraction was stimulated, in the presence or absence of various CCBs, by

exposure to increased K^+ concentrations or to endothelin-1 (Et-1). In order to assess the contribution of ECs to the effects of CCBs, the contractile response of denuded vessels was also examined. Within intact segments, endothelial integrity was observed by inhibition of contractile responses ($\geq 80\%$) upon application of the endothelium-dependent vasodilators, bradykinin (BK) or acetylcholine (ACh), to human and rat vessels respectively. Regarding the CCBs applied, verapamil ($1\mu\text{M}$) and nifedipine ($1\mu\text{M}$) were used as selective L-type CCBs. Efonidipine (21nM) and mibefradil ($1\mu\text{M}$), referred to as combined CCBs, were applied with the purpose of inhibiting both L- and T-type Ca^{2+} channels (Ball *et al.*, 2009). An important consideration is that previous studies have shown that when applied for similar time periods as used by Ball *et al.*, (2009), mibefradil ($1\mu\text{M}$) selectively inhibits vascular T-type Ca^{2+} currents but is without effect on L-type Ca^{2+} currents (Brueggemann *et al.*, 2005). Contrastingly, when applied as a mixture of its *R*(-) and *S*(+) enantiomers, efonidipine inhibits recombinant L- and T-type Ca^{2+} channels with similar potencies, without significant effect on other HVA channel subtypes (Furukawa *et al.*, 2004). As such, the classification of combined CCB within the study accurately describes efonidipine, but arguably not mibefradil. As an interesting side note, the isolated *R*(-) enantiomer of efonidipine has been found to preferentially inhibit T-type over L-type Ca^{2+} channels (Furukawa *et al.*, 2004).

Pre-treatment with each of the four CCBs was found to inhibit Et-1-induced contractile responses to similar extents within intact (i.e. endothelium present) rat aortic segments. In comparison to L-type specific CCBs, efonidipine and mibefradil were significantly more effective at inhibiting the contractile responses of intact and denuded rat and human mesenteric microvessels. As the contribution of ECs to CCB responses was ruled out, VSMC Ca^{2+} channel expression is implicated. It was also shown within rat microvessels that efonidipine produced further inhibition of contractile responses, proceeding maximal nifedipine- or verapamil-mediated inhibition. Collectively, these findings show that T-type Ca^{2+} channels contribute considerably to the vascular responses of small mesenteric blood vessels, and also to a lesser extent within the aorta (Ball *et al.*, 2009).

Alternative studies have confirmed that Ca_v channels expressed by VSMCs contribute to vasomotor function. Within isolated rat mesenteric terminal arterioles, $\text{Ca}_v3.1$,

Ca_v3.2 and Ca_v1.2 channels were shown to be expressed by VSMCs. Ca_v3.2 expression was also apparent within adjacent ECs. Ratiometric Ca²⁺ imaging revealed that potassium chloride (KCl) microinjection led to increases in VSMC [Ca²⁺]_i, observed in areas localised and remote to the site of injection. Both localised and remote increases in [Ca²⁺]_i were inhibited by bath application of nifedipine and the T-type selective CCBs, R(-)-efonidipine and NNC55-0396 (NNC). Remote [Ca²⁺]_i responses could also be inhibited by the gap-junction un-couplers carbenoxolone and palmitoleic acid. Since both nifedipine and NNC were equally capable of reducing the [Ca²⁺]_i response, it is suggested that functional coupling between L- and T-type Ca²⁺ channels occurs within VSMCs. Of key significance is that when CCBs were applied away from the site of KCl microinjection, no modification of localised or remote [Ca²⁺]_i response were observed. This study therefore concluded that whilst L- and T-type Ca²⁺ channels contribute to local electromechanical coupling, they are not critical for the conduction of vasoconstrictor responses (Braunstein *et al.*, 2009).

Expression of Ca_v3.1, Ca_v3.2, Ca_v1.2, and Ca_v1.3 channels has also been detected in adult rat basilar and middle cerebral arteries and their branches. Ca_v3.1 and Ca_v1.2 channels were expressed in the greatest abundance. Notably, the expression of Ca_v3.2 channels was considerably greater in arterial branches compared to major cerebral arteries. Electron microscopy revealed that Ca_v1.2 channels were localised to the cell membranes of SMCs and absent from ECs. In contrast, Ca_v3.1 and Ca_v3.2 channels were localised in SMCs and ECs where they exhibited both membranous and cytoplasmic patterns of distribution. In addition to L-type Ca²⁺ currents, patch-clamp electrophysiology of isolated SMCs identified nifedipine- and nimodipine-insensitive Ca²⁺ currents which also displayed characteristic T-type Ca²⁺ current kinetics. These Ca²⁺ currents accounted for approximately 20% of the total Ca²⁺ current in SMCs isolated from main arteries and approximately 45% of total current in SMCs isolated from branches. It was additionally shown that nifedipine-insensitive currents could be inhibited by mibefradil, NNC and efonidipine, strongly indicating the involvement of T-type Ca²⁺ channels (Kuo *et al.*, 2010).

Within main cerebral arteries, contractile responses were shown to be solely mediated by L-type Ca²⁺ channels, as nifedipine completely abolished vasoconstriction. In

contrast, nifedipine-insensitive vasoconstriction was observed within branches, the extent of which increased with decreasing arteriole diameter. It was correspondingly suggested that nifedipine-insensitive Ca^{2+} currents play a larger role in vasoconstriction within smaller vessels of the cerebrovascular circulation (Kuo *et al.*, 2010). It is important to consider that the nifedipine-insensitive currents, described by Kuo *et al.* (2010), are not explicitly referred to as T-type Ca^{2+} currents. This is due to the fact that they activated at voltages more characteristic of HVA channels. Subsequent studies have similarly reported nifedipine-insensitive Ca^{2+} currents within cerebral arteries which, compared to L-type Ca^{2+} currents, show more hyperpolarised I-V relationships and have faster activation and inactivation kinetics. Interestingly, these currents were blocked by low Ni^{2+} (50 μM) concentrations, thereby implicating a specific contribution of $\text{Ca}_v3.2$ channels. The nifedipine-insensitive Ca^{2+} currents appeared likely to be facilitated by T-type Ca^{2+} channels. However, when compared to the typical biophysical profile of T-type Ca^{2+} channels, activation and inactivation occurred at more positive potentials. It was thus suggested that T-type Ca^{2+} channel splice variants may be expressed within the vasculature (Harraz & Welsh, 2013). This suggestion has been confirmed by studies which have identified vascular-specific T-type Ca^{2+} channel splice variants, which arguably fit better within the HVA category (Kuo *et al.*, 2011; Kuo *et al.*, 2014).

Many recent advances in our understanding about the specific contribution of $\text{Ca}_v3.1$ and $\text{Ca}_v3.2$ channel isoforms to normal and pathological cardiovascular functions has come from studies using global $\text{Ca}_v3.1^{-/-}$ and $\text{Ca}_v3.2^{-/-}$ KO mice. Of specific consideration is that both $\text{Ca}_v3.1^{-/-}$ and $\text{Ca}_v3.2^{-/-}$ mice exhibit neurological deficits, as reviewed (Cheong & Shin, 2013). A further problem associated with KO models is that compensatory mechanisms can occur. As such, it is important that results are compared against the effects of appropriate pharmacological inhibitors where possible. The $\text{Ca}_v3.1^{-/-}$ KO mouse was developed by deleting the N-terminus of the α_{1G} subunit (Kim *et al.*, 2001), whereas the $\text{Ca}_v3.2^{-/-}$ KO mouse involved deletion of the S5 segment within DI of the α_{1H} subunit (Chen *et al.*, 2003a).

Opposing results regarding the role of $\text{Ca}_v3.1$ channels in the maintenance of vascular tone within different regions of the vasculature have been described. For example,

within intrarenal arteries, contraction induced by the α_1 adrenoceptor agonist phenylephrine was significantly greater in $\text{Ca}_v3.1^{-/-}$ mice. In contrast, phenylephrine-induced contraction within mesenteric arteries was significantly reduced in $\text{Ca}_v3.1^{-/-}$ mice. Importantly, no differences in K^+ -induced contraction of intrarenal and mesenteric vessels was observed between $\text{Ca}_v3.1^{-/-}$ and wt mice. It has therefore been proposed that $\text{Ca}_v3.1$ channels are involved in vascular responses to endogenous phenylephrine, and can also be involved in both contraction and relaxation. Further investigations are required to establish whether factors such as vessel diameter, oxidative state or NO availability, account for the disparate effects of $\text{Ca}_v3.1$ channel expression within different vessels (Hansen, 2015).

Early studies conducted on $\text{Ca}_v3.2^{-/-}$ mice revealed that, when compared to wt mice, coronary arteries were constitutively constricted and exhibited large areas of fibrosis. Whilst typical contractile responses were preserved in isolated coronary arterioles, ACh- or nitroprusside-induced relaxation was considerably reduced. In addition, low Ni^{2+} concentrations prevented relaxation, further indicating that $\text{Ca}_v3.2$ channels play an important physiological role within vasorelaxation of coronary arteries (Chen *et al.*, 2003a).

It has been suggested that the role of $\text{Ca}_v3.2$ channels in the process of vasodilation may result from their regulation by NO. Treatment of rat middle cerebral arteries with the nitric oxide synthase (NOS) inhibitor, NG-nitro-L-arginine methyl ester (L-NAME), has been shown to produce vasoconstriction. L-NAME-induced contraction could be partially inhibited by mibefradil (100nM) and NNC (300nM), implicating a role for T-type Ca^{2+} channels (McNeish *et al.*, 2010). Interestingly, incubation of cerebral vessels with L-NAME increased the expression of $\text{Ca}_v3.1$ channels within isolated VSMCs, and was accompanied by a redistribution of $\text{Ca}_v3.1$ channels from the cytoplasm to the membrane. Unfortunately, patterns of $\text{Ca}_v3.2$ expression were not determined within cerebral arterioles. Furthermore, whilst $\text{Ca}_v3.1$ and $\text{Ca}_v3.2$ staining was generally absent from cremaster muscle arterioles, treatment with L-NAME significantly increased the expression of both $\text{Ca}_v3.1$ and $\text{Ca}_v3.2$ channels (Howitt *et al.*, 2013). The contribution of L- and T-type Ca^{2+} channels to myogenic vascular tone were next examined by manipulating intraluminal pressure in the presence or absence of

nifedipine, NNC or mibefradil. A key strength of this study was that NNC and mibefradil were always applied following nifedipine treatment, thus ruling out any potential effects of mibefradil or NNC on L-type Ca^{2+} channels. Acute treatment of basilar arteries with L-NAME increased the contribution of T-type, and decreased the contribution of L-type, Ca^{2+} channels to cerebral artery tone. Significantly, these effects were attenuated in both $\text{Ca}_v3.1^{-/-}$ and $\text{Ca}_v3.2^{-/-}$ mice. These findings collectively show that both $\text{Ca}_v3.1$ and $\text{Ca}_v3.2$ contribute to vascular tone during NO deficiency (Howitt *et al.*, 2013). An alternative study found that 5,6-epoxyeicosatrienoic acid (5,6-EET) potently inhibited recombinant human $\text{Ca}_v3.1$, $\text{Ca}_v3.2$ and $\text{Ca}_v3.3$ (Cazade *et al.*, 2014). Furthermore, 5,6-EET was also shown to have vasodilatory effects on pre-constricted mesenteric arteries. In addition, the vasodilatory effects of 5,6-EET were impaired in $\text{Ca}_v3.2^{-/-}$, but not $\text{Ca}_v3.1^{-/-}$ mice (Cazade *et al.*, 2014). Collectively, these studies indicate that $\text{Ca}_v3.2$ channels specifically play an important role in the process of vasodilation.

1.5. The role of T-type Ca^{2+} channels in proliferation

Due to their overlapping voltage-dependencies of activation and inactivation, T-type Ca^{2+} channels can facilitate a window current at or around resting V_m , as shown by Figure 1.4. This tonic Ca^{2+} influx can be a key determinant of $[\text{Ca}^{2+}]_i$ (Chemin *et al.*, 2000). The issue of whether T-type Ca^{2+} channels expressed by VSMCs facilitate a window current has been debated (Perez-Reyes, 2003). This is primarily due to the fact that the resting V_m of pressurised arterioles has been shown to be between approximately -55mV and -40mV (Hirst & Edwards, 1989). At these potentials T-type Ca^{2+} channels are generally inactivated. A likely resolution for this issue was provided when vascular-specific $\text{Ca}_v3.1$ splice variants, which both activate and inactivate at more depolarised potentials, were identified (Kuo *et al.*, 2014). It remains feasible, therefore, that T-type Ca^{2+} channel splice variants expressed by VSMCs may facilitate a window current.

Central to the current investigation are observations that within VSMCs a co-ordinated elevation in $[\text{Ca}^{2+}]_i$ is required for cell cycle progression (Husain *et al.*, 1997). In relation to this, the expression of T-type Ca^{2+} channels in primary cultures of rat aortic VSMCs is

restricted to the proliferative phases of the cell-cycle. Specifically, immunohistological and electrophysiological techniques revealed that within the G_0 phase T-type Ca^{2+} channel expression was absent and Ca^{2+} currents were solely mediated by L-type Ca^{2+} channels. Within the proliferative G_1 and S phases a significant increase in T-type Ca^{2+} currents was observed alongside a dramatic reduction in L-type Ca^{2+} currents (Kuga *et al.*, 1996). As described below, subsequent studies have revealed an intimate link between T-type Ca^{2+} channel expression, VSMC proliferation and vascular remodelling, within both developmental and pathological situations.

The ductus arteriosus (DA) is a vascular shunt within the foetal circulatory system which predominantly expresses $Ca_v3.1$ in addition to $Ca_v3.2$ channels. Postpartum, VSMC proliferation and migration mediates intimal cushion formation and rapid closure of the DA (Yokoyama *et al.*, 2006). $Ca_v3.1$ channels were shown to mediate this remodelling process, as oxygenation induced an up-regulation of $Ca_v3.1$ channels in proliferating VSMCs of the neonatal rat DA. Concurrently, $Ca_v3.1$ up-regulation increased VSMC migration whilst down-regulation decreased VSMC migration. Pharmacological T-type Ca^{2+} channel inhibition using (*R*)-efonidipine produced similar anti-migratory and anti-proliferative effects on VSMCs. Furthermore, when (*R*)-efonidipine was administered *in vivo* a significant delay in the closure of the DA was observed (Akaike *et al.*, 2009).

Neointima formation is a common undesirable consequence of vascular intervention that involves increased VSMC proliferation and migration, resulting in restenosis. Early studies demonstrated that oral administration of mibefradil significantly reduced neointima formation in rats subjected to carotid balloon injury. This indicated a causative role for T-type Ca^{2+} channels in pathologically elevated VSMC proliferation (Schmitt *et al.*, 1996). Regarding KO studies, Tzeng *et al.* (2012) demonstrated that carotid artery wire injury induced neointima formation in both wt and $Ca_v3.2^{-/-}$ mice. Significantly, however, neointima formation was not observed in $Ca_v3.1^{-/-}$ mice, which importantly displayed no other vascular abnormalities. Immunohistological processing revealed that neointima formation within wt mice was due to increased VSMC proliferation. Furthermore, $Ca_v3.1$ mRNA was up-regulated in response to wire injury in wt mice prior to neointima formation, suggesting that $Ca_v3.1$ up-regulation was

crucial for the development of this pathogenic phenotype. Such evidence strongly supports a role for T-type Ca^{2+} channels in pathological vascular remodelling and VSMC proliferation (Tzeng *et al.*, 2012).

In vitro studies have also implicated T-type Ca^{2+} channels in the control of VSMC proliferation. Freshly isolated VSMCs typically exhibit a contractile phenotype and have correspondingly been shown, within isolated rat aortic VSMCs, to predominantly express L-type Ca^{2+} channels. Upon subsequent culture, VSMCs were found to revert to a proliferative phenotype. This switch in phenotype was characterised by an increase in LVA currents, alongside a corresponding decrease in HVA currents and loss of contractile activity (Richard *et al.*, 1992). In a rabbit model of neointima formation, balloon-induced arterial injury caused a rapid dedifferentiation of medial VSMCs. Proliferation assays conducted on cultured VSMCs demonstrated that mibefradil only exerted anti-proliferative effects on dedifferentiated, and not contractile, VSMCs (Louis *et al.*, 2006). Furthermore, it has been shown that down-regulation of $\text{Ca}_v3.1$ using small interfering RNA (siRNA) significantly reduced the proliferation of cultured human pulmonary artery smooth muscle cells (HPASMCs). Importantly, mibefradil was also found to reduce HPASMC proliferation whilst the specific L-type Ca^{2+} channel inhibitor diltiazem was without effect (Rodman *et al.*, 2005).

Cancer

The link between T-type Ca^{2+} channel expression and cellular proliferation is not restricted to VSMCs. Indeed, stable transfection of HEK293 cells with $\text{Ca}_v3.2$ channels has been shown to produce functional currents with corresponding increases in cellular proliferation (Wang *et al.*, 2002b). The first connection between T-type Ca^{2+} channels and cancer was discovered in T-cell leukaemia cell lines; namely Jurkat, Molt-4 and HSB. LVA currents displaying characteristic T-type Ca^{2+} channel kinetics such as rapid activation and inactivation, were recorded from all three cell lines (Densmore *et al.*, 1992). It has since been shown that both mibefradil and $\text{Ca}_v3.1$ -targeted siRNA are anti-proliferative in both human and mouse neuroblastoma cell lines, U87MG and N1E-115 respectively. Furthermore, mibefradil was shown to reduce significantly $\text{Ca}_v3.1$ and $\text{Ca}_v3.2$ expression levels in a manner similar to growth serum deprivation, thus supporting the notion that T-type Ca^{2+} channel expression is restricted to the

proliferative phases of the cell-cycle. Over-expression of $\text{Ca}_v3.2$ channels in U87MG and N1E-115 cells increased intracellular Ca^{2+} influx stimulated by modest depolarisation and concurrently doubled their rates of proliferation. As the observed Ca^{2+} influx was inhibited by mibefradil, but not by the specific L-type CCB verapamil, T-type Ca^{2+} channels are conclusively implicated in the aberrant proliferation of cancerous cells (Panner *et al.*, 2005). Similar findings have been reported in retinoblastoma, C6 glioma, prostate and breast cancer lines (Panner & Wurster, 2006).

Further evidence linking T-type Ca^{2+} channel expression, elevations in basal $[\text{Ca}^{2+}]_i$ and increased proliferative rates, has been provided by studies conducted in cancerous cell lines. Within differentiated human prostate cancer epithelial cells (LNCaP), up-regulated $\text{Ca}_v3.2$ channel expression has been shown to result in increased basal $[\text{Ca}^{2+}]_i$ (Mariot *et al.*, 2002). Similarly, electrophysiological investigations in human neuroblastoma cells (SK-N-MC) revealed functional expression of T-type Ca^{2+} channels. Peak T-type Ca^{2+} channel current amplitude was increased upon treatment with the glycoprotein, erythropoietin (Epo), which was accompanied by a corresponding increase in basal $[\text{Ca}^{2+}]_i$. Elevations in $[\text{Ca}^{2+}]_i$ were found to be dependent on Ca^{2+} influx through T-type Ca_v channels as opposed to Ca^{2+} release from internal stores (Assandri *et al.*, 1999).

Within all cell types, Ca^{2+} influx at various stages of the cell-cycle, such as the G_1/S transition phase, is fundamental for cell-cycle progression and subsequent proliferation. Specifically, at the G_1/S restriction point a concerted input of increased $[\text{Ca}^{2+}]_i$, growth factor stimulation and nutrient availability is required. Dysregulation of the G_1/S restriction point is believed to underpin the mitogen-independent cellular proliferation observed in cancerous pathologies. It has correspondingly been proposed that elevated $\text{Ca}_v3.1$ and $\text{Ca}_v3.2$ Ca^{2+} channel expression provides the “all or nothing” event that is central to the transition from graded and regulated proliferation in physiological conditions to the irreversible linear sequence of cellular proliferation characteristic of cancerous cells (Gray *et al.*, 2013).

1.6. The thioredoxin (Trx) system

Cell-surface proteins, or those within the extracellular environment, are subject to oxidising conditions and are rich in stabilising disulphides (S_2). In contrast, the intracellular environment is maintained in a reduced state and intracellular proteins contain many free thiol or sulfhydryl (SH) groups. Thioredoxin (Trx) serves as a major intracellular disulphide reductase. As such, Trx functions as an antioxidant which can counterbalance oxidative stress when up-regulated or over-expressed (Nakamura *et al.*, 1997). The Trx system is ubiquitously expressed within mammalian cells and plays a key role in the maintenance of cellular redox balance. The system is composed of Trx, thioredoxin reductase (TrxR), nicotinamide adenine dinucleotide phosphate (NADPH), and vitamin D₃ up-regulated protein (VDUP). TrxR reduces Trx to its active form using electrons donated from NADPH, whilst VDUP serves as the endogenous negative regulator. Due to the rapidly reversible nature of thiol-disulphide exchange reactions, Trx also plays a key role in the dynamic control of enzymes dependent on structural and catalytic thiol groups (Arner & Holmgren, 2000).

1.6.1. Structure-function relationships of the Trx system

For Trx to exert the majority of its biological effects the active site disulphide of oxidised Trx (oTrx) must be reduced by TrxR to generate an active site dithiol ((SH)₂) group. As such, the functions of Trx are dependent on its redox-state and correspondingly the activity of TrxR. TrxR belongs to the pyridine nucleotide disulfide oxidoreductase family, which also includes glutathione reductase (GR) and trypanothione reductase (TryR). Mammalian TrxR is a homodimeric protein made up of two 55kDa subunits, arranged head to tail. Key structural features of mammalian TrxR include; flavin adenine dinucleotide (FAD) and NADPH binding domains, an interface domain and two separate active sites. The N-terminal CVNVGC active site motif is also found within GR and TryR, whilst the second Gly-Cys-Sec-Gly selenocysteine (Sec) active site motif is unique to TrxR. Electrons are initially transferred from NADPH to the N-terminal active site of TrxR, then to the Sec TrxR active site and finally to the Trx disulphide substrates. Interestingly, TrxR isolated from lower organisms, such as bacteria and plants, has a significantly lower molecular weight ($M_r \sim 35\text{kDa}$ per subunit), does not contain the Sec active site and has a lower substrate specificity, as reviewed

(Arner, 2009; Holmgren & Lu, 2010). Following the reduction of Trx by TrxR, dithiol-exchange reactions between reduced Trx (rTrx) and target proteins can occur, as summarised by Figure 1.5.

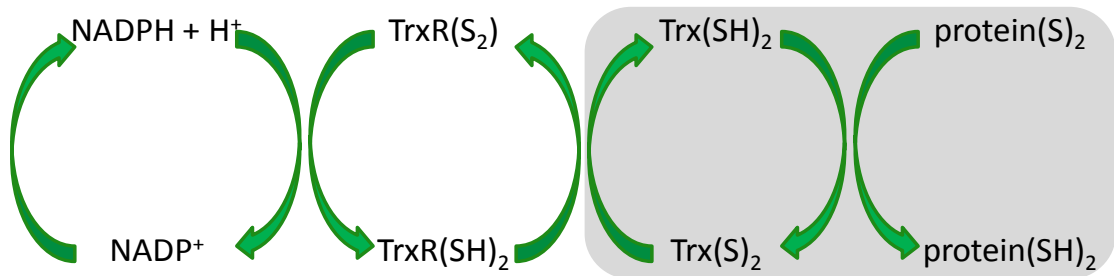


Figure 1.5. The activities of Trx rely upon reversible dithiol-exchange reactions

Schematic diagram showing the reversible redox reactions (green arrows) utilised by the Trx system. The initial source of electrons is provided by the conversion of nicotinamide adenine dinucleotide phosphate (NADPH) to NADP^+ . Electrons are then transferred to oxidised thioredoxin reductase ($\text{TrxR}(\text{S}_2)$) which is reduced to $\text{TrxR}(\text{SH})_2$. Oxidised thioredoxin ($\text{Trx}(\text{S}_2)$) is correspondingly reduced by $\text{TrxR}(\text{SH})_2$ to produce $\text{Trx}(\text{SH})_2$, which ultimately catalyses the reduction of disulphide bonds within many target proteins, highlighted by the grey box. Diagram adapted from Holmgren & Lu (2010).

Trx is a 12kDa protein which is expressed by a vast array of organisms ranging from bacteria to humans. Trx isolated from *Escherichia coli* (*E.coli*) provides the most characterised form, with early reports showing it to be composed of 108 amino acid residues. This same study also identified that the functional group of Trx involved two cysteine residues at positions 32 and 35 (Cys^{32} and Cys^{35}), separated by a glycine (Gly) and a proline (Pro) residue (Holmgren, 1968). When compared to *E.coli* Trx, the sequence homology of Trx isolated from different species is variable (27-69%), although the Cys-Gly-Pro-Cys active site sequence is highly conserved. The overall 3-dimensional (3D) structure of Trx, referred to as the Trx fold, is also common to all forms. As shown by Figure 1.6, the Trx fold is composed of four α -helices surrounded by a central core of five β -strands. The active site of Trx is located at the end of the β 2-strand and the beginning of the α 2-helix (Holmgren, 1995).

The high-resolution solution structure of Trx has been successfully resolved using NMR spectroscopy, thereby enabling comparisons between oTrx and rTrx and also between mammalian and bacterial forms. Regarding *E.coli* Trx, only minor structural differences between oTrx and rTrx were observed. The backbone structures were virtually

identical although a local conformational change involving Cys³² and Cys³⁵ residues within the disulphide active site was observed. Specifically regarding rTrx, the side chain of the Cys³² residue was tilted towards the solvent and away from Cys³⁵, to accommodate for the increased distance between the sulphur (S) atoms upon reduction of the disulphide. Different patterns of hydrogen bonding also indicated that rTrx has more conformational substrates compared to oTrx, which could contribute to their differences in functional activity (Jeng *et al.*, 1994).

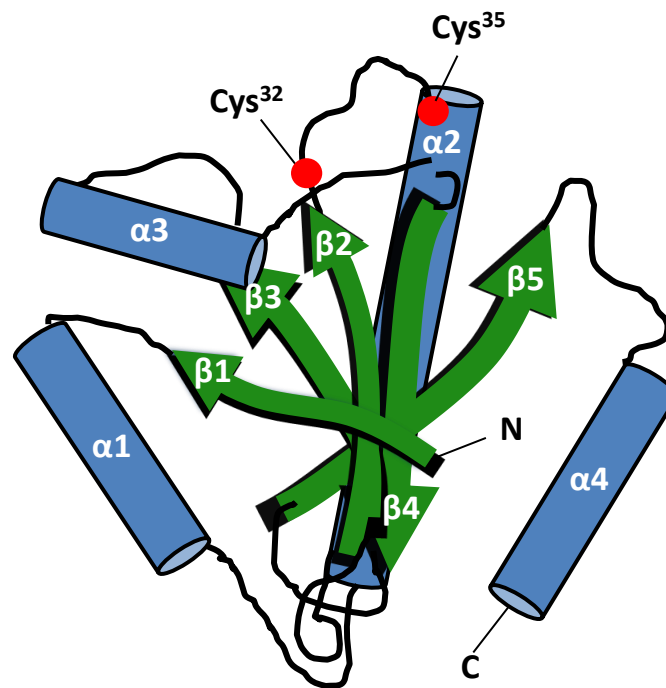


Figure 1.6. Schematic diagram of the crystal structure of oTrx

The central core of five β -strands (green arrows) are surrounded by four α -helices (blue cylinders), as numbered. The N-terminus (N) is found at the start of β 1 with the C-terminus (C) at the end of the α 4-helix. The redox-active site cysteine residues (Cys³² and Cys³⁵, red circles) are located on a protrusion between the β 2-strand and the α 2-helix. Diagram adapted from Holmgren (1995) and Hwang *et al.* (2015).

Mammalian Trx (12kDa) has been shown to be composed of 110 amino acids (Luthman & Holmgren, 1982). The crystal structure of human Trx (hTrx) has also been determined. A key difference between hTrx and prokaryotic forms is that, in addition to active site Cys³² and Cys³⁵ residues, hTrx also contains three non-canonical Cys residues, at positions 62, 69, and 73. In agreement with findings from E.coli, the structures of human oTrx and rTrx exhibit only subtle differences involving the conserved active site. A striking difference between hTrx and E.coli Trx however, is that the crystal structure of both oxidised and reduced forms of hTrx were dimeric.

Specifically, substitution of active site Cys residues to serine residues (C32S/C35S) had no effect on hTrx dimerisation. Trx dimers were also observed when the equivalent mutation was conducted on Cys⁷³ (C73S), although C73S dimers were linked by hydrogen bonds, as opposed to stronger disulphide bonds linking dimeric wt and C32S/C35S hTrx. As dimeric Trx is not a substrate for TrxR, inter-molecule covalent bond formation via Cys⁷³ residues may provide a mechanism for the regulation of Trx inactivation (Weichsel *et al.*, 1996).

Whilst much work has been conducted to elucidate the function of active site Cys residues, the functional importance of non-canonical Cys residues is only recently emerging. Importantly, oTrx generally refers to Cys³² and Cys³⁵ residues being in their disulphide form and does not take into account the redox state of non-canonical Cys residues (Weichsel *et al.*, 1996). With respect to this, the crystal structure of fully oxidised hTrx has recently been determined (Hwang *et al.*, 2015). Significantly, fully oxidised hTrx was comprised of only 3 α -helices, surrounding the typical core of 5 β -strands. While the active site disulphide bond between Cys³² and Cys³⁵ was identical to that previously described (Weichsel *et al.*, 1996), an additional disulphide bond between Cys⁶² and Cys⁶⁹ was also identified. This bond disrupted the structure of the α 3 helix, thereby producing a bulging loop and resultantly exposed hydrophobic residues to the solvent. This modification is predicted to prevent reduction of Trx by TrxR. Confirmation that inter-molecular disulphide bonds occurring via hTrx Cys⁷³ residues mediate hTrx homodimer formation was also provided. It is consequently suggested that compared to prokaryotic Trx, hTrx responds to and regulates its environment in a much more complex way, involving all five cysteine residues (Cys³², Cys³⁵, Cys⁶², Cys⁶⁹ and Cys⁷³). The contribution of non-canonical Cys residues, in addition to active site Cys residues, to the diverse biological activities of hTrx are therefore of important consideration (Hwang *et al.*, 2015).

The primary endogenous negative regulator of Trx activity is VDUP, also referred to as Trx binding protein-2 (TBP2) or Trx interacting protein-1 (TXNIP). VDUP is a 50kDa protein which selectively inhibits the disulphide reductase activities of rTrx, as reviewed (Yoshihara *et al.*, 2014). As VDUP does not interact with oTrx it has been suggested that it may inactivate Trx by forming disulphide bonds with active site Cys

residues of rTrx. In agreement with this, two Cys residues within the VDUP protein (Cys⁶³ and Cys²⁴⁷) have been identified as being crucial for Trx binding. It was further shown that VDUP and rTrx undergo thiol-exchange reactions involving Cys²⁴⁷ of oxidised VDUP and Cys³² of rTrx. This results in the formation of a stable mixed disulphide which inhibits Trx activity. Conversely, these findings also indicate that in addition to the activities of Trx as a disulphide reductase molecule, Trx could also participate in redox signalling by forming stable mixed disulphides with other signalling molecules (Patwari *et al.*, 2006).

1.6.2. The intracellular functions of Trx as a disulphide reductase molecule

The physiological functions of Trx are extremely wide-ranging, and as such, thorough discussion is beyond the scope of this introduction. However, within the intracellular environment Trx plays a key role in numerous physiological processes including, but is not limited to, DNA synthesis, cell growth, apoptosis, inflammatory responses and redox balance control. These functions generally, although not always, require the reducing capabilities of Trx which are dictated by the active site Cys³² and Cys³⁵ residues, as summarised in Figure 1.7. Whilst new roles for Trx are constantly emerging, the intracellular functions of this protein are broadly categorised into two main groups. Firstly, as an electron carrier for biosynthetic enzymes and secondly in the protection of cytosolic proteins from oxidative formation of intra- or inter-molecular disulphide bonds, as reviewed (Arner & Holmgren, 2000).

Regarding the molecular mechanisms of the oxidoreductase actions of Trx, Cys residues within the classical Cys-Gly-Pro-Cys active site sequence undergo reversible dithiol-disulphide reactions. It is proposed that the hydrophobic surface area of rTrx binds to and subsequently makes a complex with the substrate protein. The thiolate (S⁻) group of Cys³² then acts as a nucleophile which attacks the target protein resulting in a covalently-linked mixed disulphide transition state. Finally, the now deprotonated thiolate group of the Cys³⁵ residue generates a dithiol in the target protein, thereby leaving Trx in its disulphide form. Considerable conformational changes within the Trx molecule are observed during protein binding and also within electron transfer steps, as shown in Figure 1.7 and reviewed in detail (Holmgren, 1995; Holmgren & Lu, 2010).

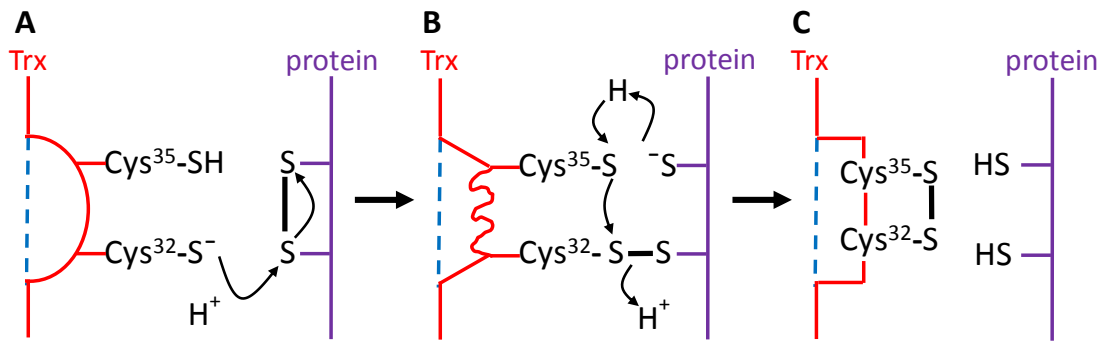


Figure 1.7. Proposed mechanism of Trx-mediated protein disulphide reduction

Schematic diagram showing electron transfer steps as represented by the black arrows. **A**, Reduced thioredoxin ($\text{Trx}(\text{SH})_2$) binds to the oxidised target protein and the thiolate group of the Cys^{32} residue then acts as a nucleophile. **B**, This results in the transient formation of a mixed disulphide between Trx and the target protein, followed by nucleophilic attack of the deprotonated Cys^{35} residue. **C**, The target protein is subsequently reduced and oxidised $\text{Trx}(\text{S}_2)$ is generated. Note, Trx undergoes conformational changes as the reaction proceeds. Diagram based on *E.coli* Trx, adapted from Holmgren (1995).

Some of the key physiological functions of Trx are conserved between lower and higher organisms. For example, by virtue of its disulphide reductase capabilities rTrx is a hydrogen donor for ribonucleotide reductase. This enzyme provides deoxyribonucleotides and is essential for DNA synthesis in both lower and higher organisms (Holmgren, 1989). Many of the antioxidant properties of Trx are also conserved across species. Within both mammalian and many bacterial cells there are two major thiol-dependent antioxidant systems, namely the Trx and glutaredoxin (Grx) systems. The antioxidant actions of Trx are generally achieved by electron transfer to peroxiredoxins (Prxs) and methionine sulfoxide reductases (MSRs). Prxs are key players in both the removal of ROS and in the defence against oxidative stress. Regarding the mechanism for this, Prxs also contain two Cys residues within their active site which are reduced and subsequently activated by rTrx. Thiol groups within the Prxs then act to remove ROS such as hydroxyl (OH^\cdot) superoxide (O_2^\cdot) and hydrogen peroxide (H_2O_2) (Lu & Holmgren, 2014). The H_2O_2 scavenging mechanism of Prx has been shown to be extremely fast within both human and yeast cells (Cox *et al.*, 2009; Oigusucu *et al.*, 2007). MSRs are also antioxidant enzymes which receive electrons donated by the Trx system. Under conditions of oxidative stress, free and protein-bound methionine is oxidised to produce methionine sulfoxide, which is accompanied by a corresponding loss in antioxidant function. When reduced by rTrx, MSR-A and MSR-B can repair

methionine sulfoxide and thus indirectly participate in ROS removal (Lu & Holmgren, 2014).

As implied by the greater structural complexity of mammalian forms of Trx, its physiological roles are more varied and extensive when compared to bacteria. A key example of the additional functions of mammalian Trx is within the activation or inactivation of a variety of transcription factors. Indeed, Trx has been shown to be crucial for redox-mediated regulation of the nuclear transcription factor- $\kappa\beta$ (NF- $\kappa\beta$). This is particularly important as NF- $\kappa\beta$ activity influences the expression of numerous inflammatory genes (Hayashi *et al.*, 1993). Interestingly, Trx can also form complexes with other proteins and correspondingly acts as a structural component of some enzymes. Trx-protein binding has been shown to be redox-dependent as rTrx, but not oTrx, binds with high affinity to T7 DNA polymerase forming a 1:1 complex and increasing enzyme activity (Huber *et al.*, 1987). Within mammalian cells, rTrx but not oTrx has also been found to make inhibitory complexes with apoptosis signalling kinase 1 (ASK1). As such, apoptosis can be stimulated when Trx becomes oxidised (Saitoh *et al.*, 1998). The activity of a large number of other transcription factors including redox effector factor (Ref-1), phosphatase and tensin homolog (PTEN) and hypoxia inducible factor- α (HIF- α), and various other proteins such as p53 and oestrogen receptors, are regulated by Trx in a redox-dependent manner. The redox state of Trx is therefore believed to be central to its extensive biological activities within the intracellular environment, as reviewed extensively (Arner & Holmgren, 2000; Holmgren, 1979; Holmgren & Lu, 2010; Lu & Holmgren, 2014).

1.6.3. Emerging roles for Trx as an extracellular signalling molecule

In addition to its extensively characterised intracellular roles, Trx can also be released from cells and therefore act as an extracellular signalling molecule. An early study examined human T-lymphotropic virus type I (HTLV-I) transformed T-lymphocytes and found that these cells secreted a protein originally termed adult T-cell leukaemia-derived factor (ADF). ADF was found to up-regulate interleukin-2 (IL-2) receptors and also had co-cytokine activity (Wakasugi *et al.*, 1990). Further investigation revealed that ADF was actually extracellular Trx (Gasdaska *et al.*, 1994). Subsequent studies

have reported that Trx is secreted into the extracellular environment by both normal and neoplastic cells in response to inflammation or oxidative stress (Rubartelli *et al.*, 1992; Rubartelli *et al.*, 1995). Extracellular Trx has been found to have chemotactic properties similar to the chemokine IL-8 inducing the migration of T lymphocytes, monocytes and polymorphonuclear leukocytes when applied at ng/ml concentrations (Bertini *et al.*, 1999). Within fibroblasts, Trx has also been shown to directly enhance the release of cytokines (Yoshida *et al.*, 1999). Whilst the mechanism of Trx secretion is not fully established, a key study conducted on activated lymphocytes has demonstrated that it occurs via a leaderless secretory pathway independent of the classical endoplasmic reticulum-Golgi route (Rubartelli *et al.*, 1992). A similar pattern of Trx secretion has been described in MCF-7 (breast cancer), HT-29 (colon carcinoma), U937 (histiocytic lymphoma), and IM9 (multiple myeloma) cells. It is noteworthy that Trx secretion was unaltered by treatment with brefeldin A, which disrupts the ER-Golgi mechanism, and was also independent of cell lysis (Tanudji *et al.*, 2003).

An important consideration is whether the redox state of Trx influences its secretion or indeed its extracellular functions, as shown for its numerous intracellular physiological roles. Mutation of the Trx active site Cys residues (C32S/C35S) has been shown to prevent its chemotactic activity, suggesting extracellular Trx to be rTrx (Bertini *et al.*, 1999). However, this observation contradicts with findings that Trx is secreted in response to oxidative stress (Nakamura *et al.*, 2006); indicating that extracellular Trx is likely oTrx (Arner & Holmgren, 2000). In support of this suggestion, the effects of cellular redox status on Trx secretion was explored by Kondo *et al.* (1994), who conducted an extensive study using the T-lymphocyte cell lines, ATL2 and Jurkat. Measurement of Trx levels from culture supernatants and cell lysates confirmed that oxidative stress, achieved by treatment with H₂O₂, increased both intracellular and extracellular Trx levels. Importantly, whilst having no effect on intracellular Trx, treatment with the reducing agent and antioxidant *N*-acetylcysteine (NAC) caused a significant reduction in extracellular Trx. This provided strong evidence that cellular redox-status regulates Trx secretion (Kondo *et al.*, 2004).

Jurkat cells were also transfected with either recombinant wt Trx or mutant (C32S/C35S) Trx. Stimulation of Jurkat cells with H₂O₂ rapidly stimulated Trx secretion

from cells transfected with wt Trx, however not in cells transfected with the C32S/C35S Trx. This strongly suggested that an intact redox-active site is essential for Trx secretion (Kondo *et al.*, 2004). Interestingly, it was also observed that application of exogenous rTrx to Jurkat cell culture media decreased Trx secretion, but not intracellular levels. It is subsequently suggested that Trx regulates its own release (Kondo *et al.*, 2004). In continuation of this proposal, application of fluorescently-labelled wt Trx to the extracellular environment resulted in cellular Trx uptake. Specifically, time-dependent increases in Trx levels within cytosolic and plasma membrane fractions were observed. As no cellular uptake was observed when mutant Trx (C32S/C35S) was applied, evidence that the redox-active site of Trx determines both its secretion and cellular uptake is provided (Kondo *et al.*, 2004).

In contrast with these findings, an alternative study conducted on Chinese hamster ovary (CHO) cells indicated that Trx secretion can occur independently of the cell's redox state (Tanudji *et al.*, 2003). CHO cells transiently transfected with hTrx were found to slowly and efficiently secrete hTrx. Acute treatment with NAC did not alter Trx secretion, although treatment with NAC for 12hrs did decrease both intracellular and extracellular Trx levels. As mutation of hTrx Cys³⁵ (active site) or Cys⁷³ residues (dimerisation site) did not alter secretion, evidence that intact active sites or dimerisation sites are not required for Trx secretion was provided (Tanudji *et al.*, 2003). Further evidence that the functions of extracellular Trx are, at least not entirely, dependent on its redox active site, are provided by studies investigating non-typical Trx structural forms. In addition to its standard 12kDa form, hTrx secreted from human platelets and cytotrophoblast cell lines was shown to also be comprised of a 10kDa derivative of the 12kDa Trx (Di *et al.*, 1998). This truncated Trx form, subsequently termed Trx80, has been shown to be an extracellular product of Trx cleavage, as reviewed (Holmgren & Lu, 2010).

Despite the fact that Trx80 lacks disulphide reductase activity it has been shown to act as a mitogenic cytokine on human peripheral blood mononuclear cells (PBMCs). In PBMCs, Trx80 also stimulated the release of interleukin-2 (IL-2) whilst wt Trx was without effect (Pekkari *et al.*, 2001). Trx80 has also been referred to as eosinophil cytotoxicity-enhancing factor (ECEP). Exogenous Trx80 has also been found to increase

dramatically the expression of the human immunodeficiency virus (HIV) in human macrophages. In stark contrast, exogenous human rTrx potently inhibited the expression of HIV by human macrophage cells (Newman *et al.*, 1994). It has also been suggested that post-translational modification of non-canonical Cys residues in hTrx influences its extracellular functions (Tao *et al.*, 2004). A further consideration is that TrxR has also been shown to be present at the surface of some cells and within the extracellular environment (Soderberg *et al.*, 2000; Zhang *et al.*, 2013). Correspondingly, the redox state of secreted Trx does not necessarily correspond with its redox state in the extracellular environment. Collectively, these studies emphasise that the physiological roles of Trx within the extracellular environment are not entirely dependent on its redox active site.

1.7. Clinical implications of Trx expression in proliferative disorders

Regarding clinical situations, increased levels of circulating Trx are detected within numerous pathological conditions, including but not limited to; a variety of cancers (Baker *et al.*, 2013), acute myocardial infarction (AMI) (Miyamoto *et al.*, 2003), abdominal aortic aneurysm (Martinez-Pinna *et al.*, 2010), atherosclerosis (Okuda *et al.*, 2001), rheumatoid arthritis (Yoshida *et al.*, 1999) and HIV (Nakamura *et al.*, 1996). Elevated Trx levels are also detected in the blood plasma of patients subject to cardiopulmonary bypass operations (Nakamura *et al.*, 1998). Whilst elevations in Trx may initially serve to counterbalance oxidative stress, Trx over-expression in cancer patients is associated with aggressive tumour growth, increased proliferation, decreased apoptosis, and reduced patient survival (Raffel *et al.*, 2003).

1.7.1. Cardiovascular disorders

Oxidative stress is believed to be a key factor in the development of atherosclerosis which can ultimately lead to myocardial infarction (MI). A hallmark feature of atherosclerosis is atheromatous plaque formation resulting from elevated VSMC proliferation and increased platelet aggregation (Chistiakov *et al.*, 2015). Within non-atherosclerotic human coronary vessels, Trx expression has been shown to be localised within medial VSMCs. In contrast, within atherosclerotic coronary vessels, Trx was

additionally present throughout the vessel wall and surrounding infiltrating macrophages (Okuda *et al.*, 2001). An alternative clinical study was conducted on three groups of patients suffering from acute MI (AMI), coronary artery occlusion with stable exertional angina (SEA) or chest pain syndrome (CPS) without arterial stenosis or spasm. Plasma Trx levels were considerably elevated in the AMI group when compared to the SEA and CPS groups. Increased levels of extracellular Trx within the AMI group positively correlated with increased platelet aggregation and negatively correlated with left ventricular ejection fraction. These changes, although reduced, were still apparent four weeks post-AMI. Whilst oral administration of statins did not alter plasma Trx levels, it did significantly decrease the degree of small platelet aggregates within the AMI group. Therefore, the application of statins, which are capable of reducing oxidative stress, could improve the prognosis of AMI patients (Miyamoto *et al.*, 2003). A more recent study measured plasma Trx levels from MI patients 1, 2 and 3 days post-event. Significantly, patients who died 24hrs post-MI had the highest plasma Trx levels. Patients with coronary risk factors are subject to prolonged oxidative stress; as such, increased serum Trx levels may initially appear as a compensatory antioxidant mechanism. However, as increased Trx did not counteract oxidative stress or inflammatory responses post-MI; in fact, increased serum Trx actually provides a negative indicator of MI severity and outcome (Mongardon *et al.*, 2013). Increased levels of Trx have also been directly implicated in the differentiation and proliferation of SMCs, leading to pathological cardiac remodelling following AMI in rats (Suresh *et al.*, 2015). Cardiovascular remodelling can also occur in hypertensive patients. However, in contrast with findings reported for atherosclerosis and AMI, increased levels of oxidative stress were accompanied by reductions in Trx expression within the aorta, heart and kidney of spontaneously hypertensive rats (Tanito *et al.*, 2004).

A further complication of atherosclerosis involving the differentiation of VSMCs is the development of abdominal aortic aneurysm (AAA). Increased levels of plasma Trx have also been reported in patients suffering from AAA. Discontinuous patterns of growth and periods of acute expansion exhibited in AAA can result in fatal vessel rupture. Vessel diameter, a surrogate marker of growth rate, is therefore used to assess AAA severity and as a surgical indication. Using two cohort populations, AAA patients were shown to have significantly higher circulating Trx levels when compared to control

patients. The degree of Trx elevation correlated with increased AAA vessel diameter. Immunohistochemical processing of surgically removed thrombi revealed that Trx was produced and released by the luminal, as opposed to the abluminal, layer of the thrombus. Thrombus formation within AAA also leads to the production of ROS. Correspondingly, aspirin treatment was found to decrease circulating Trx levels in AAA patients. Importantly, these findings show that oxidative stress increases serum Trx levels, which provides an important biomarker for the severity and progression of AAA (Martinez *et al.*, 1999). In direct agreement with these findings, serum Trx levels are elevated in patients following acute ischemic stroke (AIS). High Trx levels were also shown to be an effective diagnostic and prognostic marker for AIS (Qi *et al.*, 2015). Plasma Trx levels have also been measured in patients suffering from chronic heart failure (CHF). Urinary β 2-microglobulin-creatinine ratios (UBCR) were additionally measured as a marker for renal tubular damage. Significant elevations in plasma UBCR and Trx levels were recorded in CHF patients suffering from cardiac events when compared to cardiac event-free patients. In agreement with findings from other cardiovascular disorders, the extent of Trx elevation correlated with poor CHF outcome (Otaki *et al.*, 2014).

The link between increased extracellular Trx levels and cardiovascular disorder severity is commonly associated with pathological oxidative stress. It is suggested that the antioxidant functions of up-regulated Trx may provide a compensatory mechanism in response to increased ROS generation, as reviewed (Billiet & Rouis, 2008; Burke-Gaffney *et al.*, 2005). Interestingly, many of the cardiovascular pathologies associated with increased oxidative stress and elevated Trx also involve VSMC dedifferentiation, increased proliferation and cardiovascular remodelling, as discussed in section 1.2. As such, the pathophysiological significance of elevated extracellular Trx may additionally concern the mitogenic functions of Trx. Evidence linking the Trx system to the phenotypic switching of VSMCs and vascular remodelling is provided by a retrospective study which reported that patients with T2DM had significantly elevated levels of circulating VDUP. Interestingly, increased VDUP levels correlated with carotid artery neointima thickness (Zhao *et al.*, 2015). Direct evidence of the pro-proliferative nature of Trx in VSMCs is provided by a study showing that Trx over-expression significantly increased DNA synthesis in VSMCs, a key marker of proliferation. In contrast, VDUP

over-expression reduced Trx activity and inhibited mitogen-stimulated VSMC proliferation (Schulze *et al.*, 2002). Furthermore, it has also been shown that VDUP can inhibit Trx-induced protein synthesis in cardiomyocytes. Cells with elevated VDUP were also shown to develop less hypertrophy following aortic constriction. Importantly, this study emphasised that in addition to its role as an antioxidant, Trx serves as a signalling molecule which participates in the development of pressure-induced cardiac hypertrophy (Yoshioka *et al.*, 2004). The role of Trx as an extracellular signalling molecule and the dependency of these effects on the redox-state of Trx are discussed extensively in Chapter 5.

1.7.2. Cancers

Malignant disorders characterised by aberrant cellular proliferation demonstrate increased extracellular Trx levels. It is believed that Trx upregulation can initially act to counterbalance oxidative stress induced by carcinogenic agents and thereby serve a protective role. Contrastingly, within established malignancies the pro-proliferative effects of Trx on cancerous cells considerably outweighs its initial beneficial antioxidant functions. As discussed in sections 1.6.2 and 1.6.3, due to the range of biological targets of Trx, potential mechanisms of Trx-mediated growth stimulation are numerous. This includes activating transcription factors, providing essential reducing equivalents for DNA synthesis and increasing cellular-sensitivity to growth factors and cytokines, as reviewed (Burke-Gaffney *et al.*, 2005). Specifically within tumour cells, Trx has been shown to enhance tumorigenesis by increasing the levels and activity of HIF-1 α and also protein products of hypoxia-responsive genes, such as vascular endothelial growth factor (VEGF) and NOS (Welsh *et al.*, 2002). Trx can also inhibit the tumour suppressor gene PTEN, which involves binding of the Trx Cys³² residue with the PTEN Cys²¹² residue. This results in a steric influence of Trx on the PTEN active site, and enhances tumorigenesis. A further important mechanism of tumorigenesis is that Trx has also been found to inhibit apoptosis by influencing polyamine-induced apoptosis pathways (Husbeck *et al.*, 2003) and also through its regulation of ASK1 (Powis *et al.*, 2000; Saitoh *et al.*, 1998). Given that many chemotherapy drugs act to promote cancer cell apoptosis, increased Trx levels could account for reduced effectiveness of these treatment strategies (Burke-Gaffney *et al.*, 2005).

The range of cancers associated with increased blood plasma and cellular Trx levels is constantly expanding. The current list includes, but is not limited to, pancreatic cancer (Nakamura *et al.*, 2000); lung cancer (Kahlos *et al.*, 2001; Kakolyris *et al.*, 2001; Soini *et al.*, 2001); cervical cancer (Fujii *et al.*, 1991) and hepatocellular carcinoma (Kawahara *et al.*, 1996; Nakamura *et al.*, 1992). Increased Trx levels have also been described in human primary gastric carcinomas, where elevated Trx was directly shown to promote tumour cell proliferation and inhibit apoptosis (Grogan *et al.*, 2000). A further key study examined Trx levels in human primary and metastatic colorectal cancers and found them to be significantly elevated when compared to normal colonic mucosa. Follow up studies further revealed that increased levels of Trx correlated with decreased patient survival. Crucially, it was also suggested that elevations in Trx levels occur relatively late in colorectal carcinogenesis, providing an effective biomarker of patient prognosis (Raffel *et al.*, 2003).

In light of the wealth of evidence associating Trx with cancerous cell growth, the Trx inhibitors PX-12 and AuF are currently being explored clinically as anti-cancer agents (Ramanathan *et al.*, 2011; Roder & Thomson, 2015). Importantly, cancer patients showed significantly elevated plasma Trx levels when compared to healthy controls, which were subsequently reduced following PX-12 treatment. In addition to the human studies, it was also reported that PX-12 decreased circulating Trx in non-tumour bearing mice, observed 2 and 24 hours post-treatment. Interestingly, the authors postulate that this was due to rapid cellular uptake of modified Trx, although decreased Trx secretion could also contribute to this observation (Baker *et al.*, 2013).

1.8. Aims and hypothesis:

Recent findings have shown that extracellular Trx can regulate not only recombinantly-expressed Ca_v3.2 channels (Boycott *et al.*, 2013) but also TRPC1 and TRPC-5 channels (Xu *et al.*, 2008). These observations may explain the, as of yet, undetermined functional significance of coincident upregulation of T-type Ca²⁺ channels and Trx in proliferative disorders. This thesis has therefore explored the hypothesis that Trx can regulate T-type Ca²⁺ channels and, in so doing, modulate VSMC proliferation. The specific aims of this study were to initially assess the effects of T-type Ca²⁺ expression

and pharmacological Trx inhibition on both VSMC proliferation and Ca^{2+} handling. An additional aim was to characterise the mechanism and isoform sensitivity of Trx-mediated T-type Ca^{2+} channel regulation in detail.

Chapter 2 -Methods and materials

2.1. Cell culture

All cells were maintained in a humidified incubator at 37°C, CO₂ (5%): air (95%), and all culture reagents were purchased from Gibco, Thermo Fisher Scientific, (Paisley, UK), unless otherwise stated.

2.1.1. A7r5 cells

Rat aortic smooth muscle cells (A7r5; ECACC, Public Health England, Porton Down, UK) were cultured in complete growth media consisting of Dulbecco's modified eagle medium (DMEM) supplemented with antibiotic/antimycotic (1%) and foetal bovine serum (FBS, 10%, Biosera, UK). Cells were passaged on a weekly basis from 75cm³ culture flasks by trypsinisation; media was removed and cells washed with Dulbecco's phosphate buffered saline (PBS) before trypsin-EDTA (2mL, 0.05%) was applied and incubated with cells (3mins, 37°C). Cell detachment was verified under a microscope before cells were suspended in complete growth media (10ml), transferred to a 50ml Falcon tube and centrifuged (400xg, 6mins). The trypsin containing supernatant was discarded and the cell pellet re-suspended in complete growth media (20ml). From this suspension, fresh 75cm³ culture flasks were seeded at 1:10 or 1:20 dilutions, and the remaining cell suspension was plated into various culture vessels for subsequent experiments.

Two batches of A7r5 cells purchased from the same supplier were used within the project: initial A7r5 cells referred to as "old" A7r5 cells had been sub-cultured at 90-100% confluency and stored by the group for a number of years. The "old" A7r5 cells were used between passage (p) 14-17 and exhibited phenotypic variation with increasing p number. This was hypothesised to be due to a reduction in T-type Ca²⁺ channel expression due to culture at relatively high confluency, as previously described within primary cultures of rat thoracic aortic smooth muscle cells (Richard *et al.*, 1992). In an attempt to maximise T-type Ca²⁺ channel expression, a new batch of A7r5 cells were purchased, sub-cultured at 70-80% confluency and used between p1-12. Increased T-type Ca²⁺ channel expression was validated using real-time reverse

transcriptase polymerase chain reaction (qRT-PCR, as described in section 2.2). The “new” A7r5 cells were used for all subsequent experiments.

2.1.2. wt HEK293 and recombinant HEK293/Ca_v3.1 and HEK293/Ca_v3.2 cells

Wild-type (wt) human embryonic kidney 293 (HEK293) cells (ECACC, Public Health England, Porton Down, UK) were cultured in complete growth media consisting of minimum essential medium (MEM) supplemented with antibiotic/antimycotic (1%), non-essential amino acids (1%), gentamicin (0.1%) and FBS (10%, Biosera, UK). HEK293 cells stably expressing either rat Ca_v3.1 or human Ca_v3.2 (HEK293/Ca_v3.1 and HEK293/Ca_v3.2 cells respectively, originally a gift from Dr. E. Perez-Reyes, University of Virginia, Charlottesville, VA, USA) were cultured in the same media additionally supplemented with G-418 (400µg/ml) as the selection antibiotic. For comparison, HEK293 cells stably transfected by Dr Jason Scragg in-house with the Ca_v3.2-containing mammalian expression vector to generate HEK293/Ca_v3.2/clone P cells, were also used occasionally. In addition to HEK293 cells transfected with the Cav3.2(H191Q) construct (a gift from Dr. E.Perez-Reyes) whereby the histidine (H) residue at position 191 of the Cav3.2 channel had been mutated to a glutamine (Q) residue (HEK293/Ca_v3.2(H191Q) cells). HEK293/Ca_v3.2/clone P and HEK293/Ca_v3.2(H191Q) cells were cultured in the same media as used for other recombinant cells. All cells were passaged weekly at 90-100% confluence as previously described (2.1.1). Fresh culture flasks were seeded at 1:40 dilutions for WT HEK293 and HEK293/Ca_v3.2/clone P and HEK293/Ca_v3.2(H191Q) cells and 1:80 dilutions for HEK293/Ca_v3.1 and HEK293/Ca_v3.2 cells. All HEK293 cells were used between p 1-12.

2.2. Real-time polymerase chain reaction (qRT-PCR)

To quantify native Ca_v3.1 and Ca_v3.2 channel expression in “new” A7r5 cells, and enable comparison with “old” A7r5s as previously determined (Duckles *et al.*, 2015); Ca_v3.1 and Ca_v3.2 mRNA levels were measured using qRT-PCR. This technique is superior to standard PCR as it enables real-time detection and accurate quantification of the amplified gene of interest (amplicon), typically through the inclusion of fluorescently-labelled, sequence-specific primers, measured by fluorescence detectors within specialised thermal cyclers. Initial amplification cycles, whilst producing

exponential increases in amplicon level, do not produce enough fluorescence to be detected. The cycle number which yields enough amplicon accumulation to enable fluorescence detection is referred to as the threshold cycle (C_T) and is used to calculate the amount of template initially present.

2.2.1. Cell culture and RNA extraction

A7r5 cells were plated at 1:10 or 1:20 dilutions and cultured in T75 flasks for 7 days (70-80% confluent respectively), cells were then trypsinised as described (section 2.1.1) and re-suspended in ice-cold PBS and centrifuged (400 xg , 6mins, x2). The supernatant was discarded and cell pellets triturated with 100 μ L of RNAlater® (Ambion, Cambridge, UK) and transferred to microcentrifuge tubes which were refrigerated (4°C) for 24hrs then stored at -80°C.

When required, samples were thawed, washed and centrifuged with PBS (400 xg , 6mins, x3) and all supernatant was discarded. Due to the highly unstable nature of RNA, all surfaces were thoroughly cleaned with ethanol (70%) and then RNAase AWAY (Molecular Bio Products, CA, USA); RNA extraction was conducted using the Aurum total RNA mini kit (Bio-Rad, Hemel Hempstead, UK) following manufacturer's instructions. Briefly, PBS (1ml) was added and cells were triturated and centrifuged (12,000 xg , 30secs). Supernatant was discarded and lysis buffer and ethanol was then added in equal volume (350 μ L). After thorough mixing the suspension was transferred to an RNA binding column and low-stringency wash solution (700 μ L) was added prior to centrifugation (12,000 xg , 30secs). All flow-through was discarded and RNAase-free DNAase I (80 μ L) was applied to the membrane stack at the bottom of each column and incubated at room temperature (RT, 15mins). High-stringency wash solution (700 μ L) was then added and the binding column centrifuged (12,000 xg , 1min, x3), which was repeated with low-stringency wash solution (700 μ L). Flow-through was discarded and elution buffer (80 μ L, pre-warmed to 70°C) was added to the membrane stack and incubated at RT (1min). The column was then centrifuged (12,000 xg , 2min) to elute total RNA, which was used immediately or stored at -80°C.

2.2.2. cDNA generation and qRT-PCR protocol

All surfaces were thoroughly cleaned with ethanol (70%) and RNAase AWAY then cDNA templates were generated from extracted RNA samples using the iScript cDNA synthesis kit (Bio-Rad; Hemel Hempstead, UK), according to manufacturer's instructions. Briefly, RNA samples and reagents were allowed to thaw over ice. iScript reaction mix (4 μ L), iScript reverse transcriptase enzyme (1 μ L) and RNase/DNase-free H₂O (12.5 μ L, Gibco; Thermo Fisher Scientific, Paisley, UK) were added to each RNA sample (2.5 μ L) contained within a PCR tube, which was transferred to the 3Prime thermal cycler (Techne, Staffordshire, UK). Samples were heated to 25°C (5mins), 42°C (30mins), 42°C (30mins), and held at 4°C (5mins). Samples were then centrifuged (12,000xg, 30secs) and immediately stored at -20°C.

qRT-PCR was conducted using Taqman probes for rat Cav3.1, rat Cav3.2 and the endogenous housekeepers rat hypoxanthine phosphoribosyltransferase (HPRT1), and rat large ribosomal subunit (17S), (all supplied Applied Biosystems (ABI), UK). The relevant Taqman Primer (0.5 μ L) was mixed with RNase/DNase-free H₂O (8.5 μ L, Gibco; Paisley, UK), Taqman Universal PCR Master Mix (10 μ L, ABI) and the cDNA template (1 μ L) within individual wells on a 96-well PCR plate (ABI, Cambridge, UK). The plate was sealed with an optical adhesive cover and qRT-PCR was carried out using a 7500 real-time PCR system (ABI). The reaction profile was set to 50°C (2mins), 95°C (10mins), 95°C (5secs) for 60 cycles, and 60°C (1min) before holding at 4°C. All samples were measured in triplicate.

2.2.3. Data analysis- comparative C_T method for relative quantification

Data were analysed using the 7500 software (ABI) and relative gene expression was calculated using the $2^{-\Delta\Delta CT}$ method using HPRT1 as the endogenous control. Using this method the amount of target, normalised to the endogenous control and relative to a calibrator is calculated by the formula:

$$RQ = 2^{-\Delta CT}$$

- RQ = relative quantification value.
- C_T = threshold cycle number for a particular sample and refers to a particular target (e.g. Ca_v3.1 or HPRT1).
- ΔC_T = difference between C_T values for target (Ca_v3.1 or Ca_v3.2) and reference (HPRT1)

Finally, the relative expression of Ca_v3.1 or Ca_v3.2 in relation to the housekeeper was expressed by multiplying $2^{-\Delta CT}$ by 100. All measurements were made in triplicate wells with the mean value used as n=1. Paired or un-paired Student's t-tests were conducted (GraphPad Software, Inc), as described in section 2.11.

2.3. Immunohistochemistry

To assess the subcellular localisation of Ca_v3.1 and Ca_v3.2 channels in the cell lines used for the current project, immunohistochemistry was conducted. All primary and secondary antibodies were purchased from NeuroMab (UC Davis, NIH NeuroMab Facility, CA, USA). As recommended, antibody concentrations were optimised prior to experiments. Following trypsinisation (2.1), HEK293/Ca_v3.1, HEK293/Ca_v3.2 and HEK293/Ca_v3.2/clone P cells were plated at 1:10 dilutions, whereas A7r5 cells were plated at a 1:5 dilution, onto poly-L-lysine coated sterile glass coverslips (22x22mm, thickness 0). Coverslips were held within 6-well plates containing the relevant complete growth media (2ml per well). Cells were then incubated for 3 days before media was removed and coverslips were washed with ice-cold PBS (5mins, x3). Paraformaldehyde (1ml per well, 4% in PBS, Sigma-Aldrich, UK) was applied for 40mins at 4°C. The fixative was removed and coverslips were incubated in PBS containing Triton®X-100 (0.1%, Sigma-Aldrich, UK) and bovine serum albumin (BSA, 10%, Sigma-Aldrich, UK) for 20mins at RT (1ml per well). This was to both permeabilise cells and block non-specific staining respectively. Cells were then washed with Triton®X-100 (0.1% in PBS, 1ml per well, 5mins, x3), before a final wash with BSA (1% in PBS, 1ml per well, 5mins). Primary (1°) antibodies were made up to the appropriate dilutions using PBS + BSA (1%). Coverslips were then incubated with either anti-Ca_v3.1 (1:100, mouse, clone N178A/9) or anti-Ca_v3.2 (1:1000, mouse, clone N55/10) for 12hrs at 4°C. To minimise usage, for all 1° antibody incubations coverslips were inverted on ParafilmM® (Sigma-Aldrich, UK), using 100µL of 1° antibody per coverslip.

Two fluorophore-bound secondary (2°) antibodies were used to detect anti-Ca_v3.1 or anti-Ca_v3.2 1° antibodies. Coverslips were first washed with BSA (1% in PBS, 1ml per well, 5mins, x3). AlexaFluor⁵⁵⁵ goat anti-mouse IgG1 (red) or AlexaFluor⁴⁸⁸ goat anti-mouse IgG1 (green) were then diluted to 1:1000 in PBS + BSA (1%). 2° antibodies were applied to coverslips for 1hr at RT (1ml per well), protected from light. Finally cells were washed with PBS (1ml per well, 5mins, 3x) before a final wash with double-distilled H₂O (ddH₂O, 1ml per well, 5mins). Coverslips were allowed to air-dry, then mounted onto microscope slides using Vectashield^R mounting media containing 4',6-Diamidino-2-Phenylindole Dihydrochloride (DAPI, Vector Laboratories; Peterborough, UK), to label total DNA. Coverslips were finally sealed round the edges with nail varnish and refrigerated (4⁰C) in the dark.

2.3.1. Image acquisition and analysis

Slides were removed from the fridge and allowed to warm to RT for 30mins before viewing with a light microscope (Nikon Eclipse E600, COOL LED pE illumination system, x40 magnification, used throughout). For each coverslip, 5 fields of view were randomly selected and the appropriate LEDs and filter sets used to detect different fluorophores. DAPI was visualised using the blue channel (400nm), AlexaFluor⁴⁸⁸ using the green channel (470nm) and AlexaFluor⁵⁵⁵ using the red channel (GYR). Images were captured via an integrating analogue CCD camera (JVC KYF 55B) attached to an Acquis image-capture system (Synoptics; Cambridge, UK). To examine co-localisation, images were merged post-acquisition and were adjusted for brightness and contrast using Corel photo paint.

2.4. MTT viability assays

In order to assess whether the thioredoxin inhibitors Auranofin (AuF) and PX-12 would affect cell viability, 3-(4,5-dimethylthiazol-2-yl)-2,5-diphenyl tetrazolium bromide (MTT) assays were conducted on A7r5, wt HEK293 and HEK293/Ca_v3.2 cells. The MTT assay is based on the principle that only active mitochondria are able to cleave MTTs tetrazolium ring and convert the pale yellow soluble substrate to the partially soluble, dark blue formazan product. The degree of colorimetric absorbance at 570nm is thus

directly proportional to the number of living cells present (Mosmann, 1983). 96-well plates were coated with poly-L-lysine (100 μ L) which was removed before plates were allowed to dry for 30mins. Cells were plated in complete growth media, at the appropriate cell density to achieve confluence 24, 48 or 72 hours post-drug treatment. Cells were incubated overnight and media was replaced with complete growth media (100 μ L) \pm AuF (1nM-3 μ M) or PX-12 (300nM-300 μ M). The 96-well plate layout shown within Figure 2.1 enabled 8 treatment and 2 control groups to be analysed, as the outer wells were prone to evaporation and plate reader inaccuracy.

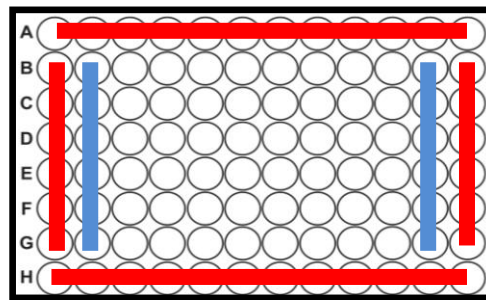


Figure 2.1. 96-well plate layout used for MTT assay
Red line, omitted from analysis, **blue line**, control wells.

Following drug treatment (24, 48 or 72 hours), MTT (11 μ L, 5mg/ml, Sigma-Aldrich) was added to each well and cells were incubated for 3 hours (37°C). A solubilising solution of propan-1-ol (Sigma-Aldrich) and 1M HCl (1:25) was added to each well (111 μ L), to lyse cell contents and standardise media coloration. Cell suspensions were thoroughly triturated and absorbance was measured at 570nm using a spectrophotometer (Glomax multi-detection system; Promega, UK). Absorbance values were normalised to control values and averages taken for each condition. The mean value of 8 wells was used as n=1. All experiments were repeated three times over different passage numbers. Data were analysed using one-way ANOVA and Dunnett's post-hoc tests (GraphPad Software, Inc), as described in section 2.11.

2.5. Proliferation assays - direct cell counting

The direct cell counting protocol used for proliferation assays was based on longstanding published methods (Porter *et al.*, 2002). Cells were trypsinised as detailed (2.1.1), and after centrifugation the cell pellet was re-suspended in complete growth

media (1ml), and cell number was counted using the T10 automated cell counter (Bio-Rad; Hemel Hempstead, UK). Cells were plated into 24-well plates at appropriate densities estimated to not exceed 100% confluency on the final day of the assay; $1 \times 10^4 \cdot \text{ml}^{-1}$ or $2 \times 10^4 \cdot \text{ml}^{-1}$ for A7r5 cells and HEK293 cells respectively. Due to poor adherence of WT HEK293, HEK293/Ca_v3.1 and HEK293/Ca_v3.2 cells, 24-well plates were coated with poly-L-lysine, allowed to dry for 30mins prior to plating. Cells were incubated in the relevant complete growth media for 9 hours to enable optimum cell adherence, washed with PBS (1ml per well), and incubated in serum free media (SFM, 0% FBS) for 12 hours to encourage cell cycle synchronisation. Day 0 counts were taken, and media changed to complete growth media \pm various drugs as listed in Table 2.1. Cells were incubated for 3 days and counted either daily or on day three alone.

All cell counts were made in triplicate (i.e. from three wells) including day 0 counts. Media was retained from a single well from each condition to enable floating cell quantification, which was added to the non-viable cell count. Adherent cells were washed with PBS (1ml) and trypsinised (200 μ L trypsin-EDTA per well). Cells were triturated and transferred to micro-centrifuge tubes (1.5ml) along with complete growth media (800 μ L per well), to inhibit further trypsin dissociation. Cells were centrifuged (400 $\times g$ for 6mins) and 950 μ L of supernatant was removed. Cell suspensions were then mixed with equal amounts of Trypan blue (50 μ L, Sigma-Aldrich, UK), to stain unviable cells and counted using the automated cell counter. For low concentration cell suspensions (i.e. floating cells and day 0) counts were performed using a haemocytometer. Un-paired Student's t-tests were conducted (GraphPad Software, Inc), as described in section 2.11.

Drug and vehicle	Working conc'	Purpose of application
Auranofin (DMSO)	300nM 100nM	A gold containing compound initially characterised as an anti-rheumatic drug (Finkelstein <i>et al.</i> , 1976) which was later shown to inhibit thioredoxin reductase (TrxR), the enzyme responsible for the reduction and subsequent activation of thioredoxin (Trx) with a K_i of 4nM when measured in the presence of 50 μ M Trx (Gromer <i>et al.</i> , 1998).
PX-12 (DMSO)	1 μ M	Trx inhibitor originally named IV-2 (1-methylpropyl 2-mercaptoimidazolyl disulfide) which inhibits Trx via irreversible thioalkylation of Cys ⁷³ . At higher concentrations reversible thioalkylation of Cys ³² and Cys ³⁵ also ($K_i=31\mu$ M) occurs (Kirkpatrick <i>et al.</i> , 1998).
NNC 55-0396 (ddH ₂ O)	1 μ M, 3 μ M	T-type selective Ca ²⁺ channel blocker (CCB), which shows no inhibition of high voltage activated (HVA) currents at 100 μ M (Li <i>et al.</i> , 2005).
ML218 (DMSO)	3 μ M	A recently developed compound, shown by high-throughput screening technique, to be T-type selective at 10 μ M (Xiang <i>et al.</i> , 2011).
Mibefradil (ddH ₂ O)	1 μ M, 3 μ M	Within VSMCs mibefradil ($\leq 1\mu$ M) selectively inhibits T-type Ca ²⁺ currents (Brueggemann <i>et al.</i> , 2005). It has also been shown its metabolite can also activate L-type Ca ²⁺ channels when applied at higher concentrations (Li <i>et al.</i> , 2005).
Nifedipine (DMSO)	2 μ M	Nifedipine (300nM) has been shown to selectively inhibit L-type Ca ²⁺ currents in arterial smooth muscle, enabling T-type Ca ²⁺ current isolation (Abd El-Rahman <i>et al.</i> , 2013).

Table 2.1. Drugs used in proliferation assays and Ca²⁺ microfluorimetry

All purchased from Sigma-Aldrich, UK, except Auranofin and PX-12 (Tocris biosciences; Bristol, UK and ML218 (kindly gifted from Craig Lindsley, Vanderbilt University, Tennessee, USA)

2.6. Proliferation assays - EdU incorporation assay

As an alternative to the direct cell counting proliferation assay, the Click-iT® EdU assay (Invitrogen Molecular Probes; Thermo Fisher Scientific, Paisley, UK) was employed to examine the effects of PX-12 on WT HEK293 and HEK293/Ca_v3.1 cell proliferation. EdU (5-ethynyl-2'-deoxyuridine) is a nucleoside analog of thymidine which becomes incorporated into newly synthesised DNA, and is detected by utilisation of the principles of click chemistry i.e. it involves a copper-catalyzed covalent reaction between an alkyne (EdU incorporated into DNA) and an azide (Alexa Fluor detection reagent). This newly developed assay can be used as a replacement for the standard

BrdU (5-bromo-2'-deoxyuridine) nucleoside incorporation assay with the main advantage that the small size of the azide allows detection without denaturing DNA, circumventing potential effects on cell morphology and nuclear counterstaining associated with BrdU. As the assay utilises bio-orthogonal moieties, high detection sensitivities and low background signals are achieved.

2.6.1. Cell culture and EdU incubation

EdU incorporation assays were performed according to manufacturer's instructions. As recommended EdU concentration/incubation time (5 or 10 μ M, 1-48 hours) and plating density (1-4x10⁴.ml⁻¹) was optimised prior to experiments. Following trypsinisation, cell number was determined as described (2.5) and wt HEK293 and HEK293/Ca_v3.2 cells were plated at 4x10⁴.ml⁻¹ onto poly-L-lysine coated sterile glass coverslips (22x22mm, thickness 0) within 6-well plates containing the relevant complete growth media (2ml per well). Cells were allowed to adhere for 24 hours, washed with PBS (2ml per well) and incubated in SFM (2ml per well) for 12 hours to encourage cell cycle synchronisation. Media was then changed to complete growth media \pm PX-12 (1 μ M) and/or NNC55-0396 (3 μ M). After 12 or 32 hours, EdU (5 μ M) was added by half changing the growth media, PX-12 and NNC concentrations were maintained. Cells were incubated for a further 12 hours.

2.6.2. Cell fixation, permeabilization and EdU detection

Following EdU incubation, media was removed and coverslips were washed with PBS (2ml per well) before paraformaldehyde (3.7% in PBS, Sigma-Aldrich, UK) was applied for 15mins at RT. The fixative was removed and coverslips were washed with PBS containing *bovine serum albumin* (BSA, x2, Sigma-Aldrich, UK) before PBS containing Triton[®]X-100 (0.5%, Sigma-Aldrich, UK) was added for 20mins at RT to permeabilise cells. Next coverslips were washed with PBS containing BSA (3%, x2) before EdU detection cocktail (50 μ L) was added to each coverslip. The EdU detection cocktail contained CuSO₄, Alexa fluor-555 azide and proprietary reaction buffers and additives and was made fresh each day. Coverslips were incubated for 30mins at RT and protected from light. The detection cocktail was then removed and coverslips washed with PBS containing BSA (3%, x2) and also then with ddH₂O. Coverslips were allowed to

air-dry, then mounted onto microscope slides using Vectashield^R mounting media containing DAPI, (Vector Laboratories; Peterborough, UK) to label total DNA, and finally sealed round the edges with nail varnish. All slides were refrigerated (4⁰C) in the dark.

2.6.3. Image acquisition and analysis

Images were acquired as detailed (2.3.1). For each coverslip, 5 fields of view were randomly selected and visualised under the blue channel (400nm) for DAPI and the red channel (GYR) for EdU. DAPI and EdU images were merged post-acquisition using Corel photo paint in order to examine co-localisation. DAPI is a well characterised nuclear stain which binds to DNA and so was used to label the total number of nuclei. As DNA synthesis, fundamental for proliferation, occurs within the nucleus; EdU incorporation labelled the nuclei of cells which had synthesised DNA within the 12hour incubation period. Therefore EdU labelling reliably co-localised with DAPI staining. In order to compare DNA synthesis between control and drug treated conditions, the number of EdU-labelled nuclei (EdU+) was expressed as a percentage of the DAPI-labelled nuclei (DAPI+) for each image.

An attempt was made to custom build an automated analysis pipeline using an open source programme CellProfiler (www.cellprofiler.org). However, due to inaccuracies in results when compared to counting the nuclei by eye (manual counting), it was decided that for the current project manual counting was the best option (discussed in Chapter 4). Using Corel photo paint, EdU+ nuclei were outlined and counted and the resultant outline was then superimposed onto the corresponding DAPI image. The percentage of EdU+/DAPI+ nuclei was calculated for each of the five images in each condition and an average taken (to count as n=1). Data were normalised to the control condition and analysed by one-way ANOVA with Dunnetts' post-hoc comparison test or un-paired Student's t-tests (GraphPad Software, Inc), as described in section 2.11.

2.7. Ca^{2+} microfluorimetry

Ca^{2+} microfluorimetry uses fluorescent indicators to measure intracellular Ca^{2+} concentration ($[\text{Ca}^{2+}]_i$) within cell populations. In the current project, Fura-2-AM (4 μM , Invitrogen Molecular Probes; Thermo Fisher Scientific, Paisley, UK) was used to load A7r5, wt HEK293, HEK293/ $\text{Ca}_v3.1$ and HEK293/ $\text{Ca}_v3.2$ cells with the ratiometric fluorophore Fura-2. As the conjugated acetoxymethyl (AM) ester group confers a high degree of lipophilicity it is readily taken up by cells. Intracellular esterases then break down the AM group, thereby preventing the charged Fura-2 from leaving the cell, enabling the use of low incubation concentrations. Fura-2 is a dual excitation fluorophore which emits light at 510nm in response to excitation at 340nm and 380nm. With increasing Ca^{2+} binding; emission intensity (510nm) increases in response to excitation at 340nm, whilst correspondingly decreasing in response to excitation at 380nm, as detailed in Figure 2.2. The ratiometric nature of Fura-2 compensates for potential differences in dye loading, cell thickness and instrument sensitivity (Grynkiewicz *et al.*, 1985).

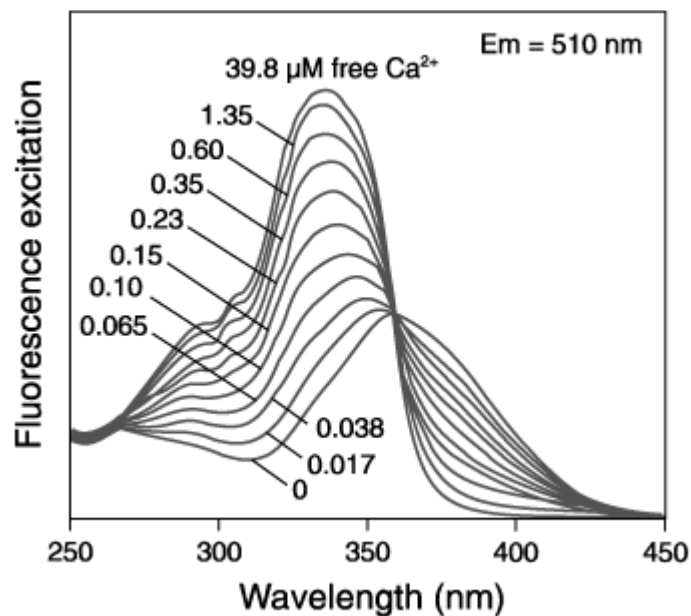


Figure 2.2. Fluorescence excitation spectra of Fura-2

As measured in solutions containing 0–39.8 μM free Ca^{2+} (diagram adapted from www.thermofisher.com).

2.7.1. Cell culture

Following trypsinisation (as described in 2.1.1) cells were plated at various dilutions onto circular sterile glass coverslips (10mm, thickness 0) within 24-well plates containing the relevant complete growth media (1ml per well). Cells were then incubated for 1-4 days until they were ~ 50-70% confluent. Coverslips were transferred to 35mm Petri dishes and incubated with Fura 2-AM (4 μ M) diluted in control buffer (see Table 2.2) at RT for 40mins. After washing with control buffer (2ml, x3), coverslips were incubated for 15mins with control buffer to allow AM group de-esterification. After fragmentation, coverslip segments were transferred to a perfusion chamber mounted over an epi-fluorescence microscope. Buffers were perfused from one of six reservoirs, connected to a 6-way Hamilton tap (Hamilton GB Ltd; UK), via Tygon tubing (0.83mm internal diameter, Merck; UK). A suction tube connected to a peristaltic pump (Gilson, Minipulse 3, Anachem) provided the outlet. Cell populations were identified and emission intensity at 510nm was recorded in response to synchronised excitation at 380nm and 340nm (ME-SE Photometry system, Cairn Research, Faversham, UK). The ratio of absorbance (340:380nm) at 1Hz, directly proportional to $[Ca^{2+}]_i$, was visualised via a computer using Acquisition Engine 1.6.1 software (Cairn Research, UK).

Chemical	Concentration (mM)		
	Control perfusate	High $[K^+]$ perfusate	Ca^{2+} free perfusate
NaCl	135	120	135
KCl	5	20	5
HEPES	5	5	5
Glucose	10	10	10
Sucrose	29	29	29
MgCl ₂	1.2	1.2	1.2
CaCl ₂	2.5	2.5	-
EGTA	-	-	1

Table 2.2. Ca^{2+} microfluorimetry perfusate compositions, all adjusted to pH = 7.4 using NaOH.

2.7.2. Depolarisation induced intracellular Ca^{2+} oscillation protocol - A7r5 cells

To study the effects of Trx inhibition, “old” A7r5 cells were incubated with auranofin (AuF, 2 μ M) dissolved in control buffer (RT, 25mins) post Fura-2 incubation. Baseline $[Ca^{2+}]_i$ measured in control buffer, replicating physiological resting state conditions, was stabilized before switching to a perfusion buffer containing a modestly elevated $[K^+]$ (20mM, control 5mM), as shown within Table 2.2. The modest $[K^+]$ elevation was designed to induce a small degree of depolarisation of ~ 35 mV as calculated by the Nernst equation detailed in Figure 2.3, with the aim of preferentially activating T-type Ca^{2+} channels recruited by small voltage increases. In control situations, this stimulus reliably produced rapid oscillations in $[Ca^{2+}]_i$ comparable to spontaneous oscillations observed in “new” A7r5 cells. After any response to the depolarising stimuli had reached a plateau, the perfusion buffer was switched back to control and baseline $[Ca^{2+}]_i$ re-established. In some conditions, dithiothreitol (DTT, 1mM; Sigma-Aldrich, UK), dissolved in control buffer, was then applied prior to repeating the depolarisation protocol for a second time.

$$E_K = \frac{RT}{zF} \left(\log \frac{[K^+]_e}{[K^+]_i} \right)$$

Where:

E_K = K^+ equilibrium potential

$[K^+]_e$ = extracellular K^+ concentration (5 or 20mM)

$[K^+]_i$ = intracellular K^+ concentration (140mM)

R = gas constant, T = temperature, z = valency of ion, F = Faraday constant

assuming room temperature of 25°C, $\frac{RT}{zF} = 58\text{mV}$

$$E_K = 58 \times \log_{10} (5/140) = -84\text{mV}$$

$$E_K = 58 \times \log_{10} (20/140) = -49\text{mV}$$

Figure 2.3. Schematic representation of the Nernst equation

As used to calculate the degree of depolarisation induced by switching extracellular $[K^+]$ from 5mM to 20mM

The effects of various Ca^{2+} channels blockers (CCBs) on $[\text{Ca}^{2+}]_i$, as used in the proliferation studies as detailed in Table 2.1 were also examined. The same initial depolarisation protocol was applied as detailed above; however CCBs were then perfused firstly in control and then in the high $[\text{K}^+]$ buffer. This enabled comparison between the first and second depolarisation responses. The perfusion buffer was then switched back to the control buffer and baseline $[\text{Ca}^{2+}]_i$ re-established.

2.7.3. Window current protocol

As T-type Ca^{2+} channels are activated at low voltages there is commonly a small population open at or around the resting membrane potential. These facilitate tonic Ca^{2+} influx, often referred to as window current, believed to be important for proliferation. In order to measure and compare any window current within A7r5, wt HEK293, HEK293/ $\text{Ca}_v3.1$ and HEK293/ $\text{Ca}_v3.2$ cells, baseline $[\text{Ca}^{2+}]_i$ in control buffer was established before switching to a Ca^{2+} free perfusate (CF, replaced with 1 mM EGTA). Any changes in $[\text{Ca}^{2+}]_i$ were allowed to stabilise before the perfusate was switched back to the control buffer. When investigating the effects of CCBs (Table 2.1), drugs were diluted and applied firstly in control and then in CF perfusate.

2.7.4. Data analysis

All data analysis was conducted using Graphing (an in-house program) and GraphPad Prism version 6 (GraphPad Software, Inc). As detailed in Figure 2.4 regarding the induced depolarisation experiments, the amplitude of the response ($\Delta[\text{Ca}^{2+}]_i$) was measured by deducting the baseline Fura-2 ratio (in control buffer, A1), from the Fura-2 ratio measured at the response plateau (A2). For drug treatments, baseline ratio was measured from drug + control buffer perfusion. To calculate the frequency of Ca^{2+} oscillations observed in response to depolarisation, the number of spikes was counted and divided by the duration of the high $[\text{K}^+]$ perfusion (T2-T1).

Regarding window current experiments, the response to removal of extracellular Ca^{2+} was calculated by deducting the baseline Fura-2 ratio in CF buffer (A2) from the baseline Fura-2 ratio in control buffer (A1) as detailed within Figure 2.4. For drug treatment conditions, baseline ratio was measured from drug + control buffer

perfusion. All data was analysed using paired or un-paired Students t-tests or one-way ANOVA with Dunnett's post-hoc comparison tests, as appropriate (section 2.11).

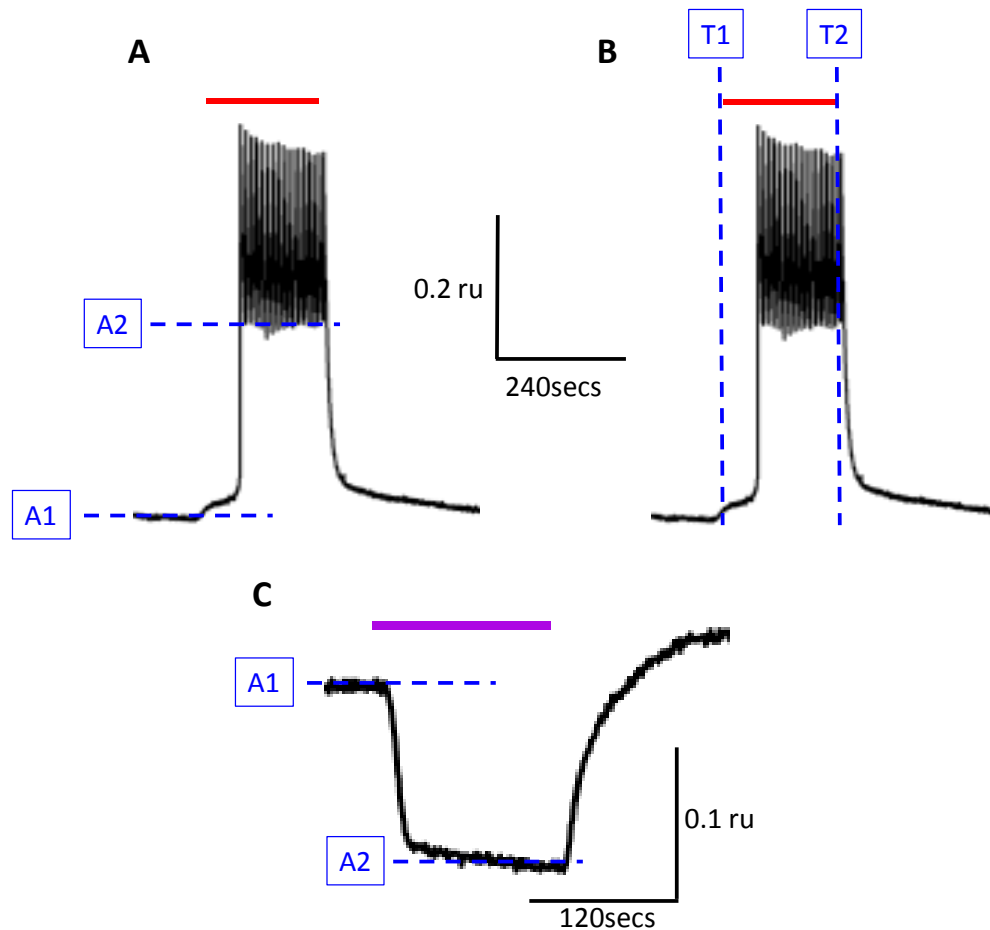


Figure 2.4. Example control Ca^{2+} microfluorimetry traces

Illustrating analysis parameters used for induced depolarisation protocols; **A**, response amplitude (A2-A1) and **B**, firing frequency in A7r5 cells ($\text{no}^\circ \text{ spikes}/(\text{T2}-\text{T1})$) and **C**, window current protocols in A7r5 and HEK293 cells (A1-A2). Red lines show high K^+ stimulus, purple line shows Ca^{2+} free perfusate. Scale bars showing time in seconds (horizontal bars) and ratio units (ru), i.e. the ratio of absorbance (340:380, vertical bars).

2.8. Electrophysiology

In order to assess whether Trx directly modulated voltage-gated Ca^{2+} (Ca_v) channels within A7r5 HEK293/ $\text{Ca}_v3.1$ and HEK293/ $\text{Ca}_v3.2$ cells, patch-clamp electrophysiology (whole-cell configuration) was implemented. All recordings were made in the presence of tetraethylammonium chloride (TEA) and CsCl (both Sigma-Aldrich, UK) to block voltage-gated K^+ channels and non-selective cation channels respectively.

2.8.1. Cell culture

Following trypsinisation (as detailed 2.1.1), cells were plated at various dilutions (1:10-1:80) onto poly-L-lysine coated sterile glass coverslips (22x22mm, thickness 0) or circular sterile glass coverslips (10mm, thickness 0) in 6 or 24-well plates, containing 2ml or 1ml of the relevant complete growth media per well, for recombinant HEK293 or A7r5 cells respectively. Cells were incubated overnight before media was replaced with antibiotic-free growth media (FBS, 10%, no added antibiotic/antimycotic, gentamicin, or G-418), which was found to increase the success rate of stable recordings. Cells were then incubated for a further 1-3 days prior to recording. Coverslips were transferred into 35mm petri dishes and fragmented, enabling small sections to be transferred into the recording chamber.

2.8.2. Electrophysiology rig set up

The recording chamber was mounted over a light microscope (Olympus CK40) and perfused by one of four reservoirs connected to a 4 way Hamilton tap (Hamilton GB Ltd) via Tygon tubing (0.83mm internal diameter, Merck, UK). A suction tube connected to a vacuum pump (JUN-AIR, Redditch, UK) provided the outlet. Patch-pipettes with a resistance of 3-7 M Ω were made from borosilicate glass capillary tubes (0.86mm internal diameter; Harvard Apparatus, Cambridge, UK) using an electrode puller (PP-83; Narishige, London, UK). Patch-pipettes were filled with intracellular solution as detailed in Table 2.3 ensuring no air bubbles were present. The patch-pipette was then attached securely to the electrode holder so that the silver/silver chloride (Ag/AgCl₂) recording electrode was connected to the headstage and was also in contact with the intracellular solution. The Ag/AgCl₂ chloride ground electrode connected to the headstage was placed in the recording chamber in contact with the extracellular solution (Table 2.3). The headstage positioning was controlled by a micromanipulator (Patch star (PS-700C), Scientifica, East Sussex, UK) enabling precise manoeuvre of the patch-pipette over three axes (x, y and z) to allow its delicate placement against cell membranes.

The electrode holder contained a side-arm air outlet attached to Tygon tubing facilitating manual suction required to rupture the cell membrane and achieve the

whole-cell configuration. This could be connected to a syringe with a three-way tap to maintain suction. To reduce electrical noise, all apparatus was contained within a Faraday cage and individual electrical items were grounded to a common earth point. Patch-clamp recordings were made using an Axopatch 200A amplifier/Digidata 1200 interface (Axon Instruments; Foster City, CA, USA) controlled by Clampex 9.0 software (Molecular Devices; Foster City, CA, USA). Signals were sampled at 10 kHz and low-pass filtered at 2 kHz.

Chemical	Concentration (mM)		
	ICaT* extracellular	ICaL * extracellular	Intracellular
NaCl	95	95	-
CsCl	5	5	120
MgCl ₂	0.6	0.6	2
TEA	20	20	20
HEPES	5	5	10
glucose	10	10	-
sucrose	20	20	-
CaCl ₂	15	-	-
BaCl ₂	-	15	-
EGTA	-	-	10
Na - ATP	-	-	2
Mg- ATP	-	-	2.5

Table 2.3. Composition of solutions used for electrophysiology

Extracellular solutions were adjusted to pH 7.4 using NaOH, whilst the intracellular solution was adjusted to pH 7.2 using CsOH. ICaT = T-type Ca²⁺ current. ICaL= L-type Ca²⁺ current. All chemicals supplied by Sigma-Aldrich, UK.

2.8.3. Whole-cell recording configuration

All electrophysiological recordings were made in the whole-cell configuration. Upon placement of the patch-pipette against the cell membrane, gentle suction was applied until a mechanically and electrically tight seal ($\geq 1\text{G}\Omega$ resistance) was formed between the patch-pipette and cell membrane. Membrane potential was set to the required voltage (-80mV for T-type Ca²⁺ currents (ICaT)) and pipette capacity transients were minimised using amplifier controls. Suction was then gradually increased until the cell

membrane ruptured, which was detected as a sudden increase in slower capacitance transients which were subsequently minimised using the whole-cell capacitance and series resistance controls.

2.8.4. Single step (SS) voltage protocols

T-type Ca^{2+} channels exhibit marked differences when compared to other members of the Ca_v family such as L-type Ca^{2+} channels ($\text{Ca}_v1.1-1.4$). Specifically they have lower voltage thresholds for activation (-70mV vs. -40mV), they inactivate rapidly, have transient kinetics and exhibit slower rates of deactivation leading to prominent tail currents after a depolarising pulse (Perez-Reyes, 1999). Correspondingly, when recording I_{CaT} cells were maintained at a holding potential of -80mV (to ensure channels were in their closed state) and step depolarisations to -20mV (voltage for peak I_{CaT} activation) were applied for 200ms (sufficient time to observe activation and inactivation), before return to the holding potential (-80mV). Repeated depolarising steps were made at 0.1 Hz.

Contrastingly, when recording L-type Ca^{2+} currents (I_{CaL}) cells were maintained at a holding potential of -50mV and step depolarisations to +20mV (voltage for peak I_{CaL} activation) were applied initially for 200ms, before returning to the holding potential (-50mV). Over this period, no inactivation was observed, however the depolarising pulse duration was reduced to 100ms to minimise current rundown. Repeated depolarising steps were made at 0.1 Hz. Ba^{2+} (15mM) was used as the charge carrier for I_{CaL} recordings to circumvent Ca^{2+} dependent inactivation associated with L-type Ca^{2+} channels and augment current amplitudes.

The two individual SS protocols detailed above were designed to maximally activate T- or L-type Ca^{2+} channels. Whilst these protocols are ideal for recording currents from recombinant expression systems, it is important to note that contamination of I_{CaT} or I_{CaL} may have occurred within A7r5 cells which natively express both subtypes of Ca^{2+} channel. $\text{Ca}_v1.2$ channels have been previously shown to begin activating ~-20mV, when expressed recombinantly (Scragg *et al.*, 2007). Furthermore, recombinant $\text{Ca}_v1.3$ channels have been shown to have considerably lower activation thresholds compared

to Ca_v1.2 channels (Lipscombe *et al.*, 2004). As such, the global Ca²⁺ influx in A7r5 cells evoked using the T-type SS protocol (-80mV to -20mV) may be a combination of I_{CaL} and I_{CaT}. Care was therefore taken when interpreting results from A7r5 cell T-type SS recordings, and nifedipine was applied to eliminate the contribution of I_{CaL} where possible.

2.8.5. Current-voltage (IV) relationship protocol and data analysis

To assess potential effects of compounds of interest on current amplitudes in response to a range of voltages, current-voltage (IV) relationship protocols were also implemented. Cells were maintained at a holding potential of -80mV and a series of 80ms depolarising steps from -100 to +40mV in 10mV increments were made, with a return to -80mV between each step.

All data analysis was performed offline using Clampfit 9.0 (Molecular Devices) and GraphPad Prism version 6 (GraphPad Software, Inc). For single-step protocols, statistical analysis was initially conducted using raw peak current amplitude values. For effective visual representation, peak amplitude in the presence of a drug was expressed as a % of peak amplitude under control conditions for each cell. For consistency, final statistical analysis was conducted on data in this format. Data were analysed using paired or un-paired Students t-tests or one-way ANOVA with Dunnett's post-hoc comparison tests, as appropriate (detailed in section 2.11).

2.9. Thioredoxin assays

As the classical function of Trx is to reduce intracellular proteins via cysteine thiol-disulphide exchange the standard way to measure Trx activity is using insulin disulfide reduction assays (Holmgren, 1979). A commercially available Trx assay was purchased (FKTRX-02-V2, IMCO Corporation Ltd AB; Stockholm, Sweden), which is based on the reduction of insulin by Trx. As shown by the three equations within Figure 2.5, the eosin-labelled insulin fluorescence signal at 545nm (after excitation at 520nm) increases upon reduction, and is applied in relative excess in addition to thioredoxin reductase (TrxR) and nicotinamide adenine dinucleotides phosphate (NADPH) (Montano *et al.*, 2014). These assays were performed with the aim of measuring

endogenous Trx activity within cell lines and to potentially examine the effects of Trx inhibitors on this activity.

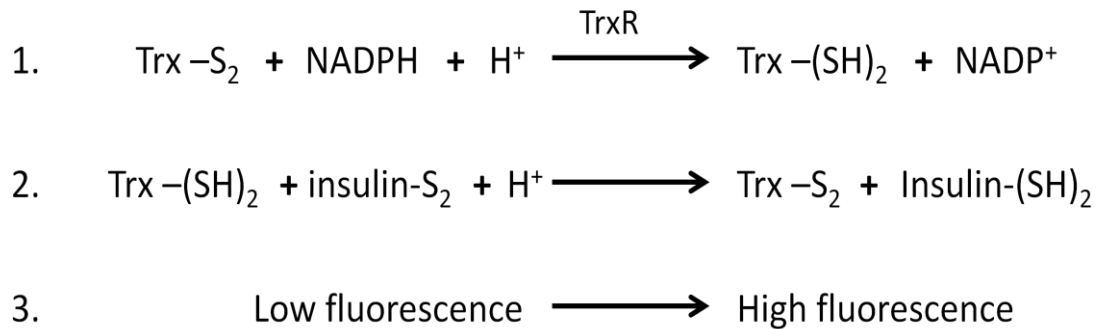


Figure 2.5. Schematic depiction of Trx activity assay reactions.

Showing, **1**, the reduction of oxidised thioredoxin (Trx-S₂) to its reduced dithiol form (Trx-(SH)₂) by thioredoxin reductase (TrxR) with nicotinamide adenine dinucleotide phosphate (NADPH) as a cofactor. **2**, Trx-(SH)₂ reduces insulin disulfide (insulin-S₂) to its dithiol form (insulin-(SH)₂) and Trx-S₂ with **3**, a corresponding increase in fluorescence (derived from (Montano *et al.*, 2014))

2.9.2. Cell sample preparation

To assess the effects of chronic application of Trx inhibitors on endogenous Trx activity levels, A7r5, WT HEK293 and HEK293/Ca_v3.1 cells were cultured in T75 flasks (as detailed 2.1.1) in the appropriate complete growth media (20mL) for three days before media was replaced with media ± AuF (300nM) or PX-12 (1µM). Cells were then cultured for a further 3 days before they were trypsinised and cell number determined (as described 2.5). Cells were then suspended in PBS (10mL) and centrifuged (1000xg, 10mins, x2). All supernatant was removed and the cell pellet re-suspended in TE buffer (500µL, pH 7.3, Qiagen, UK) and divided into 2 samples. To lyse cells, samples were sonicated (XL-2000; Misonic, NY, USA) for 5 seconds and centrifuged (10,000xg, 4°C, 20mins) to remove cellular debris. The supernatant was retained and frozen (-80°C) for subsequent Trx analysis.

To assess the effects of acute exposure to higher PX-12 concentrations HEK293/Ca_v3.1 and HEK293/Ca_v3.2 cells were cultured in T25 flasks (6ml total volume, 1:10 dilution) in the relevant complete growth media for 3 days before media was replaced for complete growth media ± PX-12 (10-300µM, 6mL) and incubated for 10mins prior to trypsinisation. Samples were then processed as detailed above.

2.9.3. *Bicinchoninic acid (BCA) assay*

Before conducting Trx assays, it was important to quantify the total protein content of each sample in order to standardise the amount loaded using the bicinchoninic acid (BCA) protein assay (Thermo Scientific; Rockford, USA). This assay involves protein mediated reduction of Cu^{2+} which is chelated by BCA producing a deep purple colour, the intensity of which is proportional to the amount of protein present, and can be measured colorimetrically (Smith *et al.*, 1985). The assay was conducted according to manufacturers' instructions. Briefly, 10 μL BSA protein standards (0, 250, 500, 750, 1000, 1250, 1500, 1750 and 2000 $\mu\text{g}/\text{ml}$) and either 2.5 or 10 μL of cell sample was loaded onto a 96 well plate and total volume was made up to 200 μL with working reagent. Plates were incubated for 30mins and absorbance was measured at 570nm (Glomax multi-detection system; Promega, UK). A calibration curve was generated from the BSA standards using GraphPad Prism version 6 (GraphPad Software, Inc) and the absorbance values of the cell sample fitted to calculate total protein.

2.9.4. *Assay protocol and data analysis*

Briefly, cell samples were allowed to equilibrate to RT and 15 μg total protein was loaded into each well. Half of the wells contained TrxR (100nM), which was omitted from the other half to enable measurement of background fluorescence. Volume (100 μL per well) was standardised with assay buffer. For calibration, reference wells containing known Trx concentrations (0-244ng) were included. To facilitate the reduction of Trx, β -NADPH (5 μL per well) was added and plates incubated for 30mins prior to fluorescent substrate (20 μL per well) addition. Emission was recorded at 545nm after excitation at 520nm (Varioskan Flash; Thermo Scientific, UK) over a 60 minute period (1Hz). All test, background and reference samples were performed in triplicate.

All data analysis was conducted offline using GraphPad Prism version 6 (GraphPad Software, Inc). Average values per minute were taken and emission intensity was plotted against time for each sample. The 10min time point which showed the most linear increase in fluorescence was selected (25-35 \pm 10 mins) and linear regression was conducted to generate a fitted line for each sample. The slope of the background

reference sample (0ng Trx) was subtracted from the other reference sample slopes (taken from the calculated fit) and a calibration curve was generated. Linear regression analysis was then conducted to obtain the Trx standard line equation, and R^2 values were noted. To calculate Trx concentrations within the cell samples the background slope values were deducted from the corresponding test sample slope. This resulting slope value was then used to calculate Trx concentration from the standard line equation generated from the Trx standards.

2.10. Preparation of reduced thioredoxin (rTRX)

In order to assess directly the effects of rTrx it was necessary to convert Trx to its reduced and active form. To do this, Trx (200 μ L, 1mg/ml; Sigma-Aldrich, UK), dissolved in binding buffer (10mM HEPES, 1mM EDTA, 50mM NaCl, pH, 7.0) was incubated with DTT (1mM) at RT (30mins). This solution was then transferred to a strong anion exchange spin column (Pierce mini; Life technologies, UK) which was pre-washed with binding buffer (400 μ L) and centrifuged (2000 xg , 5mins). The column was then washed and centrifuged with binding buffer (400 μ L, 2000 xg , 5mins, x3) with the flow-through discarded each time to completely remove any DTT. Elution buffer (250 μ L, 10mM HEPES, 1mM EDTA, 1mM NaCl, pH, 7.0) was added and the column centrifuged (2000 xg , 5mins) enabling collection of rTrx. BCA assays were conducted (as described 2.9.3) to determine rTrx concentrations and rTrx was used immediately to minimise oxidation. The effects of oxidised Trx (oTrx), i.e. non-reduced Trx were also examined.

2.11. Statistical analysis

Prior to the selection of statistical analysis, where sample sizes allowed, D'Agostino-Pearson normality tests were conducted, to ensure that parametric tests were appropriate. Unless otherwise stated, Student's t-tests were subsequently conducted when examining differences between two groups, whilst one-way ANOVA with multiple comparison tests were used to examine three or more groups. Regarding ANOVA, Dunnett's post-hoc comparison tests were chosen when comparing the mean of a control condition with the mean of every other condition. In contrast, Tukey's post-hoc comparison tests were used to compare the mean of each condition with the mean of every other condition. As a final option, Bonferroni's post-hoc comparison

tests were used when comparing a selected set of means. When assessing the effects of different experimental conditions on the same cell(s) i.e. matched groups, paired Student's t-tests or repeated-measures one-way ANOVA were used. When experimental groups comprised of different populations of cells, un-paired Student's t-tests or ordinary one-way ANOVA tests were conducted. All statistical analysis described within this thesis was conducted using GraphPad Prism version 6 (GraphPad Software, Inc), p values <0.05 were considered statistically significant.

Chapter 3 -The role of T-type Ca²⁺ channels in cellular proliferation and [Ca²⁺]_i mobilisation.

3.1. Introduction

The current project has been conducted using the commercially-available VSMC cell line, A7r5 cells in addition to HEK293 cells stably expressing recombinant Ca_v3.1 or Ca_v3.2 channels. A7r5 cells were originally derived from rat thoracic aorta (Kimes & Brandt, 1976) and have been widely used as a convenient and relatively well characterised *in vitro* VSMC model, particularly for studying mechanisms of Ca²⁺ regulation (Carre *et al.*, 2015; Erac *et al.*, 2014; Simard *et al.*, 2015; Sperti & Colucci, 1991). HEK293 cells contain all the essential biochemical machinery required for post-translational modifications, they have enabled functional expression of a huge range of recombinant proteins such as ion channels, and have been used extensively over the past 35 years as both transient and stable expression systems. Originally derived from epithelial cells of the human embryonic kidney, HEK293 cells are small in size and have minimal processes which make them ideal for patch-clamp electrophysiology (Thomas & Smart, 2005).

Previous projects conducted by the Peers group investigating the effects of novel T-type Ca²⁺ channel regulators CO and H₂S on VSMC proliferation, have utilised the same cell lines as reported here (Duckles *et al.*, 2015; Elies *et al.*, 2015). As variations in ion channel expression can occur with prolonged cell culture (Richard *et al.*, 1992), it was important to re-validate T-type Ca²⁺ channel expression and dissect the contribution of individual Ca_v channel isoforms to proliferation and Ca²⁺ handling. Mibefradil is a widely used T-type Ca²⁺ channel blocker (CCB), although when applied at high concentrations also inhibits L-type Ca²⁺ currents (Mishra & Hermsmeyer, 1994). Nifedipine belongs to a family of drugs called dihydropyridines (DHPs), which are highly selective L-type CCBs. The high selectivity arises as the pore forming α_{1C} subunit of L-type Ca²⁺ channels has a unique high affinity DHP binding site involving IIS6 and IVS6 transmembrane segments (Peterson *et al.*, 1996).

3.2. Results

3.2.1. Characterisation of Ca_v channels in A7r5 cells

Two batches of A7r5 cells were used within the current project: “old” A7r5 cells were sub-cultured to 100% confluency and had been used within the group for many years whilst the “new” A7r5 cells were sub-cultured at lower confluence, in an attempt to maximise T-type Ca²⁺ channel expression (Richard *et al.*, 1992). To quantify Ca_v3.1 and Ca_v3.2 mRNA expression and allow for comparison between the two batches of cells, real-time polymerase chain reaction (rtPCR) was conducted. When using this technique, it is important to select a housekeeping gene which is expressed at similar levels to the target gene(s) of interest. It was determined that the large ribosomal subunit (17S) was expressed at higher levels than both hypoxanthine phosphoribosyltransferase (HPRT1) and the target genes Ca_v3.1 and Ca_v3.2; reflected by the lower threshold cycle (C_T) values. As the average C_T value for HPRT1 was similar to that of Ca_v3.1, it was confirmed to be an appropriate housekeeper gene and was used for all subsequent analysis (Figure 3.1). Both batches of A7r5 cells expressed Ca_v3.1 mRNA at significantly higher levels than Ca_v3.2 mRNA. Ca_v3.1 and Ca_v3.2 mRNA expression was much higher in the “new” A7r5 cells sub-cultured at low confluence (70-80%) compared to the “old” A7r5 cells sub-cultured at greater confluence (90-100%), as detailed in Figure 3.1. Consequently, the “new” A7r5 cells were used for all subsequent experiments unless otherwise stated. Note, rtPCR on the “old” A7r5 cells was conducted by Dr Hayley Duckles using an identical protocol and data are included with permission (Duckles *et al.*, 2015).

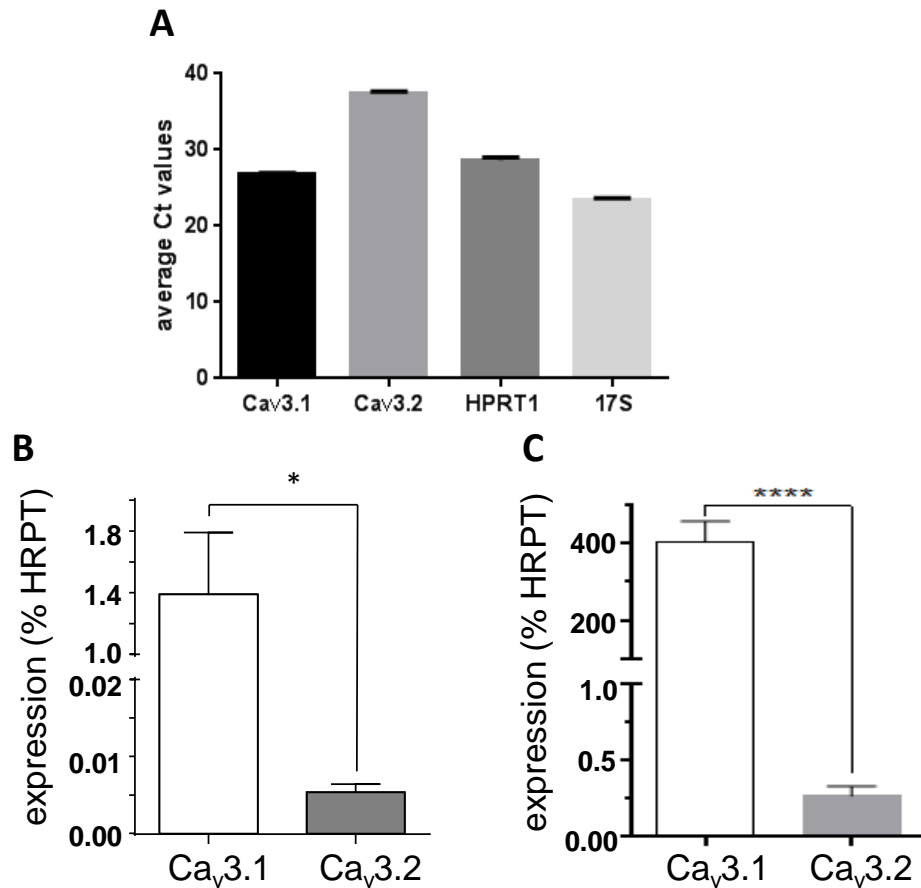


Figure 3.1. Ca_v3.1 and Ca_v3.2 mRNA is expressed by A7r5 cells

A, Bar graph showing the average (mean \pm s.e.m) threshold cycle (C_T) values for the target genes Ca_v3.1 and Ca_v3.2, and the housekeeping genes hypoxanthine phosphoribosyltransferase (HPRT1) and large ribosomal subunit (17S) within A7r5 cells (n=8). **B**, Bar graph showing relative mRNA expression of Ca_v3.1 (upper y-axis) and Ca_v3.2 (lower y-axis), channel expression is plotted as (mean \pm s.e.m) % expression of HPRT1, for “old” A7r5 cells sub-cultured at 90-100% confluence (n=7, experiments conducted by Dr H. Duckles). **C**, As B except with “new” A7r5 cells sub-cultured at 70-80% confluence (n=8, note larger axis). A7r5 cell lysates were measured in triplicate wells with the mean value used as n=1. All data were analysed using unpaired students t-tests, *p \leq 0.05, ****p \leq 0.0001.

In order to assess the sub-cellular distribution of Ca_v3.1 and Ca_v3.2 channels, immunofluorescence was conducted on “new” A7r5 cells. On all occasions, DAPI (4',6-diamidino-2-phenylindole) was co-applied to label cell nuclei. Initial attempts to detect the Ca_v3.1 and Ca_v3.2 antibodies within A7r5 cells using the Alexa Fluor 488 secondary antibody (detected in green) were unsuccessful due to prominent background fluorescence, apparent upon omission of either the primary or secondary antibodies (**Error! Reference source not found.**). NAD(P)H is a common source of autofluorescence detected within cytosolic, mitochondrial and nuclear regions. Within bovine coronary artery smooth muscle cells, NAD(P)H-mediated autofluorescence has been observed, with peaks of excitation and emission around 340nm and 450nm respectively (Gao & Wolin, 2008). Resultantly, Alexa Fluor 555 (detected in red) was used as the secondary antibody within A7r5 cells, as no background fluorescence was observed at these wavelengths (**Error! Reference source not found.**). Low levels of immuno-reactivity (IR) to both Ca_v3.1 and Ca_v3.2 antibodies were detected within some A7r5 cells. Ca_v3.2 channels were found to be localised around nuclear regions (**Error! Reference source not found.**), whereas Ca_v3.1 channels appeared to have a more generalised distribution throughout A7r5 cells (**Error! Reference source not found.**). Both Ca_v3.1 and Ca_v3.2 primary antibodies were found to be highly specific, as they showed no cross-reactivity with the opposing isoform, i.e. no Ca_v3.2 IR was apparent within HEK293/Ca_v3.1 cells and vice versa (**Error! Reference source not found.** and 0, discussed in further detail within section 3.2.4).

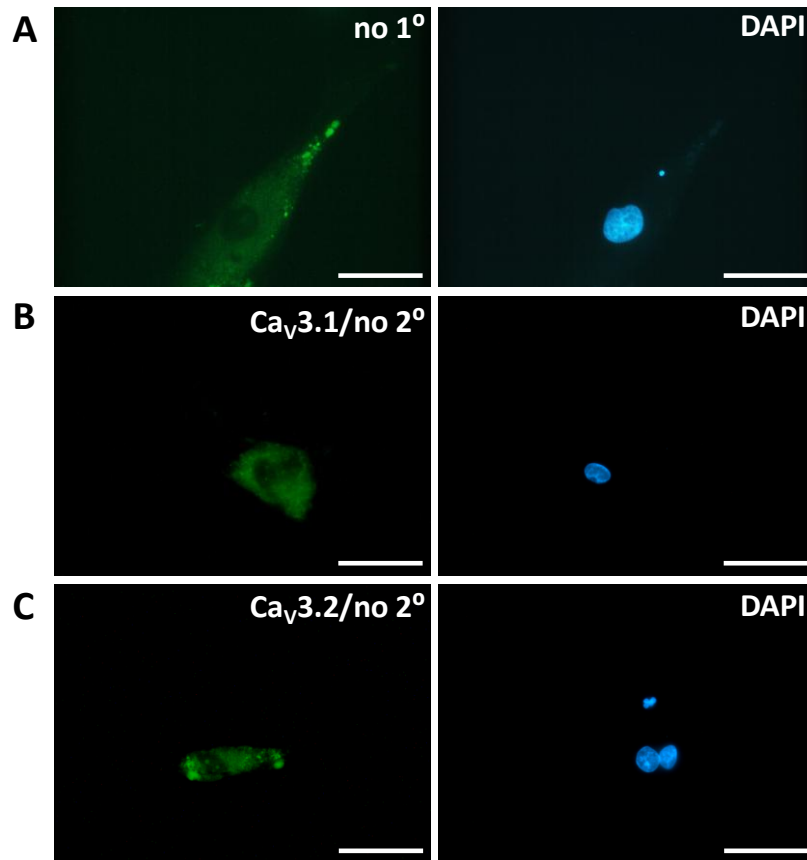


Figure 3.2. Background fluorescence is detected in “new” A7r5 cells at 488nm

Control images for dual-label immunofluorescence using anti- $\text{Ca}_v3.1$ (1:100) and anti- $\text{Ca}_v3.2$ (1:1000) primary antibodies, with Alexa Fluor-488 secondary antibody (1:1000, left panel, green images), and DAPI to label cell nuclei (right panel, blue images). Fluorescence is observed within A7r5 cells when; **A**, the Alexa Fluor 488 secondary antibody is applied alone, **B**, when the $\text{Ca}_v3.1$ primary antibody is applied alone (i.e. no secondary) and **C**, when the $\text{Ca}_v3.2$ primary antibody is applied alone (i.e. no secondary). All scale bars 50 μm .

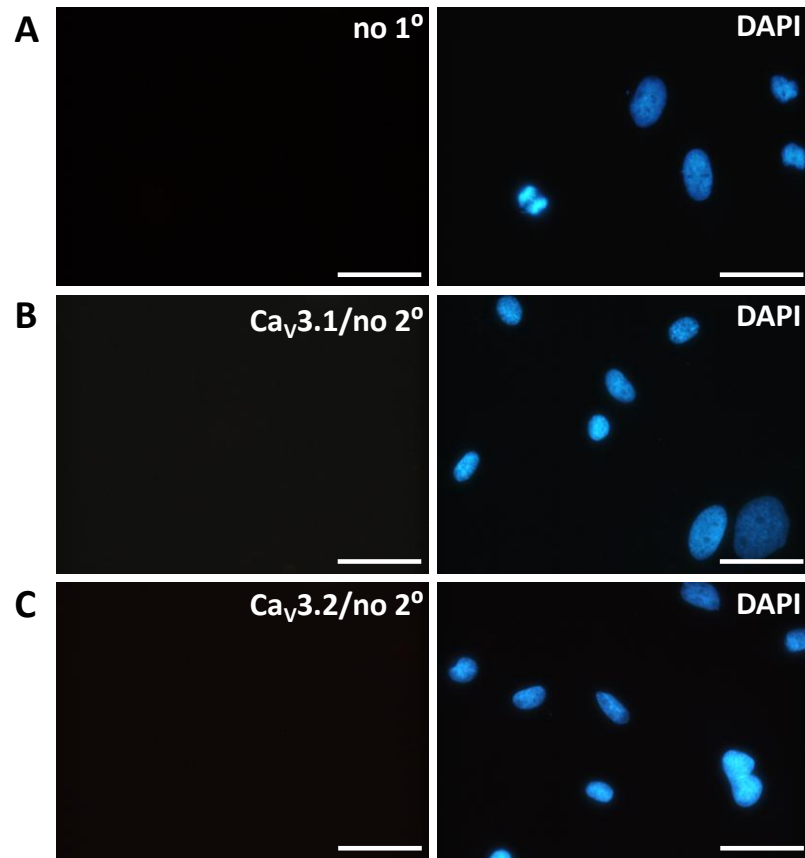


Figure 3.3. No background fluorescence is detected in “new” A7r5 cells at 555nm
Control images for dual-label immunofluorescence using anti- $\text{Ca}_v3.1$ (1:100) and anti- $\text{Ca}_v3.2$ (1:1000) primary antibodies, with Alexa Fluor-555 secondary antibody (1:500, left panel, red images), and DAPI to label cell nuclei (right panel, blue images). No fluorescence is observed within A7r5 cells when; **A**, the Alexa Fluor 555 secondary antibody is applied alone, **B**, when the $\text{Ca}_v3.1$ primary antibody is applied alone (i.e. no secondary) and **C**, when the $\text{Ca}_v3.2$ primary antibody is applied alone (i.e. no secondary). All scale bars 50 μm .

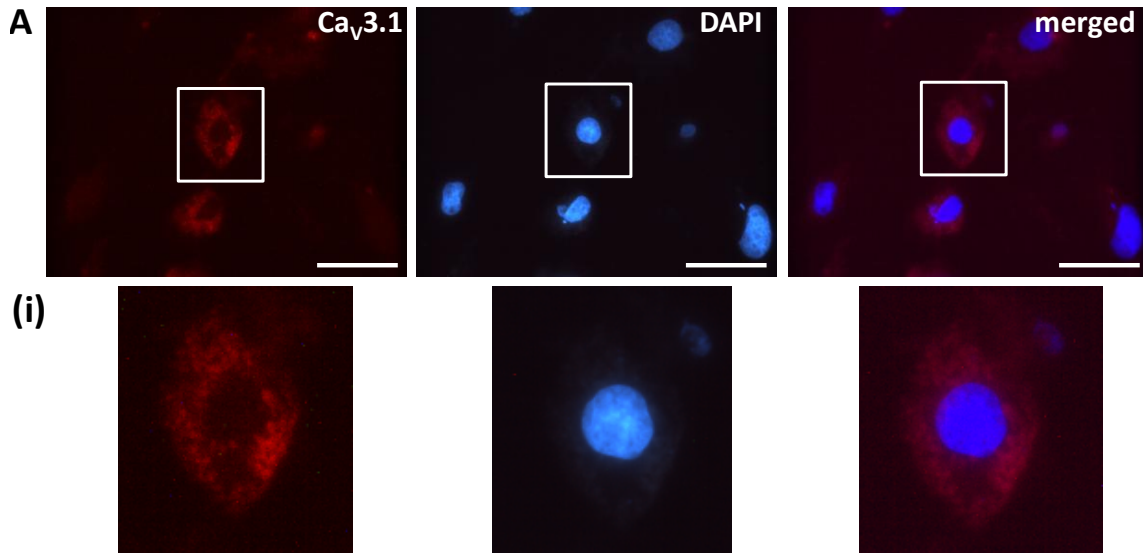


Figure 3.4. Sub-cellular distribution of Ca_v3.1 channels within “new” A7r5 cells

Dual-label immunofluorescence using anti-Ca_v3.1 (1:100) with Alexa Fluor-555 secondary antibody (1:500, left panels, red images) and DAPI to label cell nuclei (centre panel, blue images), merged Ca_v3.1 and DAPI images (right panels). **A**, A7r5 cells show low levels of diffuse Ca_v3.1 immuno-reactivity (IR), regions of interest (white box) are magnified in **(i)**. All scale bars 50μm.

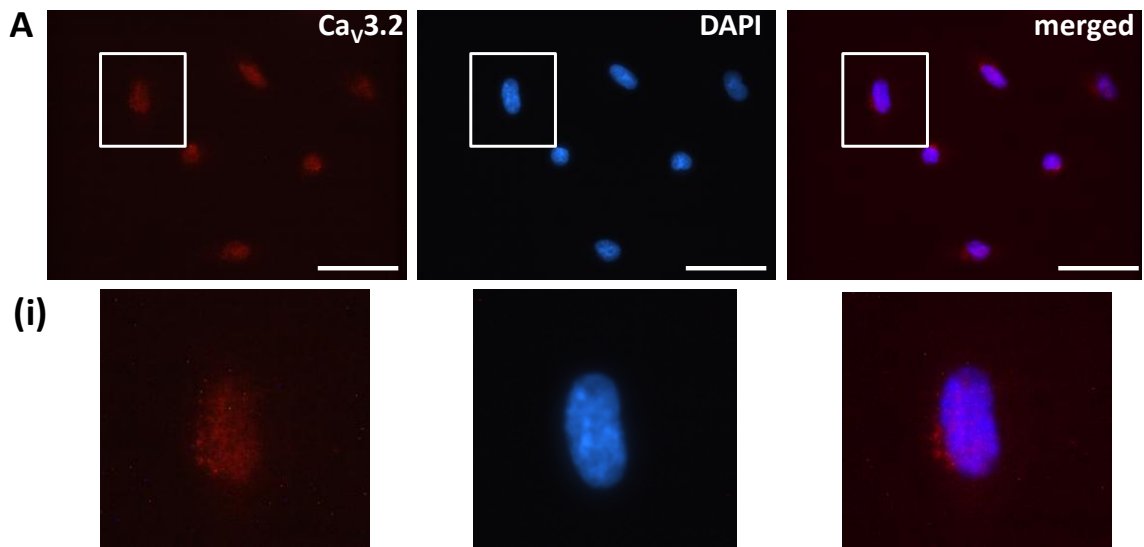


Figure 3.5. Sub-cellular distribution of Ca_v3.2 channels within “new” A7r5 cells

Dual-label immunofluorescence using anti-Ca_v3.2 (1:1000) with Alexa Fluor-555 secondary antibody (1:500, left panels, red images) and DAPI to label cell nuclei (centre panels, detected in blue), merged Ca_v3.1 and DAPI images (right panels). **A**, A7r5 cells show low levels of Ca_v3.2 immuno-reactivity (IR) localised within and around cell nuclei, regions of interest (white box) are magnified in **(i)**. All scale bars 50μm.

Due to a wide variety of factors such as post-translational modification and dynamic membrane trafficking, mRNA expression does not necessarily equate to functional ion channel expression. For example, increased T-type Ca^{2+} channel current-density observed in response to chronic insulin stimulation within rat pituitary derived GH₃ cells was shown to be due to increases in dynamic endosomal recycling and trafficking of $\text{Ca}_v3.1$ to the surface membrane and not alterations in mRNA levels or promoter activity (Toledo *et al.*, 2012). We therefore employed patch-clamp electrophysiology to assess functional T-type and L-type Ca^{2+} channel expression within A7r5 cells.

As illustrated by Figure 3.2, both the T- and L-type SS protocols evoked Ca^{2+} currents within some A7r5 cells. Whilst the SS protocols were designed to maximally activate T- or L-type Ca^{2+} channels it was possible that these voltage protocols were not entirely subtype selective (Chapter 2). As such, quotations marks are used when describing currents evoked using the SS protocols in A7r5 cells. The distribution of Ca^{2+} currents was highly heterogeneous; some A7r5 cells expressed either “T-type” or “L-type” Ca^{2+} currents in isolation, some cells expressed both types of current and many cells had no detectable Ca_v current. As approximate values, 75% of cells expressed both “T-” and “L-type” Ca^{2+} currents, 10% expressed “L-type” Ca^{2+} currents alone, 5% expressed “T-type” Ca^{2+} currents in isolation and 5% showed no detectable Ca_v current. It would have been advantageous to provide a more accurate quantification, however, on many occasions recordings did not last long enough to run both single-step protocols. In addition, to ensure effective voltage-clamp, only small A7r5 cells were recorded from which would have introduced a selection bias and decreased the validity of any quantification. Regarding current-voltage (I-V) relationships, cells exhibiting predominantly “L-type” Ca^{2+} currents showed maximal activation at +20mV. By contrast, cells exhibiting predominantly “T-type” Ca^{2+} currents displayed maximal activation at -20mV and cells with mixed populations showed maximal activation at 0mV.

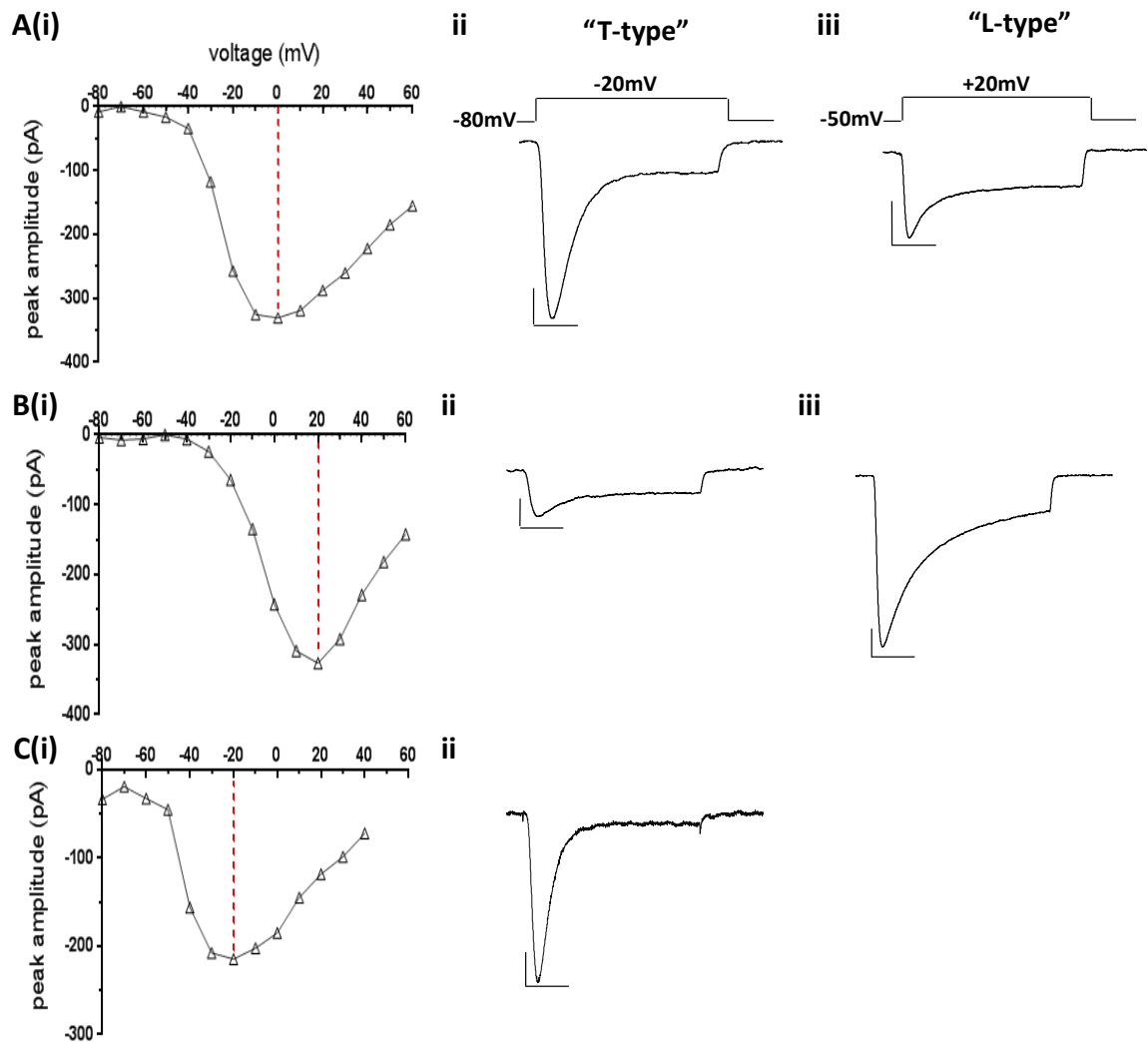


Figure 3.2. T-type and L-type Ca^{2+} channel currents are heterogeneously expressed within “new” A7r5 cells

Whole-cell patch-clamp recordings from 3 representative “new” A7r5 cells using Ca^{2+} (15mM), as the charge carrier. **A**, Cell with both T- and L-type Ca^{2+} currents. **B**, Cell with predominant “L-type” Ca^{2+} current. **C**, Cell with predominant “T-type” Ca^{2+} current. **(i)**, Current-voltage relationships with red line showing voltage producing maximal current, **(ii)**, “T-type” Ca^{2+} current traces evoked from single step(SS)-depolarisations to -20mV from a holding potential of -80mV, **(iii)**, “L-type” Ca^{2+} current traces evoked from SS-depolarisations to +20mV from a holding potential of -50mV. All scale bars 50pA (vertical), 50ms (horizontal). Due to the potential activation of L-type mediated Ca^{2+} current using the T-type SS protocol and vice versa, “T-type” and “L-type” currents are labelled with quotation marks.

For single step (SS) voltage protocols, “T-type” Ca^{2+} currents were stimulated by repetitive depolarisations (0.1Hz) to -20mV (200ms) from a holding potential (V_h) of -80mV. This evoked Ca^{2+} currents showing rapid activation and inactivation, the characteristic shape of T-type Ca^{2+} channel currents. “L-type” Ca^{2+} channel currents were stimulated by SS voltage protocols to +20mV (200ms, 0.1Hz) from a V_h of -50mV. When using Ca^{2+} as the charge carrier this produced currents with rapid activation and both a slowly inactivating and a sustained component. L-type Ca^{2+} currents are generally characterised by their sustained shape resulting from their very small degree of voltage-dependent inactivation. It should be noted however, that the kinetics and resultant current shape is highly dependent on the L-type Ca^{2+} channel isoform, splice variant and auxiliary subunits expressed. These factors can dictate varying degrees of Ca^{2+} -dependent inactivation which may account for the slowly inactivating component observed, as reviewed within (Lipscombe *et al.*, 2004).

Interestingly, the amplitude of currents recorded in response to L-type SS protocols were of smaller amplitude than those recorded at the equivalent voltage (+20mV) in I-V protocols, also illustrated in Figure 3.2. This further raises the possibility that summation of L- and T-type Ca^{2+} currents was occurring. In order to determine whether the currents evoked by the two SS protocols were mediated solely by the channel of interest, we examined the effects of specific T- and L-type Ca^{2+} channel blockers (CCBs). Currents evoked using the T-type SS voltage protocol were inhibited by the selective T-type CCB NNC55-0396 (3 μM , NNC) in a partially reversible manner, whilst the L-type selective CCB nifedipine (2 μM) had no significant effect on T-type Ca^{2+} channel current amplitudes, when applied to a limited number of cells (Figure 3.3). This suggested that only T-type Ca^{2+} channels were contributing to the Ca^{2+} influx using this SS protocol. Due to the heterogeneous patterns of T- and L-type Ca^{2+} current expression in A7r5 cells (Figure 3.2), the observation that some currents evoked using the T-type SS were nifedipine-insensitive does not necessarily translate to the whole A7r5 population

For the L-type SS voltage protocols, Ba^{2+} (20mM) was examined as an alternative charge carrier. This significantly enhanced the amplitude of L-type Ca^{2+} currents and almost completely eliminated the slowly inactivating component, resulting in a

sustained current shape more characteristic of L-type Ca^{2+} currents (Figure 3.4). Reducing the stimulating voltage-pulse duration (100ms from 200ms) whilst using Ba^{2+} had the added advantage of reducing L-type Ca^{2+} current rundown (data not shown). Consequently, Ba^{2+} was used for all SS L-type recordings. Nifedipine ($2\mu\text{M}$) inhibited currents evoked by the L-type SS protocol in a partially reversible manner. Surprisingly, L-type Ca^{2+} currents were also inhibited by NNC ($3\mu\text{M}$), indicating either that NNC was not selective for T-type Ca^{2+} channels at $3\mu\text{M}$ or that some of the current recorded using the L-type SS was being facilitated by T-type Ca^{2+} channels.

Together, these results show that A7r5 cells express functional T- and L-type Ca^{2+} channels, that both $\text{Ca}_v3.1$ and $\text{Ca}_v3.2$ mRNA is expressed with $\text{Ca}_v3.1$ in greater abundance and that $\text{Ca}_v3.1$ channels tend to be localised around the cell membrane, whereas $\text{Ca}_v3.2$ channels tend to be localised around nuclear regions.

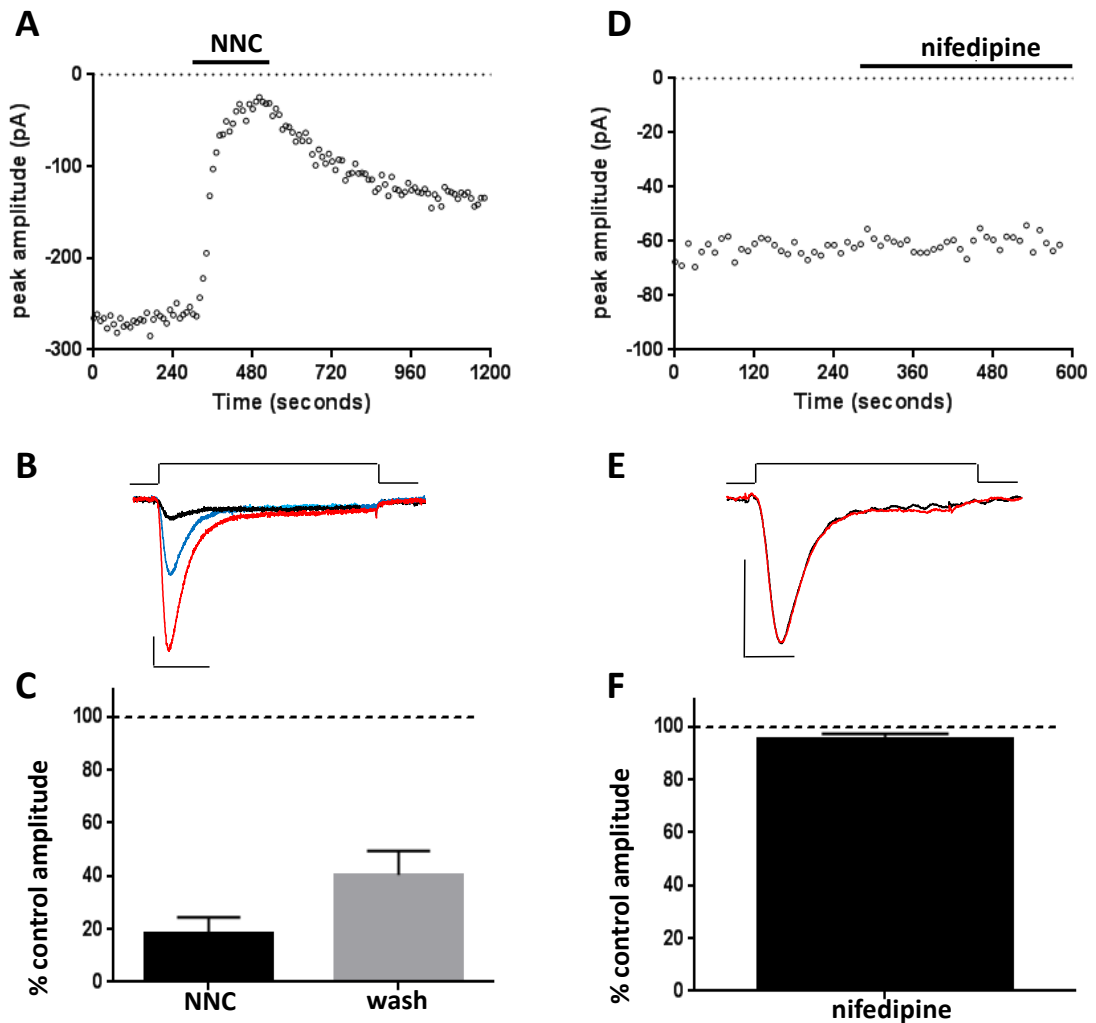


Figure 3.3. A7r5 "T-type" Ca^{2+} currents are inhibited by NNC55-0396

Whole-cell patch-clamp recordings from "new" A7r5 cells. Currents evoked by step-depolarisations (200ms duration, 0.1Hz) from -80mV to -20mV. Due to potential activation of L-type mediated Ca^{2+} currents using this protocol "T-type" is labelled with quotation marks. **A**, Example time-series plot illustrating the effects of NNC55-0396 (NNC, 3 μM , black bar) applied via the perfusate on "T-type" Ca^{2+} current amplitude **B**, Corresponding current trace (from A) showing both the effects of NNC (black trace) on control amplitude (red trace) and the small degree of washout (blue trace), scale bar 50pA (vertical), 50ms (horizontal). **C**, Bar chart illustrating (mean \pm s.e.m) peak "T-type" Ca^{2+} current amplitude (% of control) in the presence of NNC (black box) and after washout (white box), n=4. **D-F**, As (A-C), except with nifedipine (2 μM) and no washout data. **F**, n=3.

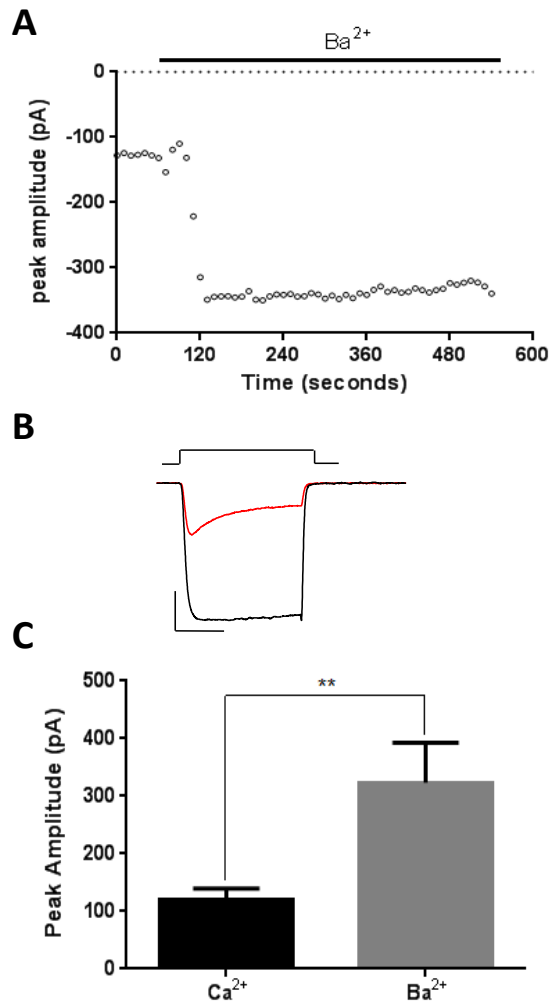


Figure 3.4. Ba²⁺ augments the size and shape of A7r5 “L-type” Ca²⁺ currents

Whole-cell patch-clamp recordings from “new” A7r5 cells. Currents evoked by step-depolarisations (100ms duration, 0.1Hz) from -50mV to +20mV. Due to potential activation of T-type mediated Ca²⁺ currents using this protocol “L-type” is labelled with quotation marks. **A**, Example time-series plot illustrating the effects of switching to Ba²⁺ (20mM, black bar) from Ca²⁺ (15mM) as the charge carrier on L-type Ca²⁺ current amplitude. **B**, Corresponding L-type Ca²⁺ current trace (from A) showing effects of Ba²⁺ (black trace) on control amplitude and current shape (red trace), scale bar 100pA (vertical), 40ms (horizontal). **C**, Bar chart illustrating peak amplitude (mean ± s.e.m) of L-type Ca²⁺ currents using either Ca²⁺ (black box) or Ba²⁺ (grey box) as the charge carrier, n=7. Data were analysed using paired Student’s t-test, **p<0.01.

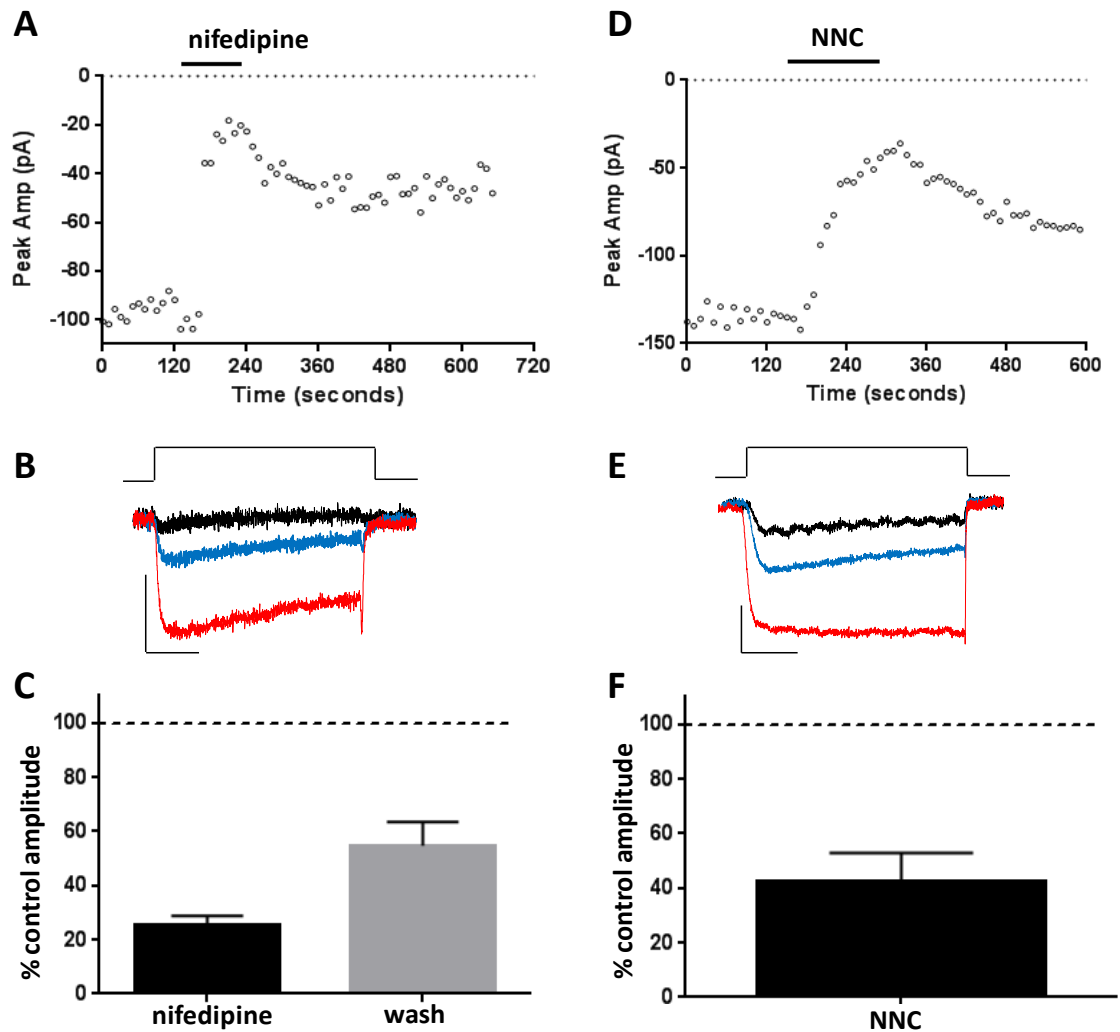


Figure 3.5. A7r5 “L-type” Ca^{2+} currents are inhibited by nifedipine and NNC55-0396
 Whole-cell patch-clamp recordings from “new” A7r5 cells. Currents evoked by step-depolarisations (200ms duration, 0.1Hz) from -50mV to +20mV, using Ba^{2+} (20mM) as the charge carrier. Due to potential activation of T-type mediated Ca^{2+} currents using this protocol “L-type” is labelled with quotation marks. **A**, Example time-series plot illustrating the effects of nifedipine (nif, $2\mu\text{M}$, black bar) applied via the perfusate (black bar) on L-type Ca^{2+} current amplitude, **B**, Corresponding L-type Ca^{2+} current trace (from A) showing both the effects of nif (black trace) on control amplitude (red trace) and the small degree of washout (blue trace), scale bar 50pA (vertical), 50ms (horizontal). **C**, Bar chart illustrating (mean \pm s.e.m) peak L-type Ca^{2+} current amplitude (% of control amplitude) in the presence of nif (black box, $n=12$) and after washout (white box, $n=6$). **D-F**, As (A-C), except showing the effects of NNC ($3\mu\text{M}$). **F**, $n=5$, (no washout data).

3.2.2. The effects of subtype specific CCBs on A7r5 proliferation and Ca^{2+} handling

We then examined what effects subtype specific CCBs would have on proliferation. As shown by the control growth profiles within Figure 3.6, both batches of A7r5 cells were proliferative, reflected by the significant increase in cell number between day 0 and day 3 (d0-d3). This also confirmed that a three day assay was a suitable time-course for proliferation assays. Both batches similarly exhibited slow rates of growth over the first day of the assay following serum deprivation (d0-d1) indicating that effective synchronisation of the cell cycle had been achieved.

Upon comparing the average daily increases in A7r5 cell number within Figure 3.6 key differences between the two batches are apparent. Between d1-d2 only the “new” batch of A7r5 cells significantly increased in cell number whereas between d2-d3 only the “old” A7r5 cells significantly increased. This shows that the newer A7r5 cells began and ceased to proliferate more quickly. As T-type Ca^{2+} channel expression is associated with proliferation (Kuga *et al.*, 1996; Rodman *et al.*, 2005; Tzeng *et al.*, 2012); the faster initiation may be due to the higher levels of T-type Ca^{2+} channel expression as detailed in Figure 3.1. The “new” A7r5 cells were larger in size (Figure 3.7) and correspondingly showed greater confluency on day three of the assay, despite a much lower average cell number compared to “old” A7r5 cells. Cultured cells do not proliferate within confluent cultures due to a well-defined process termed contact inhibition of proliferation (CIP), which is evident by a plateau in growth curves (McClatchey & Yap, 2012). With consideration to this, the greater confluence of the “new” A7r5 cells likely explains the faster decline in proliferation. In addition to their smaller size, the morphology of “new” A7r5 cells was flatter and less spindle-shaped when compared to the “old” A7r5 cells (Figure 3.7). A decline in the spindle-shaped “hill and valley” morphology within VSMCs has been previously reported alongside increased proliferative responses to serum. These morphological changes are associated with the switch from contractile to proliferative phenotypes (Faries *et al.*, 2001; Pandolfi *et al.*, 2003). An alternative explanation for the morphological differences currently observed could be contamination of the “new” A7r5 cell culture with fibroblasts. Further studies using immunohistochemistry with antibodies directed against SMC markers such as smooth muscle myosin heavy chain, calponin-1 and smooth muscle α -actin (SMA) would address this possibility.

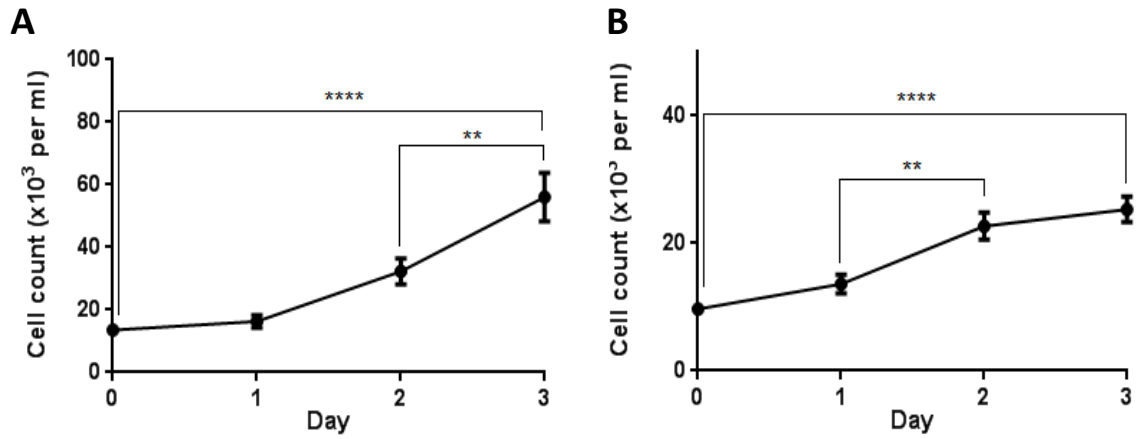


Figure 3.6. Different A7r5 batches exhibit contrasting growth profiles

Line graphs showing average A7r5 cell number (mean \pm s.e.m) over three day proliferation assays. **A**, “Old” A7r5 cells proliferate between day 0 and day 3, with the greatest daily increase between day 2 and 3 (n=7). **B**, As (A) except with “new” A7r5 cells showing greatest daily increase between day 1 and 2, (note different y axis, n=10). All cell counts were made in triplicate with the mean value counting as n=1. Data were analysed by one-way ANOVA followed by Bonferroni’s multiple comparison test, **p<0.01, ****p<0.0001.

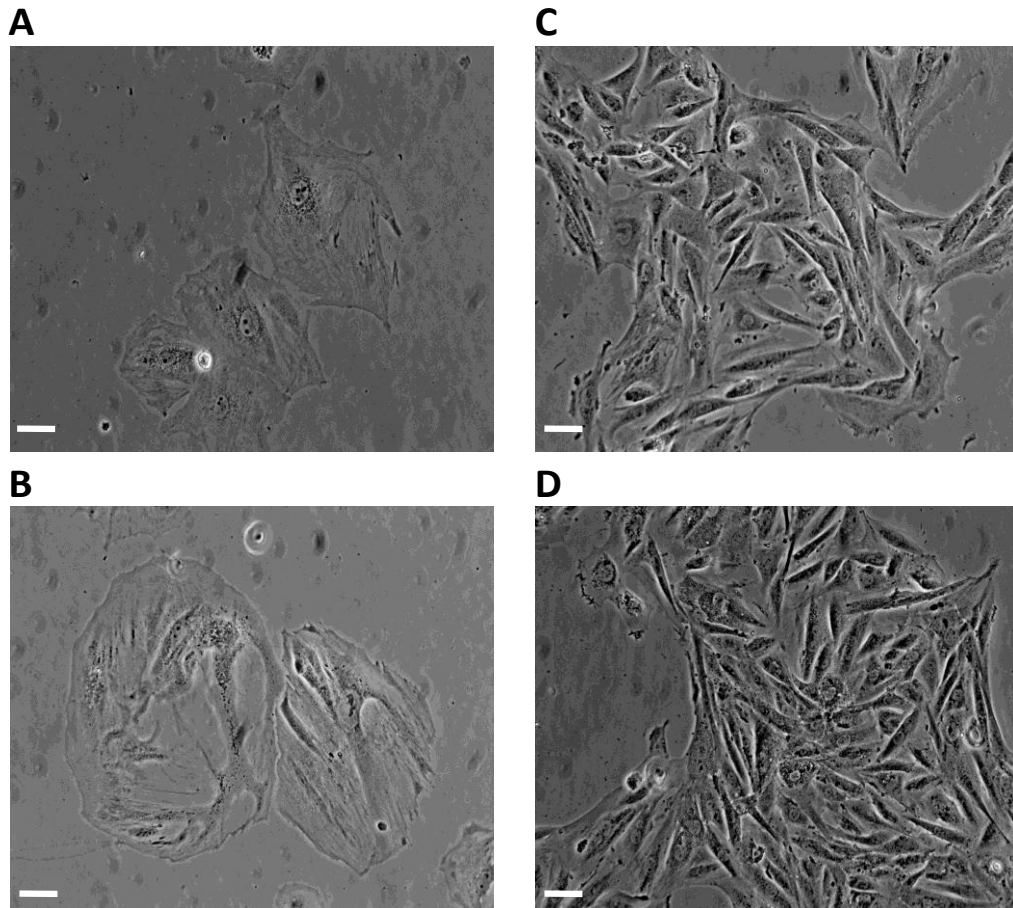


Figure 3.7. “New” A7r5 cells are larger in size than “old” A7r5 cells

Representative phase-bright images showing: A-B, “new” A7r5 and C-D, “old” A7r5 cell morphology. Scale bars 50 μ m.

Proliferation assays examining the effects of CCBs using the “old” A7r5 cells were previously conducted by Dr Hayley Duckles. Mibefradil was shown to cause a concentration-dependent decrease in proliferation without any significant effect on cell viability (1-5 μ M). Contrastingly, nifedipine was without significant effect on “old” A7r5 cell proliferation or viability (Figure 3.8, (Duckles *et al.*, 2015). These data were used to select appropriate concentrations of mibefradil and nifedipine for subsequent proliferation assays.

Similar observations were made when these experiments were repeated with “new” A7r5 cells (Figure 3.9). Mibefradil (3 μ M) significantly inhibited A7r5 proliferation without any effect on viability, whilst nifedipine (2 μ M) was without effect. The effects of the more recently developed T-type Ca^{2+} channel inhibitors ML218 and NNC were also examined over a range of concentrations. NNC caused a concentration-dependent reduction in A7r5 proliferation without effecting cell viability. At higher concentrations, NNC (10-30 μ M) was cytotoxic as reflected by the dramatic increase in average dead cell counts. ML218 also reduced proliferation in a concentration-dependent manner, with ML218 (30 μ M) showing the greatest reduction in average A7r5 cell number with no significant increase in cell death. As many of the drugs used were dissolved in DMSO, we also examined the potential effects of exposing cells to the vehicle alone. DMSO (1:1000) was the highest concentration used throughout the project, and as shown, had no effect on A7r5 proliferation (Figure 3.9). Together, these findings demonstrate that T-type Ca^{2+} channels regulate A7r5 proliferation and rule out the contribution of L-type Ca^{2+} channels.

As intracellular Ca^{2+} (Ca^{2+}_i) plays an integral role in VSMC proliferation, it was important to assess the effects of CCBs on A7r5 Ca^{2+} handling. For “old” A7r5 populations, a modest depolarising stimulus was applied with the aim of preferentially activating T-type, rather than L-type Ca^{2+} channels, achieved by switching to a perfusate containing a modestly elevated K^+ concentration ($[\text{K}^+]$ 20mM, 5mM control). Under control conditions, the high K^+ stimulus reliably induced a rapid increase in $[\text{Ca}^{2+}]_i$ leading to sustained high frequency oscillations. Removal of the depolarising stimulus was accompanied by a rapid cessation of oscillations and gradual return of $[\text{Ca}^{2+}]_i$ back to baseline levels (Figure 3.10 & Figure 3.11).

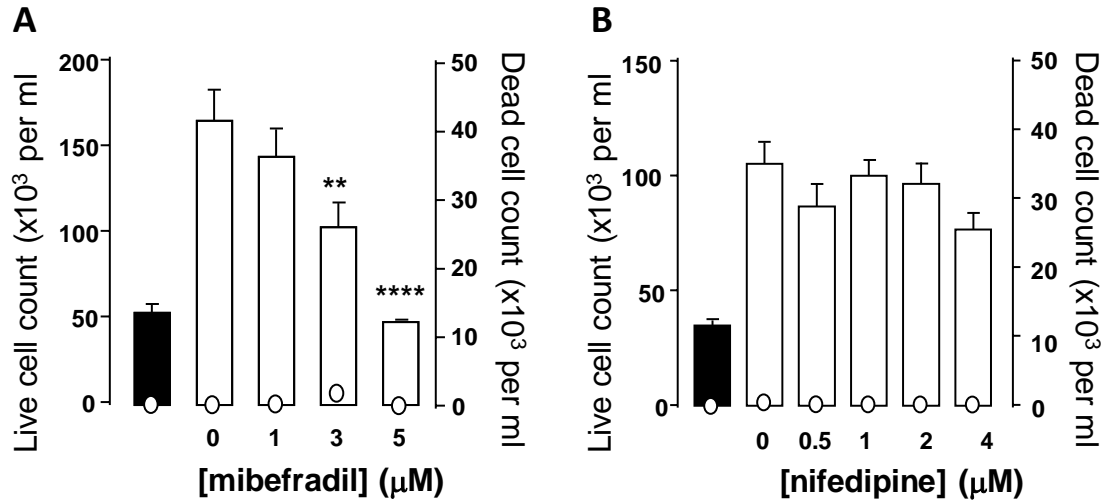


Figure 3.8. Mibefradil suppresses proliferation of “old” A7r5 cells

Bar graphs showing the proliferative response (mean \pm s.e.m) of A7r5 cells to increasing concentrations of specified drugs. Proliferation (plotted as bar graphs, corresponding to the left-hand y-axis) was monitored on day 0 (solid bars) and on day 3 (open bars) in the absence or presence of either mibefradil (**A**, n=4) or nifedipine (**B**, n=3). The open circles show the corresponding non-viable cell count (plotted against corresponding right-hand y-axis). All cell counts were made in triplicate with the mean value representing n=1. Data were analysed via ratio repeated measures one-way ANOVA followed by Dunnett’s multiple comparison test using day 3 control (no drug) counts as control, **p<0.01,****p<0.0001. Data was taken with permission from Duckles et al. (2015).

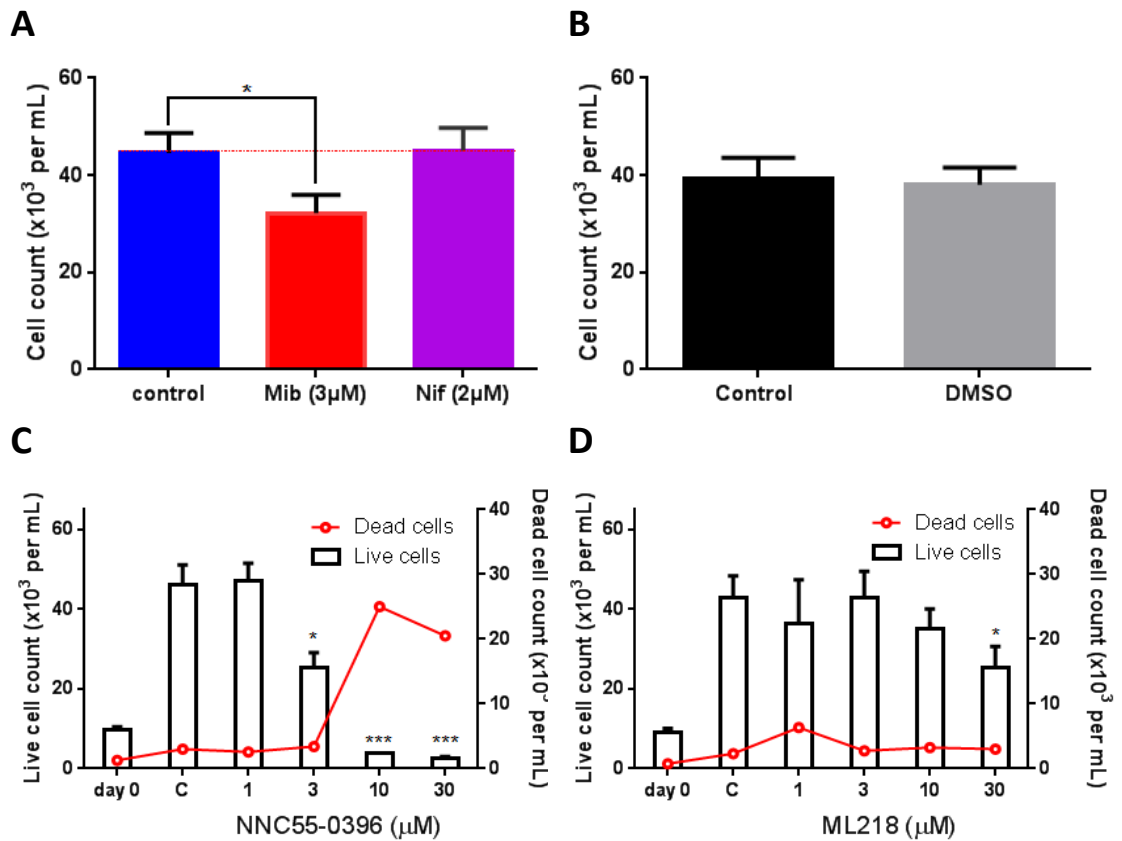


Figure 3.9. T-type Ca²⁺ channel inhibitors reduce “new” A7r5 proliferation

Bar graphs showing the proliferative response (mean \pm s.e.m) of “new” A7r5 cells to specified drugs, as monitored on day 3. **A**, Effects of mibefradil (mib, 3µM) and nifedipine (nif, 2µM) both (n=9) and **B**, DMSO (1:1000, n=6) on A7r5 proliferation as monitored on day 3, data analysed using unpaired students t-tests. **C**, Proliferation with increasing concentrations of NNC55-0396 (plotted against the left-hand y-axis) monitored on day 0 and on day 3. The red circles show the corresponding non-viable cell count (plotted against the right-hand y-axis). Data were analysed via one-way ANOVA followed by Dunnett’s multiple comparison test (n=7 (n=2 for 10 and 30µM)). **D**, As (C), except with ML218 (n=4). All cell counts were made in triplicate with the mean value representing n=1, for all graphs *p \leq 0.05, **p \leq 0.01.

For all experiments, control responses were individually recorded to ensure that when the depolarising stimulus was reapplied to the same cell population there was no significant difference in the amplitude of responses (Figure 3.10 & Figure 3.11).

A variety of CCBs were applied to “old” A7r5 cells prior to and during the 2nd depolarisation, and it was found that the selective T-type CCBs ML-218 (30µM) and mibefradil (1µM) significantly reduced the amplitude of the response to the 2nd depolarisation when compared to the corresponding 1st depolarisation (Figure 3.10). A Mibefradil (3µM) was also shown to produce a similar degree of inhibition. The L-type Ca²⁺ channel specific inhibitor nifedipine (2µM) also reduced the amplitude of the 2nd response (Figure 3.11). Collectively, these findings show that Ca²⁺ oscillations observed in response to depolarisation within “old” A7r5 cells are facilitated by both T-type and L-type Ca²⁺ channels.

The effects of NNC were also examined, however, for these experiments a decline in the amplitude of response between the 1st and 2nd depolarisations was apparent alongside a dramatic reduction in Ca²⁺ oscillations within control situations (data not shown). This indicated a phenotypic variation within the “old” A7r5 cells and prevented reliable conclusions regarding NNC effects. New A7r5 cells, were resultantly purchased and shown to express significantly higher levels of Ca_v3.1 and Ca_v3.2 mRNA (Figure 3.1). These “new” A7r5 cells were used for the majority of subsequent experiments.

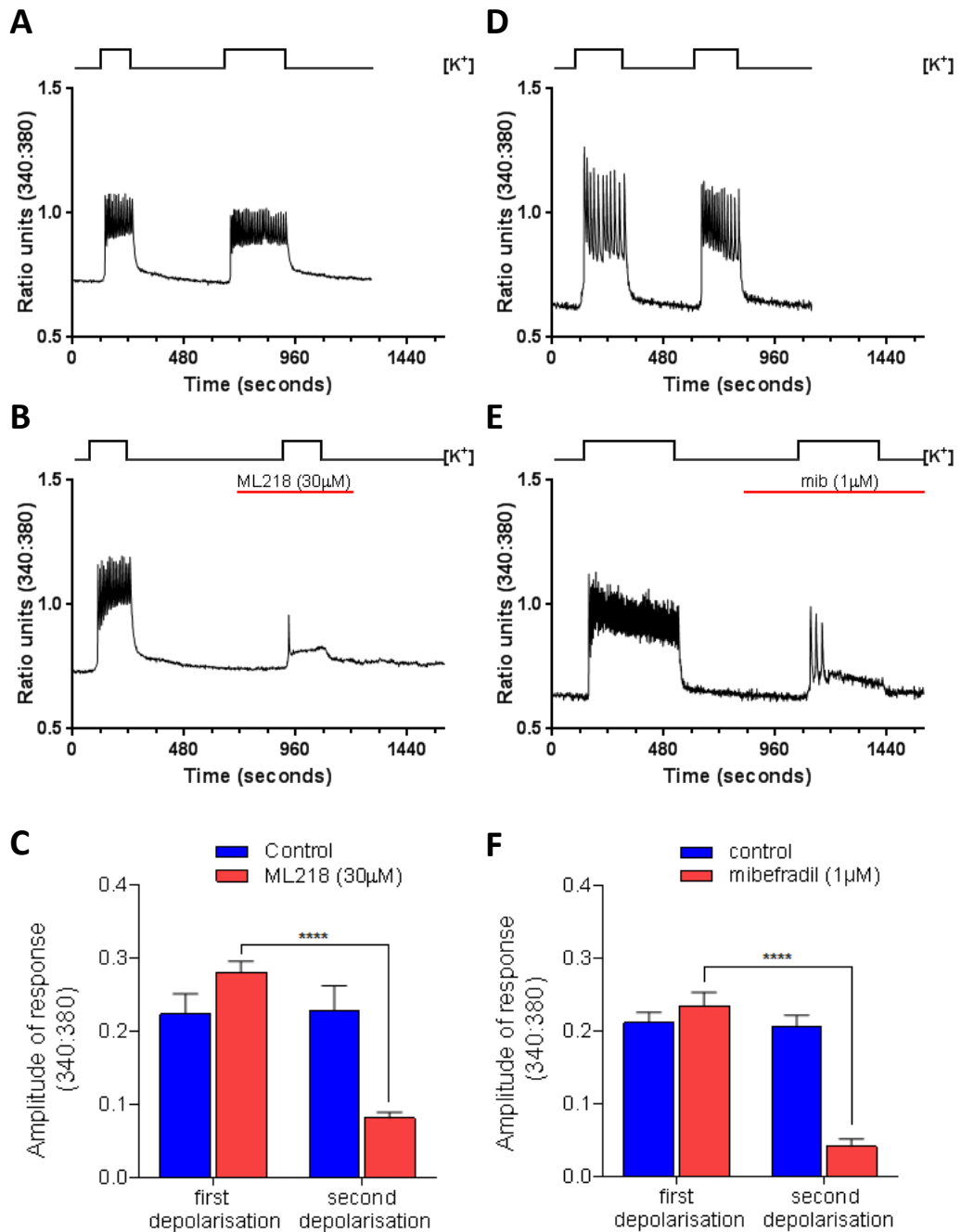


Figure 3.10. T-type CCBs reduce depolarisation-induced Ca^{2+} entry in “old” A7r5 cells
 Example Ca^{2+} microfluorimetry traces showing the effects of CCBs on Fura 2 ratio units (340:380), representing $\Delta [\text{Ca}^{2+}]_i$ in response to depolarisation. Black bars above traces show periods where perfusate containing elevated $[\text{K}^+]$ (20mM, control 5mM) was applied in order to depolarise cells. Red lines show the period of CCB application (as stated). **A**, Example control trace matched with, **B**, Example trace showing the effects of ML218 (30 μM) applied between the 1st and 2nd depolarisations. **C**, Bar graph showing the (mean \pm s.e.m) response amplitude to the 1st and 2nd depolarisations in control (blue bar, n=4) and ML218 (30 μM, red bar, n=7) conditions. **D-E**, As (A-B), except showing the effects of mibefradil (1 μM). **F**, As (C), except showing control (blue bar, n=9) and mibefradil (1 μM, red bar, n=11). All data were analysed using paired Student’s t-tests, **** $p \leq 0.0001$.

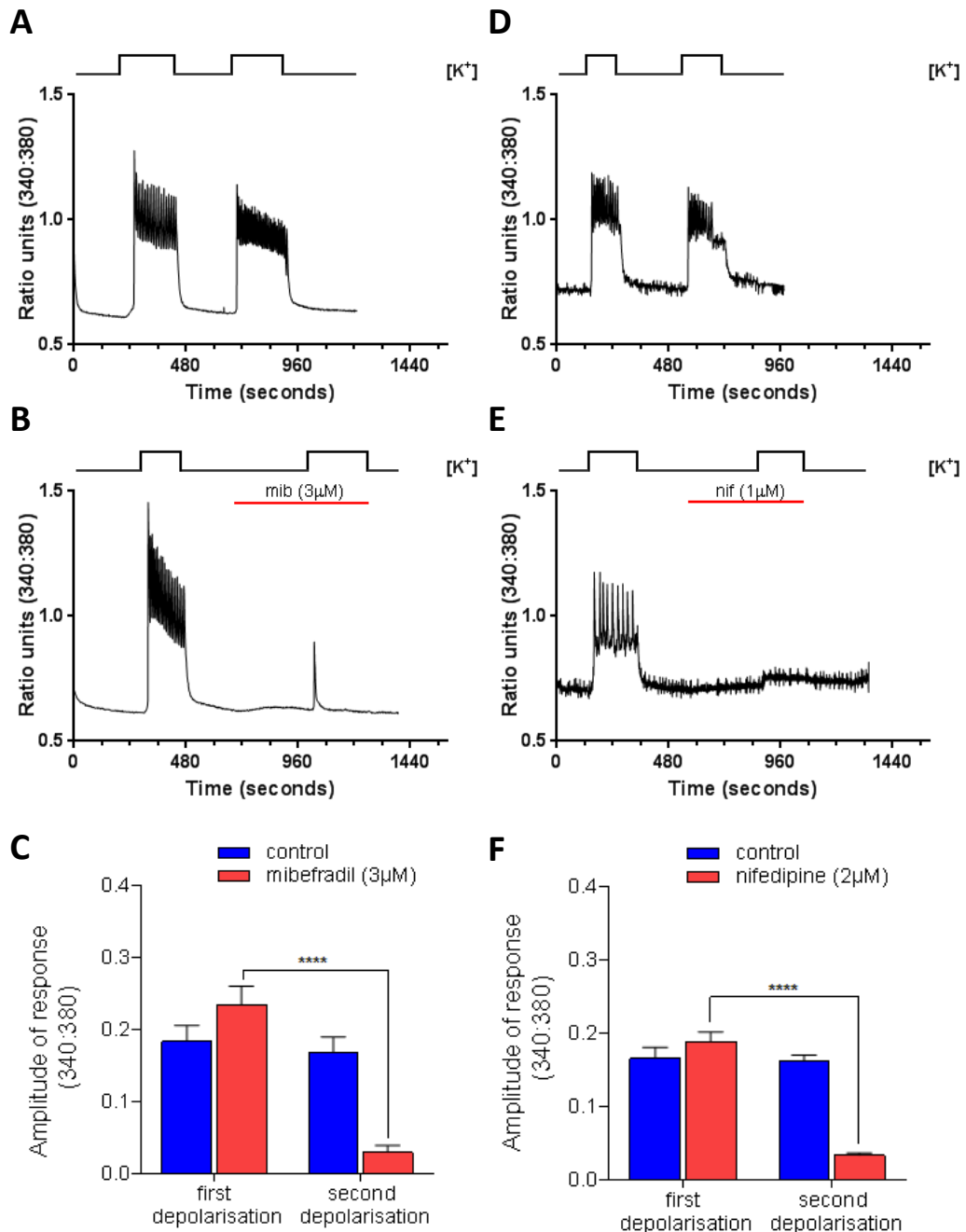


Figure 3.11. T-type and L-type CCBs reduce depolarisation-induced Ca^{2+} entry in “old” A7r5 cells

Example Ca^{2+} microfluorimetry traces showing the effects of CCBs on Fura 2 ratio units (340:380), representing $\Delta [\text{Ca}^{2+}]_i$ in response to depolarisation. Black bars above traces show periods where perfusate containing elevated $[\text{K}^+]$ (20mM, control 5mM) was applied in order to depolarise cells. Red lines show the period of CCB application (as stated). **A**, Example control trace matched with, **B**, Example trace showing the effects of mibefradil (3µM) applied between the 1st and 2nd depolarisations. **C**, Bar graph showing the (mean \pm s.e.m) response amplitude to the 1st and 2nd depolarisations in control (blue bar, n=9) and mibefradil (3µM, red bar, n=11) conditions. **D-E**, As (A-B), except with nifedipine (2µM), **F**, As (C), except with nifedipine (2µM, control n=12, mibefradil n=11). All data were analysed using paired Student’s t-tests, **** $p \leq 0.0001$.

Upon examination of basal Ca^{2+} levels within the “new” A7r5 cells, spontaneous Ca^{2+} oscillations of variable frequencies were apparent under control conditions within some A7r5 populations as represented in Figure 3.12. These oscillations rapidly ceased upon removal of extracellular Ca^{2+} (Ca^{2+}_e) suggesting that they were mediated by Ca^{2+} channel influx, presumably via channels present within the cell membrane. As T-type Ca^{2+} channels have well established roles in pacemaker activity within the sinoatrial node and various brain regions (Mesirca *et al.*, 2014; Nelson *et al.*, 2006), this spontaneous oscillatory activity may be attributable to increased levels of T-type Ca^{2+} channels.

Further investigation revealed that removal of Ca^{2+}_e also caused a decrease in baseline Ca^{2+} levels within “new” A7r5 populations which did not exhibit spontaneous oscillations. This suggested that a small degree of Ca^{2+} influx was occurring under control conditions in the absence of oscillations. As T-type Ca^{2+} channels exhibit a characteristic overlap in activation and steady-state inactivation voltages, they can be open without fully inactivating at the cell’s resting membrane potential (V_m). This commonly facilitates tonic basal Ca^{2+} influx, referred to as a “window current”, as reviewed (Perez-Reyes, 2006). As no measurable window current was detectable within the “old” A7r5 cells (data not shown) which expressed significantly lower levels of T-type Ca^{2+} channels, it was likely that the recorded window current within the “new” A7r5 cells was mediated by these channels. In order to investigate this further, NNC ($3\mu\text{M}$) was applied to A7r5 populations and, as illustrated in Figure 3.13, such an exposure decreased basal Ca^{2+} levels. After pre-treatment with, and in the continued presence of NNC ($3\mu\text{M}$), the fall in ratio units (ru) in response to removal of Ca^{2+}_e was considerably lower when compared to control conditions. These findings clearly demonstrate that T-type Ca^{2+} channels contribute a window current within “new” A7r5 cells.

Following an identical protocol, the effects of nifedipine ($2\mu\text{M}$) were also assessed. Nifedipine was surprisingly found to have similar effects on “new” A7r5 cell basal $[\text{Ca}^{2+}]_i$ as was observed for NNC. Removal of Ca^{2+}_e , after both pre-treatment and in the continued presence of nifedipine, caused a reduction in $[\text{Ca}^{2+}]_i$, which was significantly lower than observed in control conditions (Figure 3.13). This suggested that the

observed window currents were also partially facilitated by L-type Ca^{2+} channels. This was unexpected as these channels are activated at relatively high voltages and are therefore usually presumed to be closed at resting V_m . Whilst, electrophysiological recordings had shown that T-type Ca^{2+} currents were insensitive to nifedipine (Figure 3.3), further investigation was conducted within recombinant HEK293/ $\text{Ca}_v3.1$ cells to assess the potential non-specific effects of nifedipine on basal Ca^{2+} levels (Figure 3.17).

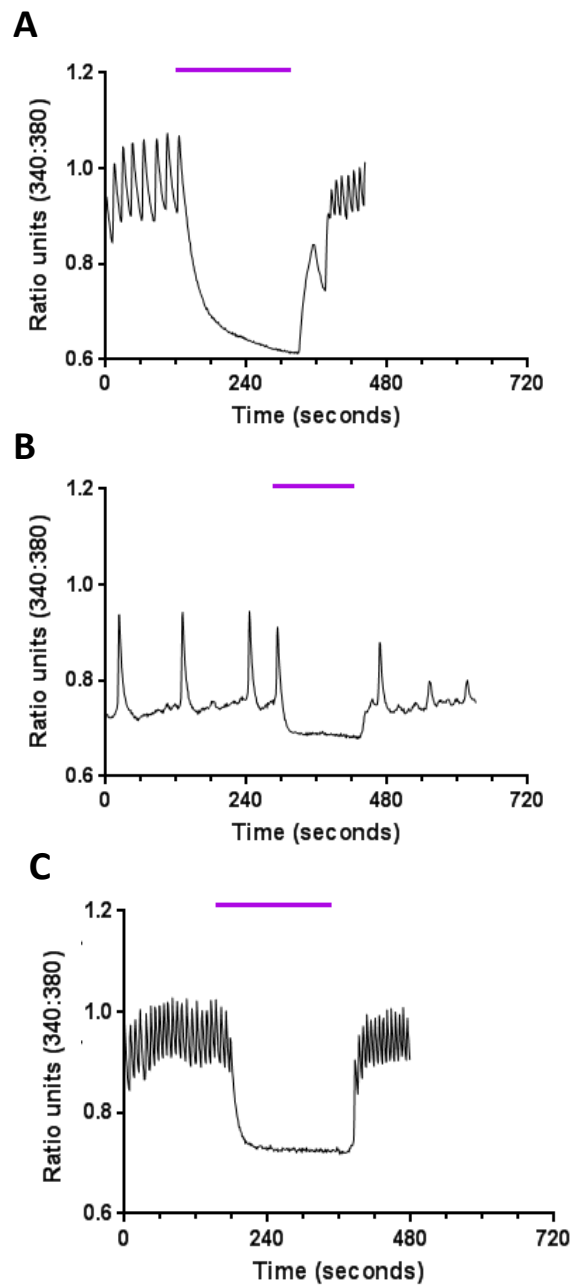


Figure 3.12. “New” A7r5 cells with higher T-type Ca^{2+} channel expression exhibit spontaneous Ca^{2+} oscillations

Example Ca^{2+} microfluorimetry traces showing the Fura 2 ratio units (340:380), representing $\Delta [\text{Ca}^{2+}]_i$, under both control conditions and following the removal of extracellular Ca^{2+} (purple bar), and clearly showing different patterns of oscillatory activity within 3 different A7r5 populations (**A-C**).

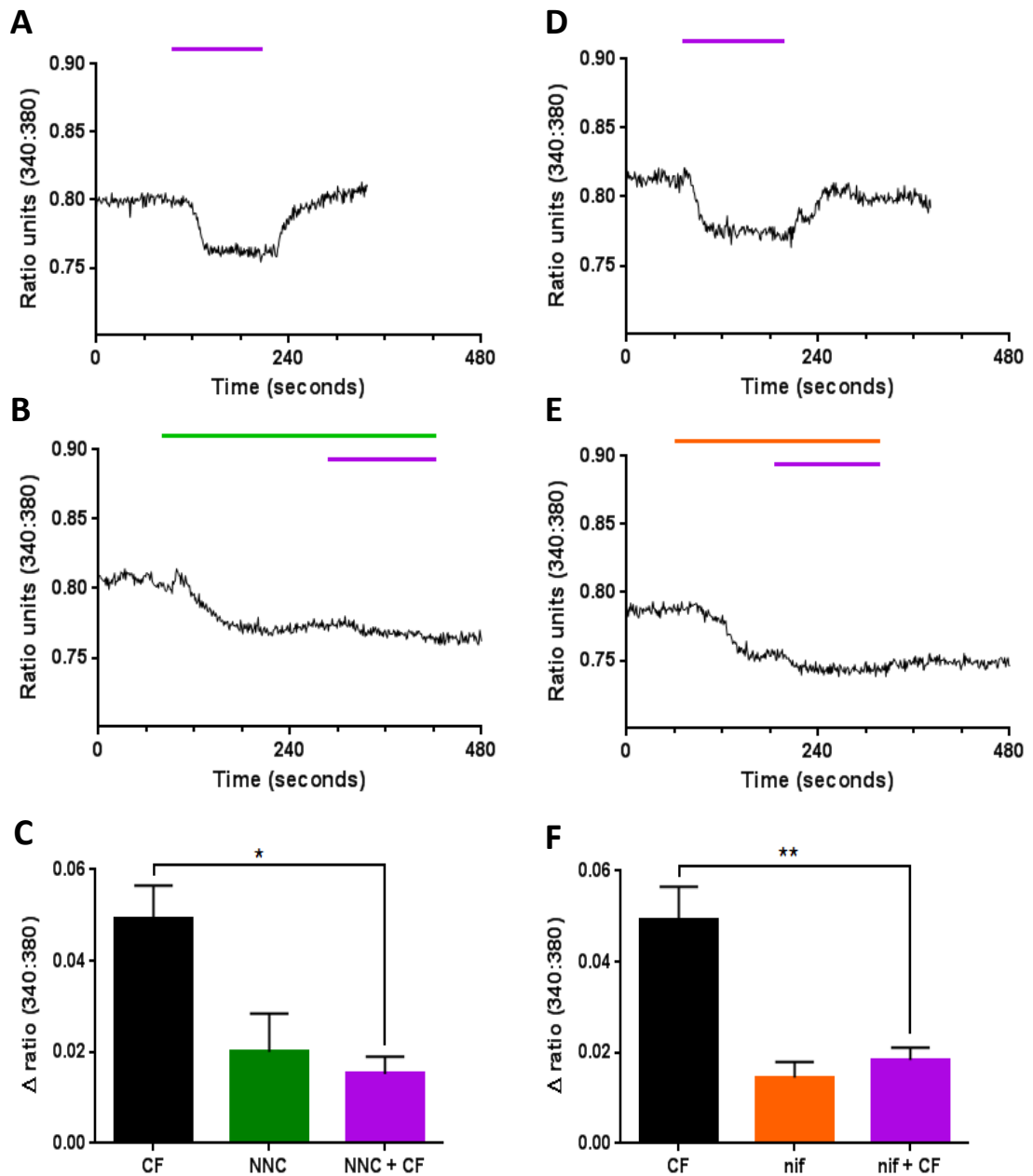


Figure 3.13. NNC55-0396 and nifedipine inhibit the “new” A7r5 Ca^{2+} window current
 Example Ca^{2+} microfluorimetry traces showing Fura 2 ratio units (340:380), representing $\Delta [\text{Ca}^{2+}]_i$, upon removal of extracellular Ca^{2+} (CF, purple bar) under: **A,D**, control conditions, **B**, after pre-treatment and in the continuous presence of NNC55-0396 (green bar, NNC, 3 μM). **E**, As (B), except with nifedipine (orange bar, nif, 2 μM). **C**, Bar graph showing (mean \pm s.e.m) decrease in ratio units (340:380) in response to: CF in control conditions (black box, CF, $n=44$), during NNC pre-treatment (green box, 3 μM , $n=12$), and during CF with NNC present (purple box, 3 μM , $n=12$). **F**, As (C), except showing control conditions (black box, $n=44$), nif pre-treatment (orange box, 2 μM , $n=25$), and CF with nif present (purple box, 2 μM , $n=25$). Effects of CF between control and NNC or nif conditions were analysed using unpaired Student’s t-tests, * $p \leq 0.05$, ** $p \leq 0.01$.

3.2.3. Effects of $Ca_v3.1$ and $Ca_v3.2$ expression on HEK293 cell proliferation and Ca^{2+} handling

In order to examine the effects of T-type Ca^{2+} channel expression on cellular proliferation and Ca^{2+} handling in isolation, and also to assess potential isoform differences, recombinant HEK293 cells stably transfected with either $Ca_v3.1$ or $Ca_v3.2$ channels (HEK293/ $Ca_v3.1$ and HEK293/ $Ca_v3.2$ respectively) were employed. Proliferation assays, conducted over a three day period, revealed that both HEK293/ $Ca_v3.1$ and HEK293/ $Ca_v3.2$ cells proliferated at a significantly greater rate when compared to untransfected (control) HEK293 cells (wt HEK293), as shown by the differences in average cell number on day 3 (Figure 3.14). NNC was applied at a lower concentration (1 μ M) than used for A7r5 proliferation assays as NNC (3 μ M) caused an increase in HEK293 non-viable cells counts on some occasions (data not shown). Figure 3.15 demonstrates that NNC (1 μ M) caused a significant reduction in HEK293/ $Ca_v3.1$ and HEK293/ $Ca_v3.2$ cell proliferation but was without effect on wt HEK293 cells. Despite this observed reduction, the average HEK293/ $Ca_v3.1$ and HEK293/ $Ca_v3.2$ cell numbers in NNC conditions remained elevated when compared to wt HEK293 cells under control conditions. As the IC_{50} of NNC within HEK293/ $Ca_v3.1$ cells is 7 μ M (Li *et al.*, 2005) it is likely that NNC (1 μ M) only partially inhibited T-type Ca^{2+} channels, which may explain why the proliferative rate of recombinant cells remains higher than for wt HEK293 cells. These data demonstrate that $Ca_v3.1$ or $Ca_v3.2$ expression increases HEK293 cell proliferation.

The proliferative rate of a HEK293/ $Ca_v3.2$ cell line generated within the Peers group by Dr Jason Scragg (HEK293/ $Ca_v3.2$ /clone P) was also examined and, as shown in Figure 3.15, proliferated at a similar rate to wt HEK293 cells. Furthermore, no inhibition in HEK293/ $Ca_v3.2$ /clone P proliferation was observed with NNC (1 μ M). This demonstrates that $Ca_v3.2$ expression in itself does not augment proliferation and indicates that some form of post-translational modification, sub-cellular localisation and/or trafficking mechanism may be critical for development of the highly proliferative phenotype. NNC treatment was shown also shown to be without effect on viability for any of the cell lines examined (Figure 3.15).

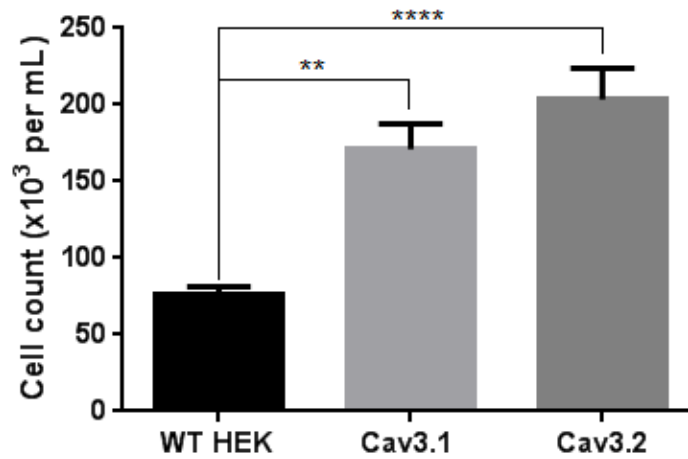


Figure 3.14. Recombinant HEK293/Ca_v3.x cells proliferate at a greater rate compared to wild type HEK293 cells

Bar graph showing the proliferative rates (mean \pm s.e.m) of untransfected (control) HEK293 cells (WT HEK, n=8) and HEK293 cells stably expressing Cav3.1 and Cav3.2 (HEK293/Ca_v3.1, n=12; and HEK293/Ca_v3.2, n=10, respectively), as counted on day 3. All cell counts were made in triplicate with the mean value counting as n=1. Data were analysed using one-way ANOVA with Dunnett's post-hoc comparison test, **p \leq 0.01, ****p \leq 0.0001.

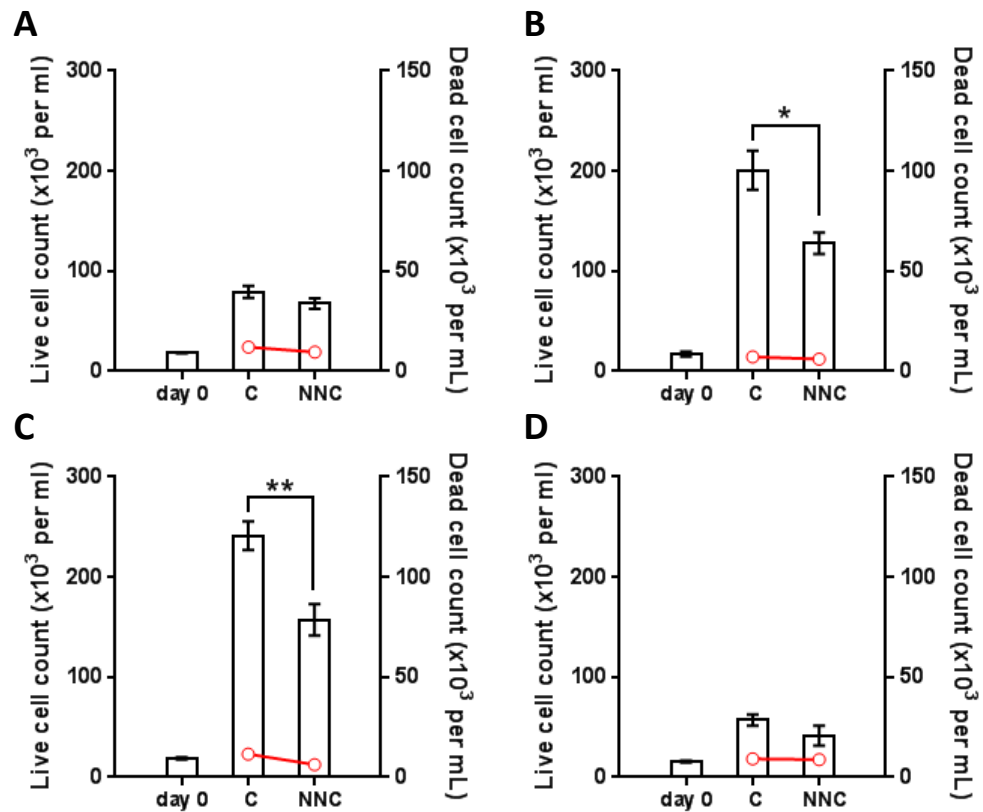


Figure 3.15. NNC55-0396 reduces elevated HEK293/Ca_v3.x cell proliferation

Bar graphs showing the proliferative responses (mean \pm s.e.m) of recombinant HEK293/Ca_v3.x and wt HEK293 cells in the presence of NNC55-0396 (NNC, 1 μ M) or DMSO (1:1000) as counted on day 3; day 0 counts also shown (plotted against the left-hand y-axis), red circles show the corresponding non-viable cell count (plotted against the right-hand y-axis). **A**, wt HEK293 cells (n=5). **B**, HEK293/Ca_v3.1 cells (n=4). **C**, HEK293/Ca_v3.2 cells (n=4). **D**, HEK293/Ca_v3.2/clone P cells (n=6). All cell counts were made in triplicate with the mean value counting as n=1. All data were analysed via one-way ANOVA followed by Dunnett's multiple comparison test *p \leq 0.05, **p \leq 0.01.

3.2.4. Sub-cellular localisation of $Ca_v3.1$ and $Ca_v3.2$ within recombinant HEK293 cells

Immunohistochemistry using monoclonal antibodies directed against $Ca_v3.1$ or $Ca_v3.2$ was conducted on recombinant HEK293 cells in order to both validate antibody specificity and enable comparison of the sub-cellular localisation of T-type Ca^{2+} channels within HEK293/ $Ca_v3.1$, HEK293/ $Ca_v3.2$ and HEK293/ $Ca_v3.2$ /clone P cell lines. DAPI was co-applied to label cell nuclei. Both the $Ca_v3.1$ and $Ca_v3.2$ antibodies were shown to be highly specific (**Error! Reference source not found.** and 0 respectively) as they showed no cross reactivity with the opposing isoform; i.e. no staining was detected when the $Ca_v3.1$ antibody was applied to HEK293/ $Ca_v3.2$ cells and vice versa. In addition, no fluorescence was observed when either the primary or secondary antibodies were omitted, thus ruling out auto-fluorescence and non-specific labelling as confounding factors.

Within HEK293/ $Ca_v3.1$ cells, $Ca_v3.1$ channels were found to be widely distributed throughout most cells (0). Dense clusters of $Ca_v3.1$ immuno-reactivity ($Ca_v3.1$ -IR) were commonly apparent and adjacent to cell nuclei, i.e. displaying perinuclear distribution. In addition, punctate regions of $Ca_v3.1$ -IR were often observed localised in or around the plasma membrane (0). A small number of cells (highlighted by white circle) that did not express $Ca_v3.1$ were also apparent, labelled by DAPI but showing no $Ca_v3.1$ -IR. As illustrated within 0, a virtually identical pattern of $Ca_v3.2$ immuno-reactivity ($Ca_v3.2$ -IR) was observed in HEK293/ $Ca_v3.2$ cells with dense perinuclear and punctate regions of $Ca_v3.2$ -IR reliably detected. Contrastingly, although $Ca_v3.2$ -IR was prominent throughout HEK293/ $Ca_v3.2$ /Clone P cells the distribution was comparatively diffuse, and no clustering of $Ca_v3.2$ channels was identifiable (0). This observation may explain why HEK293/ $Ca_v3.2$ /Clone P did not show an elevated proliferative rate; suggesting that sub-cellular localisation and/or compartmentalisation of $Ca_v3.2$ channels may be critical for the development of the highly proliferative phenotype.

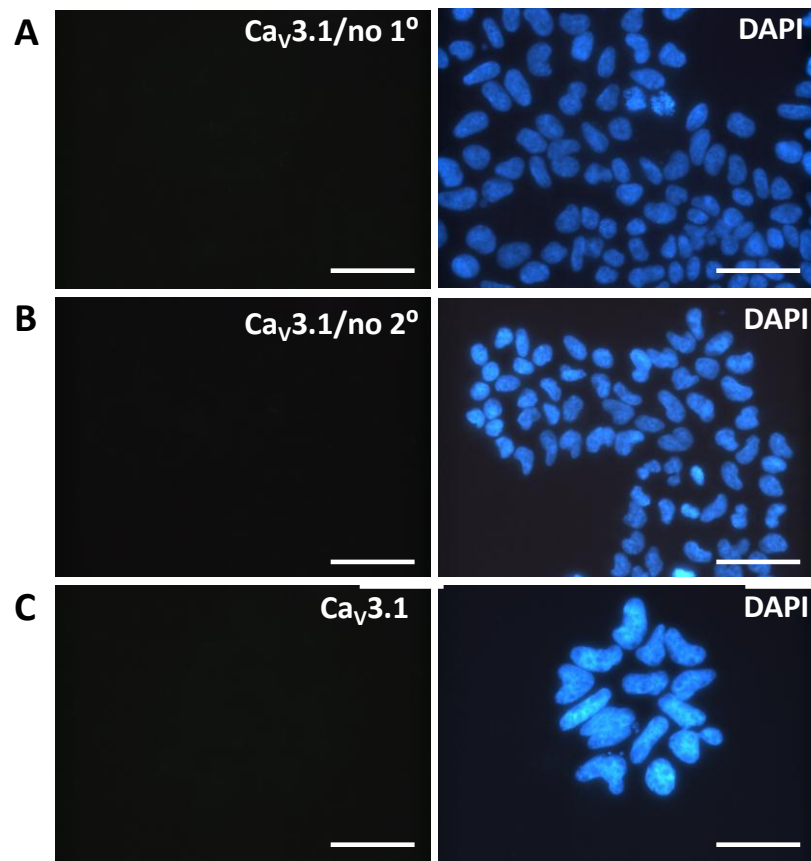


Figure 3.20. Ca_v3.1 antibody is highly specific

Dual-label immunofluorescence using anti Ca_v3.1 (1:100) with Alexa Fluor-488 secondary antibody (1:1000, left panels, green images) and DAPI to label cell nuclei (right panel, blue images). Negative controls showing no Ca_v3.1 immunoreactivity (IR) is detected within; **A**, HEK293/Ca_v3.1 cells when the primary (1°) anti-Ca_v3.1 antibody is omitted, **B**, within HEK293/Ca_v3.1 cells when the secondary (2°) antibody is omitted and **C**, within HEK293/Ca_v3.2 cells when both anti-Ca_v3.1 (1°) and 2° antibodies are applied. All images shown are typical representations of findings from a minimum of three repeats.

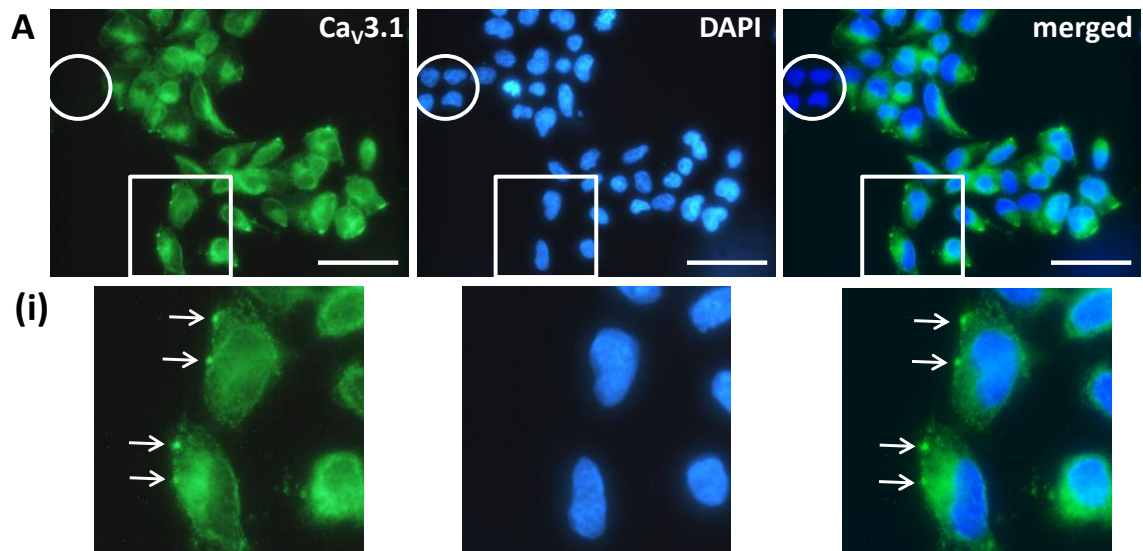


Figure 3.21. Sub-cellular localisation of Ca_v3.1 channels within HEK293/Ca_v3.1 cells
 Dual-label immunofluorescence using anti-Ca_v3.1 (1:100) and Alexa Fluor-488 secondary antibody (1:1000, left panels, green images) and DAPI to label cell nuclei (centre panel, blue images), merged Ca_v3.1 and DAPI images (right panels). **A**, HEK293/Ca_v3.1 cells show extensive Ca_v3.1 immunoreactivity (IR) with highly pronounced clusters adjacent to nuclei and punctate regions of Ca_v3.1-IR around the plasma membranes; regions of interest (white box) are magnified in **(i)** where white arrows highlight punctate Ca_v3.1-IR within the plasma membrane. All images shown are typical representations of findings from a minimum of three repeats. All scale bars 50μm.

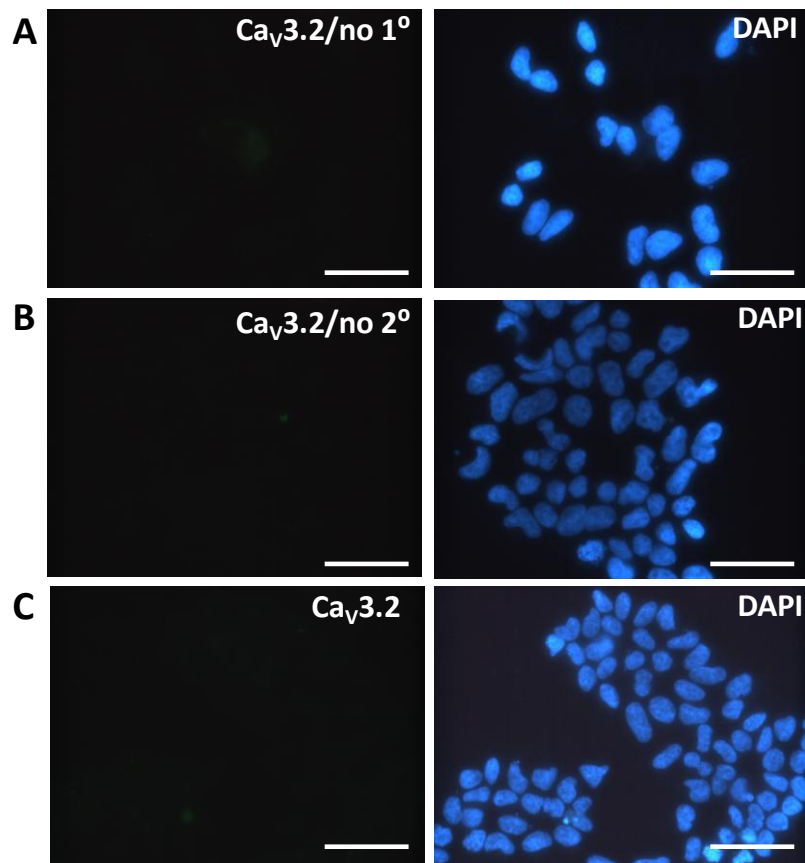


Figure 3.22. Ca_v3.2 antibody is highly specific

Dual-label immunofluorescence using anti-Ca_v3.2 (1:1000) and Alexa Fluor-488 secondary antibody (1:1000, left panels, green images) and DAPI to label cell nuclei (right panel, blue images). Negative controls showing no Ca_v3.2 immunoreactivity (IR) detected within; **A**, HEK293/Ca_v3.2 cells when the primary (1°) anti-Ca_v3.2 antibody is omitted, **B**, within HEK293/Ca_v3.2 cells when the secondary (2°) antibody is omitted and **C**, within HEK293/Ca_v3.1 cells, when both anti-Ca_v3.2 (1°) and 2° antibodies are applied. All images shown are typical representations of findings from a minimum of three repeats. All scale bars 50μm.

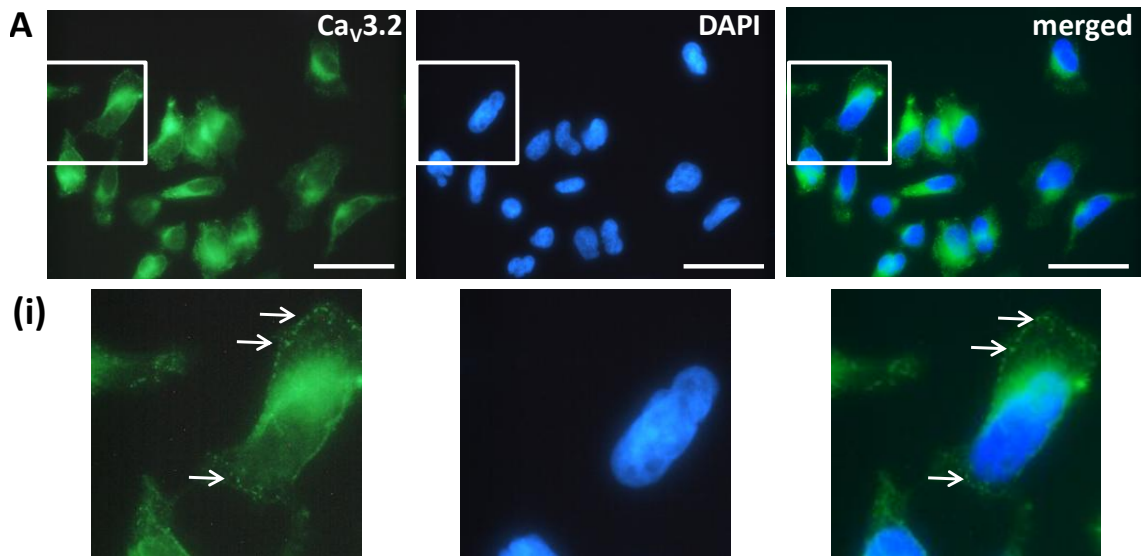


Figure 3.23. Sub-cellular localisation of Ca_v3.2 channels within HEK293/Ca_v3.2 cells
 Dual-label immunofluorescence using anti-Ca_v3.2 (1:1000) and Alexa Fluor-488 secondary antibody (1:1000, left panels, green images) and DAPI to label cell nuclei (centre panel, blue images), merged Ca_v3.2 and DAPI images (right panels). **A**, HEK293/Ca_v3.2 cells show extensive Ca_v3.2 immunoreactivity (IR) with highly pronounced clusters adjacent to nuclei and punctate regions of Ca_v3.2-IR around plasma membranes; regions of interest (white box) are magnified in **(i)** where white arrows highlight punctate Ca_v3.2-IR within the plasma membrane. All images shown are typical representations of findings from a minimum of three repeats. All scale bars 50μm.

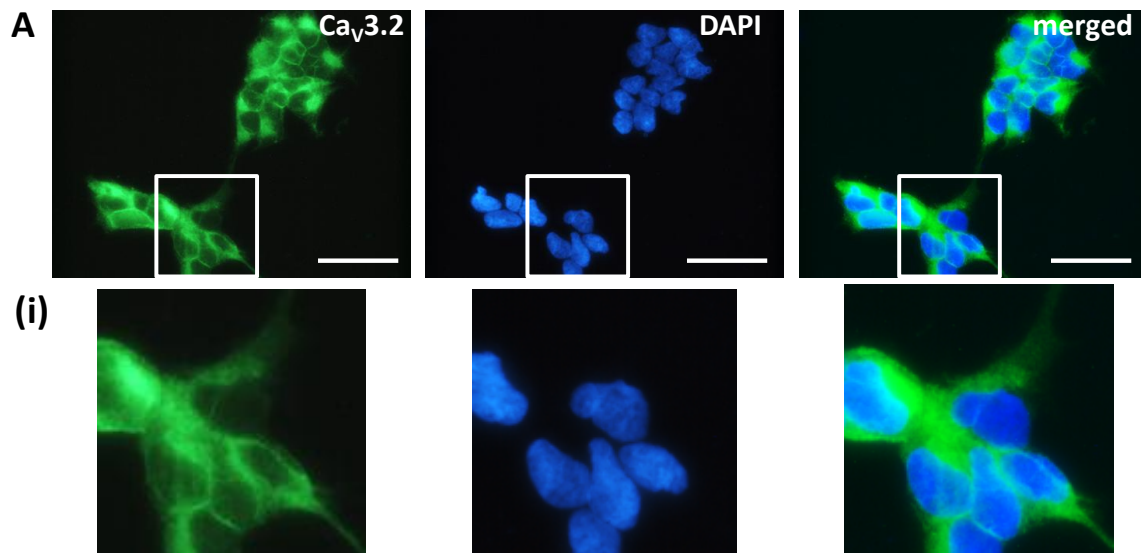


Figure 3.24. Sub-cellular localisation of Ca_v3.2 channels within HEK293/Ca_v3.2/Clone P cells

Dual-label immunofluorescence using anti-Ca_v3.2 (1:1000) and Alexa Fluor-488 secondary antibody (1:1000, left panels, green images) and DAPI to label cell nuclei (centre panel, blue images), merged Ca_v3.2 and DAPI images (right panels). **A**, HEK293/Ca_v3.2 cells show extensive and diffuse Ca_v3.2 immunoreactivity (IR); regions of interest (white box) are magnified in **(i)**. All images shown are typical representations of findings from a minimum of three repeats. All scale bars 50μm.

3.2.5. T-type Ca^{2+} channels facilitate the window current in recombinant HEK293 cells.

Ca^{2+} microfluorimetry was then used to assess the effects T-type Ca^{2+} channel expression on basal Ca^{2+}_i levels. Removal of extracellular Ca^{2+} (Ca^{2+}_e) was achieved by switching the standard perfusate to one where EGTA was substituted for Ca^{2+} (CF). For cells facilitating tonic Ca^{2+} influx (window current) this produced a measurable fall in $[Ca^{2+}]_i$, represented by a decrease in the Fura-2 ratio (340:380). Figure 3.16 shows that HEK293/ $Ca_v3.1$ cells conduct a significantly larger window current compared to wt HEK293 cells. As the decrease in response to CF for HEK293/ $Ca_v3.1$ cells is significantly reduced after both pre-treatment and in the continual presence of NNC (3 μ M), which is without effect on wt HEK293 cells, it is apparent that $Ca_v3.1$ expression increases basal $[Ca^{2+}]_i$ levels within HEK293 cells. The small fall in $[Ca^{2+}]_i$ in wt HEK293 cells also suggests that other routes of Ca^{2+} entry may be present in these cells, but these were dominated by the much larger responses in transfected cells.

The aforementioned CF protocol was also used to demonstrate that nifedipine was without effect on the HEK293/ $Ca_v3.1$ window current, as shown in Figure 3.17, ruling out potential non-specific effects of nifedipine on the T-type mediated window current. This provides supporting evidence to the observation that the decrease in basal Ca^{2+} observed with nifedipine in A7r5 cells, as shown in Figure 3.13, is due to L-type Ca^{2+} channels partially mediating the A7r5 window current rather than non-specific effects of nifedipine. Previous work conducted by Dr Hayley Duckles showed that HEK293/ $Ca_v3.2$ cells also mediate a window current of significantly larger amplitude than that observed in wt HEK293 cells. Figure 3.18, reproduced with permission from Duckles *et al.* (2013), additionally demonstrates that NNC (3 μ M) caused a significant reduction in basal $[Ca^{2+}]_i$ in HEK293/ $Ca_v3.2$ cells but not in wt HEK293 cells. Collectively, these data demonstrate that $Ca_v3.1$ or $Ca_v3.2$ expression increases tonic Ca^{2+} influx within HEK293 cells.

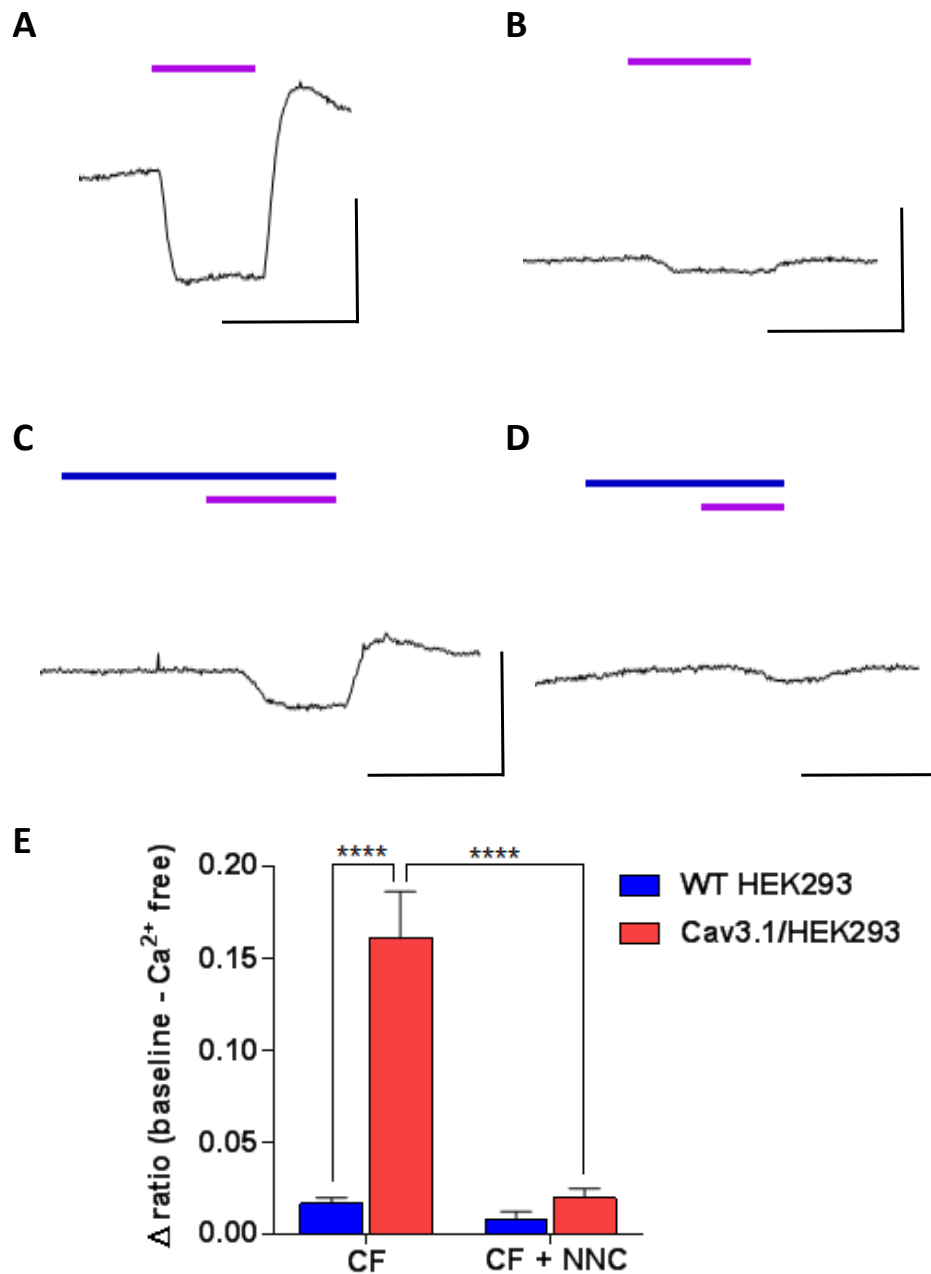


Figure 3.16. Ca_v3.1 expression influences basal [Ca²⁺]_i in HEK293 cells

Example Ca²⁺ microfluorimetry traces illustrating Δ[Ca²⁺]_i (ratio of absorbance), upon removal of extracellular Ca²⁺ (CF, purple line, replaced with 1 mM EGTA) for **A**, HEK293/Ca_v3.1 cells and **B**, wt HEK293 cells. Also shown are the effects of NNC55-0396 (NNC, 3 μM, blue line) before and during CF application for **C**, HEK293/Ca_v3.1 cells and **D**, wt HEK293 cells. **E**, Bar chart showing the (mean ± s.e.m) Δ[Ca²⁺]_i in response to CF exposure in control conditions for wt HEK293 cells (blue bars, n=6) and HEK293/Ca_v3.1 cells (red bars, n=11), and also in the presence of NNC55-0396 (3 μM, CF+NNC) for wt HEK293 cells (n=6) and HEK293/Ca_v3.1 cells (red bars, n=7). All scale bars 0.1 ru (vertical), 120 seconds (horizontal). Data were analysed via one-way ANOVA followed by Tukey's multiple comparison test, ***P<0.001.

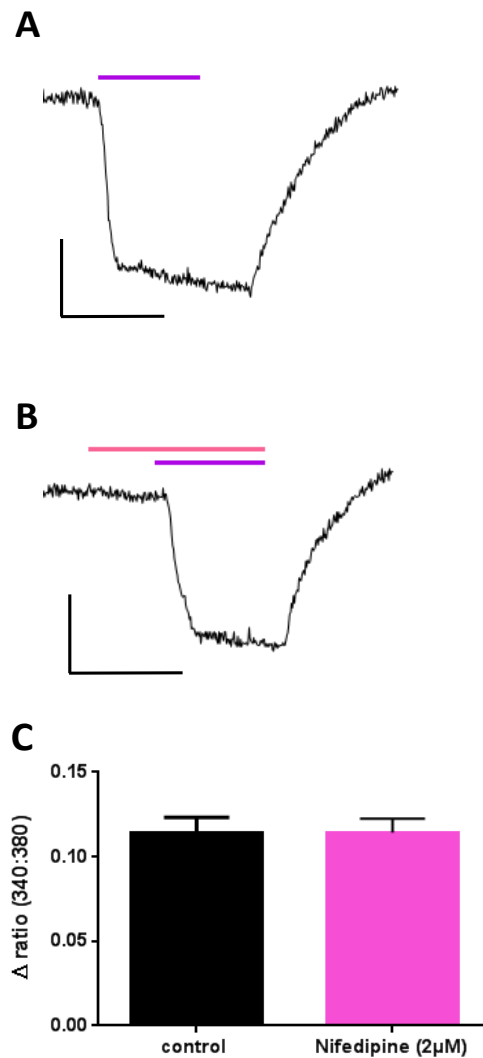


Figure 3.17. Nifedipine has no effect on the Ca_V3.1-mediated window current

Example Ca²⁺ microfluorimetry traces showing Fura 2 ratio units (340:380) representing the $\Delta[\text{Ca}^{2+}]_i$ upon removal of extracellular Ca²⁺ (purple bar) under **A**, control conditions and **B**, after both pre-treatment and in continuous presence of nifedipine (nif, 2 μM). **C**, Bar graph showing the (mean ± s.e.m) decrease in ratio units (340:380) in response to removal of extracellular Ca²⁺ in control conditions (black bar, n=6) and during nif (2 μM) pre-treatment (pink bar, n=7). Scale bars 0.05 ru (vertical), 120 seconds (horizontal). Data analysed using unpaired Student's t-tests, **p≤0.01.

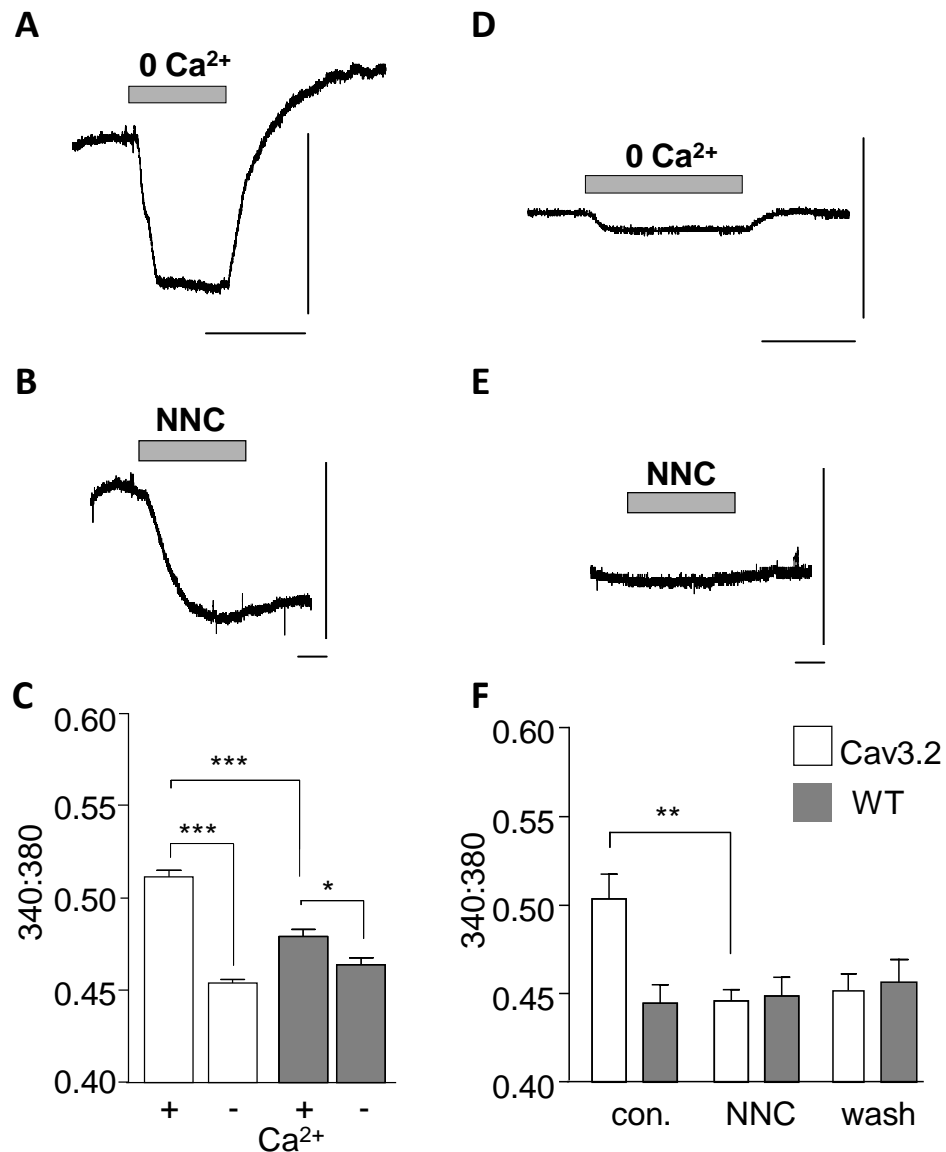


Figure 3.18. $Ca_v3.2$ expression influences basal $[Ca^{2+}]_i$ in HEK293 cells

Example Ca^{2+} microfluorimetry traces illustrating the $\Delta[Ca^{2+}]_i$ (ratio of absorbance), upon removal of extracellular Ca^{2+} (CF, grey bar, replaced with 1 mM EGTA) for; **A**, HEK293/ $Ca_v3.2$ cells and **D**, wt HEK293 cells. **C**, Bar graph illustrating (mean \pm s.e.m) basal $[Ca^{2+}]_i$ levels recorded in HEK293/ $Ca_v3.2$ cells (open bars, n=6) and wt HEK293 cells (shaded bars, n=6) in the presence and absence of extracellular Ca^{2+} as indicated. **B**, Example trace showing, effects of NNC55 0396 (NNC, 3 μ M, grey bar) on HEK293/ $Ca_v3.2$ cells and **E**, wt HEK293 cells. **F**, Bar graph illustrating (mean \pm s.e.m.) basal $[Ca^{2+}]_i$ levels recorded in HEK293/ $Ca_v3.2$ cells (open bars, n=8) and wt HEK293 cells (shaded bars, n=8) before (con), during (NNC) and after (wash) exposure to NNC as indicated. Data were analysed via paired or unpaired Student's t-tests as appropriate, * $P < 0.05$; ** $P < 0.01$, *** $P < 0.001$. All scale bars 0.1ru (vertical), 100ms (horizontal). Figure reproduced with permission from Duckles et al. (2013).

3.3. Discussion

3.3.1. A7r5 cells express functional T- and L-type Ca^{2+} channels

A7r5 cells used throughout the current project as an *in vitro* VSMC model were shown to express T-type Ca^{2+} channels and rtPCR revealed that $Ca_v3.1$ mRNA was the primary isoform expressed, but $Ca_v3.2$ mRNA was also detected. A number of previous studies using molecular biology techniques have demonstrated both $Ca_v3.1$ and $Ca_v3.2$ expression in rat, mouse and human VSMCs, throughout a range of vascular beds including rat renal, cerebral, mesenteric and cremaster arteries as reviewed recently by (Hansen, 2015). The “new” A7r5 cells cultured at lower confluence expressed considerably more $Ca_v3.1$ and $Ca_v3.2$ mRNA when compared to “old” A7r5 cells cultured at 90-100% confluence. This observation supports the findings of Richard *et al.* (1992) who used electrophysiological and pharmacological means to characterise the functional expression of low-voltage activated (LVA, i.e. T-type) channels and high-voltage activated (HVA, i.e. L-type) Ca^{2+} channels within primary cultures of rat thoracic aortic smooth muscle cells. An inhibitory effect of confluency on functional LVA channel activity was reported as LVA current expression declined dramatically, alongside a smaller decrease in HVA currents, when primary cultures were allowed to reach 100% confluence prior to passage (Richard *et al.*, 1992). Results presented here are consistent with these findings.

Immunofluorescence revealed differential staining patterns for both $Ca_v3.1$ and $Ca_v3.2$ channels in “new” A7r5 cells. Low levels of $Ca_v3.2$ immuno-reactivity (IR) was detected; localised within and around cell nuclei which were co-labelled by DAPI. Contrastingly, A7r5 cell nuclei were typically devoid of $Ca_v3.1$ -IR, with low levels of diffuse $Ca_v3.1$ -IR apparent within the cell body. Similar observations have been previously reported in cultured A7r5 cells, where diffuse cytoplasmic $Ca_v3.1$ -IR was described, alongside $Ca_v3.2$ -IR limited within some A7r5 nuclei (Brueggemann *et al.*, 2005). A similar study conducted with human pulmonary artery smooth muscle cells (HPASMCs) detected LVA currents alongside HVA currents using patch-clamp electrophysiology. Whilst both $Ca_v3.1$ and $Ca_v3.2$ mRNA was detected using rtPCR, immunohistochemistry indicated that only $Ca_v3.1$ channels were transcribed to give detectable protein levels within HPASMCs. The authors speculate that the lack of

Ca_v3.2 translation may be concerned with low expression levels, poor antibody sensitivity or post-transcriptional control of expression dependent on translational efficiency. They also discuss how temporal control as opposed to constitutive expression of Ca_v3.1 and Ca_v3.2 channels may be important for the control of proliferation (Rodman *et al.*, 2005).

Patch-clamp electrophysiology confirmed that A7r5 cells expressed functional T-type Ca²⁺ currents which, shown on some occasions to be inhibited by NNC (82%) and resistant to nifedipine. Upon development, NNC was shown in Ca_v3.1-expressing HEK293 cells to have an IC₅₀ of 7μM (Li *et al.*, 2005). In native cells such as bovine and rat embryo adrenal chromaffin cells however, the IC₅₀ of NNC on LVA T-type Ca²⁺ currents was shown experimentally to be much lower at approximately 2μM (Fernandez-Morales *et al.*, 2015). The average degree of inhibition currently observed with NNC applied at a single concentration of 3μM (82%) is therefore consistent with previous reports. This single concentration was examined as it is the NNC concentration used for proliferation assays. The contribution L-type Ca²⁺ currents to the global Ca²⁺ current evoked using the T-type SS protocol was also raised as a possibility. Future experiments requiring the isolation of T-type Ca²⁺ currents from A7r5 cells would be conducted in the continuous presence of nifedipine.

L-type Ca²⁺ currents were also recorded in A7r5 cells which were both inhibited by nifedipine (average of 75%) and of significantly larger amplitude when using Ba²⁺ as the charge carrier. In extracellular solutions containing physiological ionic concentrations, L-type Ca²⁺ channels are highly selective for Ca²⁺ over more abundant cations such as K⁺ and Na⁺ due to the presence of a selectivity filter composed of four glutamate amino acid residues, this being highly conserved amongst Ca_v channels (Yang *et al.*, 1993). A key feature of L-type Ca²⁺ channels however, is that when Ba²⁺ is substituted for Ca²⁺ they conduct Ba²⁺ much more easily (Almers & McCleskey, 1984). For example, it was demonstrated with recombinant Ca_v1.2-expressing HEK293 cells that currents were doubled in amplitude when recorded using Ba²⁺ as the charge carrier as compared to Ca²⁺ (Li *et al.*, 2010). Contrastingly, upon substitution of extracellular Ca²⁺ with Ba²⁺ T-type Ca²⁺ channels are generally equally permeable, yet in the presence of Mg²⁺ Ca_v3.1 currents have actually been shown to conduct Ca²⁺ preferentially (Serrano *et al.*, 2000). Evidence that the currents evoked using the SS

protocol using the relatively higher holding and test potentials were primarily mediated by L-type Ca^{2+} channels is therefore provided.

3.3.2. Potential expression of HVA T-type Ca^{2+} channel splice variants

As a point of interest, the potential contribution of other HVA Ca^{2+} channels was also raised as a possibility. The IC_{50} of nifedipine has previously been shown to be 55nM in $\text{Ca}_v1.2$ -expressing HEK293 cells (Scragg *et al.*, 2007), therefore it was surprising that complete inhibition of L-type currents using 2 μM nifedipine in the current investigation was not observed. In addition, NNC also caused partial inhibition of L-type Ca^{2+} currents, a finding which conflicts with the developers' original publication showing that NNC had no effect on HVA currents when applied at 100 μM to pancreatic INS-1 cells, which express P/Q, N and R-type in addition to L-type HVA channels (Li *et al.*, 2005). Furthermore, currents evoked at +20mV within IV protocols were of considerably larger amplitude than those produced using a SS protocol to the equivalent voltage, suggesting potential summation of currents facilitated by different Ca_v subtypes was occurring.

This possibility could be addressed by future experiments using protocols similar to those described in a study conducted by Harraz & Welsh, (2013). T- and L-type Ca^{2+} currents were effectively isolated in primary cultures of cerebral VSMCs. When using physiological Ca^{2+} concentrations, L- and T-type components were not clearly distinguishable as individual components on IV traces. However, when Ba^{2+} was substituted for Ca^{2+} a small rightward shift in the voltage for maximal activation was observed, likely due to the selective enhancement of L-type Ca^{2+} currents. The contribution of T-type Ca^{2+} channels to the whole-cell Ba^{2+} current was dissected by selectively inhibiting L-type currents using nifedipine (200nM). The nifedipine-insensitive components showed relatively more hyperpolarised I-V relationships, faster activation and inactivation kinetics and were abolished by NNC (1 μM). In agreement with current observations, application of NNC without prior nifedipine treatment significantly attenuated both T- and L-type mediated components. The off-target effects of NNC, emphasise the importance of applying L-type blockers prior to T-type Ca^{2+} channel inhibitors (Harraz & Welsh, 2013).

Interestingly, the activation and inactivation voltages of the isolated T-type Ca^{2+} currents were right-shifted when compared to the typical biophysical profiles of T-type Ca^{2+} channels. This was attributed to the use of Ba^{2+} as the charge carrier as replacing Ca^{2+} with Ba^{2+} also produced depolarising shifts in IV relationships when recording recombinant $\text{Ca}_v3.1$ or $\text{Ca}_v3.2$ mediated currents (Harraz & Welsh, 2013). In contrast with this explanation a growing amount of information is emerging that show tissue-specific splice variants of $\text{Ca}_v3.1$ and $\text{Ca}_v3.2$ are common within VSMCs, which arguably fit better, functionally, within the HVA category. This alternative splicing generally occurs in exons 25 and 26, within the III-IV linker region of the α_{1G} gene, producing shifts in activation and inactivation voltages to more depolarised potentials. Within the vasculature, expression of multiple T-type splice variants has been demonstrated thereby producing overlaps in T- and L-type Ca^{2+} channel activation voltages (Kuo *et al.*, 2011; Kuo *et al.*, 2014). Consequently, an interesting further investigation would be to explore whether $\text{Ca}_v3.1$ and $\text{Ca}_v3.2$ splice variants are expressed within A7r5 cells. It would also be useful to assess the extent of off-target NNC effects in recombinant HEK293 expressing a range of L-type Ca_v isoforms.

3.3.3. T-type Ca^{2+} channels regulate A7r5 proliferation.

Proliferation of all A7r5 cells used within the current project was partially inhibited by mibefradil and yet insensitive to nifedipine. A7r5 cells showing relatively higher $\text{Ca}_v3.1$ and $\text{Ca}_v3.2$ expression profiles proliferated faster than “old” A7r5 cells, and were inhibited by the newer more specific T-type Ca^{2+} channel inhibitors (NNC and ML218) to greater extents than mibefradil. These observations collectively demonstrate that A7r5 cell proliferation is regulated by T-type Ca^{2+} channels and also rule out the contribution of L-type Ca^{2+} channels. Many similar observations have been reported within the vasculature; for example, Rodman *et al.* (2005) reported that selective blockade of $\text{Ca}_v3.1$ using small interfering RNA (siRNA) completely inhibited human pulmonary artery smooth muscle cell (HPASMC) proliferation and prevented entry into the cell cycle in response to stimulation with 5% serum. In addition, mibefradil completely prevented entry into the cell cycle whilst the L-type specific inhibitor

diltiazem was without effect when applied at 3 times the IC₅₀ concentration (Rodman *et al.*, 2005).

One of the pivotal studies implicating T-type Ca²⁺ channels in the control of VSMC proliferation was conducted by Kuga *et al.* (1996) who demonstrated using both immunohistological and electrophysiological techniques that functional T-type expression was restricted to proliferative G₁ and S phases of the cell cycle in rat aortic VSMCs. In addition to *in vitro* studies, a number of *in vivo* studies have implicated a role for T-type Ca²⁺ channels in the control of VSMC proliferation as a feature of both development and pathological vascular remodelling. Neointima formation is a common undesirable aspect of vascular disease, and also a consequence of vascular intervention, involving increased VSMC proliferation and migration, resulting in restenosis. Tzeng *et al.* (2012), demonstrated that carotid artery wire injury induced neointima formation in WT mice but not, crucially, in Ca_v3.1^{-/-} knockout mice, which demonstrated no other vascular abnormalities. Immunohistological processing demonstrated that this neointima formation was due to VSMC proliferation. In WT mice, Cav3.1 mRNA was up-regulated in response to wire injury prior to neointima formation, suggesting that up-regulation of Cav3.1 was crucial for the development of this pathogenic phenotype (Tzeng *et al.*, 2012).

3.3.4. T- and L-type Ca²⁺ channels regulate basal and oscillatory Ca²⁺ levels within A7r5 cells

Oscillations in [Ca²⁺]_i are a widely discussed phenomenon reported in a variety of VSMC beds, and have been shown to be regulated by both voltage-dependent and voltage-independent mechanisms. Oscillations are thought to be observed as a result of signal integration of Ca²⁺ waves which, enabled by gap junctions, propagate through VSMCs over significant lengths of arteries without decrement. This activity has been shown to underlie spontaneous rhythmical contractions of blood vessels, a process collectively referred to as vasomotion, involving cyclical vasoconstriction and vasodilation, reviewed extensively by (Haddock & Hill, 2005)

Spontaneous oscillations in intracellular Ca^{2+} ($[\text{Ca}^{2+}]_i$) of varying frequencies were observed within some A7r5 populations. As these were abolished following the removal of external Ca^{2+} , they are thus shown to be dependent on Ca^{2+} entry through the cell membrane, most likely through Ca_v channels. Similarly, a proportion of A7r5 cells have been previously shown to exhibit spontaneous $[\text{Ca}^{2+}]_i$ oscillations, which were dependent on external Ca^{2+} and abolished by cobalt (Co^{2+}), applied for the purpose of blocking Ca_v channels (Otun *et al.*, 1992). A more recent study utilised confocal microscopy to demonstrate that spontaneous Ca^{2+} oscillations occurred in 79% of A7r5 cells within both cytoplasmic and nuclear compartments. Interestingly, the occurrence of spontaneous oscillations was correlated with greater amounts of sarcoplasmic reticulum. Whilst cytoplasmic and nuclear oscillations were of variable amplitudes they followed identical time-courses. Complete substitution of extracellular Ca^{2+} , or application of the CCBs diltiazem and nimodipine, not only rapidly abolished spontaneous cytoplasmic $[\text{Ca}^{2+}]_i$ oscillations but also gradually inhibited nuclear $[\text{Ca}^{2+}]_i$ oscillations over a 10min period, thereby showing that $[\text{Ca}^{2+}]_i$ oscillations were mediated by Ca_v channels (Fedoryak *et al.*, 2004). In the current investigation a similar but more reliable pattern of $[\text{Ca}^{2+}]_i$ oscillations was reproduced in “old” A7r5 cells through modest membrane depolarisation, achieved by slightly elevating external K^+ (20 vs. 5mM). As the response to K^+ was significantly and similarly inhibited by ML218, mibefradil and nifedipine, the induced $[\text{Ca}^{2+}]_i$ oscillations were dependent on both T- and L-type Ca^{2+} channels.

Arginine vasopressin (AVP) is a vasoconstrictor hormone important for vasomotion and has been shown *in vitro* to induce $[\text{Ca}^{2+}]_i$ oscillations in VSMCs (Brueggemann *et al.*, 2005; Otun *et al.*, 1992). Caution must be taken however as many of the studies used relatively high AVP concentrations which can induce changes in $[\text{Ca}^{2+}]_i$ through a variety of different mechanisms including, but not limited to, IP_3 production, membrane hyperpolarisation and activation of non-specific cation channels (Otun *et al.*, 1992). Application of physiologically relevant concentrations of AVP (picomolar range) however has been shown to induce reliable oscillations in A7r5 populations, which were inhibited by mibefradil in a concentration-dependent manner at concentrations the authors reported to have no effect on L-type Ca^{2+} currents. The contribution of endogenously expressed $\text{Ca}_v3.1$ channels on the oscillatory activity was

confirmed as Ca_v3.2 over-expression had no effect on basal or oscillatory patterns of [Ca²⁺]_i (Brueggemann *et al.*, 2005). A conclusive role for the involvement of Ca_v3.1 is provided by a study which expressed Ca_v3.1 channels within the neuronal NG108-15 cell line. This produced an increase in spontaneous Ca²⁺ oscillations corresponding with membrane potential oscillations (MPOs) and also an increase in basal [Ca²⁺]_i, shown to be mediated by a T-type Ca²⁺ window current (Chevalier *et al.*, 2008). The potential involvement of Ca²⁺ release from intracellular stores was also ruled out. Whilst any potential evidence for a role of [Ca²⁺]_i oscillations in proliferation is unclear, they provide an interesting phenotype involving both T- and L-type Ca²⁺ channels, which can be utilised for assessing the effects of novel signalling molecules on A7r5 Ca²⁺ handling under relatively physiological conditions.

A further key difference between the A7r5 cells expressing relatively higher T-type Ca²⁺ channels levels compared to the “old” A7r5 cells, in addition to the spontaneous nature of [Ca²⁺]_i oscillations, was that basal Ca²⁺ influx was apparent under resting conditions. Basal Ca²⁺ influx was detected by a fall in baseline [Ca²⁺]_i upon substitution of extracellular Ca²⁺ with EGTA, suggesting the presence of a window current within some A7r5 populations. As the fall in response to Ca²⁺ removal was partially inhibited by both NNC and nifedipine it is suggested that the A7r5 window current is facilitated by both T- and L-type Ca²⁺ channels. Due to a characteristic overlap in activation and steady-state inactivation voltages, T-type Ca²⁺ channels can open without fully inactivating. This commonly facilitates basal Ca²⁺ influx at resting V_m, referred to as window current, and reviewed elsewhere e.g. (Perez-Reyes, 2006). The intimate link between T-type Ca²⁺ channel-mediated window currents regulating [Ca²⁺]_i and the resulting control of proliferation is well summarised (Capiod, 2011). This review additionally considers the potential contributions of store-operated Ca²⁺ entry to cell cycle regulation. Inhibition of the T-type Ca²⁺ channel-mediated window current can therefore be directly linked to the anti-proliferative effects of T-type Ca²⁺ channel inhibition previously reported in a wide variety of cells including: A7r5 cells (Duckles *et al.*, 2015), HPASMCs (Rodman *et al.*, 2005), mesangial cells of the kidney (Cove-Smith *et al.*, 2013) and a range of different cancers including leukaemia and glioblastoma (Huang *et al.*, 2015; Zhang *et al.*, 2012), further discussed in section 3.3.3.

Current findings also revealed that L-type Ca^{2+} channels also partially facilitated the basal Ca^{2+} influx observed in A7r5 cells. Potential non-specific effects of nifedipine on T-type Ca^{2+} channels were considered unlikely as basal Ca^{2+} influx within recombinant HEK293/ $\text{Ca}_v3.1$ cells was unaltered by this agent. Previous studies have described L-type Ca^{2+} channel-mediated window currents at the single channel level within canine cardiac Purkinje cells (Shorofsky & January, 1992), and also using $[\text{Ca}^{2+}]_i$ imaging within equine tracheal myocytes (Fleischmann *et al.*, 1994). A more recent study conducted in mouse VSMCs demonstrated that in addition to their role in voltage-dependent contraction, L-type Ca^{2+} channels also mediate the window current which controls basal $[\text{Ca}^{2+}]_i$ and correspondingly basal contraction of VSMCs at physiological V_m (Fransen *et al.*, 2012). This was demonstrated through the simultaneous measurement of isometric tension and $[\text{Ca}^{2+}]_i$ in mouse aortic segments, which were correlated with V_m . To replicate voltage-clamp protocols, V_m was manipulated via modification of extracellular $[\text{K}^+]$ to achieve depolarisation and repolarisation within physiological V_m ranges (-77 to -51mV) (Fransen *et al.*, 2012).

As discussed in relation to T-type Ca^{2+} channels, a rapidly expanding body of work is currently emerging that shows not only tissue, but also cell and developmental stage specific Ca_v splice variants are common, which can impart atypical voltage-dependencies. A relevant example of this is provided by a study which demonstrated that expression of a $\text{Ca}_v1.2$ splice-variant previously isolated from VSMCs in HEK293 cells produced currents with more hyperpolarised activation profiles and with larger window currents at resting V_m , when compared to the standard full-length clone (Liao *et al.*, 2007). Consistent with current observations demonstrating that nifedipine has no effect on A7r5 cell proliferation, the potential physiological relevance of L-type Ca^{2+} channel-mediated window currents within VSMCs is therefore likely concerned with contractile activity and not proliferation. A potential explanation as to how T-type Ca^{2+} channel-mediated window current selectively influences proliferation could be that different Ca_v isoforms may have restricted subcellular distributions. This suggestion is further discussed in section 3.3.5.

3.3.5. Recombinant expression of $Ca_v3.1$ and $Ca_v3.2$ increases cellular proliferation and window current.

In direct support of observations made in A7r5 cells, expression of either recombinant $Ca_v3.1$ or $Ca_v3.2$ channels significantly increased basal Ca^{2+} influx and proliferation which could be partially inhibited by NNC. Further evidence is therefore provided that T-type Ca^{2+} channels regulate $[Ca^{2+}]_i$ and subsequently proliferation. The finding that both $Ca_v3.1$ and $Ca_v3.2$ channel expression can increase cellular proliferation is significant as many conflicting findings regarding isoform specificity have been previously reported. Due to the current lack of isoform specific $Ca_v3.1$ or $Ca_v3.2$ pharmacological inhibitors the majority of studies regarding isoform specificity have been conducted using knockout mice. Tzeng *et al.* (2012) demonstrated that $Ca_v3.1^{-/-}$ knockout mice showed reduced VSMC proliferation and were resistant to neointima formation following carotid wire injury whereas $Ca_v3.2^{-/-}$ knockout mice showed a similar degree of neointima formation compared to wt mice. Contrastingly, Chiang *et al.* (2009) demonstrated that $Ca_v3.2^{-/-}$ knockout mice were resistant to both pressure overload-induced or angiotensin II-induced cardiac hypertrophy/remodelling (Chiang *et al.*, 2009).

A further interesting observation was that HEK293/ $Ca_v3.2$ /clone P cells, transfected in-house with the $Ca_v3.2$ -containing mammalian expression vector, proliferated at a rate directly comparable to wt HEK293 cells and showed no inhibition by NNC. The similar growth profiles and lack of response to NNC suggests that the presence of $Ca_v3.2$ channels *per se* is not sufficient to drive proliferation. Similarly, Chemin *et al.* (2000) demonstrated that whilst expression of $Ca_v3.1$ or $Ca_v3.2$ in HEK293 cells increased $[Ca^{2+}]_i$, it had no effect on proliferation. A potential explanation for this can be provided by current observations that $Ca_v3.2$ -IR was highly diffuse throughout HEK293/ $Ca_v3.2$ /clone P cells whereas, contrastingly, dense perinuclear clusters and punctate membranous $Ca_v3.2$ -IR was additionally prominent within the highly proliferative HEK293/ $Ca_v3.2$ cells. Resultantly, evidence is provided that aggregation or clustering of T-type Ca^{2+} channels within specific sub-cellular domains may be crucial for increased basal Ca^{2+}_i to drive elevated cellular proliferation. As the development of highly specific $Ca_v3.1$ and $Ca_v3.2$ antibodies is only very recently improving there are very few previous studies assessing the subcellular localisation of these channels in

VSMCs. One of the few papers that exist however has shown that $\text{Ca}_v3.2 \text{ Ca}^{2+}$ channels co-localise within caveolin3 microdomains in ventricular myocytes. It was also demonstrated that when $\text{Ca}_v3.2$ and caveolin3 are co-expressed in HEK293 cells peak $\text{Ca}_v3.2$ density is decreased, indicative of important functional interplay within compartmentalisation of Ca^{2+} signalling (Markandeya *et al.*, 2011). Further investigations using antibodies against various sub-cellular markers' such as caveolin3 and mitochondrial proteins would be very useful to assess potential co-localisation with $\text{Ca}_v3.1$ and $\text{Ca}_v3.2$ channels in more detail. It would also be interesting to assess the subcellular localisation of different T- and L-type isoforms with A7r5 cells.

3.3.6. Summary and conclusions

Collectively, findings within this chapter demonstrate that T-type Ca^{2+} channels control basal Ca^{2+} levels and modulate cellular proliferation. These data additionally characterise cell lines and validate techniques subsequently used to assess thioredoxin as a novel regulator of T-type Ca^{2+} channels and VSMC proliferation.

Chapter 4 -The role of thioredoxin (Trx) in cellular proliferation and $[Ca^{2+}]_i$ handling

4.1. Introduction

The thioredoxin (Trx) system is ubiquitously expressed within all mammalian cells and plays a key role in the maintenance of cellular redox balance. The Trx system is composed of Trx, thioredoxin reductase (TrxR), NADPH, and vitamin D₃ up-regulated protein (VDUP). TrxR reduces Trx to its active form, using electrons donated from NADPH, whilst VDUP serves as the endogenous negative regulator. Trx has a range of biological activities, including antioxidant, growth promotion, inflammatory response modulation and anti-apoptosis. These functions generally require the reducing capabilities of Trx, dictated by two cysteine (Cys) residues at positions 32 and 35 within the active site (Cys³² and Cys³⁵). Trx has been shown to utilise both intracellular and extracellular signalling pathways as nuclear translocation and extracellular secretion upon activation have been demonstrated, as reviewed (Burke-Gaffney *et al.*, 2005).

Trx upregulation has been demonstrated in a variety of conditions including cancer and cardiovascular disease. For example, elevated serum Trx levels have been detected in patients with acute myocardial infarction (AMI), abdominal aortic aneurysm as detected within the aortic lumen and circulation (Martinez-Pinna *et al.*, 2010), atherosclerosis (Okuda *et al.*, 2001) and is positively correlated with platelet hyper-aggregability (Miyamoto *et al.*, 2003). Whilst elevations in Trx may initially serve to counterbalance increased oxidative stress, Trx over-expression within cancer patients is associated with aggressive tumour growth, increased proliferation, decreased apoptosis, and reduced patient survival (Raffel *et al.*, 2003).

In order to assess the effects of Trx on cellular proliferation and Ca²⁺ handling, two pharmacological Trx inhibitors, PX-12 (1-methylpropyl 2-imidazolyl disulfide) and auranofin (AuF, triethylphosphinegold(I)tetraacetylthioglucose), were employed. PX-12 is a direct Trx inhibitor currently undergoing clinical trials for the treatment of a variety of cancers, including gastrointestinal and pancreatic cancer (Baker *et al.*, 2013; Ramanathan *et al.*, 2007; Ramanathan *et al.*, 2011). PX-12 has been shown to directly inhibit Trx through thioalkylation of redox-sensitive Cys residues. Thioalkylation of

Cys³² and Cys³⁵ residues found within the redox-active site of Trx has been shown to occur in a reversible manner with a K_i of 31 μ M. Contrastingly, thioalkylation of the Cys⁷³ residue found outside the active site occurs at PX-12 concentrations several orders of magnitude lower, and in an irreversible manner (Kirkpatrick *et al.*, 1998). Whilst the reducing capabilities and corresponding cellular functions of Trx generally concern Cys³² and Cys³⁵ within the active site (Oblong *et al.*, 1994); other studies have demonstrated that Cys⁷³ is also important for the growth promoting effects of Trx (Gasdaska *et al.*, 1996).

AuF is a gold-containing compound originally developed as an oral treatment for rheumatoid arthritis (RA) (Finkelstein *et al.*, 1976). Due to its potent anti-inflammatory effects, AuF has been used as an effective RA treatment for over 30 years, although the mechanism of action *in vivo* is not yet fully established (Kean *et al.*, 1997; Madeira *et al.*, 2012). Whilst intramuscular injection of gold compounds such as aurothiomalate and aurothioglucose have generally replaced AuF in the treatment of RA (Kean *et al.*, 1997), AuF has also been shown to inhibit TrxR. Consequently, AuF is currently being explored as a re-profiled anti-cancer agent (Roder & Thomson, 2015; Tonissen & Di, 2009). TrxR is a pyridine nucleotide-disulfide oxidoreductase which uses electrons donated from NADPH to reduce Trx. Whilst TrxR is closely related to glutathione reductase (GR), it additionally contains a rarely found selenocysteine (Sec) sequence (Cys-Sec). Unfortunately, the presence of this Sec sequence has complicated the successful recombinant expression of mammalian TrxR. Isolation of TrxR from placenta is therefore generally required for experimental studies. In the presence of NADPH and Trx, AuF has been shown to inhibit TrxR isolated from human placenta with a K_i of 4nM. Contrastingly, the effects of AuF on GR were shown to be at least three orders of magnitude lower. Interestingly, the effects of AuF on TrxR were attributed to the gold moiety within the AuF molecule as gold-free thioglucose was without any effect (Gromer *et al.*, 1998).

4.2. Results

4.2.1. Trx measurement within A7r5 and recombinant HEK293 cells

To quantify endogenous Trx activity within cell lines, a fluorescence-based assay utilising the reducing capabilities of Trx was conducted. The fluorescence signal of the eosin-labelled (EL) insulin substrate at 545nm (after excitation at 520nm) increases upon reduction by Trx. The rate of increasing fluorescence (Δf) is therefore proportional to Trx activity (Montano *et al.*, 2014). It is crucial to note that as TrxR) and NADPH are applied in excess, it can be assumed that all Trx is in its reduced form (rTrx). As such, Trx activity reports cellular Trx levels. Following subtraction of background fluorescence values, the Δf of cell samples was compared against known Trx standards, as detailed in Figure 4.1. Initial attempts to calibrate the assay using Trx standards (0-24ng) were unsuccessful as the resultant Δf values were similar for each concentration used (data not shown). As the assay was shown upon development to be effective with Trx (7nm-900nM) (Montano *et al.*, 2014), the concentration of Trx standards was increased (0-192ng). As shown in Figure 4.1, this produced different rates of Δf for each Trx standard which enabled effective assay calibration.

Endogenous Trx activity was reliably detected within A7r5, wt HEK293, HEK293/Ca_v3.1 and HEK293/Ca_v3.2 cells (~60-215ng per 15 μ g total protein). Trx levels within wt HEK293 cells appeared lower when compared to the other cell types; however, this difference was not statistically significant (Figure 4.2). Chronic pre-treatment (72hrs) with AuF (300nM) or PX-12 (1 μ M) was found to be without effect on A7r5, HEK293/Ca_v3.1 or HEK293/Ca_v3.2 cells Trx levels (Figure 4.3). Acute pre-treatment (10mins) with higher concentrations of PX-12 (3-300 μ M) did produce significant reductions in Trx levels for HEK293/Ca_v3.1 cells (3 μ M) and HEK293/Ca_v3.2 cells (30 μ M). Acute pre-treatment with PX-12 (300 μ M) produced a more uniform reduction in Trx activity, however this was commonly accompanied by a decrease in the background fluorescence values. As this produced an amplified final slope value, these data had to be omitted from the final analysis (Figure 4.4).

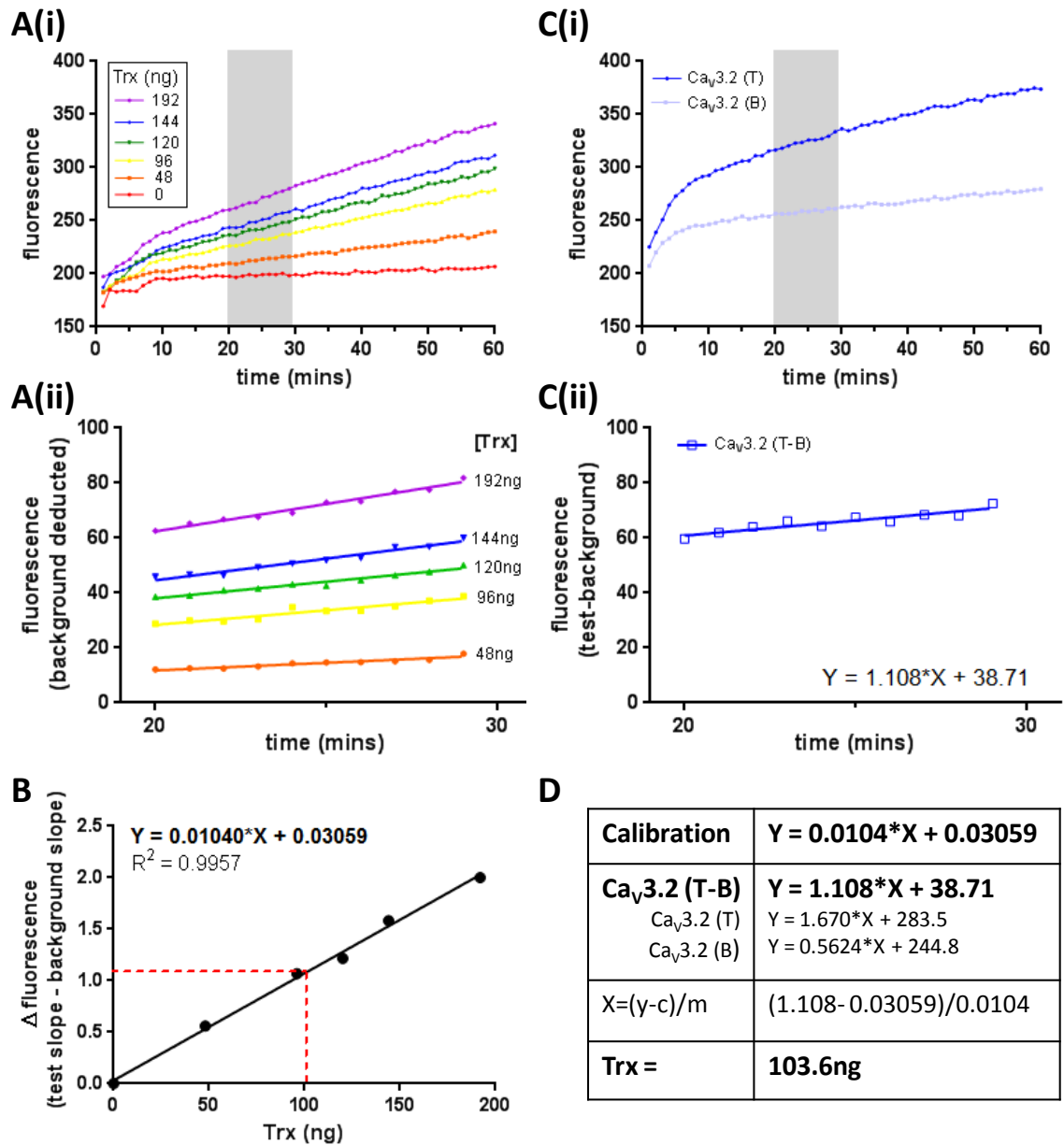


Figure 4.1. Quantification of unknown Trx concentrations using Trx activity assays
 Illustrative example of a single Trx assay: **A(i)**, mean fluorescence values of eosin-labelled (EL) insulin (545nm after 520nm excitation) with known Trx concentrations (0-192ng), monitored for 60mins at 1min intervals (triplicate wells). Grey box highlights 10min analysis region. **A(ii)**, magnified from A(i), but with background fluorescence values (i.e. 0ng Trx) deducted. Linear regression used to calculate line equations. **B**, Calibration-curve generated from slope values calculated in A(ii). Line equation and R^2 values from linear regression are included, red line estimates calculation in D. **C(i)**, As A(i), except with HEK293/Ca_v3.2 cell lysates (15 μ g), in test conditions (Ca_v3.2(T), all reagents) and background conditions (Ca_v3.2(B), TrxR omitted). **C(ii)**, As A(ii), except showing Ca_v3.2(T)-Ca_v3.2(B) fluorescence values. **D**, Equations and working calculations used to quantify Trx concentration from HEK293/Ca_v3.2 cell lysates. $Y = \Delta$ in fluorescence, $X = \text{Trx (ng)}$, $m = \text{slope/gradient}$ and $c = y$ axis intercept.

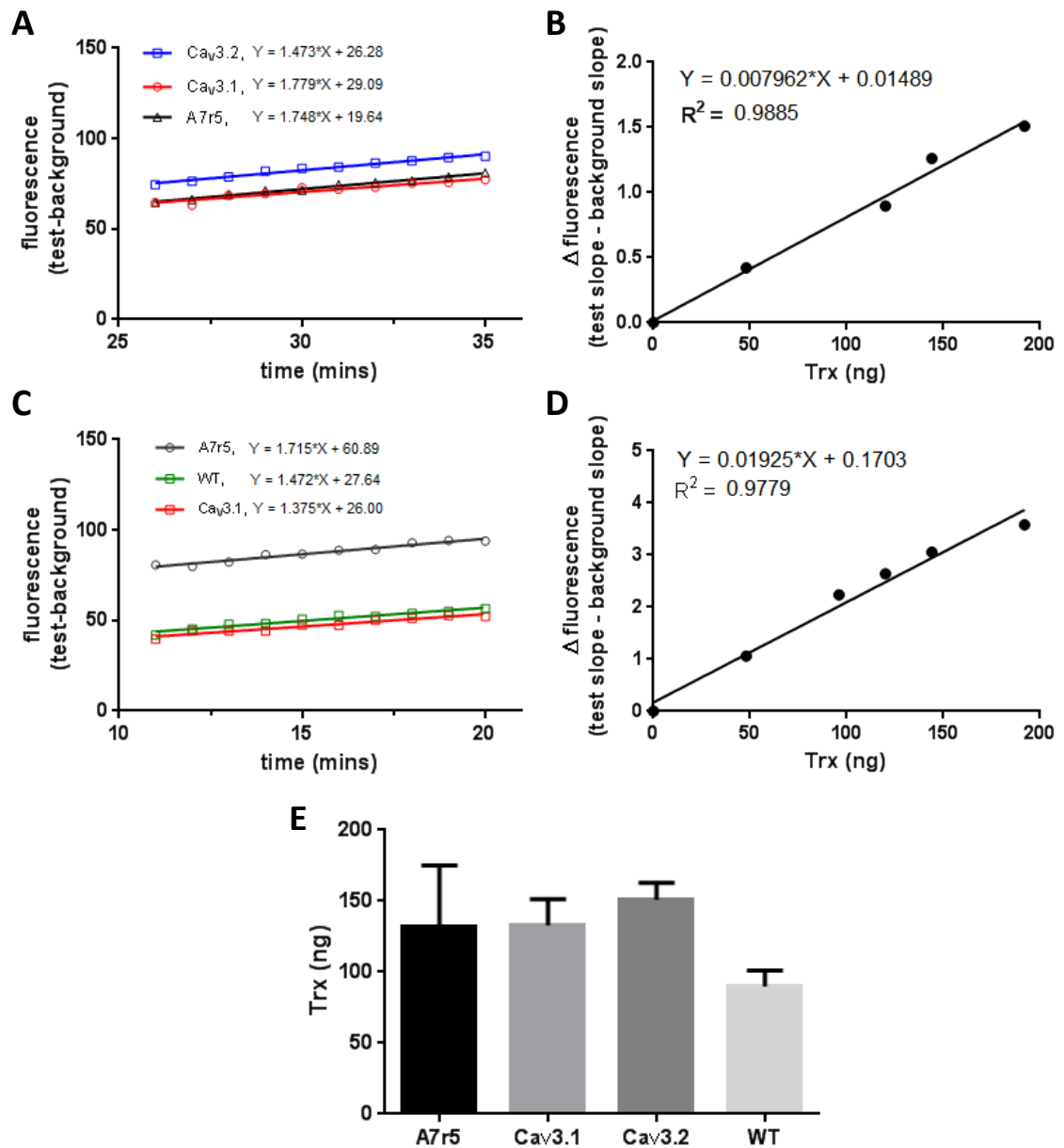


Figure 4.2. Quantification of endogenous Trx levels within cell lysates

Example traces from two Trx assays (further details provided in Figure 4.1) showing increasing mean fluorescence values and reporting endogenous Trx activity within: **A**, “new” A7r5, HEK293/Cav_v3.1 and HEK293/Cav_v3.2 cell lysates (15µg total protein, triplicate wells). **B**, Calibration-curve corresponding with (A), showing slope values of mean fluorescence of known Trx concentrations (0-192ng). Line equation and R² values are included. **C-D**, As (A-B) except, different assay with A7r5, wt HEK293 and HEK293/Cav_v3.1 cell lysates. **E**, Bar chart showing (mean ± s.e.m) endogenous Trx levels in A7r5, wt HEK293, HEK293/Cav_v3.1 and HEK293/Cav_v3.2 cell lysates (15µg total protein, all n=3 except HEK293/Cav_v3.1 (n=6)). Data were analysed via repeated measures one-way ANOVA with Dunnett’s post-hoc comparison test, with no statistically significant differences observed.

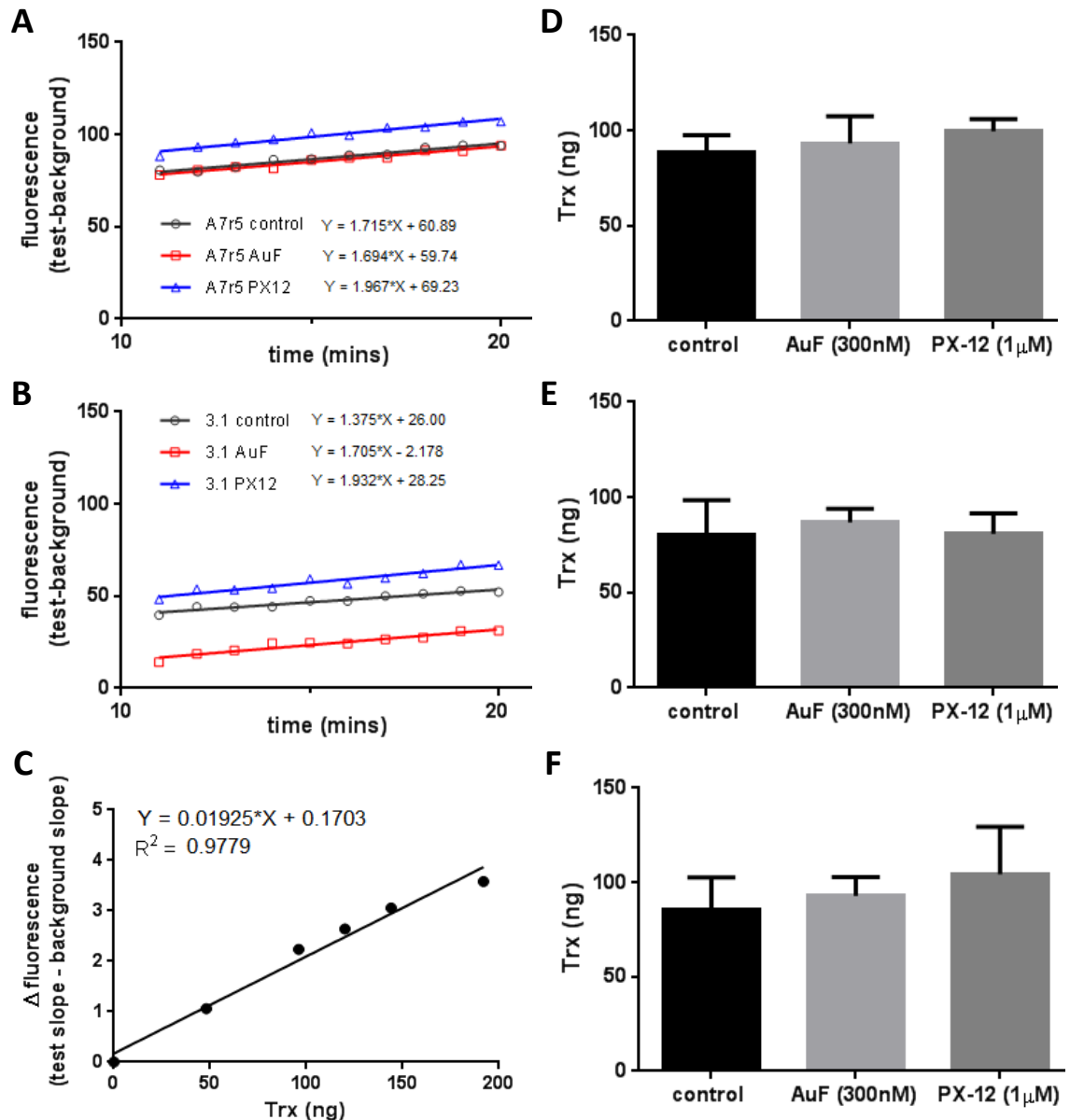


Figure 4.3. Trx assays do not detect any effect of chronic treatment with AuF (300nM) or PX-12 (1 μ M)

Example traces from a single Trx assay (details of method and analysis provided in Figure 4.1) showing increasing mean fluorescence values and reporting Trx activity under control conditions and after chronic pre-treatment (72hrs) with auranofin (AuF, 300nM) or PX-12 (1 μ M). Examples from: **A**, “new” A7r5 and **B**, HEK293/Ca_v3.1 cell lysates (15 μ g total protein, triplicate wells). Line equations are included. **C**, Calibration-curve corresponding with (A-B), showing slope values of mean fluorescence of known Trx concentrations (0-192ng). Line equation and R^2 values are included. **D-F**, Bar charts showing (mean \pm s.e.m) Trx levels under control conditions and after chronic pre-treatment (72hrs) with AuF (300nM) or PX-12 (1 μ M) within: **D**, A7r5, **E**, HEK293/Ca_v3.1 and **F**, wt HEK293 cell lysates (15 μ g total protein, all $n=2$). All data were analysed via repeated measures one-way ANOVA with Dunnett’s post-hoc comparison test, with no statistically significant differences observed.

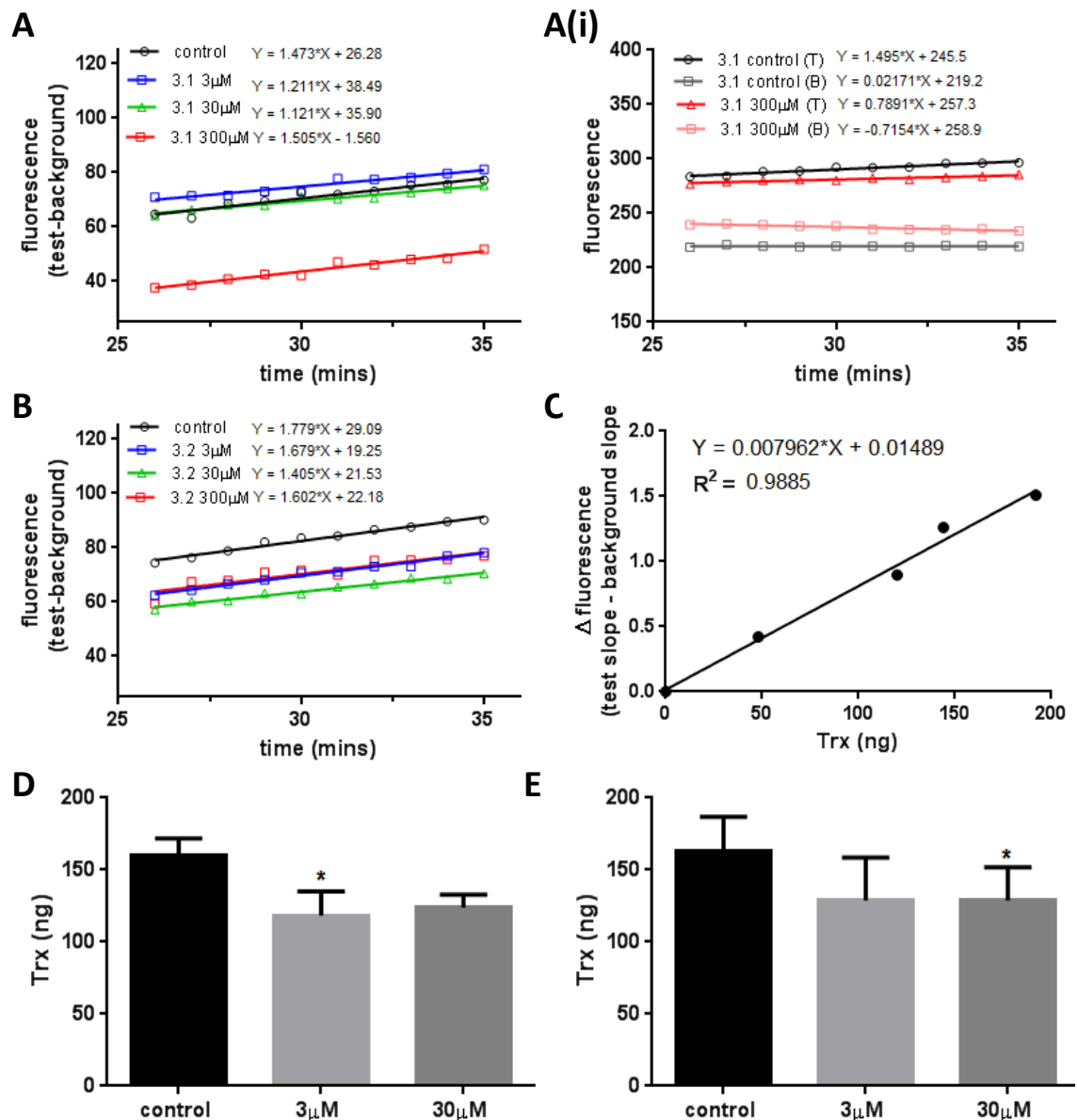


Figure 4.4. Trx levels are altered by acute treatment with PX-12

Example traces from single Trx assay (further details provided in Figure 4.1) showing increasing mean fluorescence values and reporting Trx activity under both control conditions and after acute pre-treatment (10mins) with PX-12 (3-300 μ M) within: **A**, HEK293/Ca_v3.1 and **B**, HEK293/Ca_v3.2 cell lysates (15 μ g total protein), triplicate wells. Line equations are included. **A(i)**, as A, except with individual test and background values for control and PX-12 (300 μ M) conditions. **C**, Calibration-curve corresponding with (A-B), showing slope values of known Trx concentrations (0-192ng). Line equation and R^2 values included. **D-E**, Bar charts showing (mean \pm s.e.m) Trx levels \pm PX-12 pre-treatment (10mins, 3 μ M and 30 μ M), within: **D**, HEK293/Ca_v3.1 and **E**, HEK293/Ca_v3.2 cells (both $n=3$). Note, as PX-12 (300 μ M) produced decreasing background fluorescence values, amplifying the deduced slope value shown in A(i), these data are omitted. Data analysed by repeated measures one-way ANOVA with Dunnett's post-hoc comparison test, * $p \leq 0.05$.

4.2.2. The effects of Trx inhibitors on A7r5 cell viability and proliferation

As Trx serves as an important cellular antioxidant, Trx inhibition may potentially disrupt the redox balance within cells. For example, AuF has been shown to induce apoptosis in Jurkat T-lymphoma cells (Cox *et al.*, 2008). It was therefore necessary to deduce what concentrations of PX-12 and AuF would be tolerated by A7r5 cells before using these drugs for proliferation assays. The MTT assay is a means of assessing cell viability. It is based on the principle that only active mitochondria are able to cleave MTT's tetrazolium ring and convert the pale yellow soluble substrate to the partially soluble, dark blue formazan product. The degree of colorimetric absorbance at 570nm is thus directly proportional to the number of living cells present (Mosmann, 1983).

Treatment with a single dose of AuF ($\leq 1\mu\text{M}$) or PX-12 ($\leq 1\mu\text{M}$) over a 72hr period had no significant effect on A7r5 cell viability. Significant reductions were observed with AuF ($3\mu\text{M}$) or PX-12 ($10\text{-}300\mu\text{M}$) when applied for 24-72hrs. PX-12 ($3\mu\text{M}$) was additionally shown to reduce A7r5 cell viability 48-72hrs post-treatment (Figure 4.5). Changes in A7r5 morphology that are suggestive of cell death such as rounding-up and cell detachment were observed alongside viability reductions. As these morphological changes were also apparent following a 72h exposure to $1\mu\text{M}$ AuF, it was subsequently determined that AuF (300nM) and PX-12 ($1\mu\text{M}$) were the highest concentrations to be applied for proliferation assays.

As the IC_{50} of TrxR inhibition by AuF has been shown experimentally to range between 20nM (Gromer *et al.*, 1998) and 200nM (Cox *et al.*, 2008), the effects of a variety of AuF concentrations within this range were examined on A7r5 cell growth. Concentration-response proliferation assays conducted on "old" A7r5 cells revealed that AuF (300nM , 72hrs) significantly decreased "old" A7r5 proliferation. AuF ($30\text{-}100\text{nM}$) appeared to have modest but non-significant anti-proliferative effects. As the number of dead cells present was consistent between control and drug treatment groups, it was confirmed that AuF ($10\text{-}300\text{nM}$, 72hrs) did not induce cell death (Figure 4.6). Daily cell counting of "old" A7r5 cells revealed that the anti-proliferative effects of AuF (300nM) positively correlated with the length of exposure.

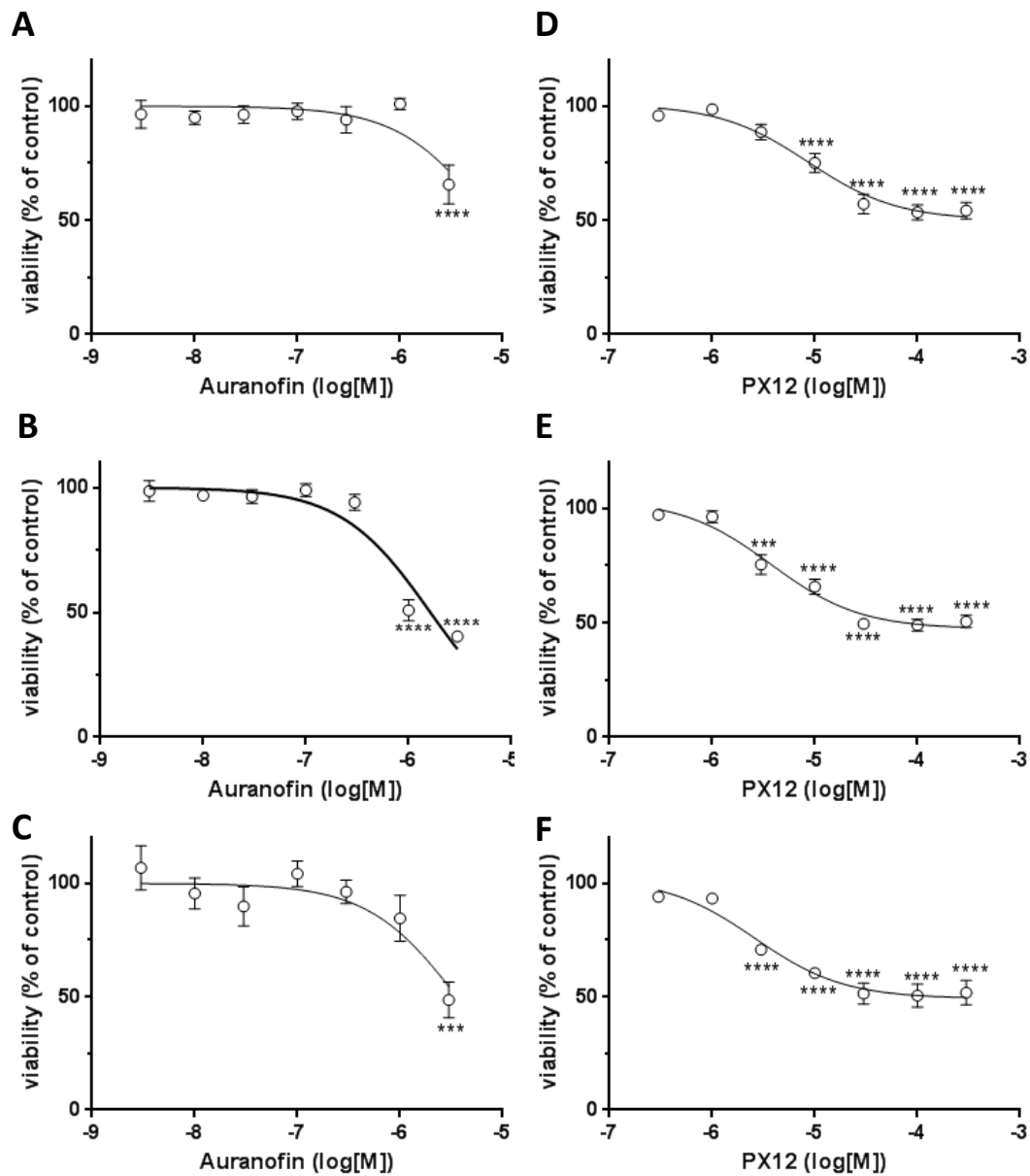


Figure 4.5. Auranofin (AuF $\leq 1\mu\text{M}$) and PX-12 ($\leq 1\mu\text{M}$) do not effect "old" A7r5 cell viability

Concentration-response graphs (mean \pm s.e.m) from MTT cell viability assays. Showing effects of AuF (1nM- $3\mu\text{M}$) on "old" A7r5 cell viability after: **A**, 24 hrs, **B**, 48 hrs and **C**, 72hrs. **D-F**, As (A-C), except with PX-12 (300nM- $300\mu\text{M}$). Data were analysed by one-way ANOVA with Dunnett's post-hoc comparison test, AuF compared to control condition, PX-12 compared to DMSO (1:1000) condition, all $n=3$, *** $p\leq 0.001$, **** $p\leq 0.0001$. Data were also fitted with log-inhibitor normalised-response curves.

The largest reduction in “old” A7r5 cell proliferation compared to control conditions was apparent on d3 (Figure 4.6). When these experiments were repeated on “new” A7r5 cells, shown to express considerably higher levels of Ca_v3.1 and Ca_v3.2 mRNA compared to the “old” A7r5 cells (further detailed in Chapter 3), a much larger anti-proliferative response to AuF was observed. The average number of “new” A7r5 cells was significantly lower in AuF (300nM) treatment groups when compared to control on d1, d2 and d3. The largest difference was apparent on d2, prior to a plateau growth phase (Figure 4.6). These data indicate that higher levels of T-type Ca²⁺ channel expression result in higher sensitivity to AuF. This also suggests that T-type Ca²⁺ channel modulation could potentially be mediating the anti-proliferative effects of AuF.

The effect of PX-12 on “new” A7r5 cell proliferation was also examined. The mechanism of Trx inhibition by PX-12 is complex as different cysteine residues within Trx are sensitive to considerably different PX-12 concentrations. Regarding its anti-proliferative effects, PX-12 has been previously shown to inhibit the growth of MCF-7 cells, with IC₅₀ values of 1.2μM or 3.2μM when using Trx or FBS as the mitogenic stimulus respectively (Kirkpatrick *et al.*, 1998). As PX-12 (≥3μM) was shown to induce significant reductions in A7r5 cell viability (Figure 4.5), a single PX-12 concentration was used in the proliferation assays. PX-12 (1μM) had small but significant anti-proliferative effects on “new” A7r5 cells, being most apparent on d2. When further experimental repeats comprising of d3 counts in isolation were conducted, PX-12 (1μM) was also found to significantly reduce average cell number on d3 (Figure 4.7).

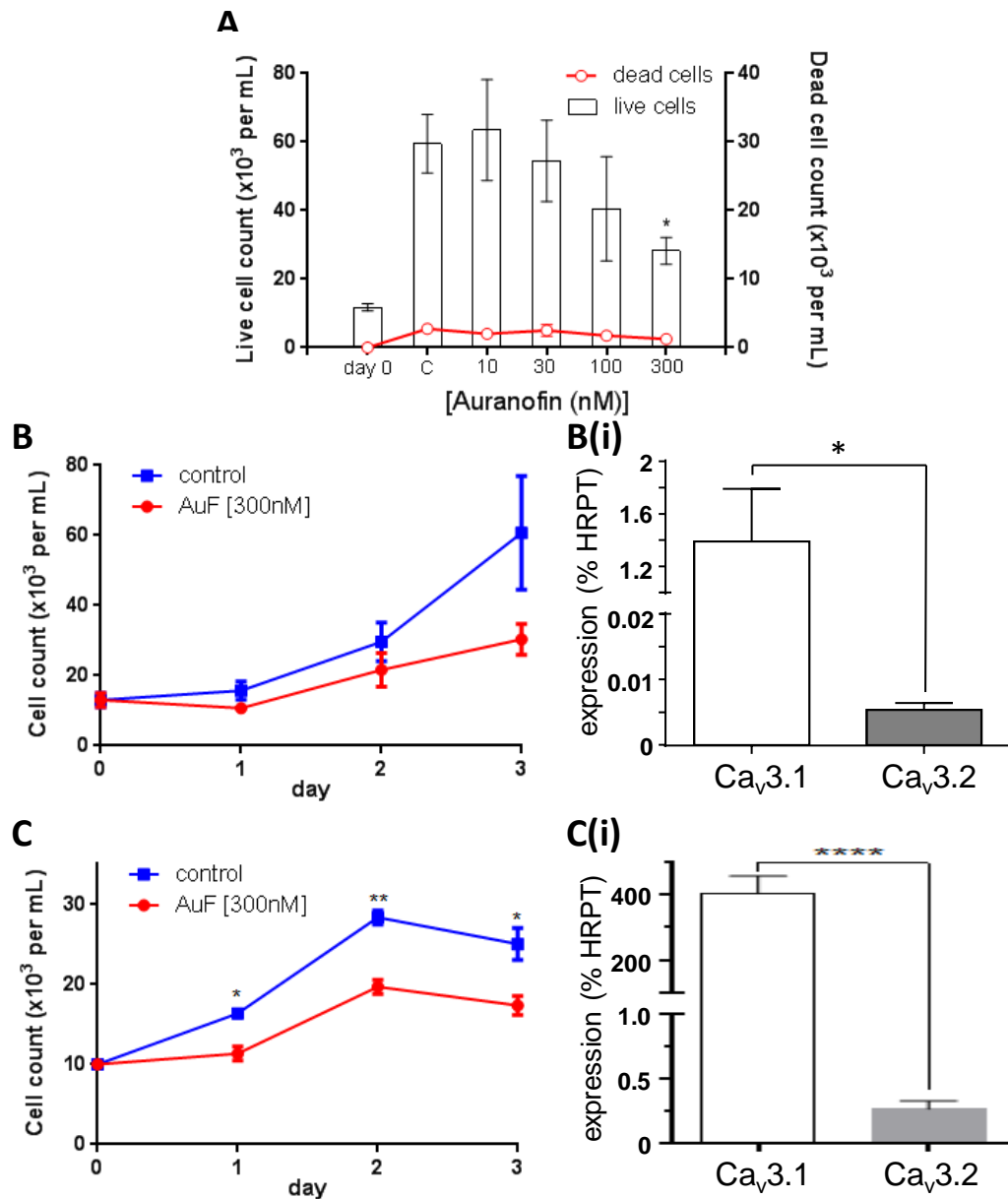


Figure 4.6. Auranofin (AuF) reduces A7r5 proliferation

Proliferation (plotted against the left-hand y-axis), was monitored on day 0 and day 3 \pm AuF (n=4). Red circles show the corresponding non-viable cell count (plotted against the right-hand y-axis). **A**, Bar graph showing the proliferative response (mean \pm s.e.m) of “old” A7r5 cells to AuF (10-300nM). **B**, Daily counts of “old” A7r5 cells illustrate that the anti-proliferative effects of AuF (300nM, red line) are most apparent on day 3 (n=3). **B(i)**, Bar graph showing Ca_v3.1 (upper y-axis) and Cav3.2 (lower y-axis) mRNA expression levels, determined in “old” A7r5 cells. Channel expression is plotted as (mean \pm s.e.m) % expression of the housekeeping gene, hypoxanthine phosphoribosyltransferase (HPRT1) (n=7) (Duckles *et al.*, 2015). **C**, As (B), except with “new” A7r5 cells showing higher sensitivity to AuF (n=3), and higher Ca_v3.1 and Ca_v3.1 expression in **C(i)**, n=8. All cell counts were made in triplicate with the mean value counting as n=1. Data were analysed by; (A,B,C), one-way ANOVA with Dunnett’s (A) or Bonferroni’s (B,C) post-hoc comparison tests, or (B(i)-C(i)), unpaired Student’s t-tests, * p \leq 0.05, ** p \leq 0.01, **** p \leq 0.0001.

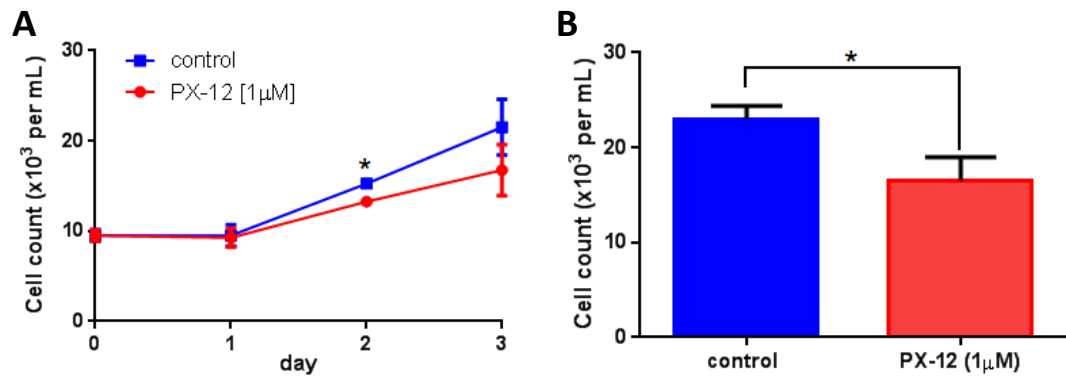


Figure 4.7. PX-12 reduces "new" A7r5 proliferation

A, Line graph showing (mean \pm s.e.m) daily cell counts of "new" A7r5 cells in both control conditions (blue line) and after PX-12 (1 μ M) treatment (red line), and thereby illustrating that the anti-proliferative effects of PX-12 are most apparent on day 2 (n=4). **B**, Bar graph (mean \pm s.e.m) showing proliferative response (mean \pm s.e.m) of "new" A7r5 cells to PX-12 (1 μ M) as counted on day 3 (n=8). All cell counts were made in triplicate with the mean value counting as n=1. Data were analysed using unpaired Student's t-tests, *p \leq 0.05.

4.2.3. The effects of AuF on A7r5 Ca^{2+} handling

As discussed in detail in Chapter 3, oscillations in intracellular Ca^{2+} levels [Ca^{2+}_i] could be stimulated by modest depolarisation of “old” A7r5 cells, achieved by application of a high [K^+] (20mM) perfusate. This project has previously demonstrated that Ca^{2+} oscillations are dependent on both T- and L-type Ca^{2+} channels (Chapter 3). In order to investigate potential effects of Trx inhibition on Ca^{2+} handling, “old” A7r5 cells were pre-treated with AuF (2 μ M, 25min). Unfortunately, PX-12 could not be used for Ca^{2+} microfluorimetry as it selectively enhanced the fluorescence signal at 340nm indicating direct interactions between Fura-2 and PX-12 (data not shown). For both control and AuF pre-treatment conditions, two high [K^+] stimuli were applied to each A7r5 population. Importantly, it was ensured that baseline [Ca^{2+}_i] was re-established prior to the 2nd high [K^+] stimulus. The effects of AuF (2 μ M, 25min) pre-treatment on the amplitude of the response were variable. When compared to control conditions, the amplitude of the response to the 1st depolarisation was significantly reduced in AuF conditions, within some experiments (Figure 4.9), although not in others (Figure 4.8). A more reproducible analysis parameter to quantify the qualitative effects of AuF was found to be the frequency of depolarisation-induced [Ca^{2+}_i] oscillations (i.e. firing frequency). To ensure that re-application of the depolarising stimulus did not produce a decline in the observed firing frequencies, matching control data was gathered for all experiments (Figure 4.8, Figure 4.9).

Pre-treatment of “old” A7r5 cells with AuF significantly reduced the frequency of [Ca^{2+}_i] oscillations, in response to the 1st and 2nd depolarisations when compared to control responses. The oscillation frequency in response to the 2nd depolarisation was significantly greater than for the 1st depolarisation in AuF conditions. The effects of AuF were therefore shown to be time-dependent (Figure 4.8). Dithiothreitol (DTT) is a commonly used reducing agent that was applied to some A7r5 populations, between the 1st and 2nd depolarisations. DTT treatment completely reversed AuF-mediated inhibition and normalised the firing frequencies in response to the 2nd depolarisation. DTT was additionally shown to significantly increase the frequency of Ca^{2+} oscillations under control conditions (Figure 4.9). As A7r5 Ca^{2+} oscillations were shown to be dependent of T- and L-type Ca^{2+} channels (Chapter 3), these data collectively indicate that AuF regulates Ca_v channels via a redox-dependent mechanism.

The effects of pre-treatment with AuF (2 μ M, 25min) on basal Ca²⁺ levels in “new” A7r5 cells were also examined. Previous investigation within the current project had shown a measurable window current in “new” A7r5 cells, detected as a fall in the baseline Ca²⁺ level upon removal of extracellular Ca²⁺ (CF) (Chapter 3). Pre-treatment with AuF significantly reduced the response to CF, revealing partial AuF-mediated window current inhibition (Figure 4.10). This window current has been shown to be partially facilitated by T-type Ca²⁺ channels (Chapter 3), and is believed to be crucial for cellular proliferation. Evidence that AuF may regulate basal Ca²⁺ levels and proliferation through modulation of Ca_v channels is therefore provided.

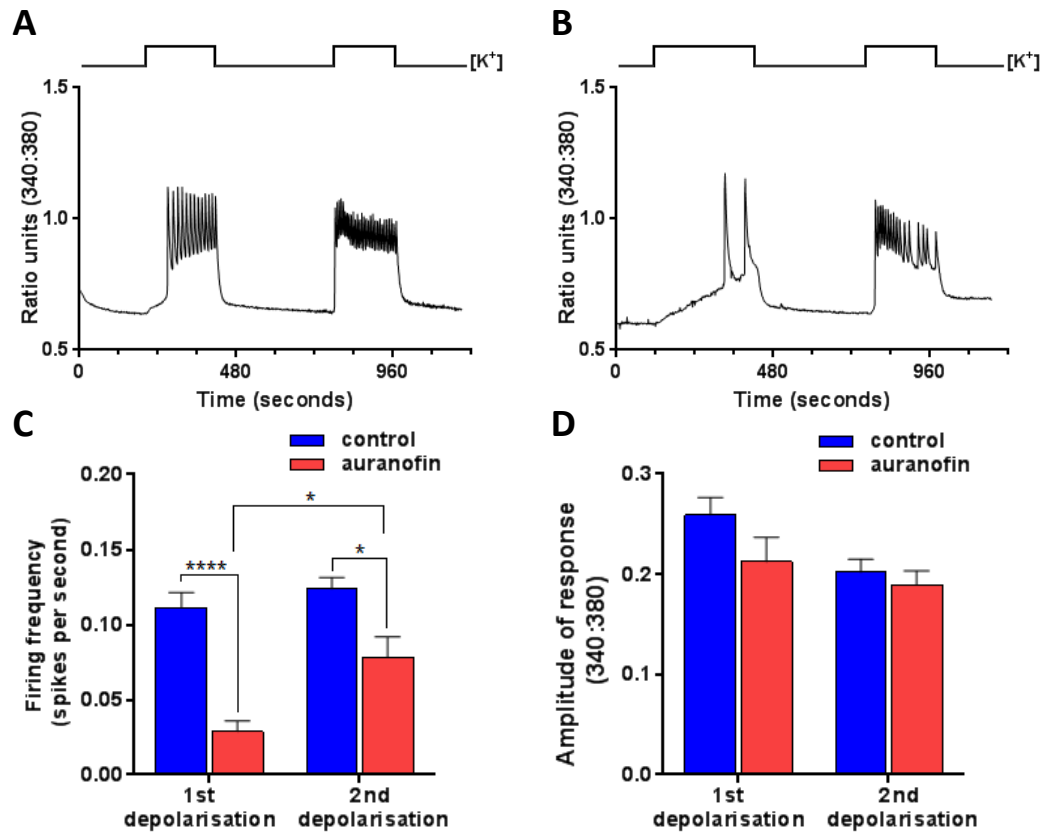


Figure 4.8. Auranofin (AuF) reduces depolarisation-induced Ca^{2+} oscillations in "old" A7r5 cells

Example Ca^{2+} microfluorimetry traces showing Fura 2 ratio units (340:380). Representing $\Delta[Ca^{2+}]_i$ in response to depolarisation, achieved by switching to a high $[K^+]$ perfusate (20mM vs. 5mM, black line above traces) under: **A**, control conditions and **B**, after auranofin pre-treatment (AuF, $2\mu M$ 25mins). **C**, Bar graph showing the (mean \pm s.e.m) firing frequency in response to the 1st and 2nd depolarisations in control (blue bars, n=19) or AuF pre-treated (red bars, n=13) conditions. **D**, As (C), except showing (mean \pm s.e.m) response amplitude. All data were analysed using one-way ANOVA with Tukey's post-hoc comparison test, (* $p \leq 0.05$, **** $p \leq 0.0001$).

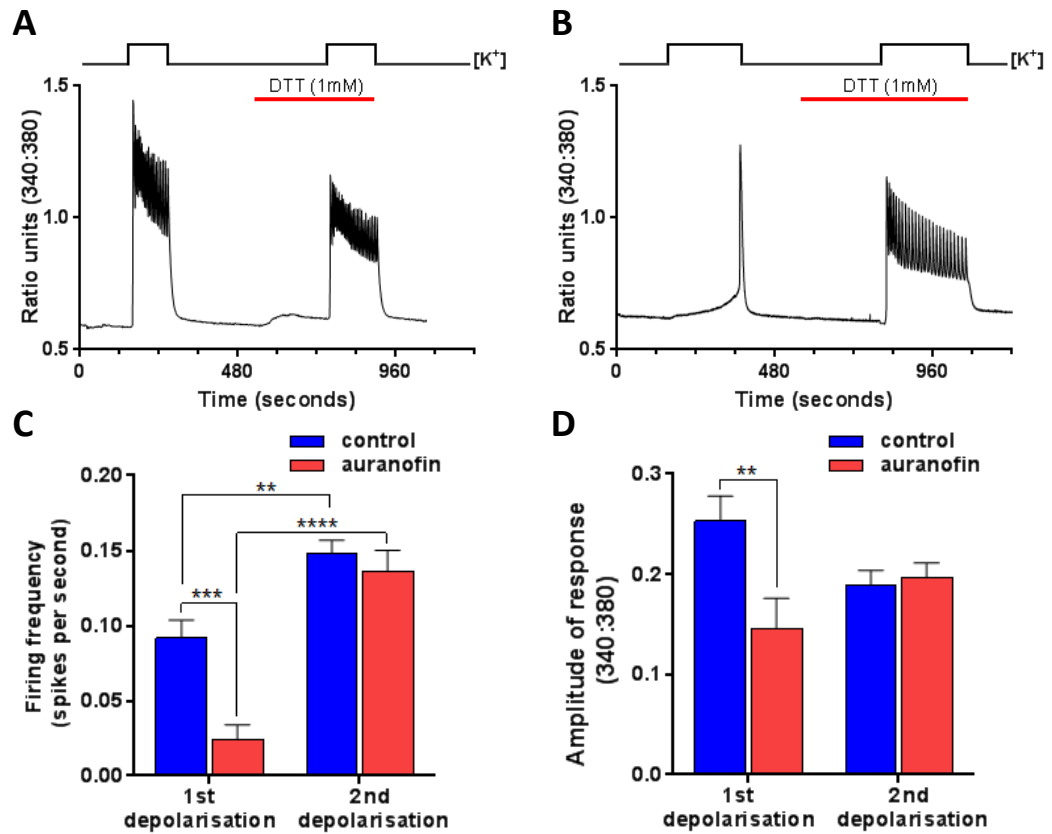


Figure 4.9. DTT reverses the effects of AuF on depolarisation-induced Ca^{2+} oscillations in "old" A7r5 cells

Example Ca^{2+} microfluorimetry traces showing the effects of dithiothreitol (DTT, 1mM, red bar) on Fura 2 ratio units (340:380). Representing $\Delta[\text{Ca}^{2+}]_i$ in response to depolarisation achieved by switching to a high $[\text{K}^+]$ perfusate (20mM vs. 5mM, black line above traces) under: **A**, control conditions and **B**, after auranofin pre-treatment (AuF, $2\mu\text{M}$, 25mins). **C**, Bar graph showing the (mean \pm s.e.m) firing frequency in response to the 1st and 2nd depolarisations (i.e. before and after DTT application), in control (blue bars, $n=24$) or AuF pre-treated (red bars, $n=18$) conditions. **D**, As C, except showing (mean \pm s.e.m) response amplitude. All data were analysed using one-way ANOVA with Tukey's post-hoc comparison test, ** $p \leq 0.01$, *** $p \leq 0.001$, **** $p \leq 0.0001$.

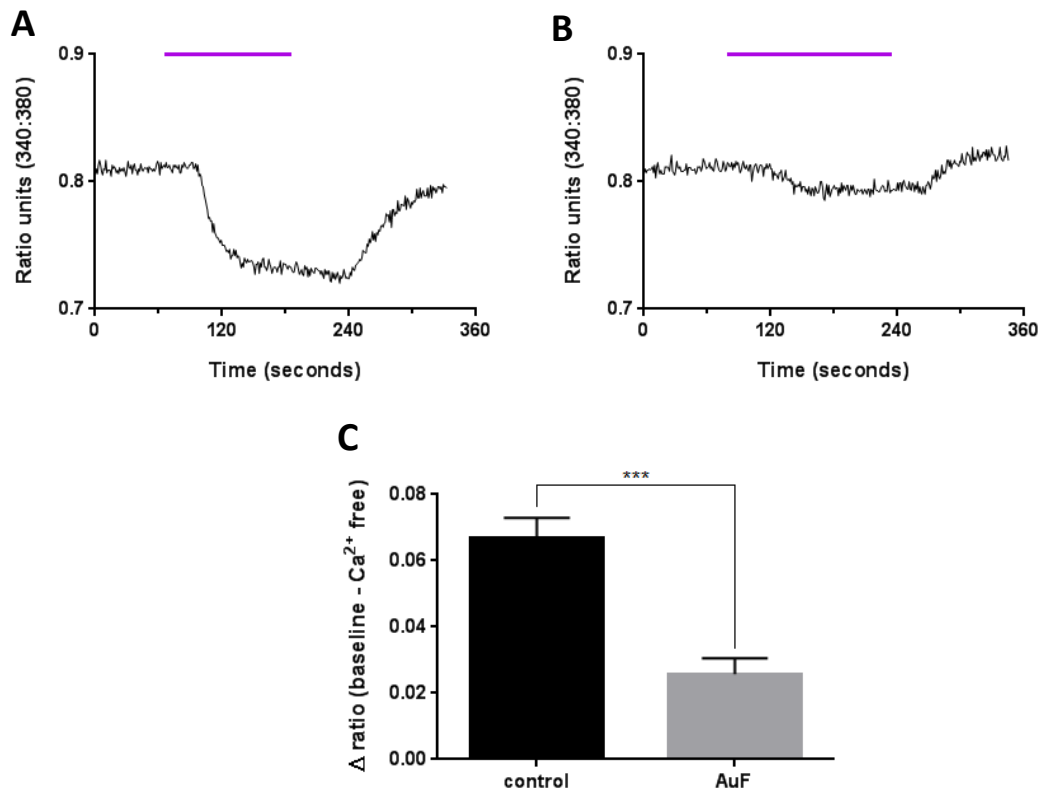


Figure 4.10. Auranofin inhibits the window current in “new” A7r5 cells

Example Ca^{2+} microfluorimetry traces showing Fura 2 ratio units (340:380) representing $\Delta[\text{Ca}^{2+}]_i$ upon removal of extracellular Ca^{2+} (CF, purple bar) under: **A**, control conditions and **B**, after pre-treatment with auranofin (AuF, $3\mu\text{M}$, 25mins). **C**, Bar graph showing (mean \pm s.e.m) the decrease in ratio units (340:380) in response to CF in: control conditions (black bar, $n=11$), and after AuF pre-treatment (grey bar, $3\mu\text{M}$, 25mins, $n=7$). Data were analysed using unpaired Student’s t-tests, *** $p \leq 0.001$.

4.2.4. Effects of Trx inhibitors on HEK293 cell viability and proliferation

Previous investigations revealed that Ca_v3.1 or Ca_v3.2 expression increased the Ca²⁺ window current and proliferation of HEK293 cells (Chapter 3). The effects of Trx inhibitors on wt HEK293, HEK293/Ca_v3.1 and HEK293/Ca_v3.2 cell proliferation were therefore next examined. These experiments enabled further investigation of the potential interactions between Trx and T-type Ca²⁺ channels and any isoform specific differences.

Firstly, MTT assays were conducted to determine the potential effects of both AuF and PX-12 on HEK293 cell viability. HEK293/Ca_v3.2 cells showed no significant reductions in cell viability after 72hrs of treatment with AuF ($\leq 300\text{nM}$) or PX-12 ($\leq 1\mu\text{M}$). At higher concentrations, AuF ($3\mu\text{M}$) and PX-12 ($10\text{-}300\mu\text{M}$) caused rapid and significant reductions in cell viability, as measured 24hrs post-treatment. Furthermore, 48-72 hrs post-treatment, AuF ($1\mu\text{M}$) and PX-12 ($3\mu\text{M}$) further reduced HEK293/Ca_v3.2 cell viability (Figure 4.11). All conditions exhibiting viability reductions were accompanied by morphological changes such as “rounding-up” and cell detachment indicating cell death. As these observations are in direct agreement with the findings from A7r5 cells (Figure 4.5), the cytotoxicity thresholds of AuF and PX-12 appears to be independent of cell type. Consequently, the optimal concentrations of AuF and PX-12, as determined for A7r5 cell proliferation assays, were also deemed appropriate for use in all HEK293 cell proliferation assays.

To assess the effects of Trx inhibition on the elevated proliferation of HEK293 cells resulting from Ca_v3.1 or Ca_v3.2 channel expression as described in Chapter 3, the effects of PX-12 and AuF were examined. For all experiments, HEK293/Ca_v3.1 and HEK293/Ca_v3.2 cells, shown on some occasions to be partially inhibited by NNC ($1\mu\text{M}$), proliferated more than wt HEK293 cells (Figure 4.13). Concentration-response proliferation assays revealed that both wt HEK293 and HEK293/Ca_v3.1 cell proliferation was unaffected by AuF ($10\text{-}300\text{nM}$), as shown in Figure 4.12. Similarly, PX-12 ($1\mu\text{M}$) was also without effect on either wt HEK293 or HEK293/Ca_v3.1 cell proliferation, when applied alone or in combination with NNC (Figure 4.13). Contrastingly, HEK293/Ca_v3.2 cell proliferation was significantly reduced by AuF (300nM) and PX-12 ($1\mu\text{M}$). The effects of PX-12 and NNC were shown to be non-

additive on HEK293/Ca_v3.2 cells, indicating that both drugs were acting via Ca_v3.2 inhibition. As the number of dead cells present was consistent between control and drug treatment groups, it was confirmed that the observed reduction in cell number was due to the anti-proliferative effects of AuF and PX-12, as opposed to increased cell death (Figure 4.12 and Figure 4.13). All drugs used for proliferation assays throughout the project were dissolved in double distilled water (ddH₂O) or DMSO. We examined the effects of DMSO at the highest concentration used (1:1000) and found that it had no effect on the proliferative rate of any of the HEK293 cell types used (Figure 4.13). Collectively, these data demonstrate that Trx regulates cellular proliferation through selective modulation of Ca_v3.2 channels.

In order to validate the observation that wt HEK293 and HEK293/Ca_v3.1 cell proliferation was insensitive to Trx inhibition, EdU assays were employed as an alternative to the direct cell counting proliferation assay. EdU (5-ethynyl-2'-deoxyuridine) is a nucleoside analog of thymidine which becomes incorporated into newly synthesised DNA. It is detected by a copper-catalyzed covalent reaction between an alkyne (EdU incorporated into DNA) and an azide (Alexa Fluor detection reagent). When DAPI is co-applied to label total cell nuclei, the percentage of proliferating cells (i.e. those labelled by EdU) can be calculated. As this assay had not been previously conducted within the group, optimisation of EdU incubation times, concentrations and analysis methods was required. Pulse-labelling i.e. incubation with EdU (10µM) for 1-4 hours, produced a small percentage of EdU positive HEK293/Ca_v3.1 cell nuclei. Contrastingly, incubation with EdU (10µM) for 16 or 24hrs resulted in EdU labelling in almost 100% of HEK293/Ca_v3.1 cell nuclei. Incubation with EdU (5µM, 12hrs) produced approximately 60-70% of EdU positive nuclei, enabling potential decreases or increases in proliferation to be observed. As pulse-labelling represented only a small percentage of cells which had proliferated within a narrow time-frame, results regarding potential anti-proliferative effects could be masked by alterations in the rate of cell cycle progression. It was subsequently decided that EdU (5µM, 12hrs) was the optimal condition and would be used for all future EdU experiments (**Error! Reference source not found.**).

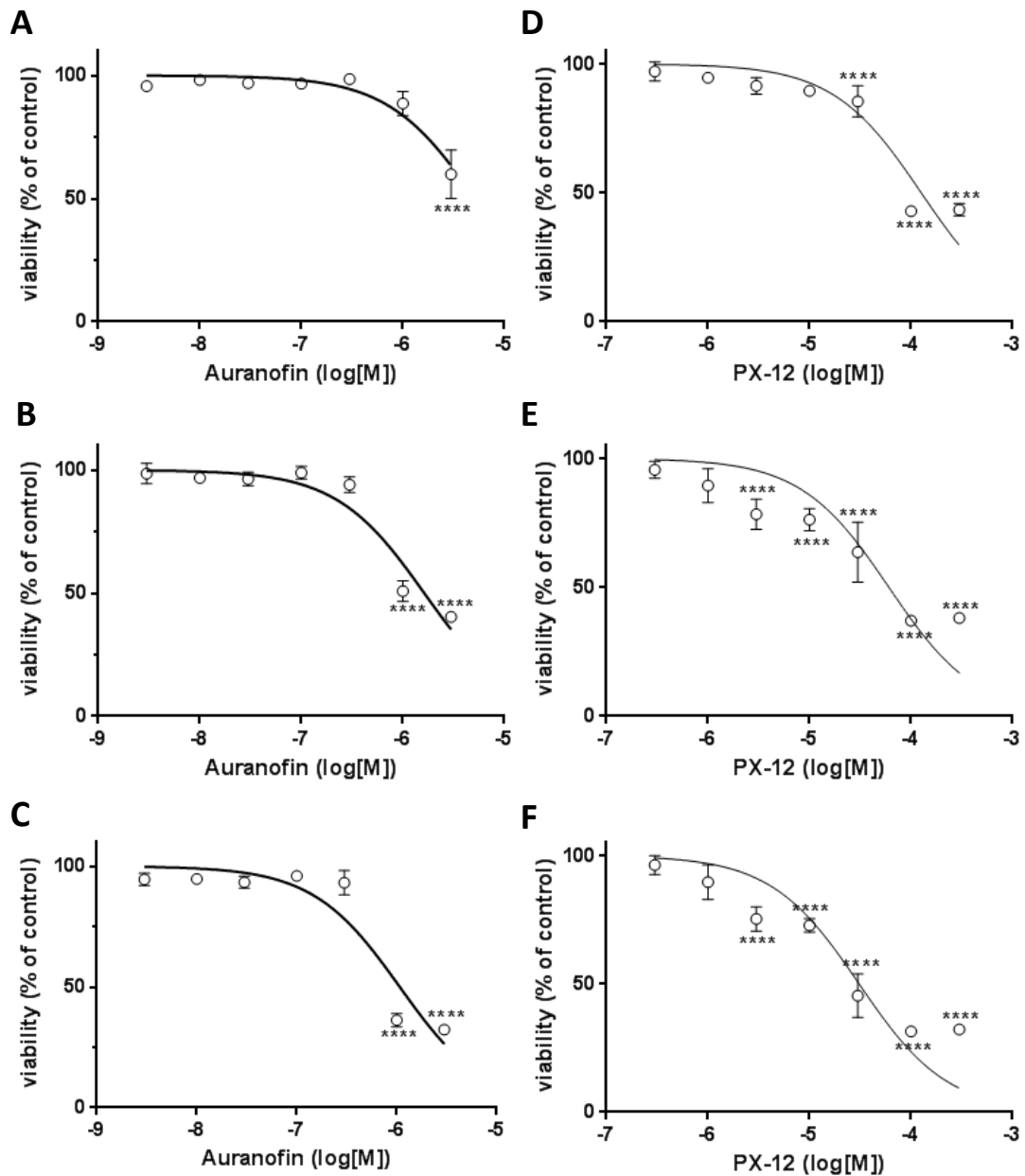


Figure 4.11. Auranofin (AuF $\leq 300\text{nM}$) and PX-12 ($\leq 1\mu\text{M}$) did not affect HEK293/ $\text{Ca}_v3.2$ cell viability

Concentration-response graphs (mean \pm s.e.m), from mitochondrial activity-based MTT cell viability assays, showing the effects of auranofin (AuF, 1nM - $3\mu\text{M}$) on HEK293/ $\text{Ca}_v3.2$ cell viability after: **A**, 24 hrs, **B**, 48 hrs and **C**, 72hrs treatment. **D-F**, As (A-C), except showing the effects of PX-12 (300nM - $300\mu\text{M}$). Data were analysed by one-way ANOVA with Dunnett's post-hoc comparison test, AuF compared to control, PX12 compared to DMSO, *** $p \leq 0.001$, **** $p \leq 0.0001$, all $n=3$. Data were fitted with log-inhibitor normalised-response curves.

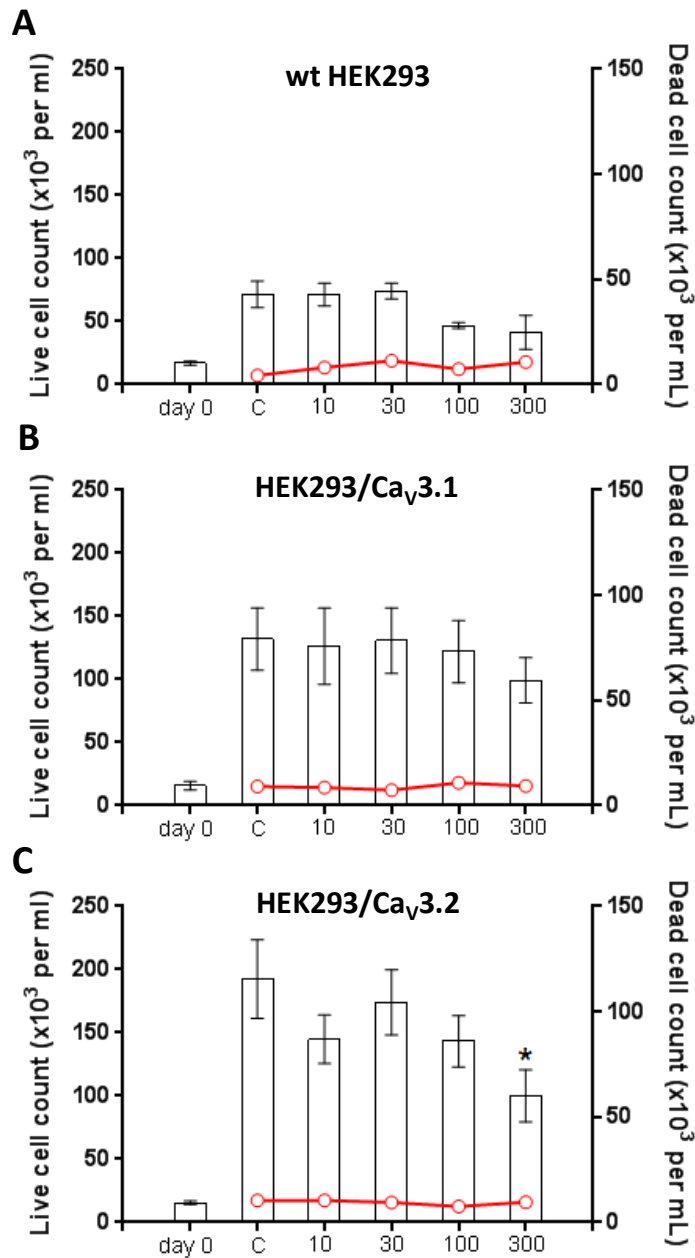


Figure 4.12. Auranofin selectively reduces HEK293/Ca_v3.2 cell proliferation

Bar charts (mean \pm s.e.m) showing live cell number (white boxes, left Y axis) and dead cell number (red circles, right Y axis), counted on day 3 of proliferation assays. Illustrating effects of auranofin (AuF, 10-300nM) on: **A**, wt HEK293 cell (n=3), **B**, HEK293/Ca_v3.1 cell (n=4), and **C**, HEK293/Ca_v3.2 cell proliferation (n=5). All cell counts were made in triplicate with the mean value counting as n=1. Data were analysed by one-way ANOVA with Dunnett's post-hoc comparison test, *p \leq 0.05, **p \leq 0.01.

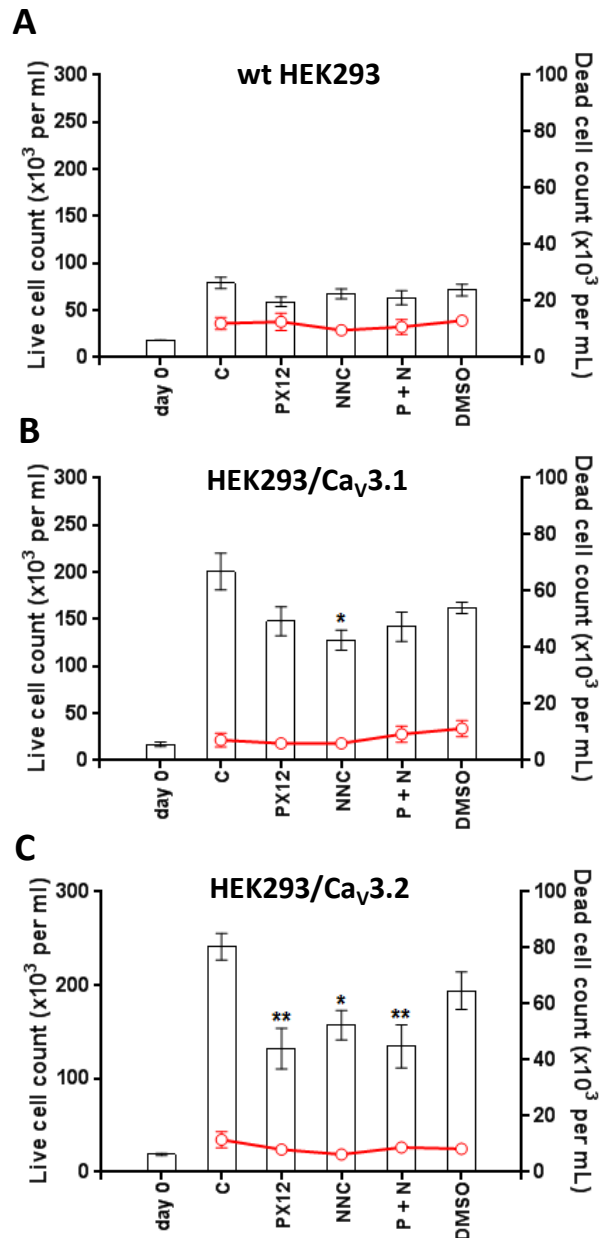


Figure 4.13. PX-12 selectively reduces HEK293/Ca_v3.2 cell proliferation

Bar charts (mean \pm s.e.m) showing live cell number (white boxes, left Y axis) and dead cell number (red circles, right Y axis), counted on day 3 of proliferation assays. Illustrating effects of PX-12 (1 μ M), applied alone or in combination with NNC55-0396 (NNC, 1 μ M) or with DMSO (1:1000) alone on: **A**, wt HEK293 cell (all n=5), **B**, HEK293/Ca_v3.1 cell (control and PX-12 n=5, NNC +/- PX-12 n=4, DMSO, n=3) and **C**, HEK293/Ca_v3.2 cell proliferation (all n=4). All cell counts were made in triplicate with the mean value counting as n=1. Data were analysed by one-way ANOVA with Dunnett's post-hoc comparison test, *p \leq 0.05, **p \leq 0.01.

CellProfiler™ is free open-source software that allows users to custom build a wide range of analysis pipelines enabling automated processing of immunofluorescence images. Comparison of the results from manual and automated counts of HEK293/Ca_v3.1 cell nuclei revealed the two counting techniques to yield significantly different results. The automated count under-estimated the number of DAPI nuclei by 30% and under-estimated the number of EdU positive nuclei by a factor of 10%, as detailed by **Error! Reference source not found.** Resultantly, all future image counting was conducted manually to ensure accuracy. Treatment with PX-12 (1μM, 48hrs) significantly reduced HEK293/Ca_v3.1 cell proliferation (**Error! Reference source not found.**) but was without significant effect on wt HEK293 cell proliferation (**Error! Reference source not found.**). A noteworthy point is that the % EdU-positive value was almost identical for HEK293/Ca_v3.1 and wt HEK293 cells, and did not reflect the elevated proliferative rate of HEK293/Ca_v3.1 and wt HEK293 cells (**Error! Reference source not found. & Error! Reference source not found.**). The average total number of HEK293/Ca_v3.1 nuclei (DAPI labelled) was considerably greater than for wt HEK293 cells (164 vs. 69 respectively, data not shown). This confirmed the proliferative advantage of Ca_v3.1 expression. In summary, these data collectively demonstrate that Ca_v3.2-expressing cells are most sensitive to Trx inhibition-mediated anti-proliferative effects. In addition, data suggest that HEK293/Ca_v3.1 cells are slightly sensitive to PX-12-mediated anti-proliferative effects, whilst wt HEK293 cells show complete insensitivity.

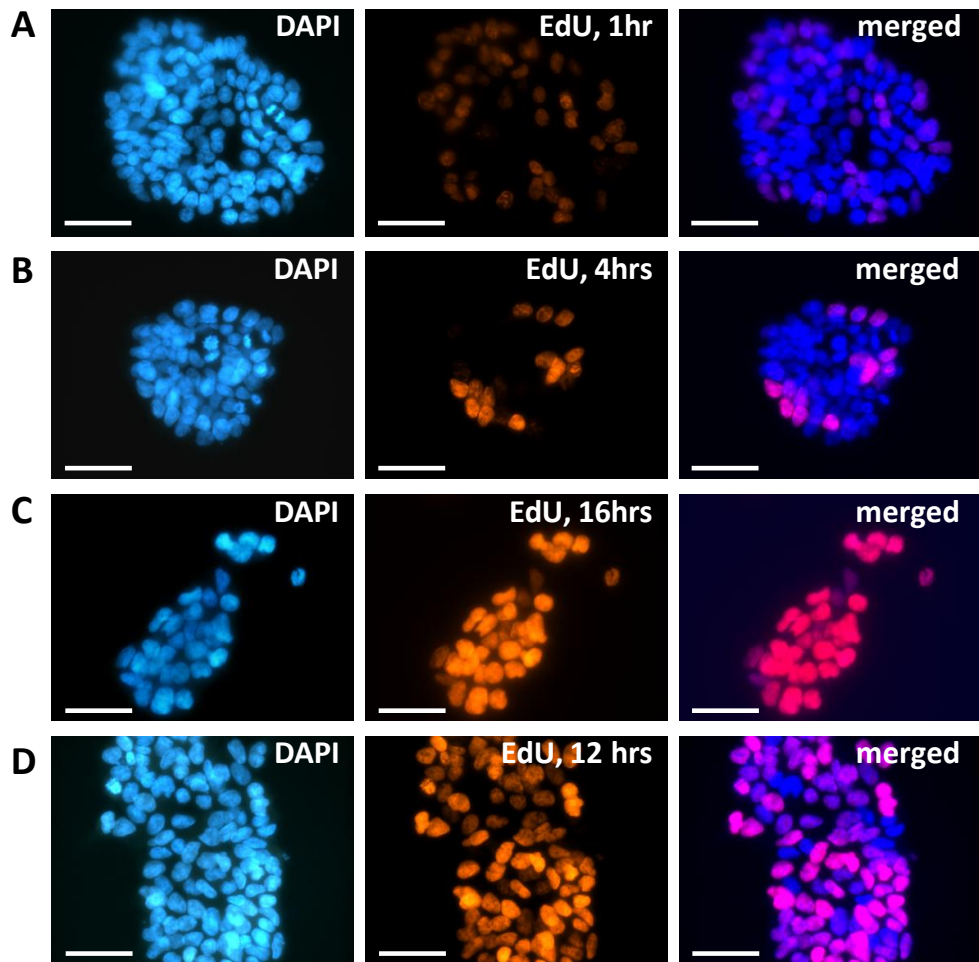


Figure 4.14. Optimisation of EdU incubation time and concentration for subsequent proliferation assays

Representative images showing EdU incorporation in HEK293/Ca_v3.1 cells following incubation with EdU (1-16hrs, 5-10 μM). Total cell nuclei are labelled by DAPI (left panel, blue images) and nuclei containing newly synthesised DNA are labelled by EdU (centre panel, orange images), merged images illustrating co-localisation (right panel, pink images). **A**, EdU (10 μM, 1hr). **B**, EdU (10 μM, 4hrs). **C**, EdU (10 μM, 16hrs). **D**, EdU (5 μM, 12hrs). Scale bars 50 μm.

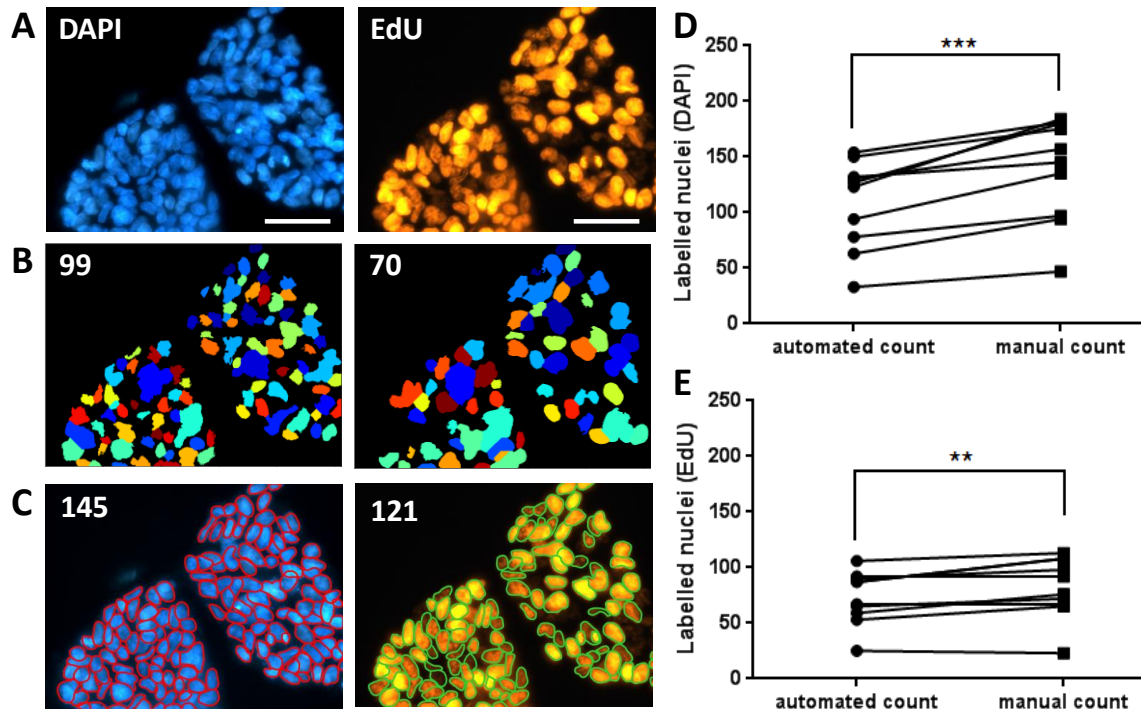


Figure 4.15. Comparison of automated and manual counting techniques for analysis of EdU incorporation assays

A-C, Representative images showing HEK293/Ca_v3.1 cell nuclei labelled by DAPI (left panel, blue images) and nuclei containing newly synthesised DNA are labelled by EdU (centre panel, orange images), from the same field of view, following incubation with EdU (5 μ M, 12hrs). Scale bars 50 μ m. **B**, Nuclei identified by automated analysis software CellProfilerTM using DAPI and EdU images, number of identified nuclei given in top left corner of each image. **C**, As B, except nuclei counted and outlined manually. **D**, Trend graph showing the difference in the number of counted nuclei labelled by DAPI; between automated and manual techniques. Data were analysed using paired student's t-tests, ** $p \leq 0.01$, *** $p \leq 0.001$, $n=10$. **E**, As D, except for EdU labelled nuclei.

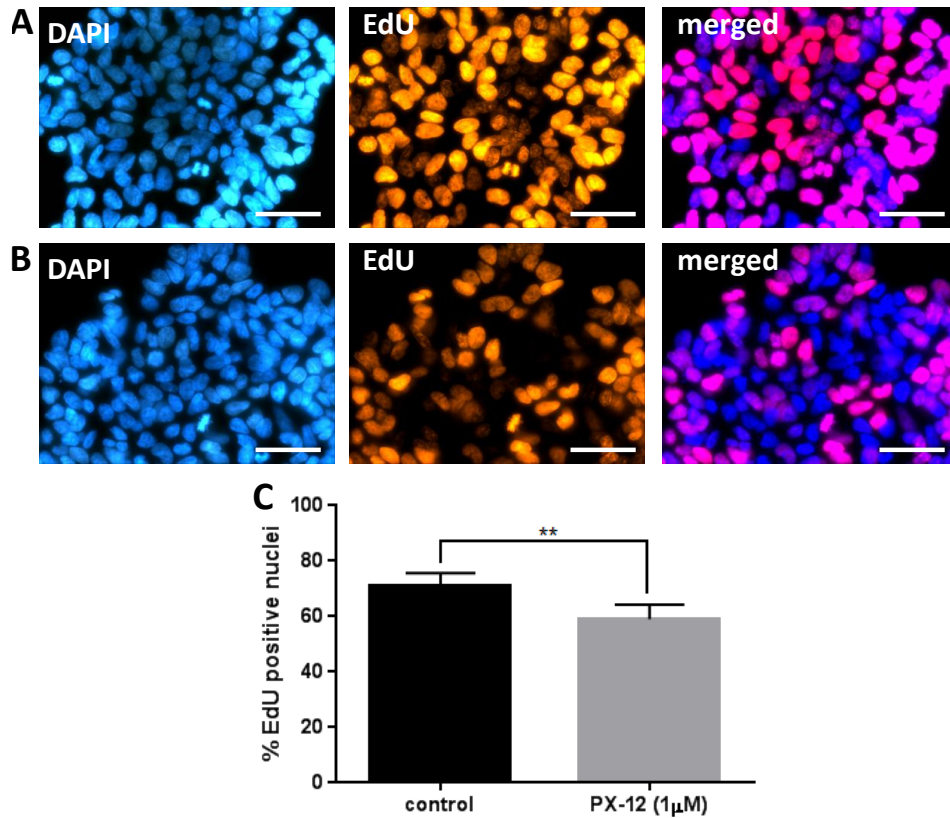


Figure 4.16. PX-12 (1µM) reduces HEK293/Ca_v3.1 cell proliferation

Representative images showing EdU incorporation in HEK293/Ca_v3.1 cells following incubation with EdU (12hrs, 5µM). Total cell nuclei are labelled by DAPI (left panel, blue images) and nuclei containing newly synthesised DNA are labelled by EdU (centre panel, orange images), merged images illustrating co-localisation (right panel, pink images). Showing differences between: **A**, control conditions and **B**, following PX-12 incubation (1µM, 48hrs). **C**, Bar graph showing, (mean ± s.e.m) EdU positive nuclei (% of DAPI labelled nuclei) within HEK293/Ca_v3.1 cells, calculated by manual counting, n=5. Five randomly selected fields of view were counted with the mean value represented as n=1. Data were analysed using paired Student's t-tests, **p<0.01.

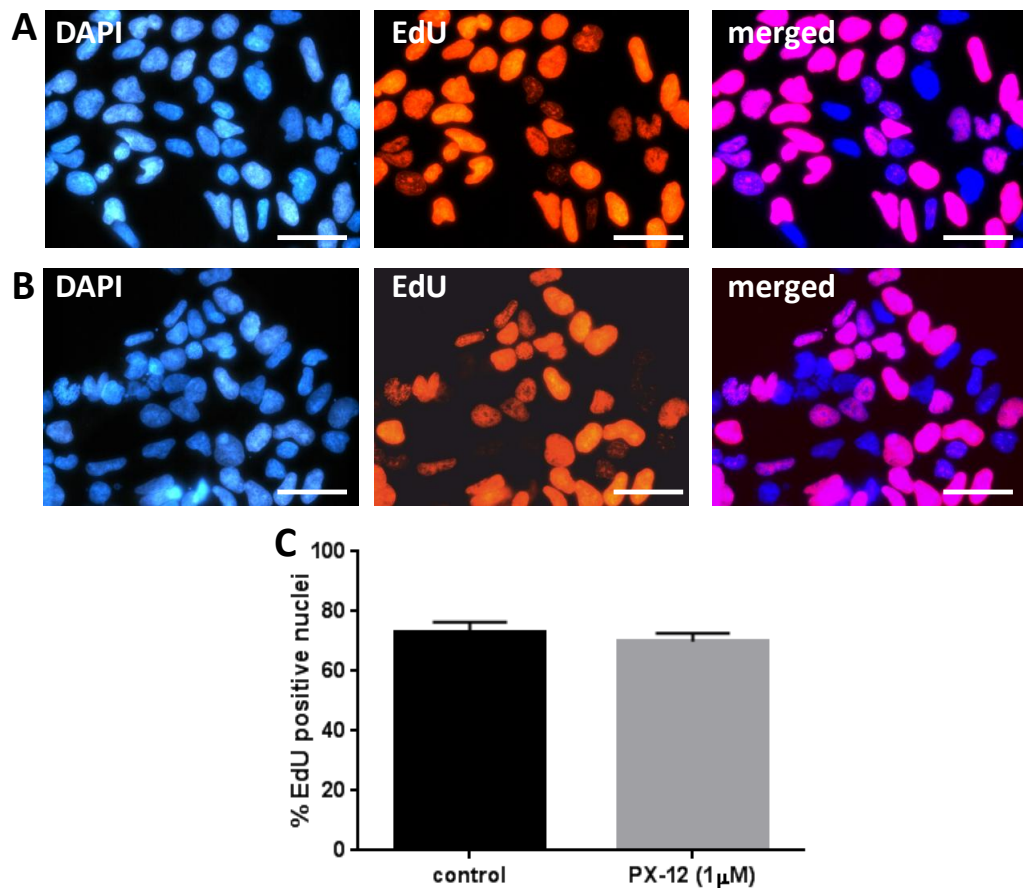


Figure 4.17. PX-12 (1µM) has no effect on wt HEK293 cell proliferation

Representative images showing EdU incorporation in wt HEK293 cells following incubation with EdU (12hrs, 5µM). Total cell nuclei are labelled by DAPI (left panel, blue images) and nuclei containing newly synthesised DNA are labelled by EdU (centre panel, orange images), merged images illustrating co-localisation (right panel, pink images). Showing differences between: **A**, control conditions and **B**, following PX-12 incubation (1µM, 48hrs). **C**, Bar graph showing, (mean ± s.e.m) EdU positive nuclei (% of DAPI labelled nuclei) within wt HEK293 cells, calculated by manual counting, n=5. Five randomly selected fields of view were counted with the mean value represented as n=1. Data were analysed using paired Student's t-tests, although significance was not observed.

4.3. Discussion

Trx is ubiquitously expressed in both prokaryotic and eukaryotic organisms and is known to have a variety of important functions. In light of this, literature regarding the structure, function and localisation of Trx is extremely wide ranging and so reference is constrained to studies conducted within mammalian cells. Trx inhibitors are currently being explored clinically as anti-cancer agents. Consequently, much of the following discussion concerns malignant cell lines. Angiogenesis involves excessive VSMC proliferation and is a key pathological phenotype crucial for tumour growth. Malignant cells also share other similarities with proliferative VSMCs, such as elevated T-type Ca^{2+} channel expression (Dziegielewska *et al.*, 2014) and increased Trx levels (Powis *et al.*, 2000). As such, studies examining the effects of Trx inhibition on cancer cells relate well to the current investigation.

4.3.1. Comparison of methods for the quantification of endogenous Trx levels

The principles of determining Trx activity spectrophotometrically, using insulin reduction assays, utilise the properties of Trx as a major cellular protein disulphide reductase. Whilst this technique is longstanding, many different fluorescent reporters have been used. Upon initial development, turbidity analysis was used to detect the precipitation of free A and B chains, resulting from Trx-mediated reduction of two inter-chain disulphide bonds, within the insulin molecule. This was detected as increases in absorbance at 650nm (Holmgren, 1979). Other spectrophotometric variants include monitoring (i) NADPH consumption, observed as a decrease in absorbance at 340nm (Zhang *et al.*, 2014), (ii) reduction of tryptophan, observed as an increase in fluorescence at 350nm (Holmgren, 1979), and (iii) reduction of 5,5-dithiobis(2-nitrobenzoic acid) (DTNB), detected as increasing fluorescence at 412nm (Huang *et al.*, 2014; Schulze *et al.*, 2002). A key problem with these assays however, is that they lack substrate specificity which results in large background values. Two key advantages of the newly developed assay currently used are: it does not require the addition of DTT to reduce Trx, and due to the high degree of substrate specificity it enables more accurate quantification of unknown Trx concentrations (Montano *et al.*, 2014).

Within the current investigation, Trx levels were measured by assessing the rate of increasing fluorescence of eosin-labelled insulin which in turns corresponds with the rate of Trx-mediated reduction. As insulin reduction requires Trx to be in its reduced and active form (rTrx), the assay involves pre-incubation with excess amounts of both TrxR and NADPH. Resultantly, it is assumed that all endogenous oxidised Trx (oTrx) is converted to rTrx. It is important to emphasise that as known Trx standards were used to calibrate the assay, Trx levels are deduced from Trx activity. Endogenous Trx was reliably detected within A7r5, HEK293/Ca_v3.1, HEK293/Ca_v3.2 and wt HEK293 cells. Despite standardising the total amount of protein loaded for each sample (15µg), Trx levels were highly variable between experimental repeats and cell types. As previous studies looking at Trx levels in cell lysates often only report increases or decreases in Trx activity with reference to control values (Schulze *et al.*, 2002), only limited comparison is possible. Using an identical protocol as currently implemented, Trx levels within peripheral blood mononuclear cells (PBMCs) and human histocytic lymphoma (U937) cell lysates have been shown to be 1.75ng and 2.25ng per 1µg total protein respectively (Montano *et al.*, 2014). Although performed in different cell types, current values were relatively higher (~4-16ng/µg). Further investigations, comparing A7r5 and U937 Trx levels within the same assay, would be useful to establish whether this difference is due to disparate Trx levels between cell lines or inter-laboratory assay variability.

In the current investigation, chronic treatment of A7r5, wt HEK293 or HEK293/Ca_v3.1 cells with low concentrations of AuF (300nM, 72hrs) did not produce any measurable decrease in Trx levels. This observation is consistent with the indirect nature by which AuF inhibits Trx, i.e. via TrxR. As the assay requires the addition of exogenous TrxR and NADPH in excess, potential effects of TrxR inhibition by AuF were unlikely to be detected. A very similar fluorescence assay which requires Trx to be added in excess, as opposed to TrxR, has been used successfully to study TrxR activity within cell lysates (Cox *et al.*, 2008; Lessa *et al.*, 2011). This alternative assay would be more suitable for subsequent investigations into the interactions between AuF and Trx.

The effects of PX-12 treatment on Trx activity were also examined. This indicated that chronic PX-12 pre-treatment (1µM, 72hrs) had no effect on Trx levels within A7r5, wt

HEK293 or HEK293/Ca_v3.1 cells. Contrastingly, acute PX-12 treatment (3μM or 30μM, 10mins) did produce a small but significant reduction in Trx levels within HEK293/Ca_v3.1 and HEK293/Ca_v3.2 cells respectively. Whilst, PX-12 (300μM) produced a clear and uniform reduction in Trx activity, it also caused the rate of background fluorescence to decrease. Resultantly, this concentration was excluded from the final analysis. The effects of PX-12 on Trx were originally described by Kirkpatrick *et al.*, (1998), who used spectrophotometric analysis alongside electrophoresis and mass spectrometry. The mechanism by which PX-12 inhibited human Trx (hTrx) was shown to be highly complex as different Trx cysteine (Cys) residues were found to be sensitive to considerably different PX-12 concentrations.

Firstly, Cys³² and Cys³⁵ within the redox active site of Trx were shown to be rapidly inhibited by reversible thioalkylation, with a dissociation constant (K_i) of 31μM (Kirkpatrick *et al.*, 1998). As redox-sensitive Cys residues within the active site are known to mediate the disulphide reductase abilities of Trx, this mechanism appears to correspond with the reductions in Trx activity currently observed following acute pre-treatment with PX-12 (3μM or 30μM, 10mins). In addition, Cys⁷³ found outside of the Trx active site was also originally shown to be modified by irreversible thioalkylation, at PX-12 concentrations several orders of magnitude lower than observed for Cys³² and Cys³⁵, and with a considerably slower rate of reaction. Furthermore, irreversible thioalkylation of Cys⁷³ as a result of pre-treating hTrx with PX-12 for 24hrs prior to measuring Trx activity was reported to prevent TrxR-mediated reduction of Trx. As substitution of Cys⁷³ with a serine (Ser) residue (C73S Trx mutant) did not prevent the effects of TrxR on Trx, it was suggested that irreversible thioalkylation of Cys⁷³ produced a steric blockade of the interaction between Trx and TrxR (Kirkpatrick *et al.*, 1998). This mechanism would also theoretically prevent Trx-mediated insulin reduction, which would be detected currently as a decrease in Trx levels. However, as PX-12 (1μM, 72hrs) was currently found to be without effect on Trx levels, evidence against this alternative mechanism of Trx inhibition is provided.

It should be noted that the reductions in Trx levels observed following acute PX-12 pre-treatment were not concentration-dependent and also highly variable between cell types and experimental repeats. A potential explanation for this could be the

reversible nature of Cys³² and Cys³⁵ thioalkylation. Specifically, PX-12 could not be directly applied to cell lysate samples using the current technique due to known interactions of alkylating agents with reaction components. As such, PX-12 had to be washed off immediately prior to measuring its effects on Trx. This could theoretically result in some reversal of the effects of PX-12 upon the NADPH and TrxR pre-incubation step. An alternative explanation, which would also additionally account for the general variability in results, may concern the sensitivity of the recording equipment used for Trx assays. The current investigation used a dual-monochromator microplate reader (Varioskan Flash; Thermo Scientific, UK), whereas quad-monochromator devices (Enspire or Victor3, PerkinElmer) are recommended by the assay developers. In support of this, especially when compared to the findings of Montana *et al.* (2014), the current investigation required higher Trx reference samples to generate accurate calibration curves and the absolute fluorescence values were much lower. Suggested improvements to the current assay would be to ensure that a quad-monochromator spectrophotometric recording device was used, and that the alternative TrxR assay was implemented to assess the effects of AuF. Further investigation could then be conducted to conclusively establish potential differences in both endogenous Trx levels between different cell lines and also the effects of AuF and PX-12.

As a final note on the subject of Trx quantification, the majority of previously described methods do not differentiate between reduced and oxidised forms. As the balance between oTrx and rTrx is a crucial feature of its activity, important effects of AuF and PX-12 may be masked when reducing agents are applied exogenously. The redox western blot provides a way of independently measuring oTrx and rTrx. This technique requires incubating Trx with a maleimide derivative prior to separating samples using non-reducing SDS gel electrophoresis and detecting with antibodies. Maleimide is only able to bind to rTrx and thereby selectively increases its molecular size, whilst having no effect on oTrx. The ratio of rTrx/oTrx can be calculated using band densitometry, and the redox state quantified using the Nernst equation (Hansen, 2012). To investigate Trx activity within HeLa cells, redox western blotting using iodoacetamide and iodoacetic acid to detect the redox state of Trx has been used effectively alongside a spectrophotometric assay identical to that currently used (Zhang *et al.*, 2014).

4.3.2. High concentrations of Trx inhibitors induce cell death

The current investigation demonstrated that AuF (1-3 μ M) and PX-12 (3-300 μ M) significantly reduced A7r5 and HEK293/Ca_v3.2 cell viability following 72hrs of treatment. Similar findings have been previously reported within a variety of cell lines. A key point to emphasise is that MTT assays were used in the current investigation to assess cell viability and not cell number as referenced in some other studies (Raniga *et al.*, 2015; Shin *et al.*, 2013; You *et al.*, 2014). It is possible that a reduction in cell number could correspond with reduced production of the formazan product (i.e. absorbance at 560nm), due to a lower number of cells and thus total mitochondria. However, within the current investigation morphological changes indicating cell death, such as rounding-up and cell detachment, were observed within all treatment groups exhibiting reduced absorbance. This supported the conclusion that reduced absorbance values were due to reductions in cell viability and not anti-proliferative effects. Resultantly, previous studies which used MTT assays to quantify cell number will be interpreted with this caveat in mind.

Treatment of tumour cell lines, including Jurkat and MCF-7 cells, with high concentrations of AuF (10 μ M, 48hrs) has been shown to induce significant reductions in cell viability, as measured using MTT assays. MCF-7 cells showed the greatest sensitivity and also exhibited cellular DNA fragmentation in approximately 20% of cells. This indicated that the cytotoxic effects of AuF were mediated, in part, by apoptosis induction. Spectrophotometric TrxR activity assays using DTNB as the fluorescent reporter were also implemented and revealed that AuF (500nM) inhibited TrxR activity by 79%. Whilst these findings confirmed that TrxR is a biological target of AuF, they employ considerably higher AuF concentrations than currently used to investigate effects on cell viability (Lessa *et al.*, 2011). The effects of lower AuF concentrations on Jurkat T-lymphoma cell viability were also examined in an alternative study. Using propidium iodide uptake as a measurement, AuF (0.5-4 μ M, 24hrs) was found to reduce Jurkat cell viability in a concentration-dependent manner with a half maximal lethal dose (LD₅₀) of 1.4 μ M. In addition, AuF (2-3 μ M, 24hrs) increased caspase-3 activity, confirming a role of apoptosis in AuF-mediated cell death (Cox *et al.*, 2008). These findings are in close agreement with current observations that AuF (\geq 1 μ M) reduced A7r5 and HEK293/Ca_v3.2 cell viability. In contrast with the current finding that

the cytotoxicity threshold of AuF was independent of cell type, Cox *et al.* (2008) also reported that not all cells responded to AuF in the same manner. Compared to Jurkat cells, mouse B cell hybridoma (B9) cells were comparatively resistant to AuF-induced apoptosis. Treatment of B9 cells with AuF (3 μ M, 24hrs) had no effect on cell viability, although direct cell counting revealed that it did completely halt cell proliferation. All of the effects of AuF in this study are attributed to inhibition of TrxR, confirmed directly using DTNB reduction assays to have an IC₅₀ of 200nM (Cox *et al.*, 2008). Of note, however, is that AuF was applied at relatively higher concentrations for apoptosis experiments than were shown necessary to inhibit TrxR. Though potential off-target effects of AuF should be considered, this discrepancy in concentrations may be due to the indirect nature of Trx inhibition. Specifically, it could take more than 24hrs for the effects of TrxR inhibition on the redox-state of Trx to fully equilibrate. Current observations that AuF (1 μ M) was without significant effect on HEK293/Ca_v3.2 cell viability after 24hrs, although did reduce viability 48 and 72hrs post-treatment, are in agreement with this interpretation.

Regarding the PX-12 ($\geq 3\mu$ M)-mediated reductions in A7r5 and HEK293/Ca_v3.2 cell viability currently observed, a limited number of studies exploring the effects of PX-12 on cellular apoptosis have also recently been reported. Treatment of hepatocellular carcinoma (HCC) cell lines HepG2 and SMMC-7721 with PX-12 (48hrs) was shown to reduce average cell number with IC₅₀ values of 6.32 μ M and 13.38 μ M respectively. Importantly, these findings were demonstrated using a commercially-available cell counting kit (CCK-8, Dojindo, Japan) which although referred to as a viability assay, did not differentiate between cytotoxic and anti-proliferative effects. Further investigation was subsequently conducted using Annexin V-FITC assays to directly measure apoptosis, dichlorofluorescein (DCF) assays to quantify reactive oxygen species (ROS) levels and flow cytometry for cell cycle analysis. This revealed that PX-12 reduced average cell number via both ROS-induced apoptosis and S-phase cell cycle arrest. Furthermore, these effects were prevented by pre-treatment with the antioxidant N-acetyl cysteine (NAC). As PX-12 was also found to sensitise HCC cells *in vitro* and *in vivo* to 5-fluorouracil (5-FU), the principal cytotoxic chemotherapy agent for HCC, the authors suggest that these drugs provide an effective drug combination to reduce tumour growth (Li *et al.*, 2015a). An alternative study implemented MTT assays to

show that PX-12 decreased human cervical adenocarcinoma (HeLa) cell number with an IC_{50} value of $7\mu M$. This reduction was shown to involve both ROS-induced apoptosis and cell cycle G_2/M -phase arrest. In direct agreement with current findings, PX-12 ($1\mu M$, 72hrs) was without effect on the MTT signal at 570nm (Shin *et al.*, 2013). In addition, the growth of A549 lung cancer cells has also been shown to be reduced by PX-12 (IC_{50} $20\mu M$) and similarly found to be mediated through G_2/M -phase arrest and ROS-dependent apoptosis (You *et al.*, 2014).

Of final interest is a study which explored the suitability of PX-12 and AuF as novel treatments for multiple myeloma (MM), a haematological disorder involving aberrant growth and accumulation of clonal plasma cells. Human PBMCs were isolated from healthy volunteers and used as control cells to directly compare against MM cell lines. Elevated Trx and TrxR protein levels alongside higher ROS levels were detected in MM cells when compared to PBMCs, as measured using western blotting and DCF analysis respectively. In direct contrast with current methodologies, the authors incorrectly used direct cell counting as a measure of cell viability and MTT assays to quantify proliferation. Following incubation with AuF ($\leq 8\mu M$) or PX-12 ($\leq 40\mu M$) for 24hrs the average number of cells was reduced in a concentration-dependent manner. MM cell lines showed the greatest sensitivity to these reductions. MM cells cultured in methylcellulose additionally revealed that PX-12 ($5\mu M$) and AuF ($4\mu M$) reduced colony formation. Regarding the potential mechanisms of these anti-clonogenic effects, PX-12 ($5\mu M$) was found to induce ROS-mediated apoptosis in MM cells but not in PBMCs. In addition, PX-12 sensitised cells to apoptosis induced by nuclear transcription factor (NF) $NF-\kappa\beta$ inhibitors such as curcumin (Raniga *et al.*, 2015). This may be significant as $NF-\kappa\beta$ regulates the expression of various genes involved in cell proliferation and tumorigenesis (Matthews *et al.*, 1992).

In conclusion, the ability of the AuF ($\leq 1\mu M$) and PX-12 ($\leq 3\mu M$) to induce cell death are well established. Whilst the ROS-induced apoptotic effects of Trx inhibition may have therapeutic potential in the treatment of cancer, apoptosis could have detrimental effects on healthy VSMCs. Therefore, when assessing the suitability of Trx inhibitors as novel treatments for proliferative cardiovascular disorders, only AuF and PX-12 concentrations below those directly shown to reduce cell viability are considered.

4.3.3. Low concentrations of Trx inhibitors selectively reduce cellular proliferation in Ca_V -expressing cells.

The current investigation demonstrated that PX-12 (1 μ M) and AuF (300nM) significantly reduced A7r5 and HEK293/ Ca_V 3.2 cell proliferation following 72hrs of treatment. Notably, direct cell counting suggested that the proliferation of wt HEK293 and HEK293/ Ca_V 3.1 cells was not significantly altered. To confirm this observation, DNA synthesis was assessed using EdU nucleoside incorporation assays over a 12hr period. Results confirmed that the proliferation of wt HEK293 was unaltered by PX-12 (1 μ M, 48hrs). In contrast, significant reductions in the number of HEK293/ Ca_V 3.1 cells which had progressed through the G₁-S phase of the cell-cycle were apparent. Findings within HEK293 cells therefore indicate that Trx inhibitors selectively reduce the proliferation of T-type Ca^{2+} channel expressing cells. In support of this conclusion, “new” A7r5 cells were shown using qRT-PCR to express considerably higher levels of T-type Ca^{2+} channels when compared to “old” A7r5 cells and were much more sensitive to the anti-proliferative effects of AuF. Whilst this proposal is novel, many previous studies report anti-proliferative effects of Trx inhibitors within cell lines coincidentally shown to express T-type Ca^{2+} channels.

In addition to studies in cancer cell lines showing AuF- and PX-12-mediated cell cycle arrest (as described in section 4.3.2), the anti-proliferative effects of Trx inhibition have also been examined in a variety of other cell types. Interestingly, early studies provided conflicting findings regarding the effects of Trx on cell growth. For example, AuF (100-500nM) significantly decreased the proliferation of primary cultures of vascular endothelial cells (VECs) when determined using thymidine incorporation measurements and without affecting viability (Matsubara & Ziff, 1987). Contrastingly, an alternative study additionally used direct cell counting to show that application of Trx to the culture media inhibited the growth of HepG2 cells. This same study also reported opposing stimulatory growth effects of Trx on the B-cell lymphoma cell line, A20 (Rubartelli *et al.*, 1995).

Within pulmonary hypertensive (PH) diseases associated with hypoxia, pathological pulmonary artery SMC (PASMC) proliferation leads to vascular remodelling. A recent study determined that Trx levels from lung homogenates, isolated from mice

maintained in hypoxic conditions (10% oxygen, 4 weeks) were double that of controls (normoxia) (Chen *et al.*, 2013). *In vitro* studies additionally compared Trx levels in HPASMCs cultured in hypoxic conditions (1% O₂, 24-72hrs) to controls, using western blotting. Under normoxic conditions, Trx expression remained constant whilst hypoxia-exposed HPASMCs showed considerable elevations in Trx (65%, 72hrs). HPASMCs cultured for 120 days under normoxia or hypoxia were also counted using a direct cell counting approach. Hypoxia was found to increase HPASMC proliferation. Furthermore, genetic knockdown of Trx using siRNA abolished hypoxia-induced elevations in proliferation, and also reduced HPASMC proliferation under normoxic conditions. In close agreement with current observations, PX-12 (2µM) was found to fully reproduce the anti-proliferative effects of genetic Trx inhibition. Regarding potential mechanisms for the pro-proliferative effects of Trx, increased Trx expression was found to correlate with activation of hypoxia-inducible factor (HIF) and phosphatidylinositol 3-kinase (PI3K)/serine/threonine kinase (Akt). It was concluded that Trx regulates hypoxia-induced PASMCM proliferation via HIF-dependent mechanisms with downstream effects on PI3KAkt signalling (Chen *et al.*, 2013). Of significant interest to the current investigation is that chronic hypoxia has also been shown to up-regulate the expression of Ca_v3.2 channels in HPASMCs (Wan *et al.*, 2013). These findings are therefore also consistent with the suggestion that Trx regulates T-type Ca²⁺ channels and controls cell proliferation.

The effects of AuF on vascular endothelial cell (VEC) proliferation have also been studied recently. Angiogenesis is the process by which existing blood vessels form a network of new vessels, and involves the proliferation, invasion, migration and tube formation of VECs. Human umbilical VECs (HUVECs) were used to examine the anti-proliferative effects of AuF *in vitro*. Using a cell-counting kit-8, the number of HUVECs was found to be reduced by AuF in a concentration-dependent manner with an IC₅₀ value 178nM. It should be noted however, that this technique does not differentiate between cytotoxic and anti-proliferative effects. To compensate for this, cellular migration was assessed using a wound-healing assay, whereby a small strip of cells are removed from a confluent monolayer of cultured HUVECs. HUVECs cultured under control conditions for 10hrs showed significant migration into the denuded region, which was inhibited by AuF (25-390nM) in a concentration-dependent manner. As no

morphological changes, such as blebbing, cell shrinkage, nuclear fragmentation or chromatin condensation were observed potential cytotoxic effects of AuF were therefore ruled out. In addition, under control conditions, culture of HUVECs on matrigel resulted in tube formation which was also significantly inhibited by AuF (98-390nM) (He *et al.*, 2014). The concentrations of AuF shown to be anti-angiogenic within this study are very similar to those currently found to reduce A7r5 and HEK293/Ca_v3.2 cell proliferation.

The anti-angiogenic properties of AuF were confirmed *in vivo* using transgenic zebrafish. In addition to its anti-angiogenic effects, treatment of zebrafish embryos with AuF (98nM) was found to up-regulate vascular endothelial growth factor (VEGF) expression whilst higher doses caused a sharp down-regulation in VEGF mRNA. Expression of the VEGF receptors *flt-1* and *kdr* was consistently down-regulated by AuF in a concentration-dependent manner. As the expression of TrxR remained unaltered by AuF treatment, the authors postulate that the anti-proliferative and anti-angiogenic effects of AuF are due to direct interaction with VEGF signalling. This conclusion is debateable however as AuF exerts its effects by altering the activity of TrxR (Gromer *et al.*, 1998) and has not previously been shown to alter TrxR expression. Downstream regulation of VEGF signalling pathways by Trx is therefore an equally plausible conclusion, though not explored within the study (He *et al.*, 2014). As T-type Ca²⁺ channels have been previously shown to be expressed within VECs, for example Ca_v3.1 within HUVECs (Wang *et al.*, 2006), these observations may also correspond with the proposed regulation of T-type Ca²⁺ channels by Trx.

Confirmation that the anti-proliferative effects of AuF and PX-12 are mediated by Trx is provided by genetic studies. Vitamin D₃-upregulated protein (VDUP), also known as Trx interacting protein or Trx-binding protein interacts with the redox active site of Trx and functions as its endogenous inhibitor. Over-expression of Trx or VDUP using adenovirus-mediated gene transfer has been conducted in primary aortic SMCs. Trx transfection increased Trx activity (2.8- fold), as determined by spectrophotometric insulin reduction assays. Correspondingly, cellular DNA synthesis was also increased (3.8- fold) when determined by methyl-[³H] thymidine incorporation over a 5hr period. Platelet derived growth factor (PDGF), a powerful mitogenic stimulus, was found to

increase both Trx activity and cellular DNA synthesis within SMCs. As Northern analysis did not detect any increases in Trx mRNA with PDGF treatment, it was suggested that changes to the redox status of Trx was mediating its effects. Furthermore, as PDGF treatment significantly decreased VDUP mRNA and protein levels, and subsequently inhibited by NAC, evidence suggested that VDUP expression is a redox-regulated process. Conversely, transfection with VDUP reduced Trx activity (61%) in SMCs and also completely blocked PDGF-induced increases in Trx activity. Whilst VDUP over-expression alone did not alter methyl-[³H] thymidine incorporation it did block PDGF-induced increases in SMC proliferation. VDUP over-expression was also shown to have no effect on the apoptotic rate. The authors therefore conclude that VDUP suppression increases Trx activity, and as such endogenously regulates cellular redox state and SMC mitogenesis. Findings also suggest that the pro-proliferative effects of PDGF act via this mechanism (Schulze *et al.*, 2002).

Schulze *et al.* (2002) also assessed the cellular distribution of Trx using immunohistochemistry. In quiescent cells serum starved for 48hrs, a homogenous cytoplasmic Trx distribution was detected with nuclear staining evident in only ~10% of cells. Interestingly, PDGF induced rapid translocation of Trx to cell nuclei in 58% of cells. This nuclear translocation was inhibited by VDUP over-expression. Translocation of Trx to VSMC nuclei has been previously shown to produce lipopolysaccharide and interleukin 1 (IL1)-induced increases in the DNA-binding activity of the transcription factor AP-1 (Wiesel *et al.*, 2000). These findings therefore suggest an alternative potential mechanism for the growth modulating effects of Trx which could be influenced by intracellular Ca²⁺ levels. Furthermore, as discussed previously in Chapter 3, T-type Ca²⁺ channels are widely expressed in VSMCs and therefore the anti-proliferative effects of VDUP may also concern reduced interaction between Trx and T-type Ca²⁺ channels.

The effects of genetic-mediated Trx over-expression have also been examined. Following myocardial infarction (MI), pathological cardiac remodelling commonly occurs. Engraftment of mesenchymal stem cells (MSCs) is currently being explored as a potential therapeutic approach to mediate myocardial repair following MI. Rat MSCs were genetically modified to over-express Trx via adenoviral transfection. The

proliferation and differentiation potential of wild type MSCs (wt-MSC), MSCs over-expressing Trx (Trx-MSC) and MSCs transfected with control plasmids (LacZ-MSC) were compared. Immunohistochemical markers such as α -tubulin to label microtubules and Ki-67 as a marker of proliferation were applied. This revealed that under hypoxia Trx-MSCs had increased proliferative capacity and maintained better pluripotency when compared to wt-MSCs and LacZ-MSCs. This enabled successful differentiation into cardiomyocytes, SMCs and endothelial cells (Suresh *et al.*, 2015).

The effects of Trx expression *in vivo* were also examined. Rats were subject to MI prior to administration of pre-conditioned Trx-MSCs or LacZ-MSCs into the peri-infarct region. Interestingly, 7 days post MI, the number of proliferating cells was elevated in mice treated with Trx-MSCs. Furthermore, 60 days post MI, echocardiography and immunohistochemistry revealed increased myocardial function and capillary density alongside reduced fibrosis in Trx-MSC mice when compared to MSC-LacZ or sham MI controls. A significantly smaller improvement was observed in mice treated with wt-MSCs. Western blot analysis of MI mice exposed to Trx-MSCs revealed increased expression of the pro-angiogenic factors VEGF and heme oxygenase-1. Furthermore, the expression of chemokine receptor CXCR4 was also increased, thus indicating the contribution of paracrine effects. It was subsequently concluded that administration of MSCs over-expressing Trx provides therapeutic potential in the treatment of ischemic disease (Suresh *et al.*, 2015).

Electrophysiological and biochemical investigations in embryonic SCs, has revealed that Ca^{2+} currents within these cells are primarily mediated by $\text{Ca}_v3.2$ channels. As $\text{Ca}_v3.2$ expression peaked at the G_1/S transition phase of the cell-cycle it was suggested that $\text{Ca}_v3.2$ channels play an important role in the maintenance of undifferentiated states (Rodriguez-Gomez *et al.*, 2012). Collectively, these studies support the view that Trx is pro-proliferative. Findings are also indirectly consistent with the potential involvement of T-Type Ca^{2+} channels in Trx-mediated growth regulation.

A final interesting point to consider is what structural determinants of Trx mediate its growth promoting effects. The characterised actions of Trx as a ubiquitous disulphide reductase generally involve Cys³² and Cys³⁵ within the active site. Resultantly, these

residues appear most likely to mediate the stimulatory growth effects. In support of this notion, a study conducted by Oblong *et al.* (1994) used site-directed mutagenesis to substitute either or both of the Cys³² and Cys³⁵ residues in the Trx active site to serine residues (C32S, C35S, C32S/C35S). When applied to murine fibroblasts, Trx stimulated both DNA synthesis and proliferation. When the C32S, C35S, or C32S/C35S mutated forms of Trx were applied however, no such effects were observed. This indicated that the Cys residues in the redox-active site were required for Trx-mediated growth stimulation (Oblong *et al.*, 1994). In contrast, current observations indicated that low PX-12 concentrations not expected to modify catalytic Cys residues did have anti-proliferative effects in both A7r5 and HEK293/Ca_v3.2 cells. This was similarly observed for MCF-7 cells where low concentrations of PX-12 inhibited proliferation, with IC₅₀ values of 1.2µM or 3.2µM, when using Trx or FBS as the mitogenic stimulus respectively (Kirkpatrick *et al.*, 1998). Collectively, this emphasises that the slower irreversible thioalkylation of Cys⁷³ residues in Trx, which occurs at low PX-12 concentrations (Kirkpatrick *et al.*, 1998), may account for the growth inhibitory effects of PX-12.

The above studies conclusively support current findings that Trx inhibition using low concentrations of PX-12 or AuF reduces cellular proliferation. They also propose a range of intracellular mechanisms which may account for this effect, including regulation of VEGF signalling (He *et al.*, 2014; Suresh *et al.*, 2015), HIF and Akt activation (Chen *et al.*, 2013), increased expression of HO-1 and chemokine receptors (Suresh *et al.*, 2015) and also modulation of AP-1 transcription factor activity (Schulze *et al.*, 2002). Of potential significance is the observation that the majority of these studies were conducted on cells which have also previously been shown to express T-type Ca²⁺ channels. Indirect support is therefore also provided to current observations that only Ca_v3.1 and/or Ca_v3.2-expressing cells are sensitive to the anti-proliferative effects of Trx inhibition. Changes in intracellular Ca²⁺ regulates a huge variety of signalling cascades, including those which mediate proliferation and gene transcription (Berridge *et al.*, 2000). It is subsequently possible that alterations in Ca²⁺ influx, via modulation of T-type Ca²⁺ channels by Trx, provides an initial upstream signalling event which controls cell proliferation. This proposal is summarised by the following

schematic diagram, which also provides examples of how Ca^{2+} and Trx-mediated signalling pathways regulate gene transcription (Figure 4.14).

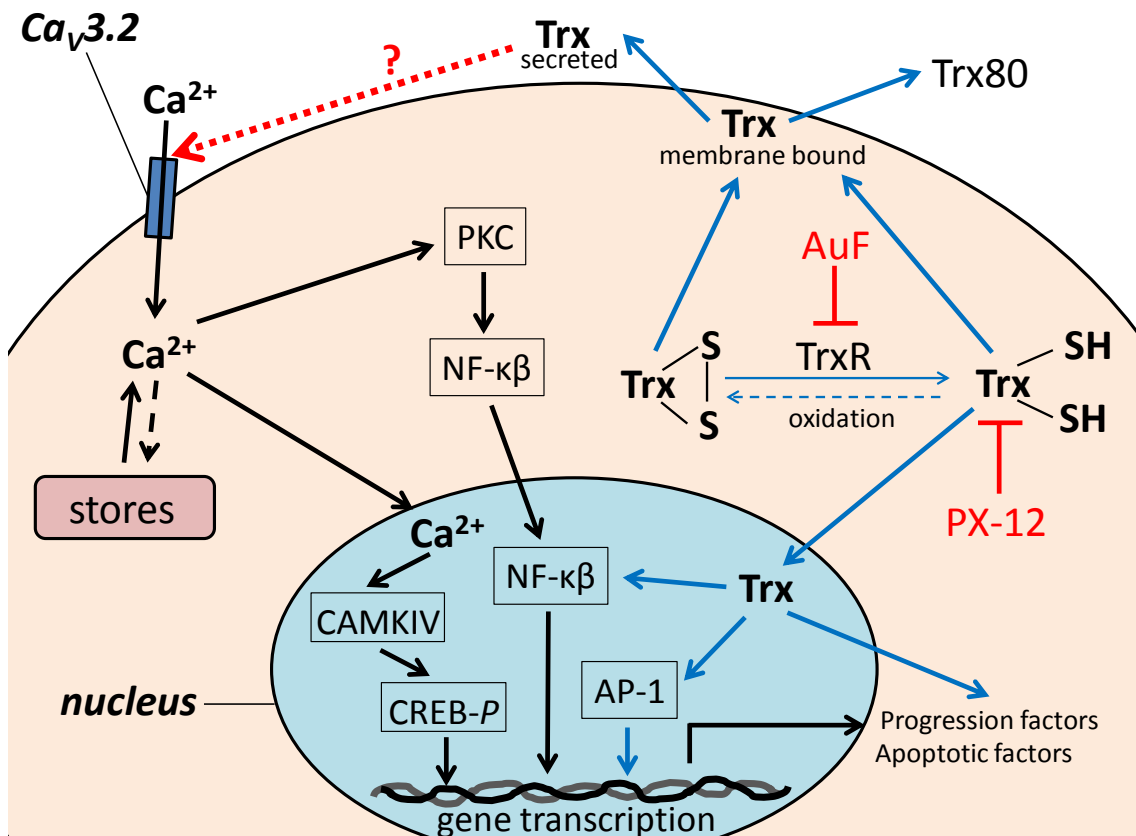


Figure 4.14. Schematic diagram showing how Trx and Ca^{2+} can regulate proliferation Showing examples of both Ca^{2+} (black lines) and Trx (red lines)-mediated signalling pathways that function to control gene transcription and cell proliferation. Potential interactions between these pathways, i.e. via $\text{Ca}_v3.2$ channel regulation (red dashed line) are highlighted. Ca^{2+} enters the cell membrane through voltage-gated Ca^{2+} channels (e.g. $\text{Ca}_v3.2$) which may lead to Ca^{2+} -induced Ca^{2+} release from internal stores. Cytosolic Ca^{2+} regulates protein kinase C (PKC) leading to nuclear translocation of nuclear transcription factor (NF- κ B). In addition, nuclear Ca^{2+} stimulates the transcription factor CREB via Ca^{2+} /calmodulin-dependent protein kinase type IV (*CaMKIV*) (Berridge *et al.*, 2000). Reduced Trx (Trx(SH)₂) is generated by thioredoxin reductase (TrxR) which in turn regulates the activity of transcription factors NF- κ B and AP-1, in addition to various progression factors. Oxidised Trx (Trx(S)₂) is then re-generated via oxidation. Trx is also found bound to the cell membrane and is secreted extracellularly; occasionally in the form of Trx80. The molecular targets of the direct and indirect Trx inhibitors, PX-12 and auranofin (AuF) are also shown. Diagram adapted from Arner & Holmgren (2000) and Lu & Holmgren (2014).

4.3.4. The potential for Trx as a T-type Ca^{2+} channel modulator

Current observations that AuF augments Ca^{2+} handling in A7r5 cells support the suggestion that modulation of T-type Ca^{2+} channels may mediate the growth promoting effects of Trx. Specifically, AuF pre-treatment reduced depolarisation-induced Ca^{2+} oscillations in “old” A7r5 cells, and also partially inhibited the Ca^{2+} -mediated window current recorded from “new” A7r5 cells. Both of these measures of A7r5 Ca^{2+} handling were previously confirmed to involve T-type Ca^{2+} channels (Chapter 3). As AuF-mediated inhibition of Ca^{2+} oscillations in “old” A7r5 cells was reversed by DTT, evidence is also provided that the Trx-mediated regulation of T-type Ca^{2+} channels occurs via a redox-dependent mechanism. Unfortunately, the effects of PX-12 on Ca^{2+} handling could not be examined as PX-12 was found to interfere with microfluorimetric signals, selectively increasing the fluorescence signal excited at 340nm but not at 380nm. In addition, due to time constraints of the project, the effects of AuF on recombinant HEK293 cell window currents were not determined.

Previous investigations looking at the effects of AuF on $[\text{Ca}^{2+}]_i$ levels are limited and their findings somewhat contrast with current observations. A previous study used Fura-2 Ca^{2+} microfluorimetry to demonstrate that AuF (10-50 μM) induced Ca^{2+} release from intracellular stores, thus elevating basal $[\text{Ca}^{2+}]_i$. These findings do not translate well to the present discussion however, as considerably higher AuF concentrations likely to induce apoptosis were applied (Wong *et al.*, 1990). A more recent study examined the effects of AuF on $[\text{Ca}^{2+}]_i$ within MCF-7 cells. MTS assays (an alternative to the MTT assay) were used to assess cell viability. Using fluo-4 as the ratiometric indicator, baseline $[\text{Ca}^{2+}]_i$ levels were monitored for 30mins before AuF was perfused continually for 2hrs. It was subsequently demonstrated that AuF (1-10 μM) produced a sustained increase in $[\text{Ca}^{2+}]_i$ in a concentration- and time-dependent manner. AuF (24hrs) was also shown to cause apoptotic cell death, confirmed using flow cytometry, with a calculated IC_{50} value of 3.37 μM . Whilst the mechanism of Ca^{2+} entry was not established, these data suggest that the apoptosis-inducing effects of higher AuF concentrations may also be dependent on $[\text{Ca}^{2+}]_i$ (Varghese & Busselberg, 2014). Whilst these findings contrast with current observations (i.e. AuF decreases Ca^{2+} influx), they refer specifically to cytosolic $[\text{Ca}^{2+}]_i$ and not Ca^{2+} influx. It would therefore be interesting to determine whether higher doses of AuF, applied for longer periods of

time, alters Ca^{2+} influx in A7r5 cells. In addition, further investigation to determine the effects of AuF on wt HEK293, HEK293/ $\text{Ca}_v3.1$ and HEK293/ $\text{Ca}_v3.2$ window currents would be useful to establish any potential isoform specific effects.

4.3.5. *Summary and conclusions*

Findings discussed within chapter 3 demonstrate that T-type Ca^{2+} channels contribute to the regulation of basal Ca^{2+} levels. In addition, they emphasise that selective T-type Ca^{2+} channel inhibition reduces A7r5, HEK293/ $\text{Ca}_v3.1$ and HEK293/ $\text{Ca}_v3.2$ cell proliferation, whilst inhibition of L-type Ca^{2+} channels is without effect. Findings reported in the current chapter demonstrate that Trx inhibition using high concentrations of AuF or PX-12 increases cell death, whilst lower concentrations reduce the proliferation of HEK293/ $\text{Ca}_v3.2$ and A7r5 cells. AuF was also found to reduce Ca^{2+} influx within A7r5s cells. The degree of the anti-proliferative effect of AuF was similar to those observed with the selective T-type Ca^{2+} channel inhibitor NNC. Furthermore, as the effects of PX-12 and NNC on HEK293/ $\text{Ca}_v3.2$ cell proliferation were shown to be non-additive, evidence is provided that both drugs may act via the same target, i.e. $\text{Ca}_v3.2$ channels. Further investigation (using EdU incorporation assays as an alternative measure of cellular proliferation) confirmed that wt HEK293 cells were insensitive to the anti-proliferative effects of PX-12. They also indicated that DNA synthesis within HEK293/ $\text{Ca}_v3.1$ cells was altered by PX-12 (1 μM , 48hrs). This highlighted the potential involvement of $\text{Ca}_v3.1$, in addition to $\text{Ca}_v3.2$, channels as targets for Trx regulation and should also be considered in subsequent investigations. Support is therefore provided that Trx controls cellular proliferation via modulation of T-type Ca^{2+} channels.

Chapter 5 -The effects of thioredoxin (Trx) and inhibitors on voltage-gated Ca²⁺ (Ca_v) channels

5.1. Introduction

Cell-surface proteins within the extracellular environment are subject to oxidising conditions and are rich in stabilising disulphides (S₂). In contrast, intracellular proteins contain many free sulfhydryl or thiol (SH) groups as the intracellular environment is maintained in a reduced state. Thioredoxin (Trx) serves as a major disulphide reductase and can counterbalance the effects of oxidative stress when up-regulated or over-expressed (Nakamura *et al.*, 1997). Whilst the intracellular actions of Trx are well characterised, it can be excreted by cells, via a leaderless secretory pathway (Rubartelli *et al.*, 1992; Tanudji *et al.*, 2003). Although the physiological consequences of extracellular Trx remain relatively undetermined, it has been found to have both mitogenic and co-cytokine effects on monocytes (Bertini *et al.*, 1999; Pekkari *et al.*, 2001). Significantly, increased levels of circulating extracellular Trx are detected within pathological conditions involving aberrant cellular proliferation including, but not limited to, a variety of cancers (Baker *et al.*, 2013), abdominal aortic aneurysm (Martinez-Pinna *et al.*, 2010) and atherosclerosis (Okuda *et al.*, 2001).

Within rat vascular smooth muscle cells (VSMCs), a coordinated elevation in [Ca²⁺]_i is required for cell cycle progression (Husain *et al.*, 1997). Whilst L-type Ca²⁺ channels have been shown to mediate VSMC contraction, T-type Ca²⁺ channel expression is restricted to proliferative phases of the cell-cycle (Kuga *et al.*, 1996). As such, T-type Ca²⁺ channels can control basal Ca²⁺ levels and regulate cellular proliferation, as discussed extensively in Chapter 3. A key feature of Ca_v3.2 channels which distinguishes them from other T-type Ca²⁺ channel isoforms is their unique sensitivity to redox modulators and trace metals, such as ascorbate (Nelson *et al.*, 2007a), Ni²⁺ (Kang *et al.*, 2006; Lee *et al.*, 1999) and Zn²⁺ (Kang *et al.*, 2010). As described in Chapter 4, Ca_v3.2-expressing cells were the most sensitive to the anti-proliferative effects of Trx inhibitors. In addition, previous findings from the research group have shown that Trx selectively regulates Ca_v3.2 channels (Boycott *et al.*, 2013). This chapter will therefore examine the potential interactions between Trx and T-type Ca²⁺ channels using whole-cell patch-clamp electrophysiology.

5.2. Results

5.2.1. The effects of Trx inhibitors on native and recombinant T-type Ca^{2+} currents

Findings detailed within Chapters 3 & 4 show that Trx inhibitors and selective T-type Ca^{2+} channel blockers (CCBs) reduce A7r5 cell proliferation and Ca^{2+} window currents to similar extents. In order to explore potential interactions between Trx and T-type Ca^{2+} channels directly, electrophysiology was employed. Firstly, the effects of PX-12 on native T- and L-type Ca^{2+} currents were examined in A7r5 cells. Due to the potential activation of L-type mediated Ca^{2+} current using the T-type SS protocol and vice versa, current subtypes are labelled with quotation marks. Initial experiments revealed that PX-12 (30 μM) partially inhibited native “T-type” Ca^{2+} currents, but at a slow rate (data not shown). As A7r5 recordings did not typically last for long periods of time, quantification of the maximal effects of PX-12 ($\leq 30\mu\text{M}$) was unreliable. PX-12 (100 μM) was found to produce a faster rate of inhibition and was applied for subsequent experiments. As shown in Figure 5.1, bath application of PX-12 (100 μM) partially inhibited T-type Ca^{2+} currents in a poorly reversible manner. L-type Ca^{2+} currents were similarly inhibited by PX-12 (100 μM ; Figure 5.1) although to a slightly lesser extent than was observed for T-type Ca^{2+} currents. T-type Ca^{2+} currents were recorded under conditions which favour T-type Ca^{2+} channels (i.e. low stimulating-voltages and using Ca^{2+} as the charge carrier). However, the sustained component of some T-type Ca^{2+} current traces indicated a small contribution of high voltage-activated (HVA) channels (Figure 5.1). Due to the potential summation of A7r5 T- and L-type Ca^{2+} currents, further discussed in Chapter 3, recombinant HEK293/ $\text{Ca}_v3.1$ and HEK293/ $\text{Ca}_v3.2$ cells were used for all subsequent recordings.

Proliferation studies described in Chapter 4 demonstrated that HEK293/ $\text{Ca}_v3.2$ cells were more sensitive to the anti-proliferative effects of PX-12 and AuF, when compared to HEK293/ $\text{Ca}_v3.1$ and wild-type (wt) HEK293 cells. In order to investigate this isoform specific difference further, $\text{Ca}_v3.1$ and $\text{Ca}_v3.2$ currents were recorded from HEK293/ $\text{Ca}_v3.1$ and HEK293/ $\text{Ca}_v3.2$ cells respectively. Bath application of PX-12 (1-300 μM) was found to inhibit both $\text{Ca}_v3.1$ and $\text{Ca}_v3.2$ channels in a concentration-dependent manner, with almost complete inhibition achieved with 300 μM PX-12. The

sensitivity of each channel type was similar, although PX-12 was slightly more potent in inhibiting Ca_v3.2 compared to Ca_v3.1 currents (Figure 5.2).

Current-voltage (I-V) protocols demonstrated that PX-12 (30μM) significantly inhibited Ca_v3.1 and Ca_v3.2 currents at all activating test potentials (-100mV to +60mV), as shown in Figure 5.3. This revealed that PX-12-mediated inhibition was voltage-independent. Importantly, no significant effects on Ca_v3.1 and Ca_v3.2 current amplitude were observed when the vehicle control (DMSO) was applied alone. As PX-12 washout was not accompanied by any recovery in current amplitude, PX-12-mediated inhibition was shown to be irreversible, at least over the ~10-15min timescale examined. Contrastingly, following inhibition with PX-12 (30μM) the amplitude of both Ca_v3.1 and Ca_v3.2 currents was essentially fully recovered by exposure to the reducing agent dithiothreitol (DTT, 1mM). DTT also enhanced Ca_v3.1 and Ca_v3.2 current amplitudes when applied in isolation, as shown by Figure 5.4 and Figure 5.5 for Ca_v3.1 and Ca_v3.2 currents respectively. These findings show that PX-12 inhibits both Cav3.1 and Cav3.2 channels by a redox-sensitive mechanism.

During its development PX-12 was shown to inhibit Trx directly, through both reversible and irreversible thioalkylation of Cys residues (Kirkpatrick *et al.*, 1998). In order to determine whether PX-12-mediated inhibition of Ca_v3.1 and Ca_v3.2 currents was due to Trx inhibition, the effects of reduced thioredoxin (rTrx) on current amplitudes was examined. As illustrated in Figure 5.6, bath application of rTrx (4μg/ml) was without significant effect on Ca_v3.1 currents. In addition, rTrx failed to reverse the inhibitory effects of PX-12. In direct contrast, rTrx caused significant reversal of the effects of PX-12 on Ca_v3.2 currents, and also modestly enhanced the amplitude of Ca_v3.2 currents when applied in isolation (Figure 5.7). These findings demonstrate that PX-12-mediated inhibition of Ca_v3.2, but not Ca_v3.1, is in part due to Trx inhibition. They also indicate that a Trx-independent mechanism of PX-12-mediated T-type Ca²⁺ channel inhibition occurs, which does not discriminate between Ca_v3.1 and Ca_v3.2 channels.

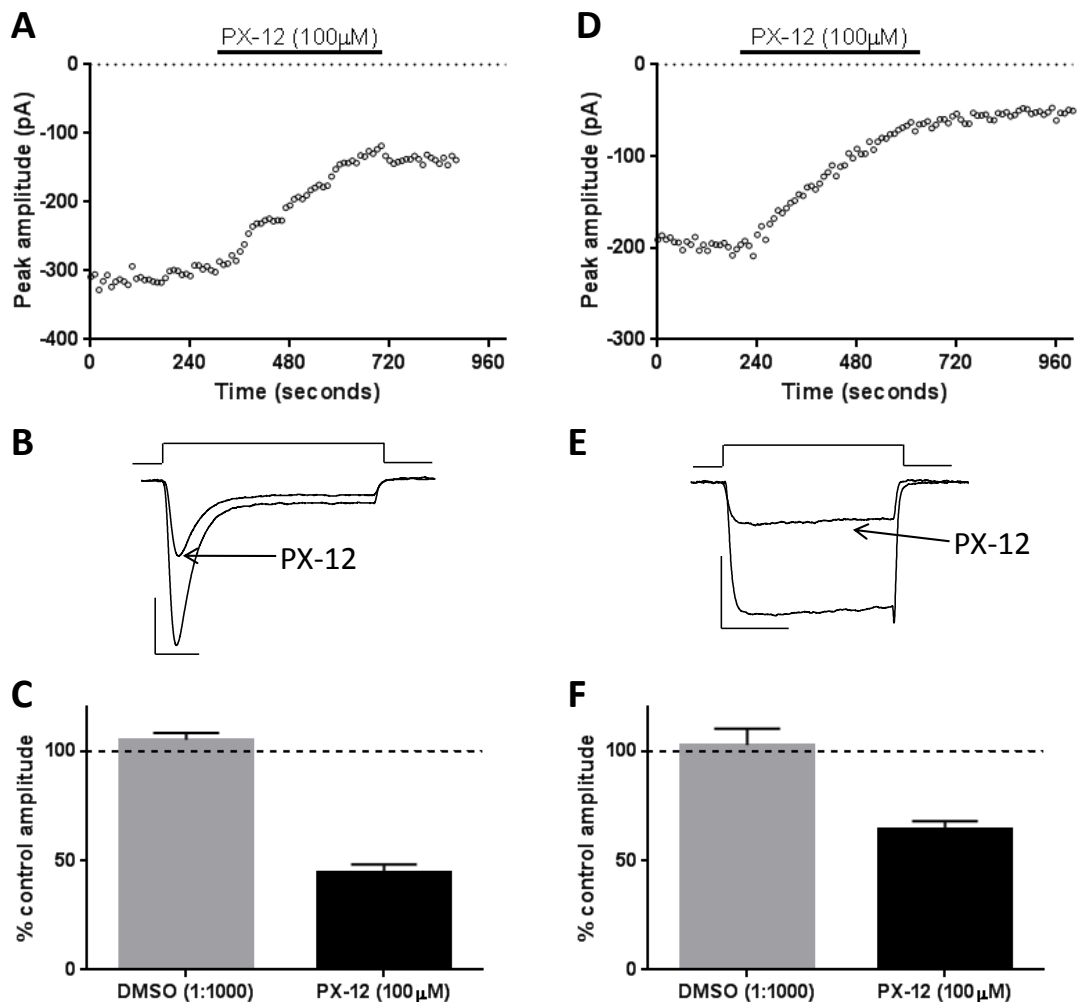


Figure 5.1. PX-12 inhibits native T-type and L-type Ca²⁺ currents in A7r5 cells

Whole-cell patch-clamp recordings from A7r5 cells; **A-C**, “T-type” Ca²⁺ channel recordings evoked by 200ms step-depolarisations from -80 to -20mV (0.1Hz), with Ca²⁺ (15mM) as the charge carrier. **D-F**, “L-type” Ca²⁺ channel recordings evoked by 100ms step-depolarisations from -50 to +20mV (0.1Hz), with Ba²⁺ (20mM) as the charge carrier. Due to the potential activation of L-type mediated Ca²⁺ current using the T-type SS protocol and vice versa, “T-type” and “L-type” currents are labelled with quotation marks. **A**, Example time-series plot illustrating “T-type” Ca²⁺ current amplitude and the effects of bath application of PX-12 (100 μM, black bar). **B**, Example “T-type” Ca²⁺ current trace corresponding with (A) showing effects of PX-12 (as labelled), scale bar, 100pA (vertical), 40ms (horizontal). **C**, Bar chart illustrating peak (mean ± s.e.m) “T-type” Ca²⁺ current amplitude (% of control amplitude) following exposure to DMSO (vehicle control 1:1000, grey box, n=4) and PX-12 (100 μM, black box, n=6). **D-F**, As (A-C), except showing L-type Ca²⁺ currents. **F**, DMSO n=4, PX-12 n=7.

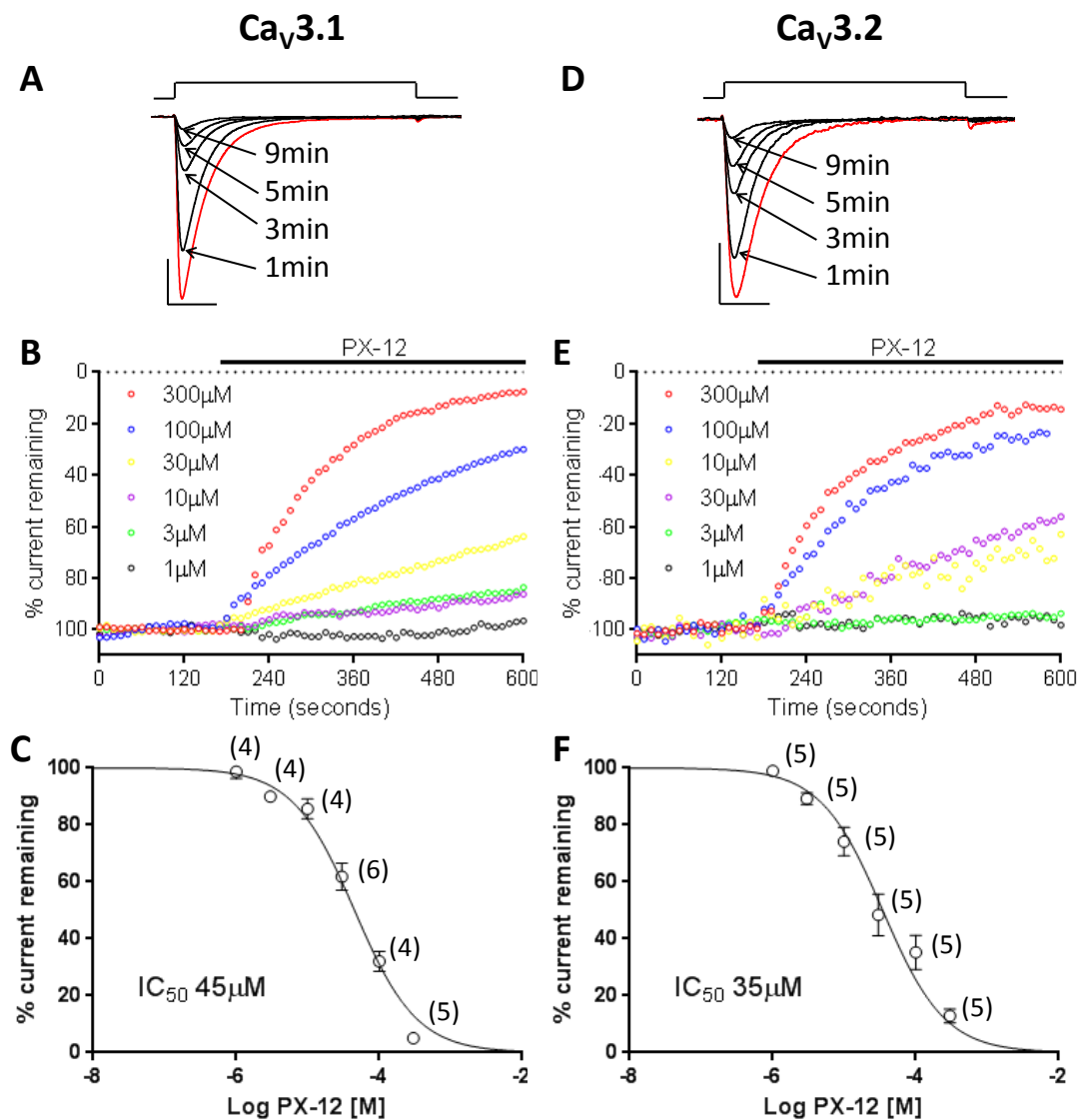


Figure 5.2. PX-12 inhibits Ca_v3.1 and Ca_v3.2 channels in a concentration-dependent manner

Whole-cell patch-clamp recordings from HEK293/Ca_v3.1 (A-C) and HEK293/Ca_v3.2 cells (D-F), currents evoked by step-depolarisations (200ms duration, 0.1Hz) from -80mV to -20mV. **A**, Example Ca_v3.1 current trace under control conditions (red trace) and during exposure to PX-12 (300μM) over a 10 minute period as labelled. Scale bar 400pA (vertical), 40ms (horizontal). **B**, Example time-series plots showing representative examples of the effects of PX-12 (1-300μM, as indicated), applied to the extracellular solution (black bar), on peak Ca_v3.1 current amplitude (% of control amplitude). **C**, Concentration-response (mean ± s.e.m) relationship graph showing the effects of PX-12 (1-300μM) on peak Cav3.1 current amplitude (% of control amplitude), n numbers in parentheses. Data were fitted with log-inhibitor normalised-response curves with extended ranges. **D-F**, As (A-C), except showing Ca_v3.2 currents. **D**, Scale bar 200pA (vertical), 40ms (horizontal).

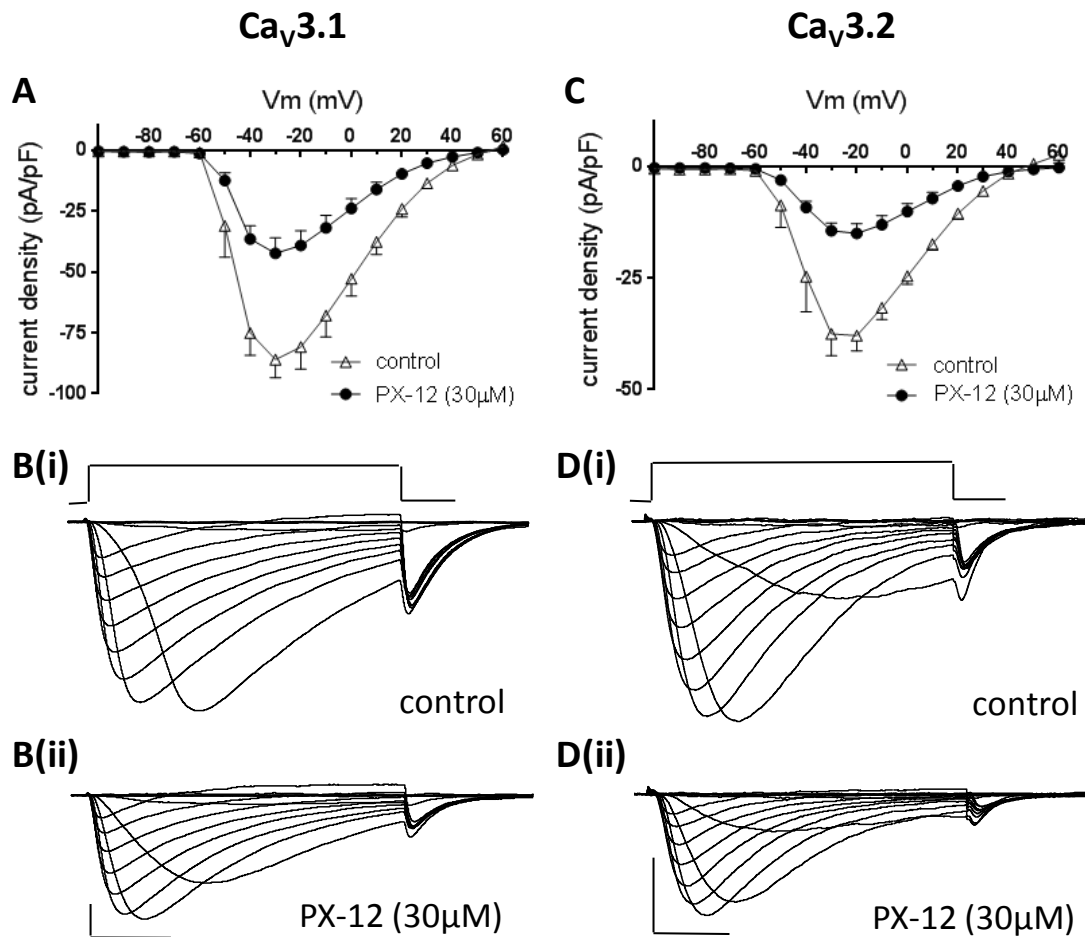


Figure 5.3. PX-12 inhibits Ca_v3.1 and Ca_v3.2 currents in a voltage-independent manner

Whole-cell patch-clamp recordings from HEK293/Ca_v3.1 (A-B) and HEK293/Ca_v3.2 (C-D) cells. Currents evoked by 80ms step-depolarisations (-100mV to +60mV in 10mV increments) from -80mV (V_h). **A**, Current-density (mean ± s.e.m.) vs. voltage (I-V) relationships for Ca_v3.1, before (open triangles) and during (solid circles) exposure to PX-12 (30 μM, n=6). **B**, Example Ca_v3.1 I-V traces in **(i)** control conditions and **(ii)** during PX-12 (30 μM) treatment. **C-D**, As (A-B), except showing Ca_v3.2 responses, n=11.

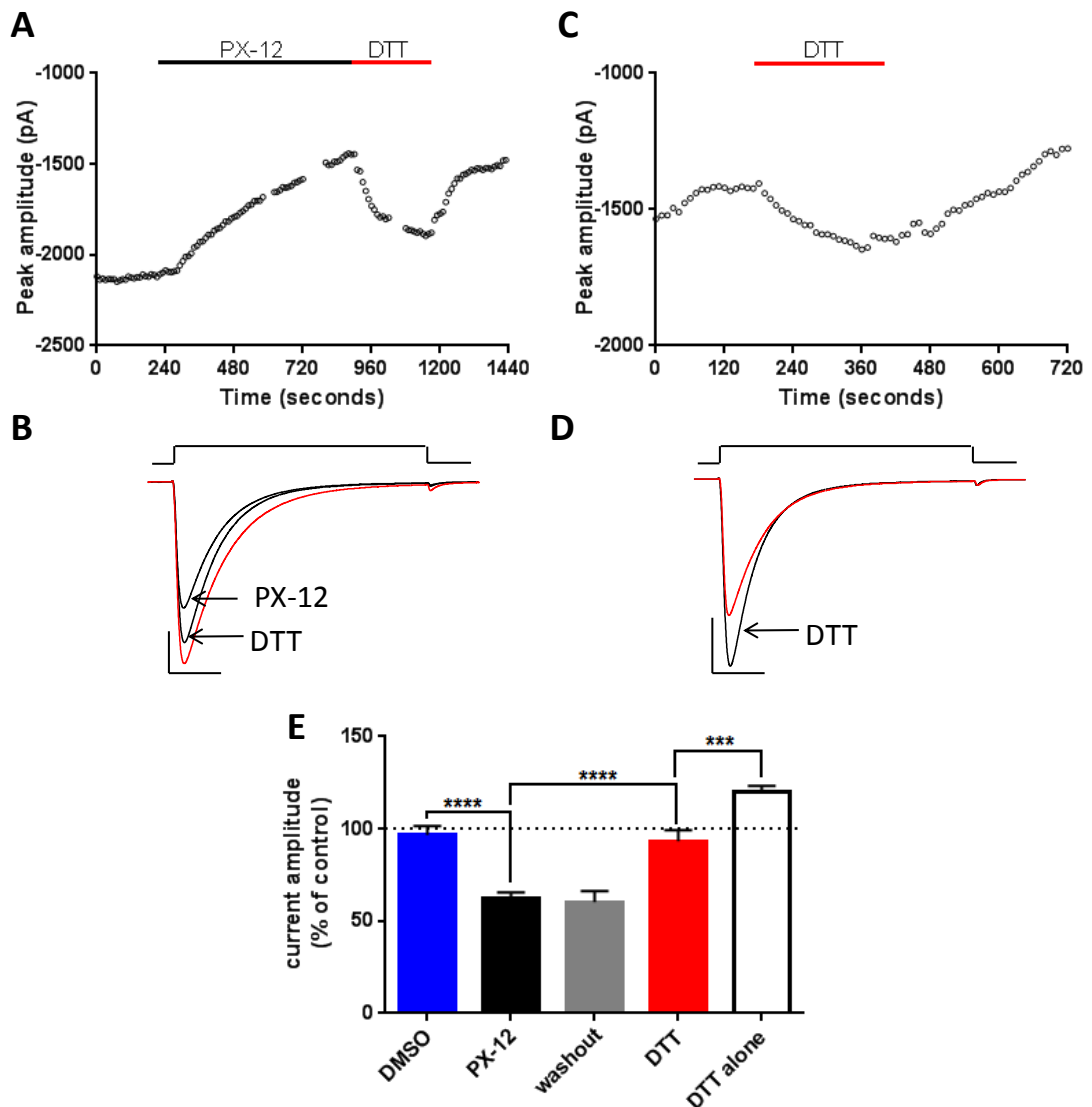


Figure 5.4. DTT fully reverses PX-12-mediated inhibition of $Ca_v3.1$ channels

Whole-cell patch-clamp recordings from HEK293/ $Ca_v3.1$ cells, currents evoked by 200ms (0.1Hz) step-depolarisations from -80 to -20mV. **A**, Example time-series plot showing inhibition of $Ca_v3.1$ current amplitude by PX-12 (30 μ M, black bar) and reversal by DTT (1mM, red bar). **B**, Corresponding, $Ca_v3.1$ current traces (from A) under control conditions (red trace) and during exposure to PX-12 and DTT (as labelled). Scale bar 500pA (vertical), 40ms (horizontal). **C-D**, As (A-B), except showing the effects of DTT (1mM) applied in isolation. **E**, Bar chart (mean \pm s.e.m) showing the effects on $Ca_v3.1$ current amplitude (% of control) of DMSO (blue bar, 1:1000, n = 5), PX-12 (black bar, 30 μ M, n=12), PX-12 washout (grey bar, n=5), DTT (1mM) applied after PX-12 (red bar, n=7) and DTT applied in isolation (white bar, 1mM, n=11). Data were analysed by one-way ANOVA with Bonferroni's post-hoc comparison test, *** p <0.001, **** p <0.0001.

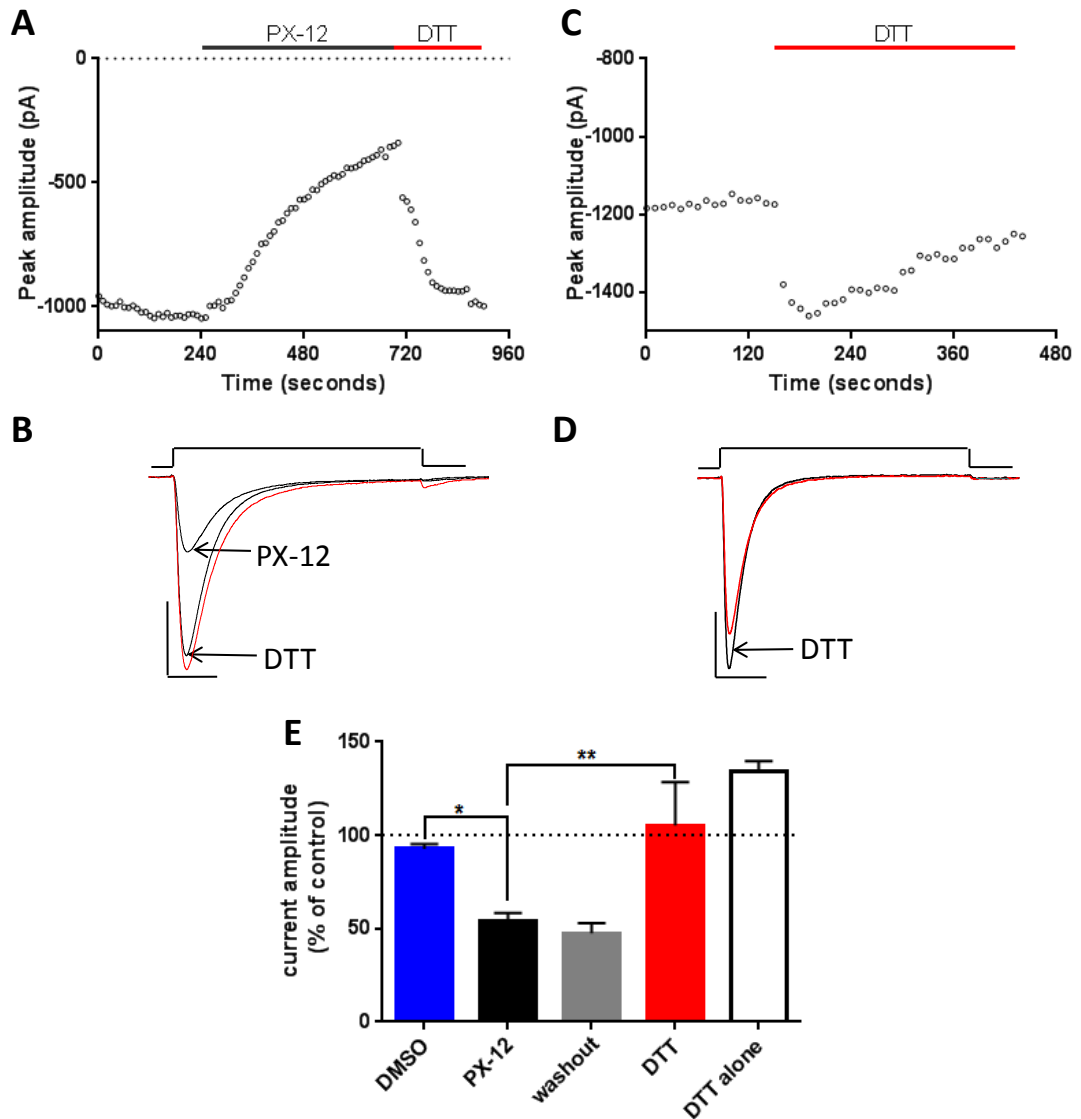


Figure 5.5. DTT fully reverses PX-12-mediated inhibition of $Ca_v3.2$ currents

Whole-cell patch-clamp recordings from HEK293/ $Ca_v3.2$ cells, currents evoked by 200ms (0.1Hz) step-depolarisations from -80 to -20mV. **A**, Example time-series plot showing inhibition of peak $Ca_v3.2$ current amplitude by PX-12 (30 μ M, black bar) and reversal by DTT (1mM, red bar). **B**, Corresponding $Ca_v3.2$ current traces (from A) under control conditions (red trace), and during exposure to PX-12 and DTT (as labelled). Scale bar 400pA (vertical), 40ms (horizontal). **C-D**, As (A-B), except showing the effects of DTT (1mM) applied in isolation. Scale bar 500pA (vertical), 40ms (horizontal). **E**, Bar chart (mean \pm s.e.m) showing the effects on $Ca_v3.2$ current amplitude (% of control) of DMSO (blue bar, 1:1000, n = 5), PX-12 (black bar, 30 μ M, n=13), PX-12 washout (grey bar, n=6), DTT applied after PX-12 (red bar, 1mM, n=7) and DTT applied alone (white bar, 1mM, n=12). Data were analysed using one-way ANOVA with Bonferroni's post-hoc comparison test, * $p \leq 0.05$, ** $p \leq 0.01$.

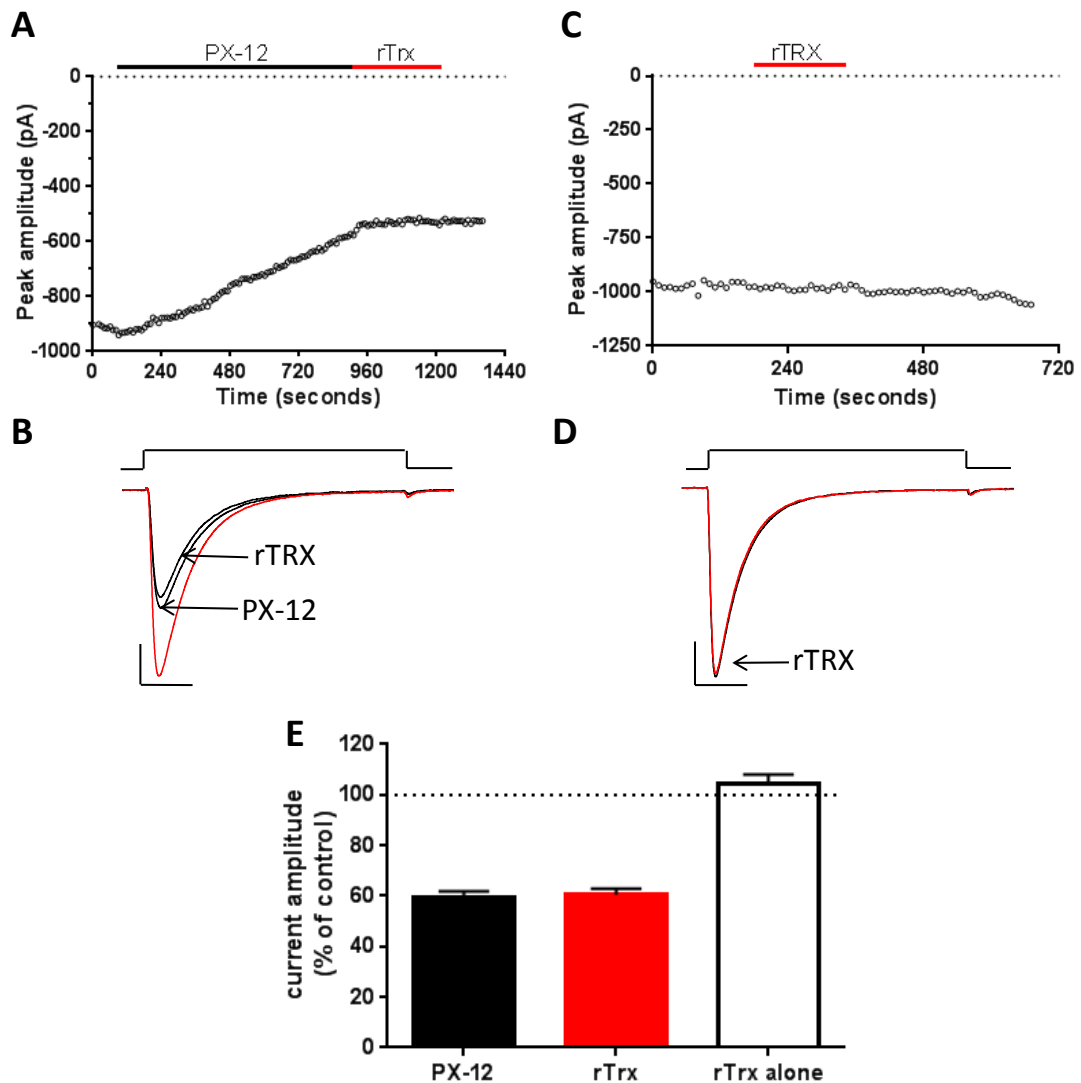


Figure 5.6. rTrx does not reverse PX-12-mediated inhibition of $Ca_v3.1$ channels

Whole-cell patch-clamp recordings from HEK293/ $Ca_v3.1$ cells, currents evoked by 200ms (0.1Hz) step-depolarisations from -80 to -20mV. **A**, Example time-series plot showing inhibition of peak $Ca_v3.1$ current amplitude by PX-12 (30 μ M, black bar) and the lack of effect of rTrx (4 μ g/ml, red bar). **B**, Corresponding $Ca_v3.1$ current traces (from A) under control conditions (red trace), and during exposure to PX-12 and rTrx (as labelled). Scale bar 200pA (vertical), 40ms (horizontal). **C-D**, As (A-B), except showing no effect of rTrx (4 μ g/ml, red bar) applied in isolation. **E**, Bar chart (mean \pm s.e.m) showing the effects on $Ca_v3.1$ current amplitude (% of control) of PX-12 (black bar, 30 μ M, n=13), rTrx (4 μ g/ml) applied after PX-12 (red bar, n=13) or rTrx applied in isolation (white bar, 4 μ g/ml, n=11). PX-12 and rTrx conditions were analysed using paired Student's t-tests, no significant differences were observed.

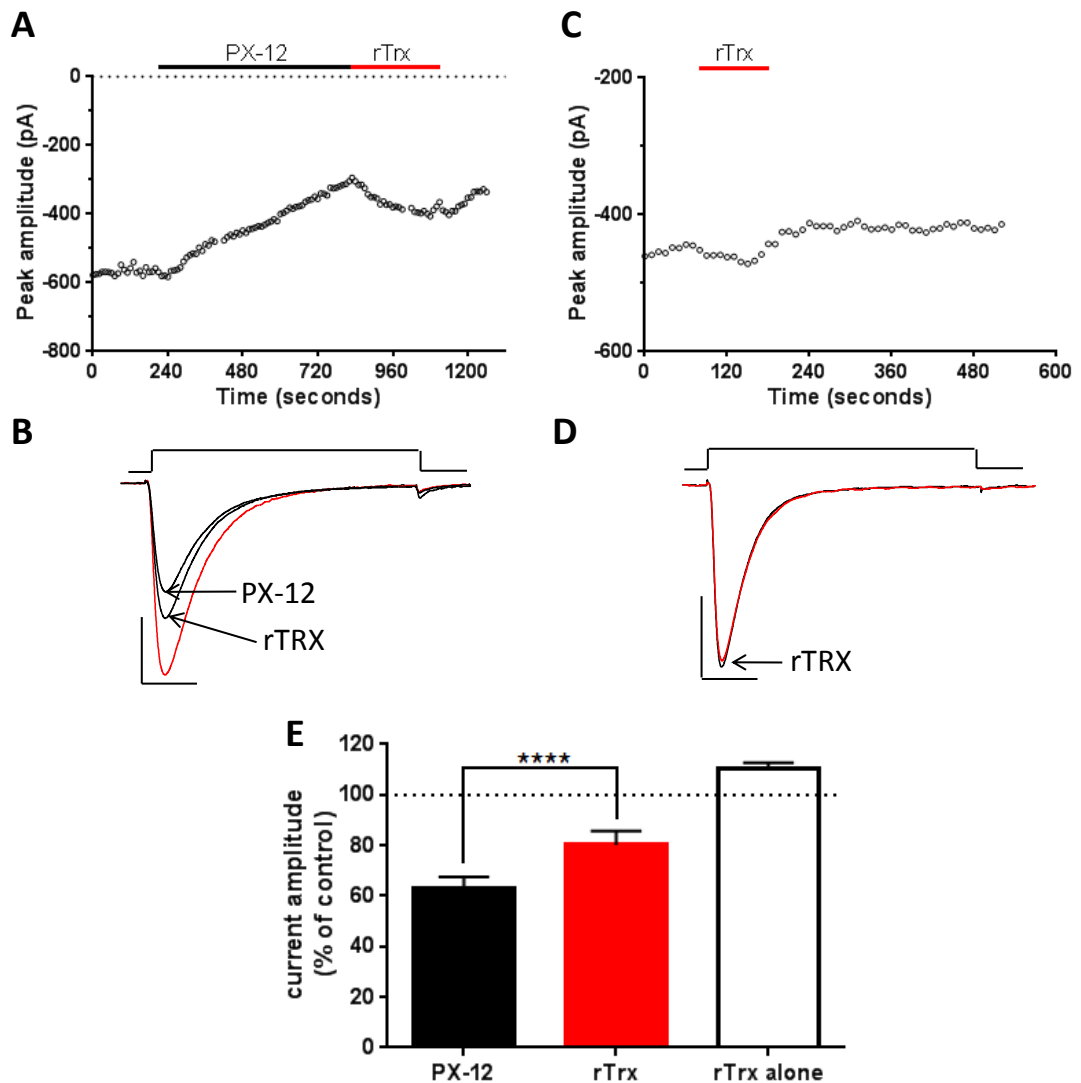


Figure 5.7. rTrx partially reverses PX-12-mediated inhibition of $Ca_v3.2$ channels

Whole-cell patch-clamp recordings taken from HEK293/ $Ca_v3.2$ cells, currents evoked by 200ms (0.1Hz) step-depolarisations from -80 to -20mV. **A**, Example time-series plot showing inhibition of peak $Ca_v3.2$ current amplitude by PX-12 (30 μ M, black bar) and partial reversal by rTrx (4 μ g/ml, red bar). **B**, Corresponding $Ca_v3.2$ current trace (from A) under control conditions (red trace), and during exposure to PX-12 and rTrx (as labelled). Scale bar 200pA (vertical), 40ms (horizontal). **C-D**, As (A-B), except showing the effects of rTrx (4 μ g/ml, red bar) in isolation. **E**, Bar chart (mean \pm s.e.m) showing the effects on $Ca_v3.2$ current amplitude (% of control) of PX-12 (black bar, 30 μ M, n=10), rTrx (4 μ g/ml) applied after PX-12 (red bar, n=10) or rTrx applied alone (white bar, 4 μ g/ml, n=6). Data were analysed using paired Student's t-tests, ****p \leq 0.0001.

To further investigate the apparent selective regulation of $Ca_v3.2$ channels by Trx, the effects of AuF on HEK293/ $Ca_v3.1$ and HEK293/ $Ca_v3.2$ currents were also examined. As AuF inhibits Trx indirectly via inhibition of thioredoxin reductase (TrxR), cells were pre-treated with AuF ($3\mu\text{M}$, 30mins) prior to recording currents to allow the effects of AuF on Trx to equilibrate. As illustrated in Figure 5.8, the current-density of HEK293/ $Ca_v3.1$ cells was not significantly altered by pre-treatment with AuF. Furthermore, the degree of $Ca_v3.1$ current potentiation by DTT was similar between control and AuF conditions. In stark contrast however, AuF pre-treatment significantly reduced the current-density of HEK293/ $Ca_v3.2$ cells, and also dramatically increased the degree of $Ca_v3.2$ current enhancement by DTT (Figure 5.9). These data confirmed that Trx positively and selectively regulates $Ca_v3.2$ channels.

Initial experiments in A7r5 cells had shown that both native T- and L-type Ca^{2+} currents were inhibited by PX-12, indicating that both Ca_v subtypes were regulated by Trx (Figure 5.1). However, as PX-12 was subsequently found to inhibit recombinant $Ca_v3.1$ currents via a Trx-independent mechanism (Figure 5.6), further investigation was required to establish if Trx regulates native Cav3 channels in these cells. As illustrated in Figure 5.10, bath application of rTrx did not significantly reverse PX-12-mediated inhibition of T-type Ca^{2+} current amplitudes, confirming that PX-12 was acting independently of Trx. Furthermore, rTrx did not generally alter T-type Ca^{2+} current amplitude when applied in isolation (Figure 5.10). As previous investigations had shown that Trx selectively regulated $Ca_v3.2$ currents, this observation is consistent with $Ca_v3.1$ being the primary T-type Ca^{2+} channel isoform expressed within A7r5 cells (Chapter 3). These findings indicate that Trx does not regulate A7r5 T-type Ca^{2+} currents, and also supports the finding that PX-12-mediated inhibition of Ca_v channels is Trx-independent.

Of considerable interest however, is that the amplitude of a very limited number of T-type Ca^{2+} currents in A7r5 cells (1 of 5 cells) was clearly enhanced by rTrx under control conditions (i.e. when applied without prior treatment with PX-12). Corresponding immunohistochemistry conducted on the same batch of A7r5 cells revealed a dramatic increase in $Ca_v3.2$ -immunoreactivity (IR) when compared to $Ca_v3.1$ -IR, which very likely accounted for the observed increase in sensitivity to Trx (**Error! Reference source**

not found.) Additionally, whilst Ca_v3.1-IR was directly comparable in terms of intensity and localisation to that previously reported (Chapter 3), findings regarding Ca_v3.2-IR were contrasting. Specifically, the pattern of Ca_v3.2-IR was much brighter with dense peri-nuclear regions detected alongside the nuclear staining previously reported (Chapter 3). Whilst this observation is only preliminary it suggests that Ca_v3.2 expression may be dynamically regulated in A7r5 cells. It is also consistent with the idea that only T-type Ca²⁺ currents facilitated in part by Ca_v3.2 channels in A7r5 cells are regulated by Trx. This suggests that the pro-proliferative effects of Trx in VSMCs may be dependent on Ca_v3.2 expression levels.

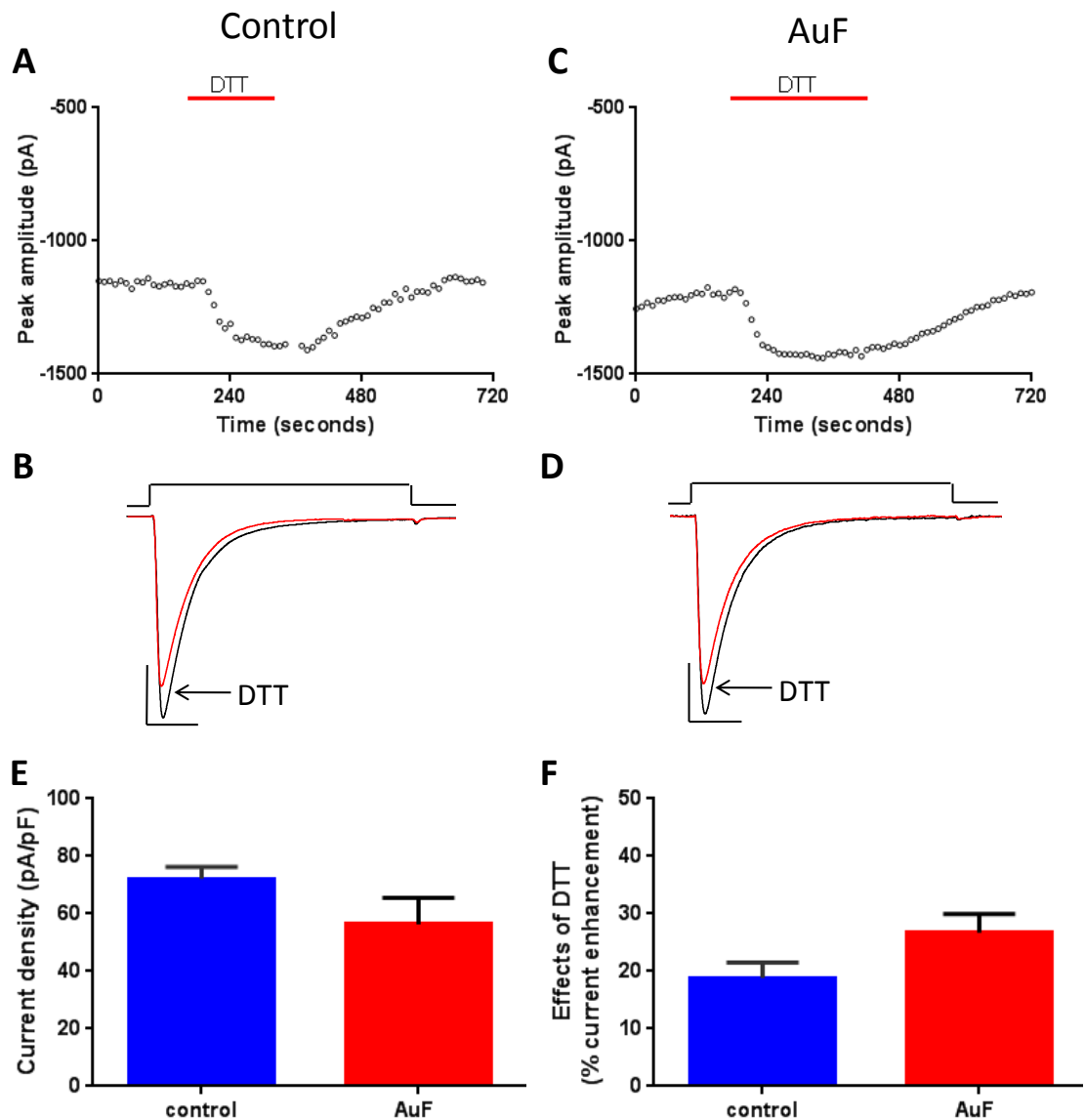


Figure 5.8. Pre-treatment with AuF has no effect on Ca_v3.1 currents

Whole-cell patch-clamp recordings from HEK293/Ca_v3.1 cells under control conditions (A-B) and following pre-treatment with AuF (3μM, 30mins, C-D). Currents evoked by 200ms (0.1Hz) step-depolarisations from -80 to -20mV. **A**, Example time-series plot showing effects of DTT (1mM) on Ca_v3.1 current peak amplitude under control conditions. **B**, Corresponding Ca_v3.1 current trace (from A) under control conditions (red trace) and during exposure to DTT (as labelled). Scale bar 400pA (vertical), 40ms (horizontal). **C-D**, As (A-B), except showing the effects of DTT (1mM) following AuF pre-treatment. **E**, Bar chart showing (mean ± s.e.m) Ca_v3.1 current-density under control conditions (blue bar, n=5) and after pre-treatment with AuF (3μM, 30mins, red bar, n = 6). **F**, Bar chart showing (mean ± s.e.m) Ca_v3.1 current amplitude enhancement by DTT (1mM), applied under both control conditions (blue bar, n=6) and after pre-treatment with AuF (3μM, 30mins, red bar, n = 6). Data were analysed using unpaired Student's t-tests, no significant differences observed.

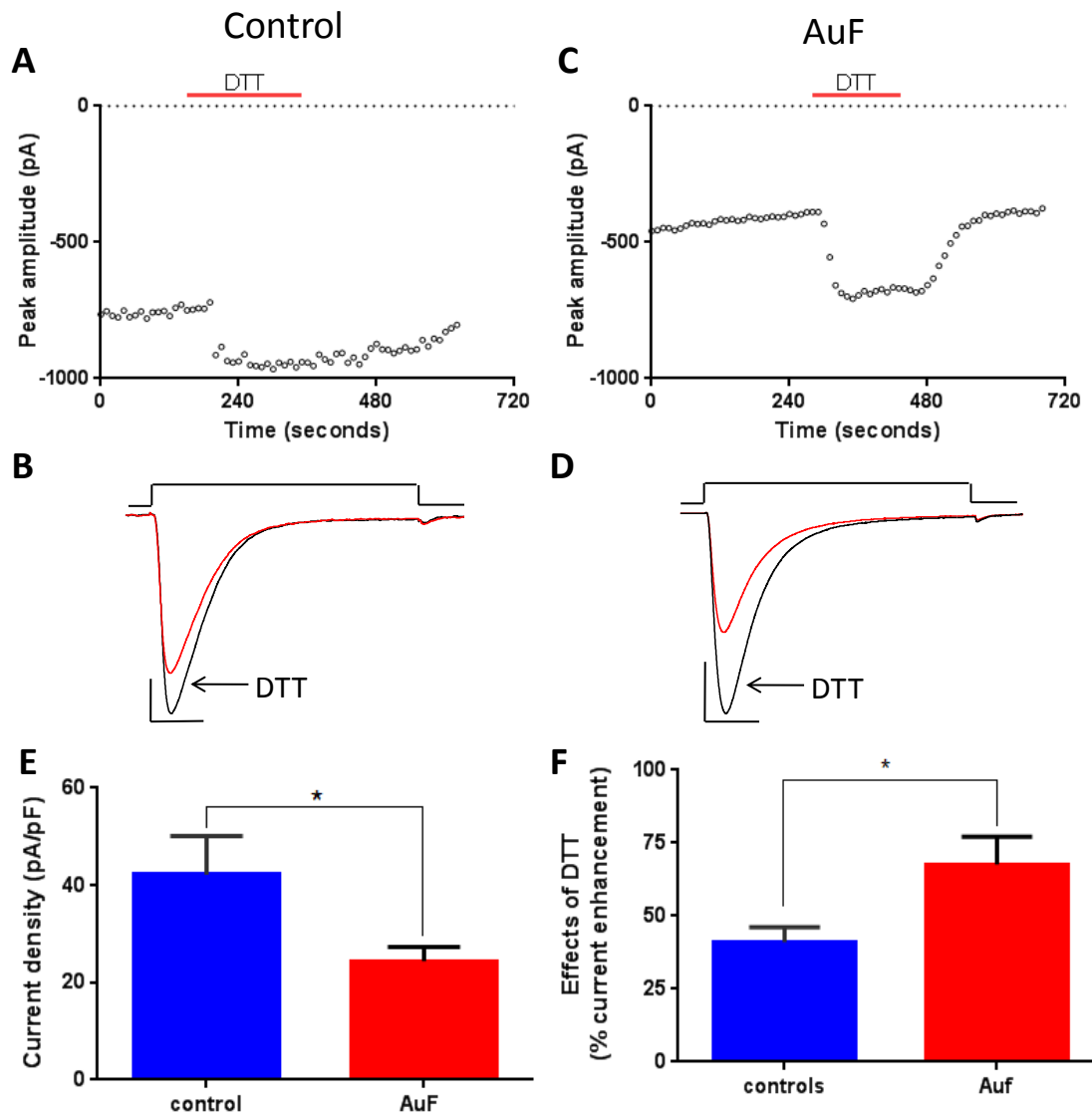


Figure 5.9. AuF reduces HEK293/ $Ca_v3.2$ cell current-density and increases DTT-mediated current enhancement

Whole-cell patch-clamp recordings from HEK293/ $Ca_v3.2$ cells under control conditions (A-B) and following AuF ($3\mu\text{M}$, 30mins) pre-treatment (C-D). Currents evoked by 200ms (0.1Hz) step-depolarisations from -80 to -20mV . **A**, Example time-series plot showing effects of DTT (1mM) on $Ca_v3.2$ current peak amplitude under control conditions. **B**, Corresponding $Ca_v3.2$ current trace (from A) under control conditions (red trace), and during exposure to DTT (as labelled). Scale bar 200pA (vertical), 40ms (horizontal). **C-D**, As (A-B) except showing the effects of DTT (1mM) following AuF pre-treatment. **E**, Bar chart showing (mean \pm s.e.m) $Ca_v3.2$ current-density under control conditions (blue bar, $n=11$) and after pre-treatment with AuF ($3\mu\text{M}$, 30mins, red bar, $n = 14$). **F**, Bar chart showing (mean \pm s.e.m) $Ca_v3.2$ current amplitude enhancement by DTT (1mM), applied under both control conditions (blue bar, $n=13$) and after pre-treatment with AuF ($3\mu\text{M}$, 30mins, red bar, $n = 14$). Data were analysed using unpaired Student's t-tests, $*p\leq 0.05$.

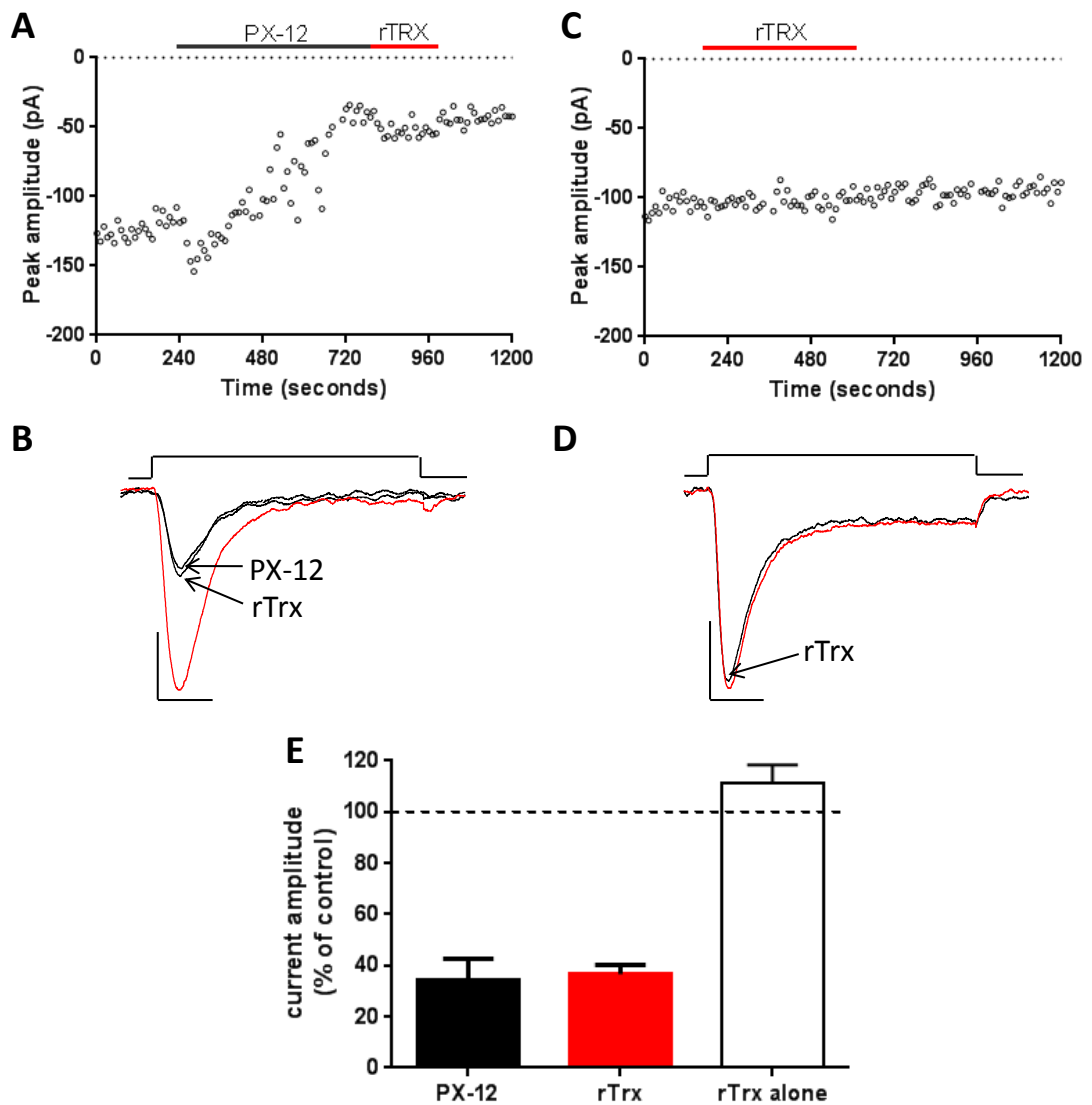


Figure 5.10. rTrx does not reverse PX-12-mediated inhibition of A7r5 T-type Ca^{2+} currents

Whole-cell patch-clamp recordings from A7r5 cells, currents evoked by 200ms (0.1Hz) step-depolarisations from -80 to -20mV. **A**, Example time-series plot showing inhibition of T-type Ca^{2+} current peak amplitude by PX-12 (30 μM , black bar) and the lack of effect of rTrx (4 $\mu\text{g}/\text{ml}$, red bar) when applied to the perfusate. **B**, Corresponding T-type Ca^{2+} current trace (from A) under control conditions (red trace), and during exposure to PX-12 and rTrx (as labelled). Scale bar 40pA (vertical), 40ms (horizontal). **C-D**, As (A-B), except showing the effects of rTrx (4 $\mu\text{g}/\text{ml}$, red bar) in isolation. **E**, Bar chart (mean \pm s.e.m) showing the effects of PX-12 (black bar, 100 μM , n=4) and rTrx (4 $\mu\text{g}/\text{ml}$) applied after PX-12 (red bar, n=4) or rTrx applied alone (white bar, 4 $\mu\text{g}/\text{ml}$, n=5), on A7r5 T-type Ca^{2+} current amplitude (% of control). Data were analysed using unpaired Student's t-tests, no significant differences were observed.

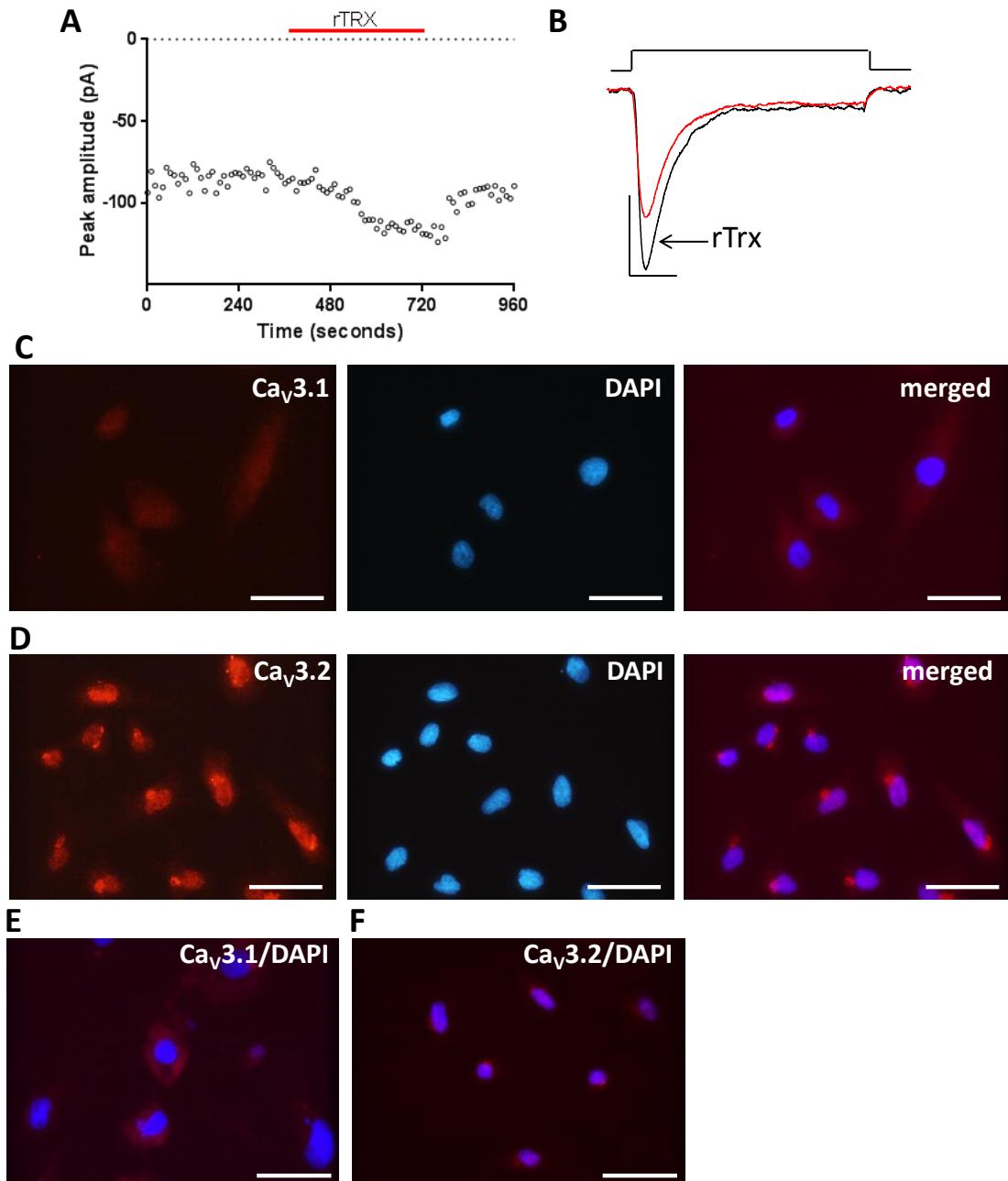


Figure 5.11. Increased A7r5 Ca_v3.2 channel expression correlates with T-type Ca²⁺ current rTrx-sensitivity

Electrophysiology and immunohistochemistry was conducted on the same batch of A7r5 cells (A-D). **A-B**, Whole-cell patch-clamp recordings from A7r5 cells, currents evoked by 200ms (0.1Hz) step-depolarisations from -80 to -20mV. **A**, Example time-series plot showing regulation of T-type Ca²⁺ current amplitude by rTrx (4µg/ml, red bar) applied to the perfusate. **B**, Corresponding T-type Ca²⁺ current traces (from A) under control conditions (red trace), and during exposure to rTrx (as labelled). Scale bar 50pA (vertical), 40ms (horizontal). **C-D**, Dual-label immunofluorescence using anti-Ca_v3.1 (1:100, **C**) or anti-Ca_v3.2 (1:1000, **D**) with Alexa Fluor-555 secondary antibody (1:500) (left panels, red images) and DAPI to label cell nuclei (centre panel, blue images), merged Ca_v3.1 or Ca_v3.2 and DAPI images (right panels). Scale bars 50µm. **E-F**, As (C-D), except conducted on a different batch of A7r5 cells (images reproduced from Chapter 3) and showing only merged DAPI/Ca_v3.1 (**E**), and DAPI/Ca_v3.2 (**F**), images.

5.2.2. Mechanism of Trx-mediated $Ca_v3.2$ regulation

After establishing that $Ca_v3.2$ channels were positively and selectively regulated by Trx, the mechanism and molecular determinants of Trx sensitivity were next explored using HEK293/ $Ca_v3.2$ cells. I-V protocols revealed that AuF preferentially inhibited $Ca_v3.2$ currents at lower stimulating voltages, and produced a rightwards shift in I-V profiles (Figure 5.11). Interestingly, as T-type Ca^{2+} channels activate and inactivate at similar voltages they can facilitate a window current at resting membrane potential (V_m), which can control basal $[Ca^{2+}]_i$. In confirmation of this suggestion, $Ca_v3.2$ -mediated window currents were recorded directly from HEK293/ $Ca_v3.2$ cells using Ca^{2+} microfluorimetry (Chapter 3). As a “window current” is operationally defined as the overlap between activation and steady-state inactivation curves (Perez-Reyes, 2003), the observed AuF-mediated shift in I-V profile (Figure 5.11) could theoretically decrease the $Ca_v3.2$ -mediated Ca^{2+} window current. The AuF-mediated reduction in HEK293/ $Ca_v3.2$ current-density observed (Figure 5.9) is also likely to reduce basal Ca^{2+} influx.

$Ca_v3.2$ currents were augmented by bath-application of rTrx (Figure 5.7) indicating that the molecular determinant(s) of rTrx-sensitivity was located on the extracellular surface of the channel. As Trx uptake has been previously reported in Jurkat T-lymphoma cells (Kondo *et al.*, 2004), it was also important to assess any potential effects of applying rTrx to the intracellular environment. As shown by Figure 5.12, inclusion of rTrx (20 μ g/ml) to the patch-pipette solution did not significantly alter the current-density in HEK293/ $Ca_v3.2$ cells, after a minimum of 5 min dialysis. Furthermore, intracellular rTrx had no effect on the degree of PX-12-mediated $Ca_v3.2$ channel inhibition. Interestingly, whilst intracellular application of rTrx did not significantly alter HEK293/ $Ca_v3.2$ cell current-density, a modest enhancement was detected (Figure 5.12). This may potentially be due to cellular Trx secretion.

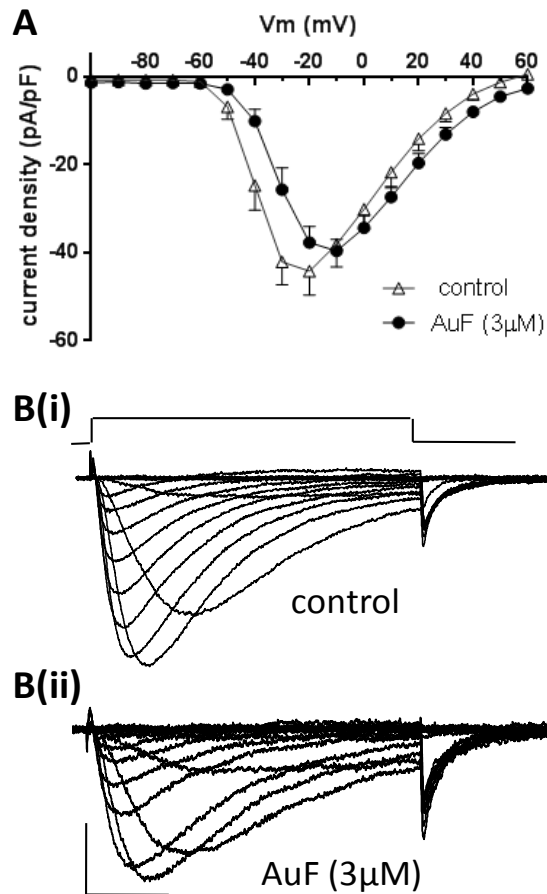


Figure 5.11. AuF inhibits $Ca_v3.2$ currents in a voltage-dependent manner

Whole-cell patch-clamp recordings from HEK293/ $Ca_v3.2$ cells, currents evoked by 80ms step-depolarisations (-100mV to +60mV in 10mV increments) from -80mV (Vh). **A**, Current-density (mean \pm s.e.m.) vs. voltage (I-V) relationships for $Ca_v3.2$ currents under control conditions (open triangles, n=11) or following AuF (3 μ M, 25mins) pre-treatment (solid circles, n=7). **B**, Example $Ca_v3.2$ I-V traces under **(i)**, control conditions and **(ii)**, following AuF (3 μ M, 25mins) pre-treatment. Scale bar 400pA (horizontal), 20ms (vertical).

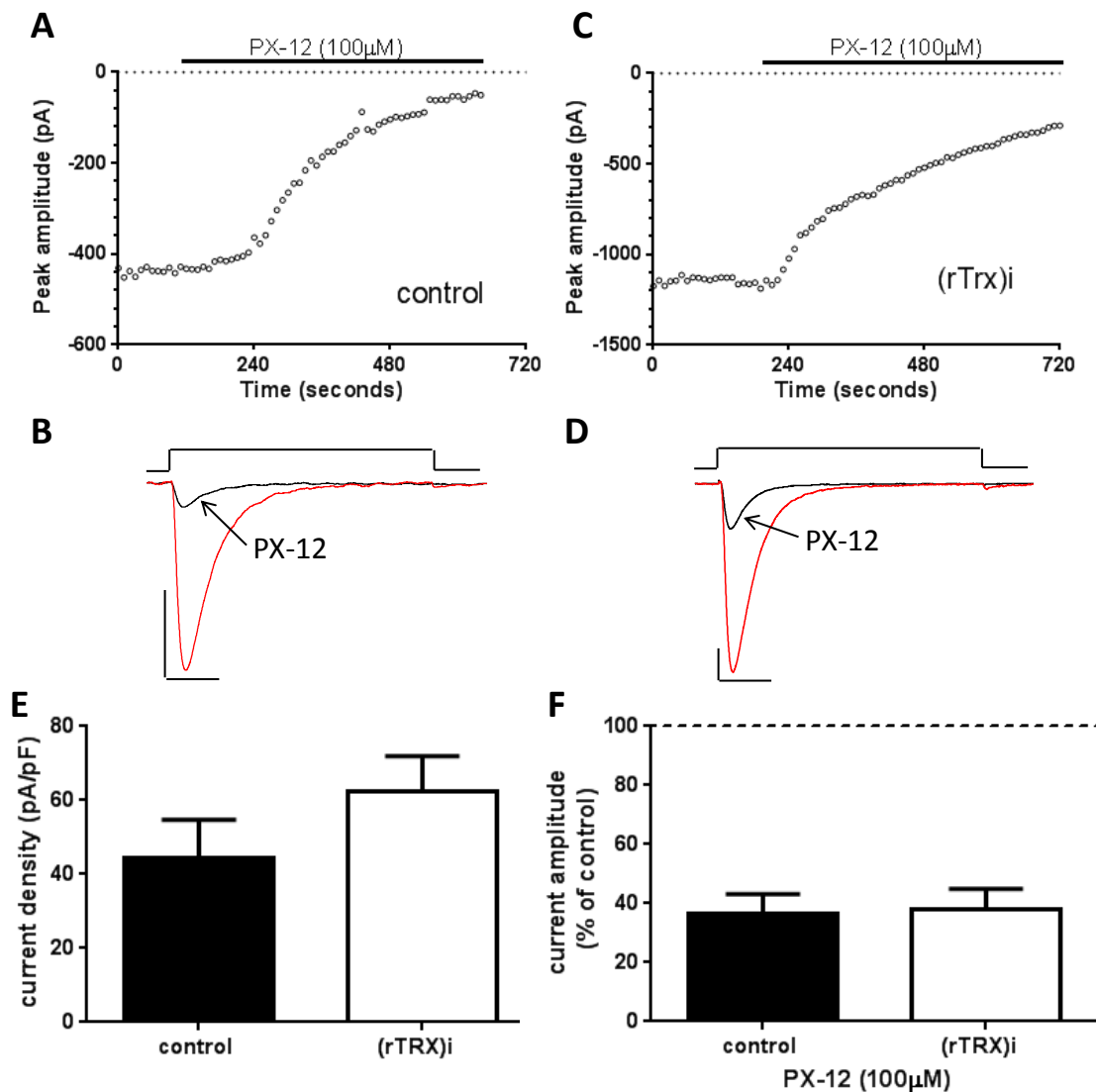


Figure 5.12. Intracellular rTrx application has no effect on Ca_v3.2 currents

Whole-cell patch-clamp recordings from HEK293/Ca_v3.2 cells under control conditions (A-B) and with rTrx (20 μg/ml) applied to the intracellular solution ((rTrx)_i) (C-D). Currents evoked by 200ms (0.1Hz) step-depolarisations from -80 to -20mV. **A**, Example time-series plot showing the effects of PX-12 (100 μM) on the peak Ca_v3.2 current amplitude recorded using standard intracellular solution. **B**, Corresponding Ca_v3.2 current traces (from A) under control conditions (red trace), and during exposure to PX-12 (as labelled). Scale bar 200pA (vertical), 40ms (horizontal). **C-D**, As (A-B), except showing the effects of PX-12 (100 μM) when rTrx (20 μg/ml) is applied to the intracellular solution. **E**, Bar chart showing (mean ± s.e.m) Ca_v3.2 current-density under control conditions (black bar, n=5) and with intracellular rTrx (20 μg/ml, (rTrx)_i) (white bar, n=5) exposure. **F**, Bar chart showing (mean ± s.e.m) inhibition of Ca_v3.2 current amplitudes (% of control) by PX-12 (100 μM) applied under control conditions (black bar, n=5) or with intracellular rTrx (20 μg/ml, (rTrx)_i) application (white bar, n=5). Data were analysed using unpaired Student's t-tests, no significant differences were observed.

A distinguishing feature of Ca_v3.2 channels is their unique sensitivity to both redox modulators and trace metals. For example, Ca_v3.2 channels are blocked by significantly lower Ni²⁺ concentrations (IC₅₀ value of 13μM) than either Ca_v3.1 and Ca_v3.3 channels (IC₅₀ values of 250μM and 216μM respectively), (Lee *et al.*, 1999). Interestingly, mutation of a single extracellular His residue at position 191 (H191) to a glutamine (Q) residue (Ca_v3.2(H191Q)), located within the S3-S4 loop of domain I, significantly reduced Ni²⁺ blockade of Ca_v3.2 channels (Kang *et al.*, 2006). His¹⁹¹ has also been shown to be responsible for ascorbate-mediated inhibition of Ca_v3.2 channels as the Ca_v3.2(H191Q) mutant channel is completely insensitive to ascorbate (Nelson *et al.*, 2007a). In order to explore the His¹⁹¹ residue as a potential molecular target for Trx, currents were recorded from HEK293 cells stably expressing recombinant Ca_v3.2(H191Q) mutant channels (HEK293/Ca_v3.2(H191Q)). In agreement with previous reports, bath application of ascorbate had no effect on Ca_v3.2(H191Q) activity (Figure 5.13).

When applied in isolation or in combination with ascorbate, PX-12 inhibited Ca_v3.2(H191Q) currents (Figure 5.13) to a similar degree as was observed for wt Ca_v3.2 channels (Figure 5.2). A key difference with wt Ca_v3.2 channels, however, was that rTrx was completely unable to reverse PX-12-mediated inhibition of Ca_v3.2(H191Q) currents (Figure 5.14). Application of rTrx under control conditions was also found to be without effect on Ca_v3.2(H191Q) currents (Figure 5.14), thereby showing that this single point mutation (H191Q) abolished Ca_v3.2 channel sensitivity to rTrx. Whilst PX-12 inhibited Ca_v3.2(H191Q) currents, when applied in isolation or co-applied with ascorbate (Figure 5.13), rTrx was unable to reverse the PX-12-mediated inhibition (Figure 5.14). These data provide conclusive evidence that the molecular target(s) of PX-12 is not the molecular determinant of Ca_v3.2 channel rTrx-sensitivity i.e. His¹⁹¹.

The effects of ascorbate on wt Ca_v3.2 currents were also examined, initially for control purposes. As illustrated in Figure 5.15, bath application of ascorbate inhibited Ca_v3.2 current amplitude, in contrast with its lack of effect on Ca_v3.2(H191Q) currents (Figure 5.13). Strikingly, when PX-12 was co-applied with ascorbate, wt Ca_v3.2 current enhancement and full reversal of ascorbate-mediated inhibition was observed. This

was highly unusual considering that both ascorbate and PX-12 had inhibitory effects on wt Ca_v3.2 current amplitudes when applied in isolation (Figure 5.15). Furthermore, co-application of ascorbate and PX-12 also significantly enhanced Ca_v3.2 tail current amplitudes on some occasions (7 out of 18 cells recorded), and appeared to reduce channel inactivation. Contrastingly, when PX-12 was applied initially in isolation prior to the subsequent co-application with ascorbate, a dual-inhibitory effect was observed (Figure 5.15). This indicates that the, as of yet unidentified, molecular target(s) for PX-12 may interact in a complex manner with His¹⁹¹.

The disulphide reductase capabilities of Trx are generally dictated by two Cys residues (Cys³² and Cys³⁵) within the active site. When in their reduced dithiol form ((SH)₂), these Cys residues transfer reducing equivalents to target proteins, as reviewed (Holmgren, 1995). In order to generate rTrx, Trx applied previously had been pre-incubated with DTT, which was removed prior to application. To examine whether the redox-state of Trx determined its ability to modulate HEK293/Ca_v3.2 currents, the effects of oxidised Trx (oTrx, i.e. non-reduced) were next examined. Findings were compared with the effects of rTrx, as detailed in Figure 5.7. Under control conditions, bath application of oTrx enhanced Ca_v3.2 current amplitudes to a similar extent as rTrx, (Figure 5.16), indicating that the effects of Trx were independent of its redox-status. Furthermore, oTrx also caused a small degree of Ca_v3.2 current enhancement following PX-12 application. In contrast to rTrx, the reversal of PX-12-mediated inhibition of Ca_v3.2 channels by oTrx was non-significant (Figure 5.17).

Under storage conditions (i.e. non-reduced), Trx lacks disulphide reductase activity, indicating that active site Cys residues will be in their oxidised disulphide form (Montano *et al.*, 2014). Freezing of tissue and cell samples, and also exposure to air, has been shown to oxidise active site Cys residues and inactivate Trx (Luthman & Holmgren, 1982). A further important, and generally overlooked, consideration when using mammalian Trx is the redox state of non-active site Cys residues (Cys⁶², Cys⁶⁹ and Cys⁷³). These non-canonical Cys residues do not infer disulphide reductase properties *per se*, but can influence the overall structure of Trx. Specifically, homodimer formation via inter-molecule disulphide bond formation between Cys⁷³ residues (Weichsel *et al.*, 1996), and intra-molecule disulphide bond

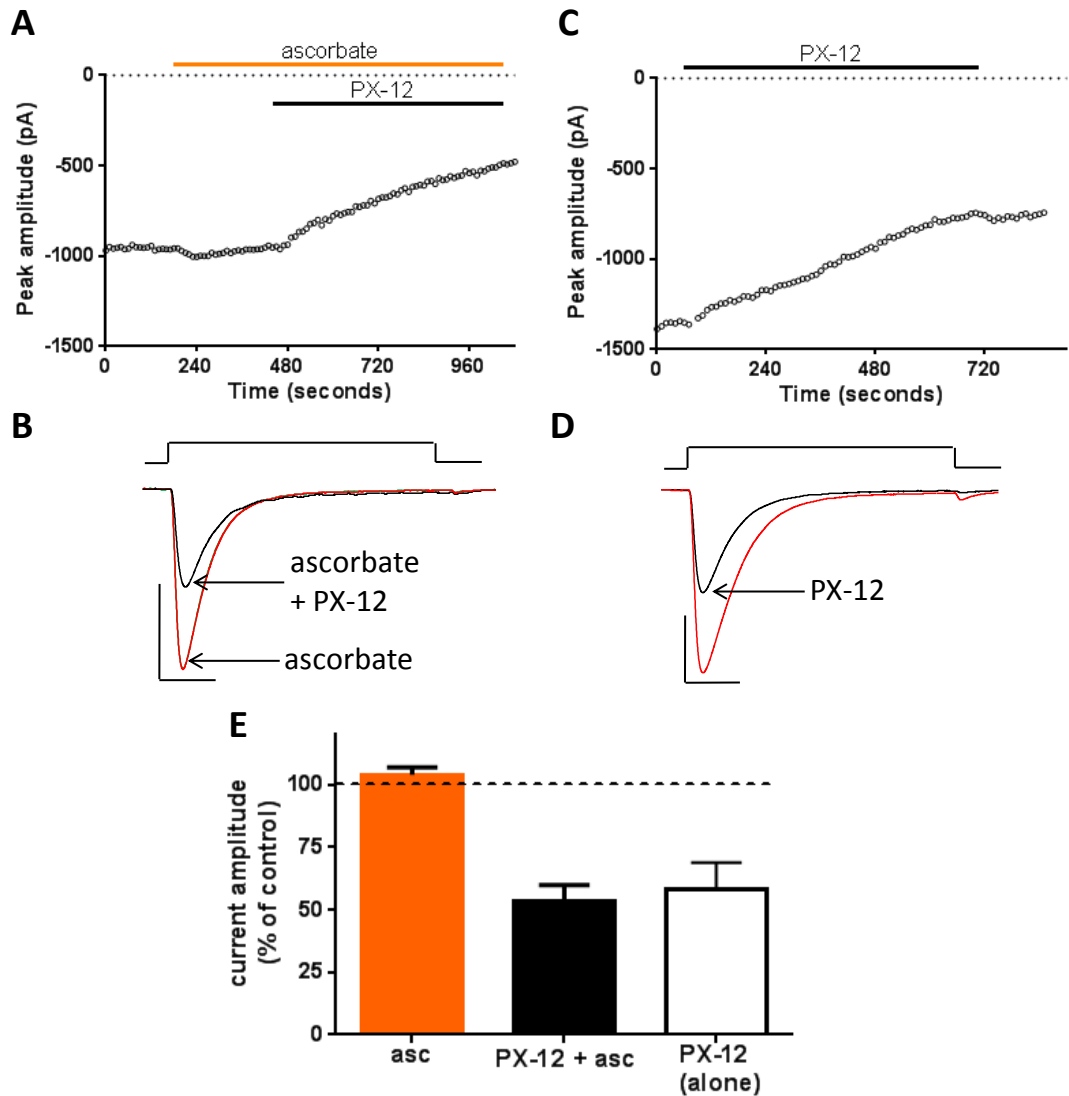


Figure 5.13. $Ca_v3.2(H191Q)$ currents are inhibited by PX-12 but not ascorbate

Whole-cell patch-clamp recordings from HEK293/ $Ca_v3.2(H191Q)$ cells, currents evoked by 200ms (0.1Hz) step-depolarisations from -80 to -20mV. **A**, Example time-series plot showing the effects of ascorbate (asc, 300 μ M, orange bar) and PX-12 (30 μ M, black bar) on peak $Ca_v3.2(H191Q)$ current amplitudes. **B**, Corresponding $Ca_v3.2(H191Q)$ current traces (from A) under control conditions (red trace) and during exposure to ascorbate (asc, 300 μ M) and PX-12 (30 μ M) as labelled. Scale bar 500pA (vertical), 40ms (horizontal). **C-D**, As (A-B), except showing the effect of PX-12 (30 μ M, black bar) in isolation. **E**, Bar chart (mean \pm s.e.m) showing the effects of ascorbate (asc, 300 μ M, orange bar, n=4), ascorbate with PX-12 (30 μ M) (black bar, n=4) and PX-12 alone (30 μ M, white bar, n=5) on $Ca_v3.2(H191Q)$ current amplitudes (% of control).

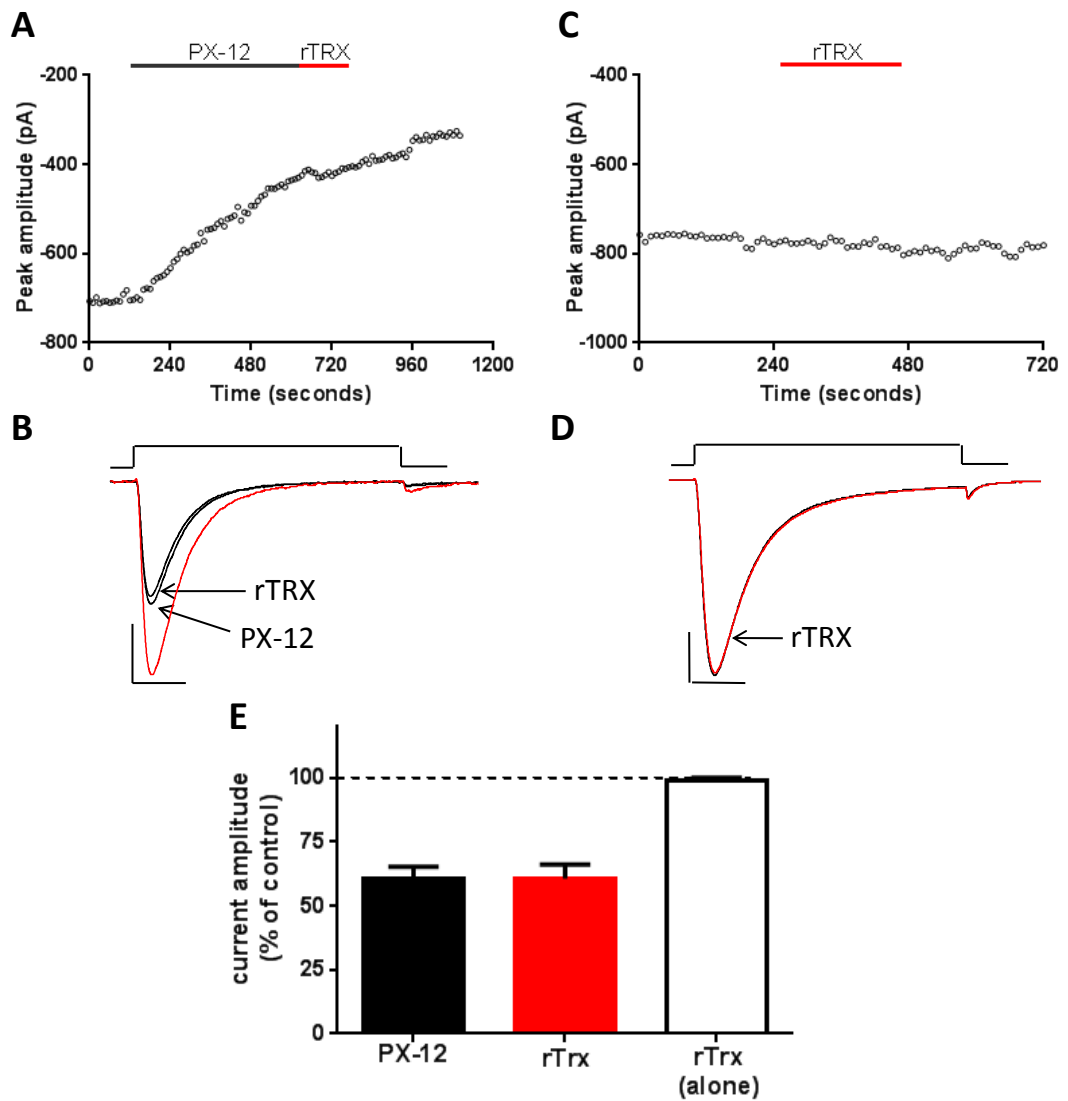


Figure 5.14. rTrx has no effect on $Ca_v3.2(H191Q)$ currents

Whole-cell patch-clamp recordings from HEK293/ $Ca_v3.2(H191Q)$ cells, currents evoked by 200ms (0.1Hz) step-depolarisations from -80 to -20mV. **A**, Example time-series plot showing inhibition of $Ca_v3.2(H191Q)$ current amplitude by PX-12 (30 μ M, black bar) and no reversal by rTrx (4 μ g/ml, red bar). **B**, Corresponding $Ca_v3.2(H191Q)$ current traces (from A) under control conditions (red trace), and during exposure to PX-12 and rTrx (as labelled). Scale bar 200pA (vertical), 40ms (horizontal). **C-D**, As (A-B), except showing the effects of rTrx (4 μ g/ml, red bar) in isolation. **E**, Bar chart (mean \pm s.e.m) showing the effects of PX-12 (black bar, 30 μ M, n=4), rTrx (4 μ g/ml) applied after PX-12 (red bar, n=4) and rTrx applied alone (white bar, 4 μ g/ml, n=4), on $Ca_v3.2(H191Q)$ current amplitudes (% of control). PX-12 and rTrx conditions were analysed using paired Student's t-tests, no significant difference was observed.

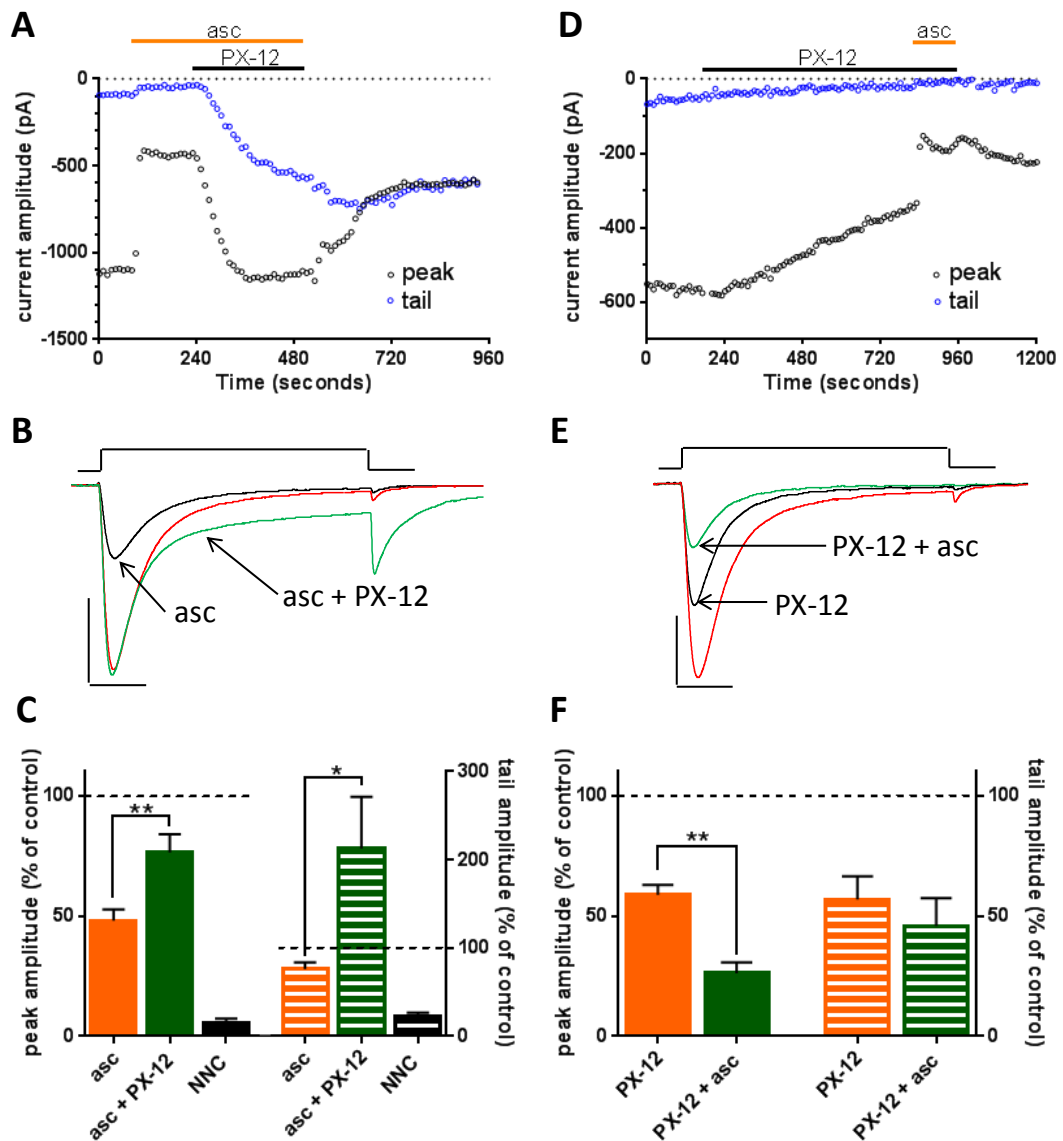


Figure 5.15. $Ca_v3.2$ currents are enhanced by co-application of ascorbate and PX-12 Whole-cell patch-clamp recordings from HEK293/ $Ca_v3.2$ cells, currents evoked by 200ms (0.1Hz) step-depolarisations from -80 to -20mV. **A**, Example time-series plot showing the effects of ascorbate (asc, 100 μ M, orange bar) in isolation and when co-applied with PX-12 (30 μ M, black bar) on both the $Ca_v3.2$ current peak amplitude (white circles) and tail current amplitude (blue circles). **B**, Corresponding $Ca_v3.2$ current traces (from A) under control conditions (red trace), and during exposure to ascorbate (asc, black trace, 100 μ M) and ascorbate + PX-12 (green trace, 30 μ M) as labelled. Scale bar 500pA (vertical), 40ms (horizontal). **C**, Bar chart (mean \pm s.e.m) showing the effects of ascorbate (asc, 100 μ M, orange bar, n=16), ascorbate co-applied with PX-12 (30 μ M) (green bar, n=16) and NNC (3 μ M, black bar, n=3) on $Ca_v3.2$ peak current amplitudes (solid bars, LHS axis) and tail current amplitudes (striped bars, RHS axis); both expressed as % of control. **D-E**, As (A-B), except showing the effects of PX-12 applied in isolation prior to co-application with ascorbate. Scale bar 200pA (vertical), 40ms (horizontal). **F**, As (C), except showing the effects of PX-12 (30 μ M, black bars, n=5) and PX-12 co-applied with ascorbate (asc, 100 μ M) (green bar, n=5). Data were analysed using paired Student's t-test, * $p \leq 0.05$, ** $p \leq 0.01$.

formation between Cys⁶² and Cys⁶⁹ residues (Watson *et al.*, 2003), modifies the structure of Trx in such a manner that it is no longer a substrate for TrxR. An early study examined differences between the crystal structures of human rTrx and oTrx; oTrx crystals were generated by allowing rTrx to oxidise in air for 2 months, without the addition of further DTT. It was subsequently demonstrated that oTrx and rTrx exhibited only very subtle structural differences, specifically concerning a slight conformational modification around the active site (Weichsel *et al.*, 1996). In stark contrast however, an alternative study generated oTrx crystals by leaving non-reduced Trx to oxidise for 6 months. This study revealed that intra-molecule disulphide bond formation occurred between Cys⁶² and Cys⁶⁹ residues within fully oxidised Trx. The non-active site disulphide bond completely disrupted the structure of the α 3 helix, exposing hydrophobic residues to the solvent (Hwang *et al.*, 2015). This study emphasises that different Cys residues within Trx show differential sensitivities to oxidation. Consequently, it was important to consider whether the redox-state of non-canonical Cys residues in Trx influenced its Ca_v3.2 channel enhancing activity.

Due to time constraints, Trx could not be allowed to oxidise for the full 6 months, as shown previously necessary to oxidise Cys⁶² and Cys⁶⁹ residues (Hwang *et al.*, 2015). In an attempt to further oxidise oTrx however, non-reduced oTrx was subject to air-mediated oxidation for 1 week and then bubbled with oxygen for 24hrs prior to use. Oxygenated oxidised Trx (ooTrx) was found to modestly enhance HEK293/Ca_v3.2 currents under control conditions. Importantly, the degree of ooTrx-mediated current enhancement under control conditions was directly comparable to those observed following rTrx and oTrx exposure (Figure 5.16). Importantly, application of the Trx elution buffer (EB) was without significant effect. However, when the effects of all Trx redox forms, applied under control conditions, were combined and compared against the effects of EB exposure, a significant enhancement in Ca_v3.2 current amplitude was apparent (Figure 5.16). In contrast to rTrx (Figure 5.7), ooTrx was without any effect on HEK293/Ca_v3.2 currents following inhibition with PX-12 (Figure 5.17). Collectively, these data show that the ability of Trx to enhance Ca_v3.2 currents under control conditions was independent of its redox state. Contrastingly, Trx-mediated reversal of PX-12-mediated Ca_v3.2 current inhibition was shown to be redox-dependent.

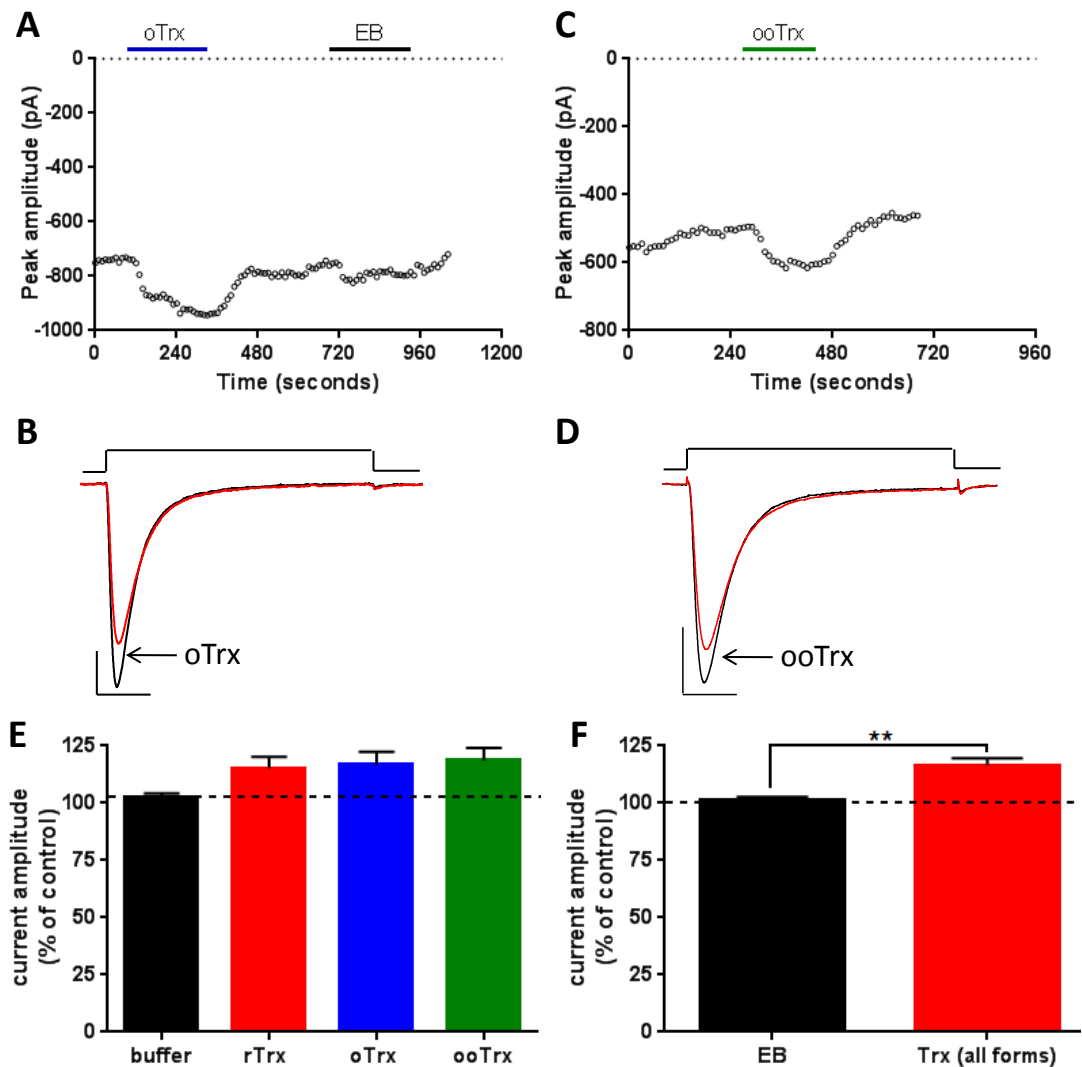


Figure 5.16. Trx-mediated regulation of $Ca_v3.2$ channels under control conditions is Trx redox state-independent

Whole-cell patch-clamp recordings from HEK293/ $Ca_v3.2$ cells, currents evoked by 200ms (0.1Hz) step-depolarisations from -80 to -20mV. **A**, Example time-series plot showing enhancement of $Ca_v3.2$ current amplitude by oxidised Trx (oTrx, 4 μ g/ml, blue bar) and no effect of the elution buffer (EB, 1:500, black bar) when applied to the perfusate. **B**, Corresponding $Ca_v3.2$ current traces (from A) under control conditions (red trace), and during exposure to oTrx (black trace). Scale bar 200pA, 40ms (horizontal). **C-D**, As A-B, except showing the effect of oxygenated oxidised Trx (ooTrx, 4 μ g/ml, green bar). **E**, Bar chart (mean \pm s.e.m) showing the effects of EB (black bar, 1:500, n=8), rTrx (red bar, 4 μ g/ml, n=7), oTrx (blue bar, 4 μ g/ml, n=8) and ooTrx (green bar, 4 μ g/ml, n=3) on $Ca_v3.2$ current amplitude (% of control). Data were analysed using one-way ANOVA followed by Dunnett's multiple comparison test, no significant difference. **F**, As E, except showing the combined effects of all forms of Trx (red bar, 4 μ g/ml, n=18) compared to the effect of the EB (black bar, 1:500, n=8) on $Ca_v3.2$ current amplitude (% of control). Data were analysed using un-paired Student's t-test, **p \leq 0.01.

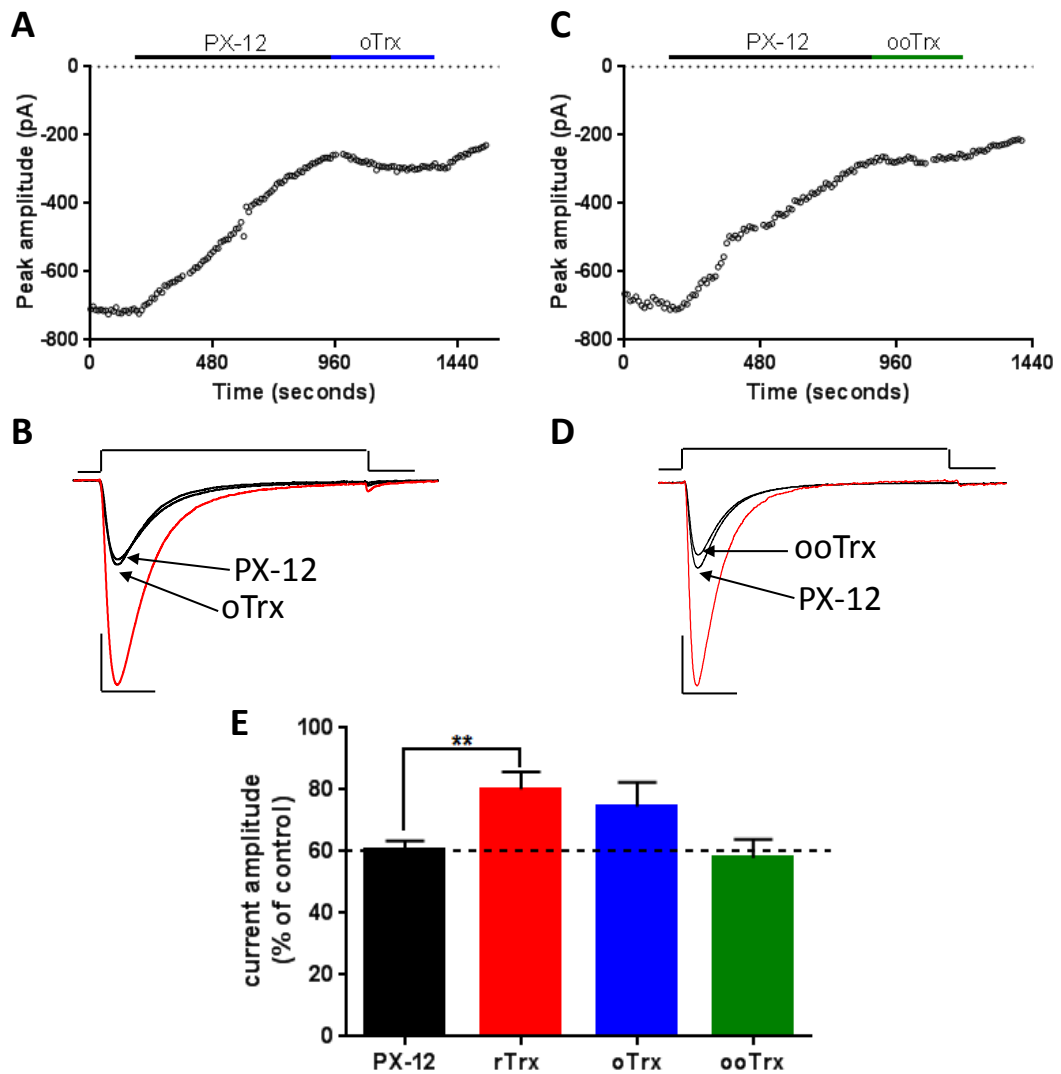


Figure 5.17. Trx-mediated reversal of PX-12 mediated $Ca_v3.2$ channel inhibition is Trx redox state-dependent

Whole-cell patch-clamp recordings from HEK293/ $Ca_v3.2$ cells, currents evoked by 200ms (0.1Hz) step-depolarisations from -80 to -20mV. **A**, Example time-series plot showing inhibition of $Ca_v3.2$ current amplitude by PX-12 (30 μ M, black bar) and a very small degree of reversal by oxidised Trx (oTrx, 4 μ g/ml, blue bar) when applied to the perfusate. **B**, Corresponding, $Ca_v3.2$ current traces (from A) under control conditions (red trace) and during exposure to PX-12 and oTrx (as labelled). Scale bar 200pA (vertical), 40ms (horizontal). **C-D**, As (A-B), except showing no reversal with oxygenated oxidised Trx (ooTrx, 4 μ g/ml, green bar). **E**, Bar chart (mean \pm s.e.m) showing the effects of PX-12 (black bar, 30 μ M, n=22), rTrx (red bar, 4 μ g/ml, n=10), oTrx (blue bar, 4 μ g/ml, n=8) and ooTrx (green bar, 4 μ g/ml, n=4) on $Ca_v3.2$ current amplitude (% of control). Data analysed using one-way ANOVA followed by Dunnett's multiple comparison test, ** $p \leq 0.01$.

5.3. Discussion

Results described within Chapters 3 and 4 show how inhibitors of both T-type Ca^{2+} channels and Trx reduced the proliferation of $\text{Ca}_v3.2$ -expressing cells. Ca^{2+} microfluorimetry further revealed that both T-type Ca^{2+} channel and Trx inhibitors decreased basal Ca^{2+} influx within A7r5 cells. These data collectively indicate that Trx may regulate proliferation via modulation of $\text{Ca}_v3.2$ channels (Chapters 3 & 4). Results described in the current chapter confirm that $\text{Ca}_v3.2$ channels are positively and selectively regulated by Trx.

5.3.1. Trx regulates $\text{Ca}_v3.2$ channels via an extracellular histidine residue at position 191 (His^{191})

The novel finding that $\text{Ca}_v3.2$ channels are selectively regulated by Trx via an interaction with His^{191} is consistent with a previous study conducted by the Peers' group. This study revealed that AuF selectively inhibited $\text{Ca}_v3.2$ channels whilst having no effect on $\text{Ca}_v3.1$ or $\text{Ca}_v3.3$ channels. Specifically, AuF (2-5 μM) pre-treatment (30-60mins) selectively reduced the current-density of HEK293/ $\text{Ca}_v3.2$ cells in a time- and concentration-dependent manner. Additionally, AuF (2 μM , 30mins) increased DTT- and rTrx-mediated enhancement of $\text{Ca}_v3.2$ current amplitudes. In contrast with the current finding that AuF shifted $\text{Ca}_v3.2$ I-V profiles to more positive potentials, the previous study indicated that AuF-mediated inhibition of $\text{Ca}_v3.2$ channels was voltage-independent. A potential explanation for this discrepancy is that a higher AuF concentration (5 μM) was applied than currently used, which was reported to cause visible damage and detachment of some cells (Boycott *et al.*, 2013).

Boycott *et al.* (2013) also determined that all 3 T-type Ca^{2+} channel isoforms ($\text{Ca}_v3.x$) were inhibited by carbon monoxide (CO). Interestingly, AuF pre-treatment selectively decreased CO-mediated inhibition of $\text{Ca}_v3.2$ currents indicating that CO was acting, in part, by disrupting tonic Trx-mediated $\text{Ca}_v3.2$ regulation. Of relevance to the current finding that Trx regulates $\text{Ca}_v3.2$ channels via His^{191} , is that mutant $\text{Ca}_v3.2(\text{H191Q})$ channels (as used currently) were shown to be equally sensitive to CO. Furthermore, the membrane-impermeant oxidising agent 5,5-dithiobis(2-nitrobenzoic acid) (DTNB) and also the endogenous reducing agent L-cysteine dramatically reduced the ability of

CO to inhibit Ca_v3.2 currents. As such, it was confirmed that CO acts via a redox-sensitive extracellular location, likely to be Cys residues that are conserved amongst Ca_v3.x channels (Boycott *et al.*, 2013). This proposed mechanism of CO-mediated inhibition of Ca_v3.x channels appears to share similarities with the isoform indiscriminate nature of PX-12-mediated inhibition of Ca_v3.1 and Ca_v3.2 channels, as currently reported. Interestingly, as CO appeared to interrupt Trx-mediated Ca_v3.2 regulation (Boycott *et al.*, 2013), it is possible that the molecular determinant(s) of CO sensitivity are in close physical proximity to His¹⁹¹. Consistent with this proposal, Cys residues conserved amongst all Ca_v3.x channels are located in close physical proximity to His¹⁹¹ in Ca_v3.2 channels, as further discussed in section 5.3.2 and illustrated in Figure 5.18.

Trx has also previously been shown to regulate transient receptor potential canonical (TRPC) channels (Xu *et al.*, 2008). TRPC channels are non-selective cation channels, which in terms of their structure and ability to form heteromultimeric channels, are most closely related to the voltage-gated K⁺ channel K_v1.2. TRPC channels are typically made up of combinations of TRPC-1, TRPC-4 or TRPC-5 subunits (Bon & Beech, 2013). Xu *et al.* (2008) determined that recombinantly-expressed TRPC5 homomultimeric and TRPC5/TRPC1 heteromultimeric channels were both regulated by extracellular rTrx. Regarding potential mechanisms, TRPC5 channels are activated by application of lanthanide. The molecular target of lanthanide is a glutamic acid (Glu) residue at position 543 (Glu⁵⁴³), located within an extracellular loop adjacent to the ion pore. The authors determined that both the membrane-impermeant disulphide reducing agent Tris(2-carboxyethyl)phosphine hydrochloride (TCEP) and DTT activated TRPC5 currents. Substitution of Cys⁵⁵³ and Cys⁵⁵⁸ with alanine residues resulted in currents which were constitutively active. The effects of DTT and TCEP were correspondingly abolished. This revealed that Cys⁵⁵³ and Cys⁵⁵⁸ residues, found in close proximity to Glu⁵⁴³, form a disulphide bridge which constrains TRPC5 channels in a state of limited open probability. In a manner comparable to DTT, rTrx stimulated both TRPC5 and TRPC5/TRPC1 channels. Contrastingly, oTrx was without effect. It was subsequently proposed that extracellular rTrx activates TRPC5 and TRPC5/TRPC1 channels by breaking the disulphide bridge which forms between Cys⁵⁵³ and Cys⁵⁵⁸ around the ion

pore. Interestingly, following activation of TRPC5 channels with lanthanide rTrx subsequently caused channel inhibition (Xu *et al.*, 2008).

Upon comparison of the findings of Xu *et al.* (2008) with current results, a key similarity was that Trx acted via an extracellular site on the ion channel, supporting the conclusion that Trx released by cells can modulate ion channel activity. Contrastingly, the molecular determinants of Trx-mediated TRPC channel regulation i.e. Cys residues, were disparate to the molecular determinant in the Ca_v3.2 channel, His¹⁹¹. Importantly, oTrx was without effect on TRPC channels suggesting that modification of TRPC channel Cys residues was reliant on the disulphide reductase abilities of Trx, imparted by active site Cys residues being in their reduced dithiol form (Xu *et al.*, 2008). In direct contrast however, Trx-mediated regulation of Ca_v3.2 channels under control conditions, but not following PX-12 mediated inhibition, was independent of the Trx redox state, and as such dithiol-exchange. Resultantly, the potential role of non-active site Trx residues will also be considered in the subsequent discussion of Trx-mediated Ca_v3.2 channel regulation.

The suggestion that some of the physiological effects of extracellular Trx are independent of active site Cys residues dithiol-exchange is not a novel proposal. A key difference between hTrx and other mammalian Trx forms when compared to bacterial forms is that in addition to highly conserved active site Cys³² and Cys³⁵ residues, hTrx contains three additional non-canonical Cys residues at positions 62, 69, and 73 (Cys⁶², Cys⁶⁹ and Cys⁷³) (Weichsel *et al.*, 1996). Significantly, when hTrx was applied to culture medium lacking serum, MCF-7 breast cancer cell proliferation was stimulated. Contrastingly, no effect on MCF-7 cell proliferation was observed when *E. coli* rTrx was applied. Mutant hTrx(C32S/C35S) was also unable to stimulate MCF-7 cell proliferation (Gasdaska *et al.*, 1995). It is important to note however, that extracellular application of bacterial Trx has been shown to exert mitogenic effects within certain cell lines. For example, a study reported that *E. coli* Trx, reduced using TrxR and NADPH, elevated cellular DNA synthesis in human B-cell lines when applied to the culture medium (Biguet *et al.*, 1994). These previous studies collectively indicate that the growth-promoting effects of extracellular Trx can be dependent on both intra- and extra-active site residues.

Interestingly, the pro-proliferative effects of hTrx were most apparent in minimal culture medium, and completely abolished by daily medium replacement. Evidence that extracellular hTrx can exert autocrine mitogenic effects was therefore provided. Application of radioisotope-labelled Trx further revealed that hTrx bound to MCF-7 cell membranes in a time-dependent manner (Gasdaska *et al.*, 1995). It was suggested that this was due to Trx binding to a specific, but undetermined, cell surface receptor. Importantly, as MCF-7 cells have been shown to express Ca_v3.2 channels which influence cell proliferation (Taylor *et al.*, 2008b), an alternative possibility consistent with current findings is that Trx binds to membranous Ca_v3.2 channels via His¹⁹¹. This proposed binding could account for both the membranous localisation of hTrx and also its stimulatory effects on MCF-7 cell proliferation (Gasdaska *et al.*, 1995). An important and interesting future experiment, using immunohistochemistry, would be to assess the subcellular localisation of Trx within both HEK293/Ca_v3.2 and A7r5 cells. The effects of AuF treatment on the potential patterns of Trx and Ca_v3.2 channel co-localisation could also be examined. A key consideration however, would be the epitope sequence to which the Trx primary antibody binds. This could be significant as a modified form of Trx has been previously identified within the extracellular environment (Di *et al.*, 1998), which may not contain the antibody recognition sequence.

The human cytotrophoblast cell lines BeWo, Jar and Jeg-3 have been shown to synthesise and secrete Trx to varying degrees (Di *et al.*, 1998). Intracellular Trx was comprised entirely of the typical 12kDa form. Contrastingly, in addition to the 12kDa form, a previously unidentified 10kDa Trx form was detected in abundant amounts within the extracellular environment. This 10kDa form of Trx was similarly isolated from the conditioned media of stimulated human platelets. N-terminal sequencing indicated that the 10kDa form was derived from the standard 12kDa form of Trx (Di *et al.*, 1998). Interestingly, subsequent investigations have confirmed the existence of a truncated form of Trx, referred to as Trx80 in the literature, and showing it to be an extracellular cleavage product of cytosolic Trx. Interestingly, Trx80 lacks C-terminal amino acid residues and correspondingly shows no disulphide reductase activity, as reviewed (Holmgren & Lu, 2010). Significantly, Trx80 has been shown to act as a

mitogenic cytokine in human peripheral blood mononuclear cells (PBMCs) and to stimulate the release of interleukin 2 (IL-2) (Pekkari *et al.*, 2001). These findings are consistent with the current suggestion that Trx residues contained outside of the active site can be important for the physiological effects of Trx within the extracellular environment. In further support of this, an alternative study reported that intra-peritoneal injection of hTrx reduced ischemic-reperfusion injury in mice, following myocardial infarction (MI). Pre-treatment of hTrx with S-nitrosoglutathione, which causes S-nitrosation of Cys⁶⁹, significantly enhanced the cardio-protective effects of hTrx. Importantly, *E. coli* Trx which lacks Cys⁶⁹ was without effect (Tao *et al.*, 2004). This study therefore illustrates how post-translational modification of Cys residues in the non-active site of Trx can determine its function(s) as an extracellular signalling molecule.

Regarding the observation that oTrx was equally capable at potentiating HEK293/Ca_v3.2 currents under control conditions as rTrx, an alternative consideration is that Trx could be endogenously reduced at the cell-surface. A previous report demonstrated that TrxR was localised at the cell membrane of both murine macrophage and human monocytes, particularly on the extracellular surface. The expression of cell-surface TrxR was also found to be increased by arylselenium compounds (Zhang *et al.*, 2013). In agreement with these findings, TrxR has also been detected in human blood plasma. This study reported that in addition to an abundant membranous localisation, TrxR was secreted from peripheral blood cells, tumour-transformed leukaemia cells and also melanoma cells. Metabolic labelling further revealed that in contrast with Trx, TrxR secretion occurred via the typical ER-Golgi pathway (Soderberg *et al.*, 2000). These studies collectively indicate that reduction of oTrx at the cell surface, within the extracellular environment, is feasible.

Bath application of mutant forms of Trx e.g. C32S/C35S, C73S and Trx80, which are available commercially (IMCO Corporation Ltd AB; Stockholm, Sweden), and subsequent assessment of their effects on Ca_v3.2 current amplitude would address this possibility. If Trx(C32S/C35S) and Trx80 did not enhance Ca_v3.2 current amplitude under control conditions, evidence, this would indicate that endogenous reduction of Trx, applied exogenously, was occurring at the cell membrane. This would

correspondingly indicate that Trx-mediated $Ca_v3.2$ channel regulation is actually dependent on the redox state of Trx. As reversal of PX-12-mediated $Ca_v3.2$ channel inhibition by Trx was currently shown to be Trx redox state-dependent, PX-12 could potentially prevent the reduction of oTrx at the cell surface (Kirkpatrick *et al.*, 1998).

5.3.2. PX-12 may inhibit $Ca_v3.x$ channels via interaction with conserved cysteine residues

Another important finding of the current investigation is that PX-12 inhibited Ca_v channels via a Trx-independent redox-regulated mechanism. Recombinant $Ca_v3.1$ and $Ca_v3.2$ channels were inhibited by PX-12 in a DTT-reversible manner, with virtually identical sensitivities. Contrastingly, only $Ca_v3.2$ channels were regulated by Trx. Whilst Cys is one of the least abundant amino acids, due to the unique chemistry of its thiol (sulfhydryl) groups, Cys residues are highly conserved within functionally important protein regions. Indeed, Cys residues are the only thiol-bearing amino acids, and are commonly found in close proximity to each other and thereby participating in disulphide bond formation. As thiol groups (R-SH) are readily deprotonated, whereby they lose H^+ to form distinct thiolate groups (R-S⁻), Cys residues are highly redox-sensitive (Poole, 2015).

Upon development, PX-12 was shown to inhibit Trx directly via thioalkylation of Cys residues. As PX-12 was without effect on TrxR or glutathione reductase, it was introduced as a selective Trx inhibitor (Kirkpatrick *et al.*, 1998). A proceeding study has however demonstrated that in addition to inhibiting Trx with an IC_{50} value of $20\mu M$, PX-12 directly oxidised Cys residues in tubulin (18 out of 20), thus preventing polymerisation. PX-12 was also shown to inhibit the protease enzymes papain and ficin via oxidative inactivation of active site Cys residues (Huber *et al.*, 2008). These findings illustrate that PX-12 is a more prolific oxidising agent than was originally described. Huber *et al.* (2008) also emphasised that the observed anti-proliferative effects of low concentrations of PX-12 on MCF-7 breast cancer cells and HUVECs were not solely attributable to Trx inhibition. Whilst MCF-7 cells express both $Ca_v3.2$ and $Ca_v3.1$ channels (Taylor *et al.*, 2008b), HUVECs primarily express $Ca_v3.1$ channels (Wang *et al.*, 2006). It is therefore possible that direct PX-12-mediated inhibition of $Ca_v3.x$ channels may contribute to the anti-proliferative effects of this drug. This conclusion is

consistent with current findings that whilst $\text{Ca}_v3.1$ channels were not sensitive to Trx, EdU incorporation assays revealed PX-12 ($1\mu\text{M}$) had small but significant anti-proliferative effects on HEK293/ $\text{Ca}_v3.1$, but not wt HEK293 cells (Chapter 4).

With regards to its stated purpose as a Trx inhibitor, PX-12 is currently undergoing clinical trials as an anti-cancer agent (Baker *et al.*, 2013; Ramanathan *et al.*, 2007; Ramanathan *et al.*, 2011). Importantly, the non-specific effects of PX-12 currently described raise important questions about the validity of its clinical use. Whilst direct inhibition of T-type Ca^{2+} channels by PX-12 could arguably contribute favourably to the drugs' anti-cancer properties, it is highly likely that indiscriminate oxidation of Cys residues would be accompanied by a host of adverse physiological effects. In support of this proposal, a recent clinical trial analysed the proteomic profile of clinical trial patients both pre- and post-PX-12 treatment. In addition to Trx modification, 8 unique peaks resulting from PX-12 treatment were observed in all patients, further indicating that the effects of PX-12 are not restricted to Trx (Baker *et al.*, 2013).

Redox regulation of T-type Ca^{2+} channels is well established. For example, $\text{Ca}_v3.2$ currents are approximately doubled in amplitude under reducing conditions i.e. when exposed to DTT or L-cysteine, and are conversely inhibited by oxidising agents such as DTNB (Todorovic *et al.*, 2001). Of key relevance to the PX-12-mediated inhibition of $\text{Ca}_v3.x$ channels currently described is α -lipoic acid (LA), a ubiquitous mitochondrial co-factor which participates in redox reactions involving thiol groups (Smith *et al.*, 2004). LA has been shown to inhibit $\text{Ca}_v3.1$ and $\text{Ca}_v3.2$ currents with similar sensitivities, via modification of extracellular Cys residues. As illustrated in Figure 5.18, the four target Cys residues of LA are highly-conserved amongst T-type Ca^{2+} channels. Three are located within the extracellular loop connecting S1-S2 in domain I (DI) (Cys¹²³, Cys¹²⁸ and Cys¹³³) and the other in the loop connecting S5 to the pore within DII (Cys⁹³⁹) (Lee *et al.*, 2009). Within biological systems, the majority of Cys residues are found in close proximity to each other and form disulphide bonds which, although crucial for protein structure, are relatively inert. Resultantly, extracellular loops containing odd numbers of Cys residues, such as those regulated by LA, appear the most likely molecular target(s) to mediate the inhibitory effects of PX-12 on Ca_v channels. Further investigation exploring whether site-directed mutagenesis of the Cys residues at

positions 123, 128, 133 and 939 of Ca_v3.x channels alters their sensitivity to PX-12 would be required to confirm this proposal.

Current findings demonstrated that reversal of PX-12-mediated Ca_v3.2 channel inhibition was dependent on Trx being in its reduced form. Due to the Trx-independent mechanism by which PX-12 inhibited Ca_v3.1 channels however, only limited conclusions can be drawn from this observation. Specifically, rTrx could potentially reverse the effects of PX-12 via a mechanism separate to the non Trx redox state-dependent mechanism found to regulate Ca_v3.2 channels under control conditions. For example, rTrx could undergo dithiol-disulphide exchange with Ca_v3.2 channel Cys residues previously oxidised by PX-12. As rTrx did not reverse PX-12-mediated inhibition of Ca_v3.1 or Ca_v3.2(H191Q) channels, this would also suggest interaction between conserved Cys residues and His¹⁹¹ in Ca_v3.2 channels, as further discussed in section 5.3.3.

Boycott *et al.* (2013) previously described that when rTrx was applied under control conditions, significantly less Ca_v3.2 current amplitude enhancement was apparent than when rTrx was applied post AuF pre-treatment. To further extend this observation, and also current findings, it would be useful to examine any variation between different redox forms of Trx on HEK293/Ca_v3.2 currents following AuF pre-treatment. This would establish whether reversal of AuF-mediated Ca_v3.2 channel inhibition is dependent on the redox status of Trx. An interesting consideration is that due to the indirect nature of AuF-mediated Trx inhibition i.e. via TrxR, a Trx redox state-dependent mechanism would arguably be predicted. Importantly however, Trx-mediated regulation of Ca_v3.2 currents under control conditions was currently shown to be redox state-independent. Correspondingly, as the redox state of Trx influences its release (Bertini *et al.*, 1999; Kondo *et al.*, 2004), the effects of AuF on Ca_v3.2 currents, proliferation and Ca²⁺ handling (Chapter 4) could be attributable to reduced extracellular Trx levels and a corresponding decrease in tonic Ca_v3.2 channel activation.

5.3.3. Potential interaction of Trx with Ca_v3.2 channel trace metal binding

Interestingly, the molecular determinant of Ca_v3.2 channel Trx-sensitivity (His¹⁹¹) is known to also contribute to the unique sensitivity of Ca_v3.2 channels to trace metals i.e. Ni²⁺, Zn²⁺ and redox modulators such as ascorbate. Initial studies described that when recombinantly expressed in *Xenopus* Oocytes or HEK293 cells, Ca_v3.2 currents were blocked by much lower Ni²⁺ concentrations (IC₅₀ value of 13μM) when compared to Ca_v3.1 and Ca_v3.3 channels (IC₅₀ values of 250μM and 216μM respectively) (Lee *et al.*, 1999). A later study generated chimeric Ca_v3.x channels to investigate the structural determinants of Ca_v3.2 Ni²⁺-sensitivity. Chimeric channels are commonly used for preliminary Ca_v channel structure-function investigations. Their construction involves the isolation of individual α1 subunit domains (DI-IV), which can then be re-assembled in various combinations and expressed recombinantly. For example, when DIII of the Ca_v3.2 channel is substituted with DIII of the Ca_v3.1 channel the chimeric channel is referred to as HHGH. As HGGG channels showed a Ni²⁺-sensitivity similar to wt Ca_v3.2 channels, it was predicted that the Ni²⁺ binding site was located within DI of the Ca_v3.2 channel (Kang *et al.*, 2006).

By aligning the amino acid sequences of DI from the three Ca_v3.x channel isoforms, un-conserved regions likely to underpin the differential isoform sensitivities were identified. Specifically, a glutamic acid (Glu or E) residue (E137) and a His residue (H191), found within the extracellular loop linking S3-S4 within DI were unique to Ca_v3.2 channels. These residues were then individually mutated to glutamine (Gln or Q) residues. Whilst the Ca_v3.2(E137Q) mutant showed Ni²⁺-sensitivity comparable to wt Ca_v3.2 channels, the Ca_v3.2(H191Q) mutant channel exhibited significantly reduced Ni²⁺-sensitivity. Furthermore, when the Gln residue found within the equivalent position of Ca_v3.1 channels (Q172) was mutated to His (Q172H), Ca_v3.1 channel sensitivity to Ni²⁺ was increased (5-fold). As such, it was concluded that His¹⁹¹ participated in Ni²⁺ binding. Importantly, as only partial Ni²⁺-sensitivity was imparted by the Ca_v3.1(Q172H) mutation, evidence that additional amino residues contributed to the Ni²⁺-binding site was also provided (Kang *et al.*, 2006).

Subsequent studies have also demonstrated that Zn²⁺ selectively inhibits Ca_v3.2 channels over other Ca_v3.x isoforms. As the Ca_v3.2(H191Q) mutant was insensitive to

Zn²⁺ a crucial role for His¹⁹¹ in metal-binding was thus confirmed. Furthermore, Zn²⁺ chelation enhanced Ca_v3.2 current amplitude, indicating that Zn²⁺ may tonically bind to Ca_v3.2 channels via His¹⁹¹ (Kang *et al.*, 2010; Nelson *et al.*, 2007b). Generation of chimeric channels, alongside site-directed mutagenesis, revealed that aspartic acid (Asp or D) and glycine (Gly or G) residues immediately preceding His¹⁹¹ (D189 and G190) within the extracellular S3-S4 loop, and a second Asp residue on the outside in S2 (D140), were also critical determinants of Ca_v3.2 Zn²⁺ sensitivity (Kang *et al.*, 2010). It was subsequently shown that this unique metal binding in Ca_v3.2 channels was responsible for trace metal binding, shown in Figure 5.18. Trace metal binding at this high affinity site is believed to stabilise Ca_v3.2 channels in their closed state, as reviewed (Perez-Reyes & Lee, 2014).

Ascorbate is an endogenous redox agent which can function as both an anti- and pro-oxidant. Regarding its functions as a pro-oxidant, ascorbate promotes the generation of reactive oxygen species (ROS) such as hydroxyl (OH[·]) superoxide (O₂^{·-}) and hydrogen peroxide (H₂O₂), via the reduction of transition metals such as iron (Fe³⁺, Fe²⁺) and copper (Cu⁺ and Cu²⁺). This process is collectively referred to as metal-catalysed oxidation (MCO). Significantly, MCO provides the major endogenous mechanism for oxidation of aliphatic and aromatic amino acids (Stadtman, 1991; Stadtman, 1993). When recorded from native tissues, or recombinantly expressed, Ca_v3.2 channels are potently inhibited by ascorbate whilst Ca_v3.1 and Ca_v3.3 channels are insensitive. Importantly, the mutant Ca_v3.2(H191Q) channel is also insensitive to ascorbate-mediated inhibition. As such, His¹⁹¹ was shown to be a structural determinant of Ca_v3.2 channel ascorbate-sensitivity. Increasing extracellular Cu²⁺ concentrations significantly enhanced ascorbate-mediated inhibition of wt Ca_v3.2 channels. It was therefore suggested that ascorbate interacted with the metal binding site in Ca_v3.2 via His¹⁹¹ to initiate MCO and thereby inhibit Ca_v3.2 channels (Nelson *et al.*, 2007a).

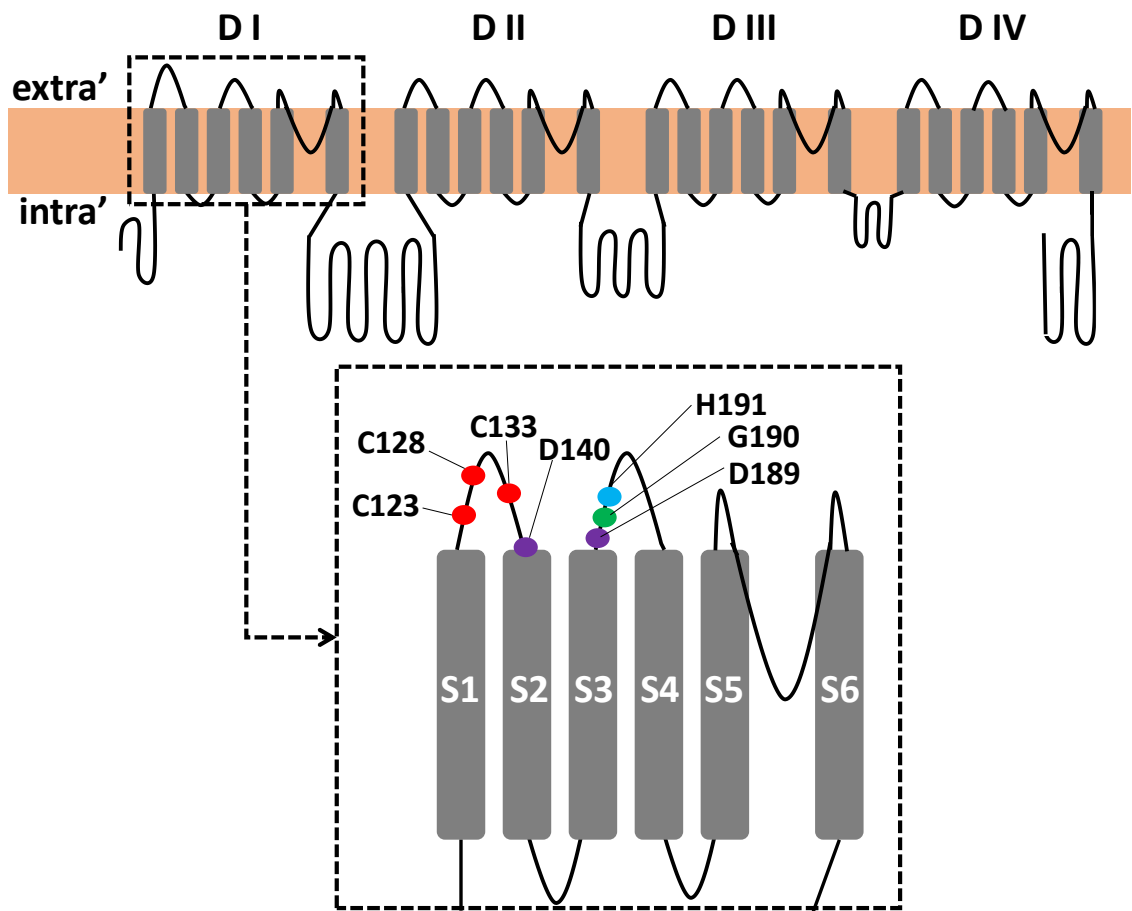


Figure 5.18. Schematic diagram highlighting key amino acid residues of $\text{Ca}_v3.2$ channels

Representative view looking through a cross-section of a stretched lipid bilayer (orange box) showing the arrangement of the α_{1H} subunit ($\text{Ca}_v3.2$ channel). Domain I (DI) is highlighted (dashed box) and magnified below. The unique metal binding site in $\text{Ca}_v3.2$ channels within DI is composed of a motif containing aspartic acid (D189, purple circle), glycine (G190, green circle) and histidine (H191, blue circle) residues found within the extracellular S3-S4 loop, and a second Asp residue on the outside S2 (D140, purple circle). Amino acid residues composing the metal binding site are in close proximity to cysteine residues (C123, C128, C133, red circles), which are conserved amongst $\text{Ca}_v3.x$ isoforms. In addition to a further cysteine residue within the extracellular region of DII(S5) (C939, not shown) these residues provide the targets of α -lipoic acid, and potentially PX-12 and CO. Figure adapted from Perez-Reyes (1999); Todorovic & Jevtovic (2014).

An as of yet undetermined consideration is whether metal binding itself, or the resultant effects of MCO on surrounding amino acids, stabilises $\text{Ca}_v3.2$ channels in their closed state. Considering the dependency of Trx-mediated $\text{Ca}_v3.2$ current enhancement on His¹⁹¹, this consideration is highly relevant when discussing potential interactions between Trx and $\text{Ca}_v3.2$ channels. As extensive further research will be required to establish which (if any) of the proposed mechanisms are relevant, corresponding future experiments will also be outlined. Firstly, Trx could bind directly

to His¹⁹¹ and prevent trace metal binding. This could destabilise the Ca_v3.2 channel closed-conformation due to a direct absence of the metal ion itself, or due to an indirect reduction in MCO. Regarding additional experiments, if pre-treatment of Ca_v3.2 currents with metal chelators prevented the effects of Trx, the requirement of trace metals to the effects of Trx would be confirmed.

The metal binding site in DI of Ca_v3.2 channels is mainly contained within the S3-S4 extracellular loop (Kang *et al.*, 2010). Also present in DI of all Ca_v3.x channels are 3 Cys residues (Cys¹²³, Cys¹²⁸, Cys¹³³), located within the extracellular S1-S2 loop. Modification of these Cys residues using LA, and potentially following PX-12 and CO exposure (discussed in sections 5.3.2 and 5.3.1 respectively), inhibits Ca_v3.2 channels (Todorovic & Jevtovic-Todorovic, 2014). In terms amino acid sequence, these Cys residues are in close proximity to metal binding site residues (Figure 5.18). Furthermore, inferences can also be made regarding their 3D proximity. Although the crystal structure of Ca_v channels remains unresolved, a single domain of the α₁ subunit is believed to bear close resemblance to K_v subunits. As such, the extracellular S1-S2 loop and the S3-S4 loop of Ca_v3.2 channels subunits are predicted to be in close 3D proximity (Long *et al.*, 2007).

Thiol-containing Cys residues are highly redox-sensitive (Poole, 2015). Interestingly, within many biological systems, Cys residues cluster around and contribute to the functional significance of metal-binding sites at the surface of proteins (Marino & Gladyshev, 2010). It is correspondingly feasible that Ca_v3.2 channel Cys residues are targets of MCO. In this regard, Cys residues may be the ultimate determinants of the stabilising effects of Zn²⁺, Ni²⁺ and ascorbate on Ca_v3.2 channels. Trx-mediated enhancement of Ca_v3.2 channels currently reported here could be explained by Trx binding to His¹⁹¹, thereby preventing metal binding and interrupting MCO of surrounding Cys residues.

Interestingly, current findings highlight the potential for interaction between the Ca_v3.2 channel metal binding site and Cys residues. For example, co-application of ascorbate and PX-12 following ascorbate treatment significantly enhanced wt Ca_v3.2, but not Ca_v3.2(H191Q) current amplitude. This starkly contrasted with the inhibitory

effects each drug had on wt Ca_v3.2 channels when applied in isolation. Furthermore, co-application of PX-12 and ascorbate to wt Ca_v3.2 channels also commonly augmented the shape of Ca_v3.2 currents. Specifically, dramatically increasing tail current amplitude and appearing to reduce inactivation. These opposing effects of co-application may concern the ability of ascorbate to function as both an anti- and pro-oxidant (Stadtman, 1991), and potential cross-reaction with PX-12. Alternatively, the targets of ascorbate (i.e. metal-binding site residues) that are unique to Ca_v3.2 channels may interact with the potential targets of PX-12 (i.e. conserved Cys residues as detailed in section 5.3.2). Point-mutation of Ca_v3.2 channel Cys¹²³ Cys¹²⁸ and Cys¹³³ residues and subsequent application of Trx, Ni²⁺ and ascorbate would confirm, or disprove, the involvement of Cys residues in MCO within Ca_v3.2 channels.

If subsequent experiments did not provide evidence in support of the aforementioned mechanisms, an alternative proposal as to the mechanism of Trx-mediated Ca_v3.2 channel regulation is that His¹⁹¹ itself provides the end target of MCO. Studies conducted in *E. coli* have determined that metal-binding sites within the glutamine synthetase (GS) enzyme facilitate MCO, which thereby inhibits enzyme activity. Specifically, MCO inhibited GS activity by converting a single His residue to asparagine (Asp) and a single arginine (Arg) residue to glutamic semialdehyde (Farber & Levine, 1986). It is correspondingly feasible that His¹⁹¹ serves as the end target for MCO. This could explain its role within, or be in addition to, the involvement of His¹⁹¹ in the Ca_v3.2 channel-stabilising effects of metal binding. With specific regard to the Trx-mediated Ca_v3.2 channel regulation currently observed here, direct binding to His¹⁹¹ could provide protection against MCO. A further possibility is that Trx does not bind to the channel directly but serves as the substrate for MCO, thus indirectly reducing the oxidative effects of MCO on Ca_v3.2 channels. If co-application of ascorbate reduced Trx-mediated Ca_v3.2 channel enhancement, evidence in support of this idea would be provided.

Many of the data presented throughout this thesis (Chapters 3, 4 and 5) are preliminary in nature but provide interesting insights which warrant further research. In order to ensure the statistical validity of future investigations, it would be useful to implement power analyses to estimate the number of experimental repeats required.

Effective power analysis requires that the effect size i.e. the difference between the hypothesis and the null hypothesis, and the standard deviation or data spread, is known. Current data therefore would enable effective power analysis to be conducted prior to each future experiment.

5.3.4. Summary and conclusions

Results in this chapter demonstrate that Ca_v3.2 channels are positively and selectively regulated by Trx, via an interaction with a singular extracellular His¹⁹¹ residue that is unique to Ca_v3.2 channels. They also suggest that Trx-mediated Ca_v3.2 channel regulation, under control conditions, is independent of the redox state of Trx. PX-12 was found to inhibit Ca_v channels indiscriminately, via a Trx-independent mechanism, raising important questions about its safety and validity as a Trx inhibitor for clinical use. Interestingly, the selective and observed reversal of PX-12-mediated inhibition of Ca_v3.2 currents by Trx was Trx redox state-dependent. This indicated that Ca_v3.2 channel regulation may be dependent on both intra- and extra-active site residues in Trx. Further work is required to establish the exact mechanism of interaction between Trx and His¹⁹¹ in the Ca_v3.2 channel. Findings detailed within previous chapters show that AuF selectively reduced the proliferation of Ca_v3.2-expressing cells, therefore providing evidence that Trx can modulate cellular proliferation via Ca_v3.2 channel regulation.

Chapter 6 - The implications of Trx-mediated Ca_v3.2 channel regulation on cellular proliferation

6.1. Principle findings

6.1.1. HEK293 cells

It is ultimately important to consider the functional significance of Trx-mediated Ca_v3.2 channel regulation on cellular proliferation. Findings from recombinant HEK293 cells are relatively simple to interpret; primarily because the contribution of Ca_v3.1 or Ca_v3.2 channel expression on cellular proliferation, basal Ca²⁺ influx and peak Ca²⁺ current amplitude can be examined individually. Expression of Ca_v3.1 or Ca_v3.2 channels significantly elevated cell proliferation and basal Ca²⁺ influx in HEK293 cells. Crucially, as NNC reduced cell proliferation and [Ca²⁺]_i influx in HEK293/Ca_v3.1 and HEK293/Ca_v3.2 cells, but not wt HEK293 cells, a causative role for both Ca_v3.1 and Ca_v3.2 channels in elevated proliferation was thus provided (Chapter 3). Significantly, inhibition of thioredoxin (Trx) using auranofin (AuF) selectively reduced HEK293/Ca_v3.2, but not HEK293/Ca_v3.1 or wt HEK293, cell proliferation (Chapter 4). These findings were consistent with previous observations that AuF and Trx selectively regulated Ca_v3.2 currents (Boycott *et al.*, 2013). Furthermore, AuF produced a rightwards shift in the I-V profile of HEK293/Ca_v3.2 currents, which is likely to shift the voltage range for the Ca_v3.2-mediated window current away from the resting membrane potential (V_m) (Chapter 5).

Both Ca_v3.1- and Ca_v3.2-facilitated window currents have been previously shown to elevate basal [Ca²⁺]_i when expressed recombinantly (Chemin *et al.*, 2000). Furthermore, recombinant expression of human Ca_v3.1 (Wang *et al.*, 2002a) and Ca_v3.2 (Wang *et al.*, 2002b) channels in HEK293 cells has been reported to confer significant growth advantages. Specifically, Ca_v3.1 or Ca_v3.2 channel expression significantly reduced population doubling times to similar extents, likely by promoting progression through the G₁/S phase of the cell cycle (Wang *et al.*, 2002a; Wang *et al.*, 2002b). The proliferative rate of HEK293/Ca_v3.2/clone P cells, transfected in-house with a Ca_v3.2-containing mammalian expression vector, was directly comparable to wt HEK293 cells and unaltered by NNC. It was coincidentally observed that in contrast to

the perinuclear clusters and punctate membranous patterns of Ca_v3.2-immunoreactivity (IR) observed in the highly proliferative HEK293/Ca_v3.2 cells, Ca_v3.2-IR in HEK293/Ca_v3.2/clone P cells was highly diffuse. This suggested that aggregation or clustering of Ca_v3.2 channels in specific sub-cellular domains might be important for increased basal Ca²⁺ to result in elevated cellular proliferation (Chapter 3).

These observations collectively indicate that Trx-mediated regulation of Ca_v3.2 channels can promote cellular proliferation, potentially by enhancing the Ca_v3.2-facilitated window current and corresponding basal [Ca²⁺]_i. Further direct assessment of the effects of AuF and Trx on recombinant HEK293 cell window currents, using either Ca²⁺ microfluorimetry or electrophysiological protocols to individually measure the voltage-dependencies of Ca_v3.2 channel activation and steady-state inactivation, would substantiate this conclusion.

6.1.2. A7r5 cells

Interpretation of results gathered in the native VSMC A7r5 cell line is somewhat more complex than the situation in HEK293 cells. Whilst the high levels of T-type Ca²⁺ channel expression and relatively small size of recombinant HEK293 cells meant they were highly conducive to patch-clamp electrophysiology, the exact opposite applied to A7r5 cells. A7r5 cells were directly shown to express Ca_v3.1 channels primarily, in addition to Ca_v3.2 channels (Chapter 3). Therefore, an important consideration (given that AuF-mediated inhibition of HEK293 cell proliferation was dependent on Ca_v3.2 channel expression) is whether Ca_v3.2 channels specifically influence VSMC proliferation. Whilst AuF reliably inhibited proliferation and basal Ca²⁺ influx in A7r5 cells (Chapter 4), Trx only potentiated A7r5 T-type Ca²⁺ currents on a small number of occasions (Chapter 5).

A potentially reconciling and preliminary observation for this discrepancy was that sensitivity of T-type Ca²⁺ channel currents to Trx was apparent when high Ca_v3.2 channel expression levels were detected using immunohistochemistry (Chapter 5). This observation also indicated that Ca_v3.2 channel expression was dynamically regulated in A7r5 cells. With regard to this, a recent study has reported that expression of Ca_v3.2

channels within the plasma membrane is regulated by asparagine-linked glycosylation of Ca_v3.2 channel residues. It was also identified that increasing external glucose concentrations increased Ca_v3.2 channel glycosylation and surface expression in human embryonic kidney tsA-201 cells (Weiss *et al.*, 2013). Interestingly, Ca_v3.2-IR in A7r5 cells reliably localised around the nucleus (Chapters 3 & 5). This directly contrasted with the diffuse pattern of Ca_v3.1-IR reliably observed in A7r5 cells (Chapter 3). In agreement with observations in recombinant HEK293 cells, it appears that the subcellular distribution of Ca_v3.2 channels determined their ability to influence cellular proliferation. Low levels of peri-nuclear Ca_v3.2 expression could potentially have a larger pro-proliferative effect than high levels of cytosolic Ca_v3.1 channel expression.

6.2. Clinical significance

Previous studies examining the contribution of Ca_v3.x channels to VSMC proliferation have implicated Ca_v3.1 channels as a major proliferative driving force in both developmental and pathological vascular remodelling. The ductus arteriosus (DA) is the foetal vascular shunt vessel which undergoes developmental remodelling postpartum. VSMCs isolated from the DA of Ca_v3.1^{-/-} mice show significantly less proliferation and migration (Akaike *et al.*, 2009). Regarding pathological vascular remodelling, carotid wire injury has been shown up-regulate Ca_v3.1 channels leading to neointima formation in mice. Significantly, Ca_v3.1^{-/-}, but not Ca_v3.2^{-/-}, mice were shown to be resistant to neointima formation following vascular injury (Tzeng *et al.*, 2012).

6.2.1. Hypoxia-induced vascular remodelling

As discussed extensively in Chapter 1, many cardiovascular disorders are associated with VSMC dedifferentiation and increased proliferation. As T-type Ca²⁺ channels are selectively expressed in the proliferative phases of the VSMC cell-cycle (Kuga *et al.*, 1996), more VSMC proliferation logically equates to increased T-type Ca²⁺ channel levels. Importantly, the specific contribution of Ca_v3.2 channels to VSMC proliferation may be more significant in pathological situations. Pulmonary hypertension (PH) can be induced by hypoxia and is associated with elevated VSMC levels, leading to vascular

remodelling. Exposure of mice to chronic hypoxia resulted in PH, observed as a significant increase in right ventricular systolic pressure alongside significant thickening of the medial layer of pulmonary vessel walls (Sato *et al.*, 2014; Wan *et al.*, 2013). Hypoxia has also been shown to induce a significant up-regulation in $Ca_v3.2$ and $Ca_v1.2$ mRNA expression in pulmonary arteries (Wan *et al.*, 2013). When pulmonary artery smooth muscle cells (PASMCs) were isolated from normoxic mice, exposure to high $[K^+]$ (40mM) caused only very small elevations in $[Ca^{2+}]_i$. In contrast, PASMCs isolated from hypoxic mice showed significant increases in $[Ca^{2+}]_i$ in response to the same high $[K^+]$ stimulus, indicating that elevated $Ca_v3.2$ and $Ca_v1.2$ mRNA levels led to increased functional Ca_v channel expression (Wan *et al.*, 2013). A more recent study conducted with rat PASMCs and pheochromocytoma (PC12) cells demonstrated that acute exposure to hypoxia (12-24hrs) induced prominent rises in $Ca_v3.2$ mRNA, protein and functional channel expression. No changes in these parameters were observed for $Ca_v3.1$ channels. It was also identified that hypoxia-induced $Ca_v3.2$ upregulation required the binding of hypoxia-inducible factor (HIF) to hypoxia-response elements within the promoter regions of the $Ca_v3.2$ channel (*CACNA1H*) gene (Sellak *et al.*, 2014).

The effects of hypoxia on $Ca_v3.2$ channel expression levels, has also been examined in other vascular beds. Coronary interventions are commonly associated with neointima formation. Internal mammary arteries (IMA) often serve as replacement conduit vessels for coronary artery bypass surgeries, as they are less prone to restenosis when compared to saphenous vein grafts (Nwasokwa, 1995). During surgical procedures and subsequent revascularisation, grafted VSMCs can be subject to periods of hypoxia. Correspondingly, supplemental oxygen has been shown to reduce neointima formation and reduce VSMC proliferation in the aortic media, following intra-aortic stent implantation in rabbits (Tretinyak *et al.*, 2002). In proliferating IMA SMCs (IMASMCs), exposure to hypoxia has been shown to increase functional T-type Ca^{2+} channels and decrease functional L-type Ca^{2+} channel levels. This was determined by measurement of depolarisation-induced Ca^{2+} entry, in the presence or absence of various specific Ca^{2+} channel blockers (CCBs). As no changes in $Ca_v1.2$ or $Ca_v3.2$ mRNA levels were detected, it was suggested that altered membrane trafficking of T-type Ca^{2+} channels accounted for the functional differences (Aley *et al.*, 2008).

Of further key interest is that when mice were subject to chronic hypoxia, a doubling of Trx levels in lung tissue was observed. In agreement with these observations, acute exposure of HPASMCs to hypoxia more than doubled Trx levels and significantly increased HPASMC proliferative rates. Final confirmation that Trx was pro-proliferative in hypoxia-exposed HPASMCs was the finding that siRNA-mediated Trx knockdown abolished hypoxia-induced elevations in proliferation. Increased activation of HIF was also reported by this study (Chen *et al.*, 2013). Collectively, these studies emphasise that the pro-proliferative effects of Trx-mediated $\text{Ca}_v3.2$ current enhancement would be increased by hypoxia. Correspondingly, this novel signal pathway is likely to be involved in pathological vascular remodelling associated with hypoxia-induced PH.

Regarding current results, A7r5 cell proliferation and basal Ca^{2+} influx was similarly inhibited by both selective T-type CCBs and AuF. Evidence that Trx-mediated regulation of $\text{Ca}_v3.2$ could modulate VSMC proliferation was therefore provided. Regarding future experiments, it would be interesting to see if high glucose concentrations, and or hypoxia, increased A7r5 $\text{Ca}_v3.2$ channel expression. If this was demonstrated, enhancement of the anti-proliferative effects of AuF would be correspondingly predicted, alongside a greater Trx-sensitivity of native A7r5 T-type Ca^{2+} currents. Conversely, genetic knockdown of $\text{Ca}_v3.2$ channels in A7r5 cells would be expected to reduce A7r5 proliferation and abolish the effects of AuF on both proliferation and Ca^{2+} handling.

6.2.2. MI-induced cardiac remodelling

The novel Trx- $\text{Ca}_v3.2$ channel signalling pathway characterised in the current investigation may also bear clinical significance to cardiac remodelling. Importantly, whilst hypertrophic remodelling involves increased growth of individual myocytes as opposed to increased proliferation, this process is also highly dependent on $[\text{Ca}^{2+}]_i$. Specifically, elevations in $[\text{Ca}^{2+}]_i$ can activate Ca^{2+} -dependent transcription factors leading to the expression of hypertrophic genes via a process termed excitation-transcription (ET) coupling (Dominguez-Rodriguez *et al.*, 2012). For example, myocardin is a transcription co-factor which plays an important role in the development of cardiac hypertrophy. Using embryonic rat heart-derived cells(H9c2),

elevated Ca^{2+} influx was shown to increase myocyte size and produce morphological phenotypic alteration to hypertrophic myocytes. Increased $[\text{Ca}^{2+}]_i$ also resulted in elevated levels of hypertrophic markers such as B-type natriuretic peptide (BNP). Levels of myocardin mRNA were also increased significantly. Importantly, genetic knockdown of myocardin using siRNA dramatically attenuated Ca^{2+} -induced hypertrophy of cardiomyocytes (Li *et al.*, 2015b).

Regarding the route of Ca^{2+} influx in Ca^{2+} -dependent hypertrophy, $\text{Ca}_v3.1$ channels are known to be important for functional cardiac remodelling; e.g. elevations in heart rate and ventricular tachycardia post-myocardial infarction (MI) (Le *et al.*, 2011). In contrast, a specific role for $\text{Ca}_v3.2$ channels in structural cardiac remodelling post-MI has been established. Within feline ventricular myocytes (or SMCs), MI-induced cardiac hypertrophy functionally up-regulated T-type Ca^{2+} channels, observed as an increased sensitivity of LVA currents to Ni^{2+} (Nuss & Houser, 1993). A subsequent study found that pressure-induced cardiac hypertrophy achieved by aortic banding was virtually abolished in $\text{Ca}_v3.2^{-/-}$ mice, but not in $\text{Ca}_v3.1^{-/-}$ mice. In direct contrast with $\text{Ca}_v3.1^{-/-}$ mice, the heart weight vs. body weight ratio measured 2 weeks post-surgery was not significantly altered in $\text{Ca}_v3.2^{-/-}$ mice when compared to control animals subject to sham surgical procedures. In wt mice, aortic banding led to a dramatic thickening of ventricular walls and a significant increase in the cross-sectional diameter of individual myocytes. No significant changes in any of these parameters were observed in the $\text{Ca}_v3.2^{-/-}$ mice. Additionally, myocytes isolated from neonatal $\text{Ca}_v3.2^{-/-}$ mice showed no hypertrophic response when stimulated with angiotensin II, as was observed for wt myocytes. As no changes in blood pressure were observed between wt and $\text{Ca}_v3.2^{-/-}$ mice, a specific role for $\text{Ca}_v3.2$ channels in structural as opposed to functional hypertrophic remodelling was indicated (Chiang *et al.*, 2009). In support of these findings, a further study in wt mice observed increased $\text{Ca}_v3.2$ channel expression in response to aortic banding. The sharp up-regulation in $\text{Ca}_v3.2$ mRNA expression provided an early event in the development of cardiac hypertrophy. It was also shown that the transcription factor early growth response 1 (Egr1) provided the initial signal leading to hypertrophic $\text{Ca}_v3.2$ over-expression (Hsu *et al.*, 2013).

Interestingly, alterations in the Trx system have also been reported in cardiac hypertrophy. Specifically, following aortic banding of mice, myocardial Trx activity was increased considerably whilst vitamin D₃ up-regulated protein (VDUP) mRNA and protein levels were decreased in ventricular cells. Concurrently, genetic over-expression of VDUP in mice significantly reduced cellular hypertrophy (Yoshioka *et al.*, 2004). *In vitro* studies of rat cardiomyocytes also revealed that Trx over-expression increased protein synthesis, whilst over-expression of VDUP reduced protein synthesis (Yoshioka *et al.*, 2004). Elevated Trx expression has also been directly implicated in the differentiation and proliferation of SMCs, leading to pathological cardiac remodelling following MI in rats (Suresh *et al.*, 2015). In light of current findings, activation of increased levels of Ca_v3.2 channels by elevated levels of Trx is likely to increase the window current. This would elevate [Ca²⁺]_i leading to ET-coupling and Ca²⁺-induced hypertrophic remodelling post-MI. The potential of disrupting the interaction between Trx and Ca_v3.2 therefore provides a novel pathway which could also potentially be targeted for therapeutic advantage in cardiac hypertrophy.

6.2.3. Cancer

The pathophysiological significance of the growth promoting effects of Trx-mediated Ca_v3.2 channel regulation also readily extends to carcinogenesis. Increased Ca_v3.2 channel expression has been specifically implicated in the increased basal Ca²⁺ levels and corresponding high proliferative rates of many cancer cells. This includes neuroblastoma (Panner *et al.*, 2005), prostate (Mariot *et al.*, 2002) and breast cancer cells (Taylor *et al.*, 2008b). In agreement with findings from VSMCs (Kuga *et al.*, 1996), expression of Ca_v3.1 and Ca_v3.2 channels in breast cancer MCF-7 cells has been shown to be restricted to the proliferative phases of the cell-cycle. High levels of Ca_v3.1 and Ca_v3.2 mRNA expression were detected in rapidly growing cultures of MCF-7 cells, but not cytostatic confluent cells. Furthermore, inhibition of T-type Ca²⁺ channels using NNC significantly reduced MCF-7 cell proliferation. A similar anti-proliferative effect was observed when Ca_v3.1 and Ca_v3.2 channels were knocked-down using siRNA (Taylor *et al.*, 2008a).

Significantly, elevated levels of extracellular Trx have also been determined in many cancers such as breast (Mariot *et al.*, 2002), pancreatic (Nakamura *et al.*, 2000), lung (Kahlos *et al.*, 2001; Kakolyris *et al.*, 2001; Soini *et al.*, 2001) and cervical cancers (Fujii *et al.*, 1991). Current findings therefore indicate that simultaneous increases in Ca_v3.2 and Trx may provide a highly detrimental positive-feedback loop. Specifically, activation of Ca_v3.2 by Trx would increase proliferation, leading to more Ca_v3.2 channel expression and further potentiation of the growth promoting effects of Trx. Resultantly, the rationale of blocking the interaction between Trx and Ca_v3.2 channels holds realistic therapeutic potential for the treatment of cancer.

In light of the broad spectrum of crucial intracellular functions of Trx, an appealing prospect by which to minimise the potential side effects of Trx inhibition would be to develop a drug which specifically targets extracellular Trx. Interestingly, a recent study has explored how modification of the structure of PX-12 could make the drug membrane impermeant and correspondingly act as a selective inhibitor of extracellular Trx (DiRaimondo *et al.*, 2013). Importantly, this study overlooks many important considerations such as the Trx-independent effects of PX-12, the potential of Trx being endogenously reduced in the extracellular environment and also the potential contribution of non-canonical Trx residues to its role as an extracellular signalling molecule and Ca_v3.2 channel modulator (Chapter 5). These issues should be of key consideration when assessing the clinical suitability of the novel asymmetric disulphide PX-12 variants engineered by DiRaimondo *et al.* (2013).

6.3. Summary and conclusion

This project has provided evidence showing that Trx-mediated Ca_v3.2 channel regulation has pro-proliferative effects. Both Ca_v3.2 channels and Trx have been associated with vascular and cardiac remodelling, induced by hypoxia or MI respectively. As such, pharmacological disruption of the interaction between Trx and Ca_v3.2 channels holds novel, therapeutic potential for the treatment of both PH and cardiac hypertrophy. Importantly however, further investigations into the mechanisms and extent of Ca_v3.2 channel upregulation, in other cardiovascular disorders involving excessive proliferation, are required to establish the full clinical relevance. The

involvement of Ca_v3.2 channels in the aberrant proliferation of cancerous cells is also well established. Current observations therefore conclusively support the rationale that Trx inhibitors provide effective chemotherapy agents. Significantly, compelling evidence that PX-12 is not a selective Trx inhibitor was provided. This is highly indicative of the potential undesirable side effects and contraindications of clinical use of PX-12 as a Trx inhibitor. As the site for Trx-mediated Ca_v3.2 channel regulation was located extracellularly (His¹⁹¹), the development of membrane impermeant Trx inhibitors may provide an opportunity to develop novel treatments for proliferative disorders involving cells which express Ca_v3.2 channels.

References

- Abd El-Rahman, R.R., Harraz, O.F., Brett, S.E., Anfinogenova, Y., Mufti, R.E., Goldman, D., & Welsh, D.G. (2013). Identification of L- and T-type Ca²⁺ channels in rat cerebral arteries: role in myogenic tone development. *Am.J.Physiol Heart Circ.Physiol* **304**, (1) H58-H71.
- Ahanchi, S.S., Varu, V.N., Tsihliis, N.D., Martinez, J., Pearce, C.G., Kapadia, M.R., Jiang, Q., Saavedra, J.E., Keefer, L.K., Hrabie, J.A., & Kibbe, M.R. (2008). Heightened efficacy of nitric oxide-based therapies in type II diabetes mellitus and metabolic syndrome. *Am.J.Physiol Heart Circ.Physiol* **295**, (6) H2388-H2398.
- Akaike, T., Jin, M.H., Yokoyama, U., Izumi-Nakaseko, H., Jiao, Q., Iwasaki, S., Iwamoto, M., Nishimaki, S., Sato, M., Yokota, S., Kamiya, Y., Adachi-Akahane, S., Ishikawa, Y., & Minamisawa, S. (2009). T-type Ca²⁺ channels promote oxygenation-induced closure of the rat ductus arteriosus not only by vasoconstriction but also by neointima formation. *J.Biol.Chem.* **284**, (36) 24025-24034.
- Aley, P.K., Wilkinson, J.A., Bauer, C.C., Boyle, J.P., Porter, K.E., & Peers, C. (2008). Hypoxic remodelling of Ca(2+) signalling in proliferating human arterial smooth muscle. *Mol.Cell Biochem.* **318**, (1-2) 101-108.
- Almers, W. & McCleskey, E.W. (1984). Non-selective conductance in calcium channels of frog muscle: calcium selectivity in a single-file pore. *J.Physiol* **353**, 585-608.
- Arner, E.S. (2009). Focus on mammalian thioredoxin reductases--important selenoproteins with versatile functions. *Biochim.Biophys.Acta* **1790**, (6) 495-526.
- Arner, E.S. & Holmgren, A. (2000). Physiological functions of thioredoxin and thioredoxin reductase. *Eur.J.Biochem.* **267**, (20) 6102-6109.
- Assandri, R., Egger, M., Gassmann, M., Niggli, E., Bauer, C., Forster, I., & Gorlach, A. (1999). Erythropoietin modulates intracellular calcium in a human neuroblastoma cell line. *J.Physiol* **516 (Pt 2)**, 343-352.
- Baker, A.F., Adab, K.N., Raghunand, N., Chow, H.H., Stratton, S.P., Squire, S.W., Boice, M., Pestano, L.A., Kirkpatrick, D.L., & Dragovich, T. (2013). A phase IB trial of 24-hour intravenous PX-12, a thioredoxin-1 inhibitor, in patients with advanced gastrointestinal cancers. *Invest New Drugs* **31**, (3) 631-641.
- Ball, C.J., Wilson, D.P., Turner, S.P., Saint, D.A., & Beltrame, J.F. (2009). Heterogeneity of L- and T-channels in the vasculature: rationale for the efficacy of combined L- and T-blockade. *Hypertension* **53**, (4) 654-660.
- Barnett, D.W., Pressel, D.M., & Mislser, S. (1995). Voltage-dependent Na⁺ and Ca²⁺ currents in human pancreatic islet beta-cells: evidence for roles in the generation of action potentials and insulin secretion. *Pflugers Arch.* **431**, (2) 272-282.

Barquera, S., Pedroza-Tobias, A., Medina, C., Hernandez-Barrera, L., Bibbins-Domingo, K., Lozano, R., & Moran, A.E. (2015). Global Overview of the Epidemiology of Atherosclerotic Cardiovascular Disease. *Arch.Med.Res.* **46**, (5) 328-338.

Berridge, M.J., Lipp, P., & Bootman, M.D. (2000). The versatility and universality of calcium signalling. *Nat.Rev.Mol.Cell Biol.* **1**, (1) 11-21.

Bertini, R., Howard, O.M., Dong, H.F., Oppenheim, J.J., Bizzarri, C., Sergi, R., Caselli, G., Pagliei, S., Romines, B., Wilshire, J.A., Mengozzi, M., Nakamura, H., Yodoi, J., Pekkari, K., Gurunath, R., Holmgren, A., Herzenberg, L.A., Herzenberg, L.A., & Ghezzi, P. (1999). Thioredoxin, a redox enzyme released in infection and inflammation, is a unique chemoattractant for neutrophils, monocytes, and T cells. *J.Exp.Med.* **189**, (11) 1783-1789.

Betz, B. & Conway, B.R. (2016). An Update on the Use of Animal Models in Diabetic Nephropathy Research. *Curr.Diab.Rep.* **16**, (2) 18.

Bezprozvanny, I. & Tsien, R.W. (1995). Voltage-dependent blockade of diverse types of voltage-gated Ca²⁺ channels expressed in *Xenopus* oocytes by the Ca²⁺ channel antagonist mibefradil (Ro 40-5967). *Mol.Pharmacol.* **48**, (3) 540-549.

Biguet, C., Wakasugi, N., Mishal, Z., Holmgren, A., Chouaib, S., Tursz, T., & Wakasugi, H. (1994). Thioredoxin increases the proliferation of human B-cell lines through a protein kinase C-dependent mechanism. *J.Biol.Chem.* **269**, (46) 28865-28870.

Billiet, L. & Rouis, M. (2008). Thioredoxin-1 is a novel and attractive therapeutic approach for various diseases including cardiovascular disorders. *Cardiovasc.Hematol.Disord.Drug Targets.* **8**, (4) 293-296.

Bogaard, H.J., Abe, K., Vonk, N.A., & Voelkel, N.F. (2009). The right ventricle under pressure: cellular and molecular mechanisms of right-heart failure in pulmonary hypertension. *Chest* **135**, (3) 794-804.

Bohn, G., Moosmang, S., Conrad, H., Ludwig, A., Hofmann, F., & Klugbauer, N. (2000). Expression of T- and L-type calcium channel mRNA in murine sinoatrial node. *FEBS Lett.* **481**, (1) 73-76.

Bon, R.S. & Beech, D.J. (2013). In pursuit of small molecule chemistry for calcium-permeable non-selective TRPC channels -- mirage or pot of gold? *Br.J.Pharmacol.* **170**, (3) 459-474.

Boycott, H.E., Dallas, M.L., Elies, J., Pettinger, L., Boyle, J.P., Scragg, J.L., Gamper, N., & Peers, C. (2013). Carbon monoxide inhibition of Cav3.2 T-type Ca²⁺ channels reveals tonic modulation by thioredoxin. *FASEB J.*

Braunstein, T.H., Inoue, R., Cribbs, L., Oike, M., Ito, Y., Holstein-Rathlou, N.H., & Jensen, L.J. (2009). The role of L- and T-type calcium channels in local and remote calcium responses in rat mesenteric terminal arterioles. *J.Vasc.Res.* **46**, (2) 138-151.

Brueggemann, L.I., Martin, B.L., Barakat, J., Byron, K.L., & Cribbs, L.L. (2005). Low voltage-activated calcium channels in vascular smooth muscle: T-type channels and AVP-stimulated calcium spiking. *Am.J.Physiol Heart Circ.Physiol* **288**, (2) H923-H935.

Burke-Gaffney, A., Callister, M.E., & Nakamura, H. (2005). Thioredoxin: friend or foe in human disease? *Trends Pharmacol.Sci.* **26**, (8) 398-404.

Capiod, T. (2011). Cell proliferation, calcium influx and calcium channels. *Biochimie* **93**, (12) 2075-2079.

Carre, G., Ouedraogo, M., Magaud, C., Carreyre, H., Becq, F., Bois, P., Supuran, C.T., Thibaudeau, S., Vandebrouck, C., & Bescond, J. (2015). Vasorelaxation induced by dodoneine is mediated by calcium channels blockade and carbonic anhydrase inhibition on vascular smooth muscle cells. *J.Ethnopharmacol.* **169**, 8-17.

Catterall, W.A. (2011). Voltage-gated calcium channels. *Cold Spring Harb.Perspect.Biol.* **3**, (8) a003947.

Cazade, M., Bidaud, I., Hansen, P.B., Lory, P., & Chemin, J. (2014). 5,6-EET potently inhibits T-type calcium channels: implication in the regulation of the vascular tone. *Pflugers Arch.* **466**, (9) 1759-1768.

Chandler, N.J., Greener, I.D., Tellez, J.O., Inada, S., Musa, H., Molenaar, P., Difrancesco, D., Baruscotti, M., Longhi, R., Anderson, R.H., Billeter, R., Sharma, V., Sigg, D.C., Boyett, M.R., & Dobrzynski, H. (2009). Molecular architecture of the human sinus node: insights into the function of the cardiac pacemaker. *Circulation* **119**, (12) 1562-1575.

Chemin, J., Monteil, A., Briquaire, C., Richard, S., Perez-Reyes, E., Nargeot, J., & Lory, P. (2000). Overexpression of T-type calcium channels in HEK-293 cells increases intracellular calcium without affecting cellular proliferation. *FEBS Lett.* **478**, (1-2) 166-172.

Chen, B., Nelin, V.E., Locy, M.L., Jin, Y., & Tipple, T.E. (2013). Thioredoxin-1 mediates hypoxia-induced pulmonary artery smooth muscle cell proliferation. *Am.J.Physiol Lung Cell Mol.Physiol* **305**, (5) L389-L395.

Chen, C.C., Lamping, K.G., Nuno, D.W., Barresi, R., Prouty, S.J., Lavoie, J.L., Cribbs, L.L., England, S.K., Sigmund, C.D., Weiss, R.M., Williamson, R.A., Hill, J.A., & Campbell, K.P. (2003a). Abnormal coronary function in mice deficient in alpha1H T-type Ca²⁺ channels. *Science* **302**, (5649) 1416-1418.

Chen, Y., Lu, J., Pan, H., Zhang, Y., Wu, H., Xu, K., Liu, X., Jiang, Y., Bao, X., Yao, Z., Ding, K., Lo, W.H., Qiang, B., Chan, P., Shen, Y., & Wu, X. (2003b). Association between genetic variation of CACNA1H and childhood absence epilepsy. *Ann.Neurol.* **54**, (2) 239-243.

Cheong, E. & Shin, H.S. (2013). T-type Ca²⁺ channels in normal and abnormal brain functions. *Physiol Rev.* **93**, (3) 961-992.

Chevalier, M., Mironneau, C., Macrez, N., & Quignard, J.F. (2008). Intracellular Ca(2+) oscillations induced by over-expressed Ca(V)3.1 T-type Ca(2+) channels in NG108-15 cells. *Cell Calcium* **44**, (6) 592-603.

Chiang, C.S., Huang, C.H., Chieng, H., Chang, Y.T., Chang, D., Chen, J.J., Chen, Y.C., Chen, Y.H., Shin, H.S., Campbell, K.P., & Chen, C.C. (2009). The Ca(v)3.2 T-type Ca(2+) channel is required for pressure overload-induced cardiac hypertrophy in mice. *Circ.Res.* **104**, (4) 522-530.

Chistiakov, D.A., Orekhov, A.N., & Bobryshev, Y.V. (2015). Vascular smooth muscle cell in atherosclerosis. *Acta Physiol (Oxf)* **214**, (1) 33-50.

Clemmons, D.R. (2007). Modifying IGF1 activity: an approach to treat endocrine disorders, atherosclerosis and cancer. *Nat.Rev.Drug Discov.* **6**, (10) 821-833.

Cove-Smith, A., Mulgrew, C.J., Rudyk, O., Dutt, N., McLatchie, L.M., Shattock, M.J., & Hendry, B.M. (2013). Anti-proliferative actions of T-type calcium channel inhibition in Thy1 nephritis. *Am.J.Pathol.* **183**, (2) 391-401.

Cox, A.G., Brown, K.K., Arner, E.S., & Hampton, M.B. (2008). The thioredoxin reductase inhibitor auranofin triggers apoptosis through a Bax/Bak-dependent process that involves peroxiredoxin 3 oxidation. *Biochem.Pharmacol.* **76**, (9) 1097-1109.

Cox, A.G., Peskin, A.V., Paton, L.N., Winterbourn, C.C., & Hampton, M.B. (2009). Redox potential and peroxide reactivity of human peroxiredoxin 3. *Biochemistry* **48**, (27) 6495-6501.

Cuspidi, C., Meani, S., Sala, C., Valerio, C., Fusi, V., Zanchetti, A., & Mancia, G. (2007). How reliable is isolated clinical hypertension defined by a single 24-h ambulatory blood pressure monitoring? *J.Hypertens.* **25**, (2) 315-320.

Densmore, J.J., Szabo, G., & Gray, L.S. (1992). A voltage-gated calcium channel is linked to the antigen receptor in Jurkat T lymphocytes. *FEBS Lett.* **312**, (2-3) 161-164.

Di, T.G., Perkins, A., & Clarke, F. (1998). Production and secretion of thioredoxin from transformed human trophoblast cells. *Mol.Hum.Reprod.* **4**, (4) 369-375.

DiRaimondo, T.R., Plugis, N.M., Jin, X., & Khosla, C. (2013). Selective inhibition of extracellular thioredoxin by asymmetric disulfides. *J.Med.Chem.* **56**, (3) 1301-1310.

Dominguez-Rodriguez, A., Ruiz-Hurtado, G., Benitah, J.P., & Gomez, A.M. (2012). The other side of cardiac Ca(2+) signaling: transcriptional control. *Front Physiol* **3**, 452.

Duckles, H., Boycott, H.E., Al-Owais, M.M., Elies, J., Johnson, E., Dallas, M.L., Porter, K.E., Giuntini, F., Boyle, J.P., Scragg, J.L., & Peers, C. (2015). Heme oxygenase-1 regulates cell proliferation via carbon monoxide-mediated inhibition of T-type Ca²⁺ channels. *Pflugers Arch.* **467**, (2) 415-427.

Dziegielewska, B., Gray, L.S., & Dziegielewski, J. (2014). T-type calcium channels blockers as new tools in cancer therapies. *Pflugers Arch.* **466**, (4) 801-810.

- Elies, J., Johnson, E., Boyle, J.P., Scragg, J.L., & Peers, C. (2015). H₂S does not regulate proliferation via T-type Ca²⁺ channels. *Biochem.Biophys.Res.Commun.* **461**, (4) 659-664.
- Elvan, A. (2000). Reexpression of T-type Ca channels after myocardial infarction: does it play a role in cardiac excitation? *Cardiovasc.Res.* **46**, (3) 361-363.
- Erac, Y., Selli, C., Filik, P., & Tosun, M. (2014). Effects of passage number on proliferation and store-operated calcium entry in A7r5 vascular smooth muscle cells. *J.Pharmacol.Toxicol.Methods* **70**, (1) 1-5.
- Fan, L. & Karino, T. (2010). Effect of a disturbed flow on proliferation of the cells of a hybrid vascular graft. *Biorheology* **47**, (1) 31-38.
- Farber, J.M. & Levine, R.L. (1986). Sequence of a peptide susceptible to mixed-function oxidation. Probable cation binding site in glutamine synthetase. *J.Biol.Chem.* **261**, (10) 4574-4578.
- Faries, P.L., Rohan, D.I., Takahara, H., Wyers, M.C., Contreras, M.A., Quist, W.C., King, G.L., & Logerfo, F.W. (2001). Human vascular smooth muscle cells of diabetic origin exhibit increased proliferation, adhesion, and migration. *J.Vasc.Surg.* **33**, (3) 601-607.
- Fearon, I.M., Randall, A.D., Perez-Reyes, E., & Peers, C. (2000). Modulation of recombinant T-type Ca²⁺ channels by hypoxia and glutathione. *Pflugers Arch.* **441**, (2-3) 181-188.
- Fedoryak, O.D., Searls, Y., Smirnova, I.V., Burns, D.M., & Stehno-Bittel, L. (2004). Spontaneous Ca²⁺ oscillations in subcellular compartments of vascular smooth muscle cells rely on different Ca²⁺ pools. *Cell Res.* **14**, (5) 379-388.
- Fernandez-Morales, J.C., Fernando, P.J., Vestring, S., Musial, D.C., de Diego, A.M., & Garcia, A.G. (2015). Blockade by NNC 55-0396, mibefradil, and nickel of calcium and exocytotic signals in chromaffin cells: implications for the regulation of hypoxia-induced secretion at early life. *Eur.J.Pharmacol.* **751**, 1-12.
- Finkelstein, A.E., Walz, D.T., Batista, V., Mizraji, M., Roisman, F., & Misher, A. (1976). Auranofin. New oral gold compound for treatment of rheumatoid arthritis. *Ann.Rheum.Dis.* **35**, (3) 251-257.
- Fleischmann, B.K., Murray, R.K., & Kotlikoff, M.I. (1994). Voltage window for sustained elevation of cytosolic calcium in smooth muscle cells. *Proc.Natl.Acad.Sci.U.S.A* **91**, (25) 11914-11918.
- Fransen, P., Van Hove, C.E., van, L.J., Schrijvers, D.M., Martinet, W., De Meyer, G.R., & Bult, H. (2012). Contribution of transient and sustained calcium influx, and sensitization to depolarization-induced contractions of the intact mouse aorta. *BMC.Physiol* **12**, 9.
- Frazier, C.J., Serrano, J.R., George, E.G., Yu, X., Viswanathan, A., Perez-Reyes, E., & Jones, S.W. (2001). Gating kinetics of the alpha1I T-type calcium channel. *J.Gen.Physiol* **118**, (5) 457-470.

- Fujii, S., Nanbu, Y., Nonogaki, H., Konishi, I., Mori, T., Masutani, H., & Yodoi, J. (1991). Coexpression of adult T-cell leukemia-derived factor, a human thioredoxin homologue, and human papillomavirus DNA in neoplastic cervical squamous epithelium. *Cancer* **68**, (7) 1583-1591.
- Furukawa, T., Miura, R., Honda, M., Kamiya, N., Mori, Y., Takeshita, S., Isshiki, T., & Nukada, T. (2004). Identification of R(-)-isomer of efonidipine as a selective blocker of T-type Ca²⁺ channels. *Br.J.Pharmacol.* **143**, (8) 1050-1057.
- Gao, F. & Zheng, Z.M. (2014). Animal models of diabetic neuropathic pain. *Exp.Clin.Endocrinol.Diabetes* **122**, (2) 100-106.
- Gao, Q. & Wolin, M.S. (2008). Effects of hypoxia on relationships between cytosolic and mitochondrial NAD(P)H redox and superoxide generation in coronary arterial smooth muscle. *Am.J.Physiol Heart Circ.Physiol* **295**, (3) H978-H989.
- Gasdaska, J.R., Berggren, M., & Powis, G. (1995). Cell growth stimulation by the redox protein thioredoxin occurs by a novel helper mechanism. *Cell Growth Differ.* **6**, (12) 1643-1650.
- Gasdaska, J.R., Kirkpatrick, D.L., Montfort, W., Kuperus, M., Hill, S.R., Berggren, M., & Powis, G. (1996). Oxidative inactivation of thioredoxin as a cellular growth factor and protection by a Cys73-->Ser mutation. *Biochem.Pharmacol.* **52**, (11) 1741-1747.
- Gasdaska, P.Y., Oblong, J.E., Cotgreave, I.A., & Powis, G. (1994). The predicted amino acid sequence of human thioredoxin is identical to that of the autocrine growth factor human adult T-cell derived factor (ADF): thioredoxin mRNA is elevated in some human tumors. *Biochim.Biophys.Acta* **1218**, (3) 292-296.
- Goldfinger, J.Z., Halperin, J.L., Marin, M.L., Stewart, A.S., Eagle, K.A., & Fuster, V. (2014). Thoracic aortic aneurysm and dissection. *J.Am.Coll.Cardiol.* **64**, (16) 1725-1739.
- Gray, L.S., Schiff, D., & Macdonald, T.L. (2013). A model for the regulation of T-type Ca(2+) channels in proliferation: roles in stem cells and cancer. *Expert.Rev.Anticancer Ther.* **13**, (5) 589-595.
- Grogan, T.M., Fenoglio-Prieser, C., Zeheb, R., Bellamy, W., Frutiger, Y., Vela, E., Stemmerman, G., Macdonald, J., Richter, L., Gallegos, A., & Powis, G. (2000). Thioredoxin, a putative oncogene product, is overexpressed in gastric carcinoma and associated with increased proliferation and increased cell survival. *Hum.Pathol.* **31**, (4) 475-481.
- Gromer, S., Arscott, L.D., Williams, C.H., Jr., Schirmer, R.H., & Becker, K. (1998). Human placenta thioredoxin reductase. Isolation of the selenoenzyme, steady state kinetics, and inhibition by therapeutic gold compounds. *J.Biol.Chem.* **273**, (32) 20096-20101.
- Grynkiewicz, G., Poenie, M., & Tsien, R.Y. (1985). A new generation of Ca²⁺ indicators with greatly improved fluorescence properties. *J.Biol.Chem.* **260**, (6) 3440-3450.
- Haddock, R.E. & Hill, C.E. (2005). Rhythmicity in arterial smooth muscle. *J.Physiol* **566**, (Pt 3) 645-656.

- Hagiwara, N., Irisawa, H., & Kameyama, M. (1988). Contribution of two types of calcium currents to the pacemaker potentials of rabbit sino-atrial node cells. *J.Physiol* **395**, 233-253.
- Hansen, J.M. (2012). Thioredoxin redox status assessment during embryonic development: the redox Western. *Methods Mol.Biol.* **889**, 305-313.
- Hansen, P.B. (2015). Functional importance of T-type voltage-gated calcium channels in the cardiovascular and renal system: news from the world of knockout mice. *Am.J.Physiol Regul.Integr.Comp Physiol* **308**, (4) R227-R237.
- Hansen, P.B., Jensen, B.L., Andreasen, D., Friis, U.G., & Skott, O. (2000). Vascular smooth muscle cells express the alpha(1A) subunit of a P-/Q-type voltage-dependent Ca(2+)Channel, and It is functionally important in renal afferent arterioles. *Circ.Res.* **87**, (10) 896-902.
- Hansen, P.B., Jensen, B.L., Andreasen, D., & Skott, O. (2001). Differential expression of T- and L-type voltage-dependent calcium channels in renal resistance vessels. *Circ.Res.* **89**, (7) 630-638.
- Harraz, O.F. & Welsh, D.G. (2013). Protein kinase A regulation of T-type Ca²⁺ channels in rat cerebral arterial smooth muscle. *J.Cell Sci.* **126**, (Pt 13) 2944-2954.
- Hassoun, P.M., Mouthon, L., Barbera, J.A., Eddahibi, S., Flores, S.C., Grimminger, F., Jones, P.L., Maitland, M.L., Michelakis, E.D., Morrell, N.W., Newman, J.H., Rabinovitch, M., Schermuly, R., Stenmark, K.R., Voelkel, N.F., Yuan, J.X., & Humbert, M. (2009). Inflammation, growth factors, and pulmonary vascular remodeling. *J.Am.Coll.Cardiol.* **54**, (1 Suppl) S10-S19.
- Hayashi, T., Ueno, Y., & Okamoto, T. (1993). Oxidoreductive regulation of nuclear factor kappa B. Involvement of a cellular reducing catalyst thioredoxin. *J.Biol.Chem.* **268**, (15) 11380-11388.
- He, M.F., Gao, X.P., Li, S.C., He, Z.H., Chen, N., Wang, Y.B., & She, J.X. (2014). Anti-angiogenic effect of auranofin on HUVECs in vitro and zebrafish in vivo. *Eur.J.Pharmacol.* **740**, 240-247.
- Heron, S.E., Khosravani, H., Varela, D., Bladen, C., Williams, T.C., Newman, M.R., Scheffer, I.E., Berkovic, S.F., Mulley, J.C., & Zamponi, G.W. (2007). Extended spectrum of idiopathic generalized epilepsies associated with CACNA1H functional variants. *Ann.Neurol.* **62**, (6) 560-568.
- Herrington, J. & Lingle, C.J. (1992). Kinetic and pharmacological properties of low voltage-activated Ca²⁺ current in rat clonal (GH3) pituitary cells. *J.Neurophysiol.* **68**, (1) 213-232.
- Hirst, G.D. & Edwards, F.R. (1989). Sympathetic neuroeffector transmission in arteries and arterioles. *Physiol Rev.* **69**, (2) 546-604.
- Holmgren, A. (1968). Thioredoxin. 6. The amino acid sequence of the protein from escherichia coli B. *Eur.J.Biochem.* **6**, (4) 475-484.

- Holmgren, A. (1979). Thioredoxin catalyzes the reduction of insulin disulfides by dithiothreitol and dihydrolipoamide. *J.Biol.Chem.* **254**, (19) 9627-9632.
- Holmgren, A. (1989). Thioredoxin and glutaredoxin systems. *J.Biol.Chem.* **264**, (24) 13963-13966.
- Holmgren, A. (1995). Thioredoxin structure and mechanism: conformational changes on oxidation of the active-site sulfhydryls to a disulfide. *Structure.* **3**, (3) 239-243.
- Holmgren, A. & Lu, J. (2010). Thioredoxin and thioredoxin reductase: current research with special reference to human disease. *Biochem.Biophys.Res.Comm.* **396**, (1) 120-124.
- House, S.J., Potier, M., Bisailon, J., Singer, H.A., & Trebak, M. (2008). The non-excitabile smooth muscle: calcium signaling and phenotypic switching during vascular disease. *Pflugers Arch.* **456**, (5) 769-785.
- Howitt, L., Kuo, I.Y., Ellis, A., Chaston, D.J., Shin, H.S., Hansen, P.B., & Hill, C.E. (2013). Chronic deficit in nitric oxide elicits oxidative stress and augments T-type calcium-channel contribution to vascular tone of rodent arteries and arterioles. *Cardiovasc.Res.* **98**, (3) 449-457.
- Hsu, S.C., Chang, Y.T., & Chen, C.C. (2013). Early growth response 1 is an early signal inducing Cav3.2 T-type calcium channels during cardiac hypertrophy. *Cardiovasc.Res.* **100**, (2) 222-230.
- Huang, B., Qin, D., Deng, L., Boutjdir, M., & Sherif, N. (2000). Reexpression of T-type Ca²⁺ channel gene and current in post-infarction remodeled rat left ventricle. *Cardiovasc.Res.* **46**, (3) 442-449.
- Huang, J., Xu, J., Tian, L., & Zhong, L. (2014). A thioredoxin reductase and/or thioredoxin system-based mechanism for antioxidant effects of ambroxol. *Biochimie* **97**, 92-103.
- Huang, W., Lu, C., Wu, Y., Ouyang, S., & Chen, Y. (2015). T-type calcium channel antagonists, mibefradil and NNC-55-0396 inhibit cell proliferation and induce cell apoptosis in leukemia cell lines. *J.Exp.Clin.Cancer Res.* **34**, 54.
- Huber, H.E., Tabor, S., & Richardson, C.C. (1987). Escherichia coli thioredoxin stabilizes complexes of bacteriophage T7 DNA polymerase and primed templates. *J.Biol.Chem.* **262**, (33) 16224-16232.
- Huber, K., Patel, P., Zhang, L., Evans, H., Westwell, A.D., Fischer, P.M., Chan, S., & Martin, S. (2008). 2-[(1-methylpropyl)dithio]-1H-imidazole inhibits tubulin polymerization through cysteine oxidation. *Mol.Cancer Ther.* **7**, (1) 143-151.
- Husbeck, B., Stringer, D.E., Gerner, E.W., & Powis, G. (2003). Increased thioredoxin-1 inhibits SSAT expression in MCF-7 human breast cancer cells. *Biochem.Biophys.Res.Comm.* **306**, (2) 469-475.
- Hwang, J., Nguyen, L.T., Jeon, Y.H., Lee, C.Y., & Kim, M.H. (2015). Crystal structure of fully oxidized human thioredoxin. *Biochem.Biophys.Res.Comm.* **467**, (2) 218-222.

- Inagami, T. (1989). Atrial natriuretic factor. *J.Biol.Chem.* **264**, (6) 3043-3046.
- Izumi, T., Kihara, Y., Sarai, N., Yoneda, T., Iwanaga, Y., Inagaki, K., Onozawa, Y., Takenaka, H., Kita, T., & Noma, A. (2003). Reinduction of T-type calcium channels by endothelin-1 in failing hearts in vivo and in adult rat ventricular myocytes in vitro. *Circulation* **108**, (20) 2530-2535.
- Jeng, M.F., Campbell, A.P., Begley, T., Holmgren, A., Case, D.A., Wright, P.E., & Dyson, H.J. (1994). High-resolution solution structures of oxidized and reduced Escherichia coli thioredoxin. *Structure.* **2**, (9) 853-868.
- Jiang, X., Yang, L., & Luo, Y. (2015). Animal Models of Diabetic Retinopathy. *Curr.Eye Res.* **40**, (8) 761-771.
- Kahlos, K., Soini, Y., Saily, M., Koistinen, P., Kakko, S., Paakko, P., Holmgren, A., & Kinnula, V.L. (2001). Up-regulation of thioredoxin and thioredoxin reductase in human malignant pleural mesothelioma. *Int.J.Cancer* **95**, (3) 198-204.
- Kakolyris, S., Giatromanolaki, A., Koukourakis, M., Powis, G., Souglakos, J., Sivridis, E., Georgoulas, V., Gatter, K.C., & Harris, A.L. (2001). Thioredoxin expression is associated with lymph node status and prognosis in early operable non-small cell lung cancer. *Clin.Cancer Res.* **7**, (10) 3087-3091.
- Kang, H.W., Park, J.Y., Jeong, S.W., Kim, J.A., Moon, H.J., Perez-Reyes, E., & Lee, J.H. (2006). A molecular determinant of nickel inhibition in Cav3.2 T-type calcium channels. *J.Biol.Chem.* **281**, (8) 4823-4830.
- Kang, H.W., Vitko, I., Lee, S.S., Perez-Reyes, E., & Lee, J.H. (2010). Structural determinants of the high affinity extracellular zinc binding site on Cav3.2 T-type calcium channels. *J.Biol.Chem.* **285**, (5) 3271-3281.
- Kapourchali, F.R., Surendiran, G., Chen, L., Uitz, E., Bahadori, B., & Moghadasian, M.H. (2014). Animal models of atherosclerosis. *World J.Clin.Cases.* **2**, (5) 126-132.
- Kawahara, N., Tanaka, T., Yokomizo, A., Nanri, H., Ono, M., Wada, M., Kohno, K., Takenaka, K., Sugimachi, K., & Kuwano, M. (1996). Enhanced coexpression of thioredoxin and high mobility group protein 1 genes in human hepatocellular carcinoma and the possible association with decreased sensitivity to cisplatin. *Cancer Res.* **56**, (23) 5330-5333.
- Kean, W.F., Hart, L., & Buchanan, W.W. (1997). Auranofin. *Br.J.Rheumatol.* **36**, (5) 560-572.
- Kim, D., Song, I., Keum, S., Lee, T., Jeong, M.J., Kim, S.S., McEnery, M.W., & Shin, H.S. (2001). Lack of the burst firing of thalamocortical relay neurons and resistance to absence seizures in mice lacking alpha(1G) T-type Ca(2+) channels. *Neuron* **31**, (1) 35-45.
- Kimes, B.W. & Brandt, B.L. (1976). Characterization of two putative smooth muscle cell lines from rat thoracic aorta. *Exp.Cell Res.* **98**, (2) 349-366.

- Kirkpatrick, D.L., Kuperus, M., Dowdeswell, M., Potier, N., Donald, L.J., Kunkel, M., Berggren, M., Angulo, M., & Powis, G. (1998). Mechanisms of inhibition of the thioredoxin growth factor system by antitumor 2-imidazolyl disulfides. *Biochem.Pharmacol.* **55**, (7) 987-994.
- Klockner, U., Lee, J.H., Cribbs, L.L., Daud, A., Hescheler, J., Pereverzev, A., Perez-Reyes, E., & Schneider, T. (1999). Comparison of the Ca²⁺ currents induced by expression of three cloned alpha1 subunits, alpha1G, alpha1H and alpha1I, of low-voltage-activated T-type Ca²⁺ channels. *Eur.J.Neurosci.* **11**, (12) 4171-4178.
- Kondo, N., Ishii, Y., Kwon, Y.W., Tanito, M., Horita, H., Nishinaka, Y., Nakamura, H., & Yodoi, J. (2004). Redox-sensing release of human thioredoxin from T lymphocytes with negative feedback loops. *J.Immunol.* **172**, (1) 442-448.
- Kuga, T., Kobayashi, S., Hirakawa, Y., Kanaide, H., & Takeshita, A. (1996). Cell cycle--dependent expression of L- and T-type Ca²⁺ currents in rat aortic smooth muscle cells in primary culture. *Circ.Res.* **79**, (1) 14-19.
- Kuo, I.Y., Ellis, A., Seymour, V.A., Sandow, S.L., & Hill, C.E. (2010). Dihydropyridine-insensitive calcium currents contribute to function of small cerebral arteries. *J.Cereb.Blood Flow Metab* **30**, (6) 1226-1239.
- Kuo, I.Y., Howitt, L., Sandow, S.L., McFarlane, A., Hansen, P.B., & Hill, C.E. (2014). Role of T-type channels in vasomotor function: team player or chameleon? *Pflugers Arch.* **466**, (4) 767-779.
- Kuo, I.Y., Wolfle, S.E., & Hill, C.E. (2011). T-type calcium channels and vascular function: the new kid on the block? *J.Physiol* **589**, (Pt 4) 783-795.
- Kwapiszewska, G., Chwalek, K., Marsh, L.M., Wygrecka, M., Wilhelm, J., Best, J., Egemnazarov, B., Weisel, F.C., Osswald, S.L., Schermuly, R.T., Olschewski, A., Seeger, W., Weissmann, N., Eickelberg, O., & Fink, L. (2012). BDNF/TrkB signaling augments smooth muscle cell proliferation in pulmonary hypertension. *Am.J.Pathol.* **181**, (6) 2018-2029.
- Lafleur, M.A., Handsley, M.M., & Edwards, D.R. (2003). Metalloproteinases and their inhibitors in angiogenesis. *Expert.Rev.Mol.Med.* **5**, (23) 1-39.
- Lawrie, A. (2014). A report on the use of animal models and phenotyping methods in pulmonary hypertension research. *Pulm.Circ.* **4**, (1) 2-9.
- Le, Q.K., Naud, P., Qi, X.Y., Duval, F., Shi, Y.F., Gillis, M.A., Comtois, P., Tardif, J.C., Li, D., Levesque, P.C., Dobrev, D., Charpentier, F., & Nattel, S. (2011). Role of T-type calcium channel subunits in post-myocardial infarction remodelling probed with genetically engineered mice. *Cardiovasc.Res.* **91**, (3) 420-428.
- Lee, J.H., Gomora, J.C., Cribbs, L.L., & Perez-Reyes, E. (1999). Nickel block of three cloned T-type calcium channels: low concentrations selectively block alpha1H. *Biophys.J.* **77**, (6) 3034-3042.

Lee, W.Y., Orestes, P., Latham, J., Naik, A.K., Nelson, M.T., Vitko, I., Perez-Reyes, E., Jevtovic-Todorovic, V., & Todorovic, S.M. (2009). Molecular mechanisms of lipoic acid modulation of T-type calcium channels in pain pathway. *J.Neurosci.* **29**, (30) 9500-9509.

Lessa, J.A., Guerra, J.C., de Miranda, L.F., Romeiro, C.F., Da Silva, J.G., Mendes, I.C., Speziali, N.L., Souza-Fagundes, E.M., & Beraldo, H. (2011). Gold(I) complexes with thiosemicarbazones: cytotoxicity against human tumor cell lines and inhibition of thioredoxin reductase activity. *J.Inorg.Biochem.* **105**, (12) 1729-1739.

Leuranguer, V., Monteil, A., Bourinet, E., Dayanithi, G., & Nargeot, J. (2000). T-type calcium currents in rat cardiomyocytes during postnatal development: contribution to hormone secretion. *Am.J.Physiol Heart Circ.Physiol* **279**, (5) H2540-H2548.

Li, G.Z., Liang, H.F., Liao, B., Zhang, L., Ni, Y.A., Zhou, H.H., Zhang, E.L., Zhang, B.X., & Chen, X.P. (2015a). PX-12 inhibits the growth of hepatocellular carcinoma by inducing S-phase arrest, ROS-dependent apoptosis and enhances 5-FU cytotoxicity. *Am.J.Transl.Res.* **7**, (9) 1528-1540.

Li, M., Hansen, J.B., Huang, L., Keyser, B.M., & Taylor, J.T. (2005). Towards selective antagonists of T-type calcium channels: design, characterization and potential applications of NNC 55-0396. *Cardiovasc.Drug Rev.* **23**, (2) 173-196.

Li, M., Wang, N., Gong, H.Q., Li, W.Z., Liao, X.H., Yang, X.L., He, H.P., Cao, D.S., & Zhang, T.C. (2015b). Ca(2)(+) signal-induced cardiomyocyte hypertrophy through activation of myocardin. *Gene* **557**, (1) 43-51.

Li, Z., Wang, X., Gao, G., Qu, D., Yu, B., Huang, C., Elmslie, K.S., & Peterson, B.Z. (2010). A single amino acid change in Ca(v)1.2 channels eliminates the permeation and gating differences between Ca(2+) and Ba(2+). *J.Membr.Biol.* **233**, (1-3) 23-33.

Liao, P., Yu, D., Li, G., Yong, T.F., Soon, J.L., Chua, Y.L., & Soong, T.W. (2007). A smooth muscle Cav1.2 calcium channel splice variant underlies hyperpolarized window current and enhanced state-dependent inhibition by nifedipine. *J.Biol.Chem.* **282**, (48) 35133-35142.

Lindner, V., Fingerle, J., & Reidy, M.A. (1993). Mouse model of arterial injury. *Circ.Res.* **73**, (5) 792-796.

Lipscombe, D., Helton, T.D., & Xu, W. (2004). L-type calcium channels: the low down. *J.Neurophysiol.* **92**, (5) 2633-2641.

Liu, J., Ren, Y., Kang, L., & Zhang, L. (2014). Oxidized low-density lipoprotein increases the proliferation and migration of human coronary artery smooth muscle cells through the upregulation of osteopontin. *Int.J.Mol.Med.* **33**, (5) 1341-1347.

Long, S.B., Tao, X., Campbell, E.B., & MacKinnon, R. (2007). Atomic structure of a voltage-dependent K⁺ channel in a lipid membrane-like environment. *Nature* **450**, (7168) 376-382.

Louis, H., Lacolley, P., Kakou, A., Cattan, V., Daret, D., Safar, M., Bonnet, J., & Daniel Lamaziere, J.M. (2006). Early activation of internal medial smooth muscle cells in the rabbit aorta after mechanical injury: relationship with intimal thickening and pharmacological applications. *Clin.Exp.Pharmacol.Physiol* **33**, (1-2) 131-138.

Lu, J. & Holmgren, A. (2014). The thioredoxin antioxidant system. *Free Radic.Biol.Med.* **66**, 75-87.

Luo, X., Xiao, Y., Song, F., Yang, Y., Xia, M., & Ling, W. (2012). Increased plasma S-adenosyl-homocysteine levels induce the proliferation and migration of VSMCs through an oxidative stress-ERK1/2 pathway in apoE(-/-) mice. *Cardiovasc.Res.* **95**, (2) 241-250.

Luthman, M. & Holmgren, A. (1982). Rat liver thioredoxin and thioredoxin reductase: purification and characterization. *Biochemistry* **21**, (26) 6628-6633.

Maarman, G., Lecour, S., Butrous, G., Thienemann, F., & Sliwa, K. (2013). A comprehensive review: the evolution of animal models in pulmonary hypertension research; are we there yet? *Pulm.Circ.* **3**, (4) 739-756.

Madeira, J.M., Gibson, D.L., Kean, W.F., & Klegeris, A. (2012). The biological activity of auranofin: implications for novel treatment of diseases. *Inflammopharmacology.* **20**, (6) 297-306.

Mao, N., Gu, T., Shi, E., Zhang, G., Yu, L., & Wang, C. (2015). Phenotypic switching of vascular smooth muscle cells in animal model of rat thoracic aortic aneurysm. *Interact.Cardiovasc.Thorac.Surg.* **21**, (1) 62-70.

Marger, L., Mesirca, P., Alig, J., Torrente, A., Dubel, S., Engeland, B., Kanani, S., Fontanaud, P., Striessnig, J., Shin, H.S., Isbrandt, D., Ehmke, H., Nargeot, J., & Mangoni, M.E. (2011). Functional roles of Ca(v)1.3, Ca(v)3.1 and HCN channels in automaticity of mouse atrioventricular cells: insights into the atrioventricular pacemaker mechanism. *Channels (Austin.)* **5**, (3) 251-261.

Marino, S.M. & Gladyshev, V.N. (2010). Cysteine function governs its conservation and degeneration and restricts its utilization on protein surfaces. *J.Mol.Biol.* **404**, (5) 902-916.

Mariot, P., Vanoverberghe, K., Lalevee, N., Rossier, M.F., & Prevarskaya, N. (2002). Overexpression of an alpha 1H (Cav3.2) T-type calcium channel during neuroendocrine differentiation of human prostate cancer cells. *J.Biol.Chem.* **277**, (13) 10824-10833.

Markandeya, Y.S., Fahey, J.M., Pluteanu, F., Cribbs, L.L., & Balijepalli, R.C. (2011). Caveolin-3 regulates protein kinase A modulation of the Ca(V)3.2 (alpha1H) T-type Ca²⁺ channels. *J.Biol.Chem.* **286**, (4) 2433-2444.

Martin, K., Weiss, S., Metharom, P., Schmeckpeper, J., Hynes, B., O'Sullivan, J., & Caplice, N. (2009). Thrombin stimulates smooth muscle cell differentiation from peripheral blood mononuclear cells via protease-activated receptor-1, RhoA, and myocardin. *Circ.Res.* **105**, (3) 214-218.

- Martinez, M.L., Heredia, M.P., & Delgado, C. (1999). Expression of T-type Ca(2+) channels in ventricular cells from hypertrophied rat hearts. *J.Mol.Cell Cardiol.* **31**, (9) 1617-1625.
- Marx, S.O., Totary-Jain, H., & Marks, A.R. (2011). Vascular smooth muscle cell proliferation in restenosis. *Circ.Cardiovasc.Interv.* **4**, (1) 104-111.
- Matchkov, V.V., Kudryavtseva, O., & Aalkjaer, C. (2012). Intracellular Ca(2)(+) signalling and phenotype of vascular smooth muscle cells. *Basic Clin.Pharmacol.Toxicol.* **110**, (1) 42-48.
- Matsubara, T. & Ziff, M. (1987). Inhibition of human endothelial cell proliferation by gold compounds. *J.Clin.Invest* **79**, (5) 1440-1446.
- Matsumoto, T. & Nagayama, K. (2012). Tensile properties of vascular smooth muscle cells: bridging vascular and cellular biomechanics. *J.Biomech.* **45**, (5) 745-755.
- Matthews, J.R., Wakasugi, N., Virelizier, J.L., Yodoi, J., & Hay, R.T. (1992). Thioredoxin regulates the DNA binding activity of NF-kappa B by reduction of a disulphide bond involving cysteine 62. *Nucleic Acids Res.* **20**, (15) 3821-3830.
- McClatchey, A.I. & Yap, A.S. (2012). Contact inhibition (of proliferation) redux. *Curr.Opin.Cell Biol.* **24**, (5) 685-694.
- McKay, B.E., McRory, J.E., Molineux, M.L., Hamid, J., Snutch, T.P., Zamponi, G.W., & Turner, R.W. (2006). Ca(V)3 T-type calcium channel isoforms differentially distribute to somatic and dendritic compartments in rat central neurons. *Eur.J.Neurosci.* **24**, (9) 2581-2594.
- McNeish, A.J., Altayo, F.J., & Garland, C.J. (2010). Evidence both L-type and non-L-type voltage-dependent calcium channels contribute to cerebral artery vasospasm following loss of NO in the rat. *Vascul.Pharmacol.* **53**, (3-4) 151-159.
- Mesirca, P., Torrente, A.G., & Mangoni, M.E. (2014). T-type channels in the sino-atrial and atrioventricular pacemaker mechanism. *Pflugers Arch.* **466**, (4) 791-799.
- Mishra, S.K. & Hermsmeyer, K. (1994). Selective inhibition of T-type Ca²⁺ channels by Ro 40-5967. *Circ.Res.* **75**, (1) 144-148.
- Miyamoto, S., Sakamoto, T., Soejima, H., Shimomura, H., Kajiwara, I., Kojima, S., Hokamaki, J., Sugiyama, S., Yoshimura, M., Ozaki, Y., Nakamura, H., Yodoi, J., & Ogawa, H. (2003). Plasma thioredoxin levels and platelet aggregability in patients with acute myocardial infarction. *Am.Heart J.* **146**, (3) 465-471.
- Mlinar, B., Biagi, B.A., & Enyeart, J.J. (1993). Voltage-gated transient currents in bovine adrenal fasciculata cells. I. T-type Ca²⁺ current. *J.Gen.Physiol* **102**, (2) 217-237.
- Mongardon, N., Lemiale, V., Borderie, D., Burke-Gaffney, A., Perbet, S., Marin, N., Charpentier, J., Pene, F., Chiche, J.D., Mira, J.P., & Cariou, A. (2013). Plasma thioredoxin levels during post-cardiac arrest syndrome: relationship with severity and outcome. *Crit Care* **17**, (1) R18.

Montano, S.J., Lu, J., Gustafsson, T.N., & Holmgren, A. (2014). Activity assays of mammalian thioredoxin and thioredoxin reductase: fluorescent disulfide substrates, mechanisms, and use with tissue samples. *Anal.Biochem.* **449**, 139-146.

Mosmann, T. (1983). Rapid colorimetric assay for cellular growth and survival: application to proliferation and cytotoxicity assays. *J.Immunol.Methods* **65**, (1-2) 55-63.

Mulvany, M.J. (2012). Small artery remodelling in hypertension. *Basic Clin.Pharmacol.Toxicol.* **110**, (1) 49-55.

Nakamura, H., Bai, J., Nishinaka, Y., Ueda, S., Sasada, T., Ohshio, G., Imamura, M., Takabayashi, A., Yamaoka, Y., & Yodoi, J. (2000). Expression of thioredoxin and glutaredoxin, redox-regulating proteins, in pancreatic cancer. *Cancer Detect.Prev.* **24**, (1) 53-60.

Nakamura, H., De, R.S., Roederer, M., Anderson, M.T., Dubs, J.G., Yodoi, J., Holmgren, A., Herzenberg, L.A., & Herzenberg, L.A. (1996). Elevation of plasma thioredoxin levels in HIV-infected individuals. *Int.Immunol.* **8**, (4) 603-611.

Nakamura, H., Masutani, H., Tagaya, Y., Yamauchi, A., Inamoto, T., Nanbu, Y., Fujii, S., Ozawa, K., & Yodoi, J. (1992). Expression and growth-promoting effect of adult T-cell leukemia-derived factor. A human thioredoxin homologue in hepatocellular carcinoma. *Cancer* **69**, (8) 2091-2097.

Nakamura, H., Masutani, H., & Yodoi, J. (2006). Extracellular thioredoxin and thioredoxin-binding protein 2 in control of cancer. *Semin.Cancer Biol.* **16**, (6) 444-451.

Nakamura, H., Nakamura, K., & Yodoi, J. (1997). Redox regulation of cellular activation. *Annu.Rev.Immunol.* **15**, 351-369.

Nakamura, H., Vaage, J., Valen, G., Padilla, C.A., Bjornstedt, M., & Holmgren, A. (1998). Measurements of plasma glutaredoxin and thioredoxin in healthy volunteers and during open-heart surgery. *Free Radic.Biol.Med.* **24**, (7-8) 1176-1186.

Nelson, M.T., Joksovic, P.M., Su, P., Kang, H.W., Van, D.A., Baumgart, J.P., David, L.S., Snutch, T.P., Barrett, P.Q., Lee, J.H., Zorumski, C.F., Perez-Reyes, E., & Todorovic, S.M. (2007a). Molecular mechanisms of subtype-specific inhibition of neuronal T-type calcium channels by ascorbate. *J.Neurosci.* **27**, (46) 12577-12583.

Nelson, M.T., Todorovic, S.M., & Perez-Reyes, E. (2006). The role of T-type calcium channels in epilepsy and pain. *Curr.Pharm.Des* **12**, (18) 2189-2197.

Nelson, M.T., Woo, J., Kang, H.W., Vitko, I., Barrett, P.Q., Perez-Reyes, E., Lee, J.H., Shin, H.S., & Todorovic, S.M. (2007b). Reducing agents sensitize C-type nociceptors by relieving high-affinity zinc inhibition of T-type calcium channels. *J.Neurosci.* **27**, (31) 8250-8260.

Newman, G.W., Balcewicz-Sablinska, M.K., Guarnaccia, J.R., Remold, H.G., & Silberstein, D.S. (1994). Opposing regulatory effects of thioredoxin and eosinophil cytotoxicity-enhancing factor on the development of human immunodeficiency virus 1. *J.Exp.Med.* **180**, (1) 359-363.

Nuss, H.B. & Houser, S.R. (1993). T-type Ca²⁺ current is expressed in hypertrophied adult feline left ventricular myocytes. *Circ.Res.* **73**, (4) 777-782.

Nwasokwa, O.N. (1995). Coronary artery bypass graft disease. *Ann.Intern.Med.* **123**, (7) 528-545.

Oblong, J.E., Berggren, M., Gasdaska, P.Y., & Powis, G. (1994). Site-directed mutagenesis of active site cysteines in human thioredoxin produces competitive inhibitors of human thioredoxin reductase and elimination of mitogenic properties of thioredoxin. *J.Biol.Chem.* **269**, (16) 11714-11720.

Ogusucu, R., Rettori, D., Munhoz, D.C., Netto, L.E., & Augusto, O. (2007). Reactions of yeast thioredoxin peroxidases I and II with hydrogen peroxide and peroxynitrite: rate constants by competitive kinetics. *Free Radic.Biol.Med.* **42**, (3) 326-334.

Okuda, M., Inoue, N., Azumi, H., Seno, T., Sumi, Y., Hirata, K., Kawashima, S., Hayashi, Y., Itoh, H., Yodoi, J., & Yokoyama, M. (2001). Expression of glutaredoxin in human coronary arteries: its potential role in antioxidant protection against atherosclerosis. *Arterioscler.Thromb.Vasc.Biol.* **21**, (9) 1483-1487.

Otaki, Y., Watanabe, T., Takahashi, H., Kadowaki, S., Narumi, T., Honda, Y., Wanezaki, M., Sasaki, S., Tamura, H., Nishiyama, S., Arimoto, T., Shishido, T., Miyamoto, T., & Kubota, I. (2014). Association of plasma thioredoxin-1 with renal tubular damage and cardiac prognosis in patients with chronic heart failure. *J.Cardiol.* **64**, (5) 353-359.

Otun, H., Gillespie, J.I., Nicholls, J.A., Greenwell, J.R., & Dunlop, W. (1992). Transients in intracellular free calcium in subconfluent and confluent cultures of a rat smooth muscle cell line. *Exp.Physiol* **77**, (5) 749-756.

Pandolfi, A., Grilli, A., Cilli, C., Patruno, A., Giaccari, A., Di, S.S., De Lutiis, M.A., Pellegrini, G., Capani, F., Consoli, A., & Felaco, M. (2003). Phenotype modulation in cultures of vascular smooth muscle cells from diabetic rats: association with increased nitric oxide synthase expression and superoxide anion generation. *J.Cell Physiol* **196**, (2) 378-385.

Panner, A., Cribbs, L.L., Zainelli, G.M., Origitano, T.C., Singh, S., & Wurster, R.D. (2005). Variation of T-type calcium channel protein expression affects cell division of cultured tumor cells. *Cell Calcium* **37**, (2) 105-119.

Panner, A. & Wurster, R.D. (2006). T-type calcium channels and tumor proliferation. *Cell Calcium* **40**, (2) 253-259.

Patwari, P., Higgins, L.J., Chutkow, W.A., Yoshioka, J., & Lee, R.T. (2006). The interaction of thioredoxin with Txnip. Evidence for formation of a mixed disulfide by disulfide exchange. *J.Biol.Chem.* **281**, (31) 21884-21891.

Paulin, R., Meloche, J., Courboulin, A., Lambert, C., Haromy, A., Courchesne, A., Bonnet, P., Provencher, S., Michelakis, E.D., & Bonnet, S. (2014). Targeting cell motility in pulmonary arterial hypertension. *Eur.Respir.J.* **43**, (2) 531-544.

- Pekkari, K., Avila-Carino, J., Bengtsson, A., Gurunath, R., Scheynius, A., & Holmgren, A. (2001). Truncated thioredoxin (Trx80) induces production of interleukin-12 and enhances CD14 expression in human monocytes. *Blood* **97**, (10) 3184-3190.
- Perez-Reyes, E. (1999). Three for T: molecular analysis of the low voltage-activated calcium channel family. *Cell Mol.Life Sci.* **56**, (7-8) 660-669.
- Perez-Reyes, E. (2003). Molecular physiology of low-voltage-activated t-type calcium channels. *Physiol Rev.* **83**, (1) 117-161.
- Perez-Reyes, E. (2006). Molecular characterization of T-type calcium channels. *Cell Calcium* **40**, (2) 89-96.
- Perez-Reyes, E. & Lee, J.H. (2014). Ins and outs of T-channel structure function. *Pflugers Arch.* **466**, (4) 627-633.
- Peterson, B.Z., Tanada, T.N., & Catterall, W.A. (1996). Molecular determinants of high affinity dihydropyridine binding in L-type calcium channels. *J.Biol.Chem.* **271**, (10) 5293-5296.
- Pirillo, A., Norata, G.D., & Catapano, A.L. (2013). LOX-1, OxLDL, and atherosclerosis. *Mediators.Inflamm.* **2013**, 152786.
- Poole, L.B. (2015). The basics of thiols and cysteines in redox biology and chemistry. *Free Radic.Biol.Med.* **80**, 148-157.
- Porter, K.E., Naik, J., Turner, N.A., Dickinson, T., Thompson, M.M., & London, N.J. (2002). Simvastatin inhibits human saphenous vein neointima formation via inhibition of smooth muscle cell proliferation and migration. *J.Vasc.Surg.* **36**, (1) 150-157.
- Porter, K.E. & Riches, K. (2013). The vascular smooth muscle cell: a therapeutic target in Type 2 diabetes? *Clin.Sci.(Lond)* **125**, (4) 167-182.
- Powell, K.L., Cain, S.M., Ng, C., Sirdesai, S., David, L.S., Kyi, M., Garcia, E., Tyson, J.R., Reid, C.A., Bahlo, M., Foote, S.J., Snutch, T.P., & O'Brien, T.J. (2009). A Cav3.2 T-type calcium channel point mutation has splice-variant-specific effects on function and segregates with seizure expression in a polygenic rat model of absence epilepsy. *J.Neurosci.* **29**, (2) 371-380.
- Powell, K.L., Cain, S.M., Snutch, T.P., & O'Brien, T.J. (2014). Low threshold T-type calcium channels as targets for novel epilepsy treatments. *Br.J.Clin.Pharmacol.* **77**, (5) 729-739.
- Powis, G., Mustacich, D., & Coon, A. (2000). The role of the redox protein thioredoxin in cell growth and cancer. *Free Radic.Biol.Med.* **29**, (3-4) 312-322.
- Qi, A.Q., Li, Y., Liu, Q., Si, J.Z., Tang, X.M., Zhang, Z.Q., Qi, Q.D., & Chen, W.B. (2015). Thioredoxin is a novel diagnostic and prognostic marker in patients with ischemic stroke. *Free Radic.Biol.Med.* **80**, 129-135.

Raffel, J., Bhattacharyya, A.K., Gallegos, A., Cui, H., Einspahr, J.G., Alberts, D.S., & Powis, G. (2003). Increased expression of thioredoxin-1 in human colorectal cancer is associated with decreased patient survival. *J.Lab Clin.Med.* **142**, (1) 46-51.

Ramanathan, R.K., Abbruzzese, J., Dragovich, T., Kirkpatrick, L., Guillen, J.M., Baker, A.F., Pestano, L.A., Green, S., & Von Hoff, D.D. (2011). A randomized phase II study of PX-12, an inhibitor of thioredoxin in patients with advanced cancer of the pancreas following progression after a gemcitabine-containing combination. *Cancer Chemother.Pharmacol.* **67**, (3) 503-509.

Ramanathan, R.K., Kirkpatrick, D.L., Belani, C.P., Friedland, D., Green, S.B., Chow, H.H., Cordova, C.A., Stratton, S.P., Sharlow, E.R., Baker, A., & Dragovich, T. (2007). A Phase I pharmacokinetic and pharmacodynamic study of PX-12, a novel inhibitor of thioredoxin-1, in patients with advanced solid tumors. *Clin.Cancer Res.* **13**, (7) 2109-2114.

Raninga, P.V., Di, T.G., Vuckovic, S., Bhatia, M., & Tonissen, K.F. (2015). Inhibition of thioredoxin 1 leads to apoptosis in drug-resistant multiple myeloma. *Oncotarget.* **6**, (17) 15410-15424.

Richard, S., Neveu, D., Carnac, G., Bodin, P., Travo, P., & Nargeot, J. (1992). Differential expression of voltage-gated Ca(2+)-currents in cultivated aortic myocytes. *Biochim.Biophys.Acta* **1160**, (1) 95-104.

Rizzoni, D., Porteri, E., Boari, G.E., De, C.C., Sleiman, I., Muiesan, M.L., Castellano, M., Miclini, M., & Agabiti-Rosei, E. (2003). Prognostic significance of small-artery structure in hypertension. *Circulation* **108**, (18) 2230-2235.

Roder, C. & Thomson, M.J. (2015). Auranofin: repurposing an old drug for a golden new age. *Drugs R.D.* **15**, (1) 13-20.

Rodman, D.M., Reese, K., Harral, J., Fouty, B., Wu, S., West, J., Hoedt-Miller, M., Tada, Y., Li, K.X., Cool, C., Fagan, K., & Cribbs, L. (2005). Low-voltage-activated (T-type) calcium channels control proliferation of human pulmonary artery myocytes. *Circ.Res.* **96**, (8) 864-872.

Rodriguez-Gomez, J.A., Levitsky, K.L., & Lopez-Barneo, J. (2012). T-type Ca²⁺ channels in mouse embryonic stem cells: modulation during cell cycle and contribution to self-renewal. *Am.J.Physiol Cell Physiol* **302**, (3) C494-C504.

Rubartelli, A., Bajetto, A., Allavena, G., Wollman, E., & Sitia, R. (1992). Secretion of thioredoxin by normal and neoplastic cells through a leaderless secretory pathway. *J.Biol.Chem.* **267**, (34) 24161-24164.

Rubartelli, A., Bonifaci, N., & Sitia, R. (1995). High rates of thioredoxin secretion correlate with growth arrest in hepatoma cells. *Cancer Res.* **55**, (3) 675-680.

Saitoh, M., Nishitoh, H., Fujii, M., Takeda, K., Tobiume, K., Sawada, Y., Kawabata, M., Miyazono, K., & Ichijo, H. (1998). Mammalian thioredoxin is a direct inhibitor of apoptosis signal-regulating kinase (ASK) 1. *EMBO J.* **17**, (9) 2596-2606.

- Satin, L.S. (2000). Localized calcium influx in pancreatic beta-cells: its significance for Ca²⁺-dependent insulin secretion from the islets of Langerhans. *Endocrine*. **13**, (3) 251-262.
- Satoh, K., Satoh, T., Kikuchi, N., Omura, J., Kurosawa, R., Suzuki, K., Sugimura, K., Aoki, T., Nochioka, K., Tatebe, S., Miyamichi-Yamamoto, S., Miura, M., Shimizu, T., Ikeda, S., Yaoita, N., Fukumoto, Y., Minami, T., Miyata, S., Nakamura, K., Ito, H., Kadomatsu, K., & Shimokawa, H. (2014). Basigin mediates pulmonary hypertension by promoting inflammation and vascular smooth muscle cell proliferation. *Circ.Res.* **115**, (8) 738-750.
- Schmitt, R., Clozel, J.P., Iberg, N., & Buhler, F.R. (1996). Prevention of neointima formation by mibefradil after vascular injury in rats: comparison with ACE inhibition. *Cardiovasc.Drugs Ther.* **10**, (2) 101-105.
- Schrier, A.D., Wang, H., Talley, E.M., Perez-Reyes, E., & Barrett, P.Q. (2001). alpha1H T-type Ca²⁺ channel is the predominant subtype expressed in bovine and rat zona glomerulosa. *Am.J.Physiol Cell Physiol* **280**, (2) C265-C272.
- Schulze, P.C., de Keulenaer, G.W., Yoshioka, J., Kassik, K.A., & Lee, R.T. (2002). Vitamin D3-upregulated protein-1 (VDUP-1) regulates redox-dependent vascular smooth muscle cell proliferation through interaction with thioredoxin. *Circ.Res.* **91**, (8) 689-695.
- Scragg, J.L., Dallas, M.L., & Peers, C. (2007). Molecular requirements for L-type Ca²⁺ channel blockade by testosterone. *Cell Calcium* **42**, (1) 11-15.
- Sellak, H., Zhou, C., Liu, B., Chen, H., Lincoln, T.M., & Wu, S. (2014). Transcriptional regulation of alpha1H T-type calcium channel under hypoxia. *Am.J.Physiol Cell Physiol* **307**, (7) C648-C656.
- Serrano, J.R., Dashti, S.R., Perez-Reyes, E., & Jones, S.W. (2000). Mg²⁺ block unmasks Ca²⁺/Ba²⁺ selectivity of alpha1G T-type calcium channels. *Biophys.J.* **79**, (6) 3052-3062.
- Shin, H.R., You, B.R., & Park, W.H. (2013). PX-12-induced HeLa cell death is associated with oxidative stress and GSH depletion. *Oncol.Lett.* **6**, (6) 1804-1810.
- Shorofsky, S.R. & January, C.T. (1992). L- and T-type Ca²⁺ channels in canine cardiac Purkinje cells. Single-channel demonstration of L-type Ca²⁺ window current. *Circ.Res.* **70**, (3) 456-464.
- Simard, E., Sollradl, T., Maltais, J.S., Boucher, J., D'Orleans-Juste, P., & Grandbois, M. (2015). Receptor for Advanced Glycation End-Products Signaling Interferes with the Vascular Smooth Muscle Cell Contractile Phenotype and Function. *PLoS.One.* **10**, (8) e0128881.
- Simms, B.A. & Zamponi, G.W. (2014). Neuronal voltage-gated calcium channels: structure, function, and dysfunction. *Neuron* **82**, (1) 24-45.

Smith, A.R., Shenvi, S.V., Widlansky, M., Suh, J.H., & Hagen, T.M. (2004). Lipoic acid as a potential therapy for chronic diseases associated with oxidative stress. *Curr.Med.Chem.* **11**, (9) 1135-1146.

Smith, P.K., Krohn, R.I., Hermanson, G.T., Mallia, A.K., Gartner, F.H., Provenzano, M.D., Fujimoto, E.K., Goeke, N.M., Olson, B.J., & Klenk, D.C. (1985). Measurement of protein using bicinchoninic acid. *Anal.Biochem.* **150**, (1) 76-85.

Soderberg, A., Sahaf, B., & Rosen, A. (2000). Thioredoxin reductase, a redox-active selenoprotein, is secreted by normal and neoplastic cells: presence in human plasma. *Cancer Res.* **60**, (8) 2281-2289.

Soini, Y., Kahlos, K., Napankangas, U., Kaarteenaho-Wiik, R., Saily, M., Koistinen, P., Paaakko, P., Holmgren, A., & Kinnula, V.L. (2001). Widespread expression of thioredoxin and thioredoxin reductase in non-small cell lung carcinoma. *Clin.Cancer Res.* **7**, (6) 1750-1757.

Sperti, G. & Colucci, W.S. (1991). Calcium influx modulates DNA synthesis and proliferation in A7r5 vascular smooth muscle cells. *Eur.J.Pharmacol.* **206**, (4) 279-284.

Stadtman, E.R. (1991). Ascorbic acid and oxidative inactivation of proteins. *Am.J.Clin.Nutr.* **54**, (6 Suppl) 1125S-1128S.

Stadtman, E.R. (1993). Oxidation of free amino acids and amino acid residues in proteins by radiolysis and by metal-catalyzed reactions. *Annu.Rev.Biochem.* **62**, 797-821.

Suresh, S.C., Selvaraju, V., Thirunavukkarasu, M., Goldman, J.W., Husain, A., Alexander, P.J., Sanchez, J.A., McFadden, D.W., & Maulik, N. (2015). Thioredoxin-1 (Trx1) engineered mesenchymal stem cell therapy increased pro-angiogenic factors, reduced fibrosis and improved heart function in the infarcted rat myocardium. *Int.J.Cardiol.* **201**, 517-528.

Swynghedauw, B. (1999). Molecular mechanisms of myocardial remodeling. *Physiol Rev.* **79**, (1) 215-262.

Talley, E.M., Cribbs, L.L., Lee, J.H., Daud, A., Perez-Reyes, E., & Bayliss, D.A. (1999). Differential distribution of three members of a gene family encoding low voltage-activated (T-type) calcium channels. *J.Neurosci.* **19**, (6) 1895-1911.

Tanito, M., Nakamura, H., Kwon, Y.W., Teratani, A., Masutani, H., Shioji, K., Kishimoto, C., Ohira, A., Horie, R., & Yodoi, J. (2004). Enhanced oxidative stress and impaired thioredoxin expression in spontaneously hypertensive rats. *Antioxid.Redox.Signal.* **6**, (1) 89-97.

Tanudji, M., Hevi, S., & Chuck, S.L. (2003). The nonclassic secretion of thioredoxin is not sensitive to redox state. *Am.J.Physiol Cell Physiol* **284**, (5) C1272-C1279.

Tao, L., Gao, E., Bryan, N.S., Qu, Y., Liu, H.R., Hu, A., Christopher, T.A., Lopez, B.L., Yodoi, J., Koch, W.J., Feelisch, M., & Ma, X.L. (2004). Cardioprotective effects of

thioredoxin in myocardial ischemia and reperfusion: role of S-nitrosation [corrected]. *Proc.Natl.Acad.Sci.U.S.A* **101**, (31) 11471-11476.

Taylor, J.T., Huang, L., Pottle, J.E., Liu, K., Yang, Y., Zeng, X., Keyser, B.M., Agrawal, K.C., Hansen, J.B., & Li, M. (2008a). Selective blockade of T-type Ca²⁺ channels suppresses human breast cancer cell proliferation. *Cancer Lett.* **267**, (1) 116-124.

Taylor, J.T., Zeng, X.B., Pottle, J.E., Lee, K., Wang, A.R., Yi, S.G., Scruggs, J.A., Sikka, S.S., & Li, M. (2008b). Calcium signaling and T-type calcium channels in cancer cell cycling. *World J.Gastroenterol.* **14**, (32) 4984-4991.

Thomas, P. & Smart, T.G. (2005). HEK293 cell line: a vehicle for the expression of recombinant proteins. *J.Pharmacol.Toxicol.Methods* **51**, (3) 187-200.

Todorovic, S.M. & Jevtovic-Todorovic, V. (2014). Redox regulation of neuronal voltage-gated calcium channels. *Antioxid.Redox.Signal.* **21**, (6) 880-891.

Todorovic, S.M., Jevtovic-Todorovic, V., Meyenburg, A., Mennerick, S., Perez-Reyes, E., Romano, C., Olney, J.W., & Zorumski, C.F. (2001). Redox modulation of T-type calcium channels in rat peripheral nociceptors. *Neuron* **31**, (1) 75-85.

Toledo, A., Sandoval, A., Gonzalez-Ramirez, R., Avila, T., Almanza, A., Monjaraz, E., Gomora, J.C., Piedras-Renteria, E.S., & Felix, R. (2012). Insulin-mediated upregulation of T-type Ca²⁺ currents in GH3 cells is mediated by increased endosomal recycling and incorporation of surface membrane Cav3.1 channels. *Cell Calcium* **52**, (5) 377-387.

Tomic, M., Koshimizu, T., Yuan, D., Andric, S.A., Zivadinovic, D., & Stojilkovic, S.S. (1999). Characterization of a plasma membrane calcium oscillator in rat pituitary somatotrophs. *J.Biol.Chem.* **274**, (50) 35693-35702.

Tonissen, K.F. & Di, T.G. (2009). Thioredoxin system inhibitors as mediators of apoptosis for cancer therapy. *Mol.Nutr.Food Res.* **53**, (1) 87-103.

Tretinyak, A.S., Lee, E.S., Uema, K.M., d'Audiffret, A.C., Caldwell, M.P., & Santilli, S.M. (2002). Supplemental oxygen reduces intimal hyperplasia after intraarterial stenting in the rabbit. *J.Vasc.Surg.* **35**, (5) 982-987.

Tsakiridou, E., Bertollini, L., de, C.M., Avanzini, G., & Pape, H.C. (1995). Selective increase in T-type calcium conductance of reticular thalamic neurons in a rat model of absence epilepsy. *J.Neurosci.* **15**, (4) 3110-3117.

Tzeng, B.H., Chen, Y.H., Huang, C.H., Lin, S.S., Lee, K.R., & Chen, C.C. (2012). The Ca(v)3.1 T-type calcium channel is required for neointimal formation in response to vascular injury in mice. *Cardiovasc.Res.* **96**, (3) 533-542.

Vaillancourt, M., Ruffenach, G., Meloche, J., & Bonnet, S. (2015). Adaptation and remodelling of the pulmonary circulation in pulmonary hypertension. *Can.J.Cardiol.* **31**, (4) 407-415.

Varghese, E. & Busselberg, D. (2014). Auranofin, an anti-rheumatic gold compound, modulates apoptosis by elevating the intracellular calcium concentration ([Ca²⁺]_i) in mcf-7 breast cancer cells. *Cancers.(Basel)* **6**, (4) 2243-2258.

Vitko, I., Chen, Y., Arias, J.M., Shen, Y., Wu, X.R., & Perez-Reyes, E. (2005). Functional characterization and neuronal modeling of the effects of childhood absence epilepsy variants of CACNA1H, a T-type calcium channel. *J.Neurosci.* **25**, (19) 4844-4855.

Wakasugi, N., Tagaya, Y., Wakasugi, H., Mitsui, A., Maeda, M., Yodoi, J., & Tursz, T. (1990). Adult T-cell leukemia-derived factor/thioredoxin, produced by both human T-lymphotropic virus type I- and Epstein-Barr virus-transformed lymphocytes, acts as an autocrine growth factor and synergizes with interleukin 1 and interleukin 2. *Proc.Natl.Acad.Sci.U.S.A* **87**, (21) 8282-8286.

Wan, J., Yamamura, A., Zimnicka, A.M., Voiriot, G., Smith, K.A., Tang, H., Ayon, R.J., Choudhury, M.S., Ko, E.A., Wang, J., Wang, C., Makino, A., & Yuan, J.X. (2013). Chronic hypoxia selectively enhances L- and T-type voltage-dependent Ca²⁺ channel activity in pulmonary artery by upregulating Cav1.2 and Cav3.2. *Am.J.Physiol Lung Cell Mol.Physiol* **305**, (2) L154-L164.

Wang, D., Hirase, T., Inoue, T., & Node, K. (2006). Atorvastatin inhibits angiotensin II-induced T-type Ca²⁺ channel expression in endothelial cells. *Biochem.Biophys.Res.Commun.* **347**, (2) 394-400.

Wang, L., Bhattacharjee, A., Zuo, Z., Hu, F., Honkanen, R.E., Berggren, P.O., & Li, M. (1999). A low voltage-activated Ca²⁺ current mediates cytokine-induced pancreatic beta-cell death. *Endocrinology* **140**, (3) 1200-1204.

Wang, L., Zhang, J., Fu, W., Guo, D., Jiang, J., & Wang, Y. (2012). Association of smooth muscle cell phenotypes with extracellular matrix disorders in thoracic aortic dissection. *J.Vasc.Surg.* **56**, (6) 1698-709, 1709.

Wang, Y.Q., Brooks, G., Yuan, W.Z., Zhu, C.B., Li, Y.Q., & Wu, X.S. (2002a). [Functional analysis of the alpha1G subunit of the T-type calcium channel in cellular proliferation]. *Shi Yan.Sheng Wu Xue.Bao.* **35**, (3) 229-235.

Wang, Y.Q., Brooks, G., Zhu, C.B., Yuan, W.Z., Li, Y.Q., & Wu, X.S. (2002b). [Functional analysis of the human T-type calcium channel alpha 1H subunit gene in cellular proliferation]. *Yi.Chuan Xue.Bao.* **29**, (8) 659-665.

Watson, W.H., Pohl, J., Montfort, W.R., Stuchlik, O., Reed, M.S., Powis, G., & Jones, D.P. (2003). Redox potential of human thioredoxin 1 and identification of a second dithiol/disulfide motif. *J.Biol.Chem.* **278**, (35) 33408-33415.

Weichsel, A., Gasdaska, J.R., Powis, G., & Montfort, W.R. (1996). Crystal structures of reduced, oxidized, and mutated human thioredoxins: evidence for a regulatory homodimer. *Structure.* **4**, (6) 735-751.

Weiss, N., Black, S.A., Bladen, C., Chen, L., & Zamponi, G.W. (2013). Surface expression and function of Cav3.2 T-type calcium channels are controlled by asparagine-linked glycosylation. *Pflugers Arch.* **465**, (8) 1159-1170.

Welsh, S.J., Bellamy, W.T., Briehl, M.M., & Powis, G. (2002). The redox protein thioredoxin-1 (Trx-1) increases hypoxia-inducible factor 1alpha protein expression: Trx-

1 overexpression results in increased vascular endothelial growth factor production and enhanced tumor angiogenesis. *Cancer Res.* **62**, (17) 5089-5095.

Wiesel, P., Foster, L.C., Pellacani, A., Layne, M.D., Hsieh, C.M., Huggins, G.S., Strauss, P., Yet, S.F., & Perrella, M.A. (2000). Thioredoxin facilitates the induction of heme oxygenase-1 in response to inflammatory mediators. *J.Biol.Chem.* **275**, (32) 24840-24846.

Wong, K., Parente, J., Prasad, K.V., & Ng, D. (1990). Auranofin modulated cytoplasmic free calcium in neutrophils by mobilizing intracellular calcium and inhibiting protein kinase. *J.Biol.Chem.* **265**, (35) 21454-21461.

Wu, S., Zhang, M., Vest, P.A., Bhattacharjee, A., Liu, L., & Li, M. (2000). A mibefradil metabolite is a potent intracellular blocker of L-type Ca²⁺ currents in pancreatic beta-cells. *J.Pharmacol.Exp.Ther.* **292**, (3) 939-943.

Xiang, Z., Thompson, A.D., Brogan, J.T., Schulte, M.L., Melancon, B.J., Mi, D., Lewis, L.M., Zou, B., Yang, L., Morrison, R., Santomango, T., Byers, F., Brewer, K., Aldrich, J.S., Yu, H., Dawson, E.S., Li, M., McManus, O., Jones, C.K., Daniels, J.S., Hopkins, C.R., Xie, X.S., Conn, P.J., Weaver, C.D., & Lindsley, C.W. (2011). The Discovery and Characterization of ML218: A Novel, Centrally Active T-Type Calcium Channel Inhibitor with Robust Effects in STN Neurons and in a Rodent Model of Parkinson's Disease. *ACS Chem.Neurosci.* **2**, (12) 730-742.

Xiao, Q., Zhang, F., Grassia, G., Hu, Y., Zhang, Z., Xing, Q., Yin, X., Maddaluno, M., Drung, B., Schmidt, B., Maffia, P., Ialenti, A., Mayr, M., Xu, Q., & Ye, S. (2014). Matrix metalloproteinase-8 promotes vascular smooth muscle cell proliferation and neointima formation. *Arterioscler.Thromb.Vasc.Biol.* **34**, (1) 90-98.

Xu, S.Z., Sukumar, P., Zeng, F., Li, J., Jairaman, A., English, A., Naylor, J., Ciurtin, C., Majeed, Y., Milligan, C.J., Bahnasi, Y.M., Al-Shawaf, E., Porter, K.E., Jiang, L.H., Emery, P., Sivaprasadarao, A., & Beech, D.J. (2008). TRPC channel activation by extracellular thioredoxin. *Nature* **451**, (7174) 69-72.

Yang, J., Ellinor, P.T., Sather, W.A., Zhang, J.F., & Tsien, R.W. (1993). Molecular determinants of Ca²⁺ selectivity and ion permeation in L-type Ca²⁺ channels. *Nature* **366**, (6451) 158-161.

Yokoyama, U., Minamisawa, S., Adachi-Akahane, S., Akaike, T., Naguro, I., Funakoshi, K., Iwamoto, M., Nakagome, M., Uemura, N., Hori, H., Yokota, S., & Ishikawa, Y. (2006). Multiple transcripts of Ca²⁺ channel alpha1-subunits and a novel spliced variant of the alpha1C-subunit in rat ductus arteriosus. *Am.J.Physiol Heart Circ.Physiol* **290**, (4) H1660-H1670.

Yoshida, S., Katoh, T., Tetsuka, T., Uno, K., Matsui, N., & Okamoto, T. (1999). Involvement of thioredoxin in rheumatoid arthritis: its costimulatory roles in the TNF-alpha-induced production of IL-6 and IL-8 from cultured synovial fibroblasts. *J.Immunol.* **163**, (1) 351-358.

Yoshihara, E., Masaki, S., Matsuo, Y., Chen, Z., Tian, H., & Yodoi, J. (2014). Thioredoxin/Txnip: redoxosome, as a redox switch for the pathogenesis of diseases. *Front Immunol.* **4**, 514.

Yoshioka, J., Schulze, P.C., Cupesi, M., Sylvan, J.D., MacGillivray, C., Gannon, J., Huang, H., & Lee, R.T. (2004). Thioredoxin-interacting protein controls cardiac hypertrophy through regulation of thioredoxin activity. *Circulation* **109**, (21) 2581-2586.

You, B.R., Shin, H.R., & Park, W.H. (2014). PX-12 inhibits the growth of A549 lung cancer cells via G2/M phase arrest and ROS-dependent apoptosis. *Int.J.Oncol.* **44**, (1) 301-308.

Zhang, G., Nitteranon, V., Guo, S., Qiu, P., Wu, X., Li, F., Xiao, H., Hu, Q., & Parkin, K.L. (2013). Organoselenium compounds modulate extracellular redox by induction of extracellular cysteine and cell surface thioredoxin reductase. *Chem.Res.Toxicol.* **26**, (3) 456-464.

Zhang, H., Du, Y., Zhang, X., Lu, J., & Holmgren, A. (2014). Glutaredoxin 2 reduces both thioredoxin 2 and thioredoxin 1 and protects cells from apoptosis induced by auranofin and 4-hydroxynonenal. *Antioxid.Redox.Signal.* **21**, (5) 669-681.

Zhang, L. & Wang, H.H. (2015). The Genetics and Pathogenesis of Thoracic Aortic Aneurysm Disorder and Dissections. *Clin.Genet.*

Zhang, S.H., Reddick, R.L., Piedrahita, J.A., & Maeda, N. (1992). Spontaneous hypercholesterolemia and arterial lesions in mice lacking apolipoprotein E. *Science* **258**, (5081) 468-471.

Zhang, Y., Zhang, J., Jiang, D., Zhang, D., Qian, Z., Liu, C., & Tao, J. (2012). Inhibition of T-type Ca(2)(+) channels by endostatin attenuates human glioblastoma cell proliferation and migration. *Br.J.Pharmacol.* **166**, (4) 1247-1260.

Zhao, Y., Li, X., & Tang, S. (2015). Retrospective analysis of the relationship between elevated plasma levels of TXNIP and carotid intima-media thickness in subjects with impaired glucose tolerance and early Type 2 diabetes mellitus. *Diabetes Res.Clin.Pract.* **109**, (2) 372-377.